Photonic Crystal Templates for Sensing Applications: Modelling, Fabrication, and Experiments

A thesis submitted in partial fulfilment for the degree of

Doctor of Philosophy

in

Physics

by

Saranya Narayanan

Registration Number: 17PHPH30

Under the supervision of

Prof. B. V. R. Tata

&

Dr. Ramchandrarao Yalla (Co-Supervisor)





School of Physics, University of Hyderabad Hyderabad – 500 046, India

July 2024

To

My Father

Declaration

I, Saranya Narayanan, hereby declare that this thesis entitled "Photonic Crystal

Templates for Sensing Applications: Modelling, Fabrication, and Experiments"

submitted by me under the supervision of Prof. B. V. R. Tata and Dr. Ramchandrarao

Yalla (co-supervisor), School of Physics, University of Hyderabad, Hyderabad is a

bonafied research work and also free from plagiarism. The work is original and has not

been submitted earlier as a whole or in part for the award of any degree/diploma to this

University or any other University / Institution.

Saranya Narayanan

Reg. No. 17PHPH30

Date: 08/07/2024

Place: Hyderabad

Ш

Certificate





This is to certify that the thesis entitled "Photonic Crystal Templates for Sensing Applications: Modelling, Fabrication, and Experiments" bearing Reg. No. 17PHPH30, in fulfilment of the requirements for the award of Doctor of Philosophy in Physics is a bonafide work carried out by Saranya Narayanan under our supervision and guidance.

This thesis is free from plagiarism and has not been submitted earlier in part or in whole to this University or any other University/Institution for the award of any degree/diploma.

Further, the student has the following publications before the submission of the thesis for adjudication.

- Saranya Narayanan, Pratyasha Sahani, Jagannath Rathod, B.V.R. Tata, Soma Venugopal Rao, Ramachandrarao Yalla, *Phys. Scr.*, 99, 035512 (2024)
- Pratyasha Sahani, Saranya Narayanan, B.V.R. Tata, Soma Venugopal Rao, Optics Communications, 528, 129026 (2023).
- 3. Saranya Narayanan, and B.V.R. Tata, AIP Conference Proceedings 2269, 030015 (2020)

and has made presentations in the following conferences:

- Saranya Narayanan, M.B. Bhavya, K. Lakshun Naidu, G. Krishna Podagatlapalli, Santhosh Kumar Balivada, and B.V.R Tata, "Detection of Dye Molecules Through Photonic Crystal Assisted Surface Enhanced Raman Scattering", 67th DAE Solid State Physics Symposium (DAE SSPS23), Vishakhapatnam, India, December 20-24, 2023
- 2. Saranya Narayanan, Nishant Shankhwar and B.V.R Tata, "Indigenous Development of Laser Diffraction Setup for Characterizing the Structure of Polystyrene colloidal crystals", Frontiers in Physics (FIP-2023), Hyderabad, India, March 3-4, 2023.
- Saranya Narayanan, Nishant Shankhwar and B.V.R Tata, "Indigenous Development of Laser Diffraction Setup for Characterizing the Structure of Photonic crystals", International Conference on Frontier Areas of Science and Technology (ICFAST-2022), 12th India-Japan Science and Technology Conclave, Hyderabad, India, September 09-10, 2022. (Best Poster Award)
- 4. Saranya Narayanan, Pratyasha Sahani , B.V.R. Tata, and Soma Venugopal Rao, "Thin Photonic Crystal Templates with Plasmonic Nanoparticles for Trace Molecule Detection using Surface Enhanced Raman Spectroscopy", DAE-BRNS National Laser Symposium (NLS-30), Mumbai, India, January 19-22, 2022. (Oral Presentation) (Best Poster Award)
- Saranya Narayanan and B. V. R. Tata, "Effect of doping on defect modes of 2D photonic band gap crystals", International Conference on Multifunctional Materials (ICMM-2019), Hyderabad, India, December 19-21, 2019
- 6. Saranya Narayanan and B. V. R. Tata, "Effect of Doping on the Reflection Spectra of 2D Photonic Band Gap Crystals", Pressing for Progress-2019, An IPA National conference towards gender equity in Physics, Hyderabad, India, September 19-21, 2019

Further, the student has passed the following course towards the fulfilment of course work required for Ph.D.

SN	Course no	Title	Credits	Pass/Fail
1	PY801	Research Methodology	4	Pass
2	PY802	Advanced Quantum Mechanics	4	Pass
3	PY803	Advanced Experimental Techniques	4	Pass

Prof. B.V.R Tata

Supervisor

School of Physics

University of Hyderabad

Hyderabad, 500 046

Dr. B.V.R. TATA

Professor School of Physics, University of Hyderabad, achibowli, Hyderabad-500 046, INDIA

Dean

School of Physics

University of Hyderabad

Hyderabad, 500 046

DEAN

School of Physics University of Hyderabad HYDERABAD - 500 046 Dr. Ramachandrarao Yalla

Co-supervisor

School of Physics

University of Hyderabad

Hyderabad, 500 046

Dr. RAMACHANDRAKAO YALLA Assistant Professor School of Physics University of Hyderabad Hyderabad, INDIA - 500 046

VI

Acknowledgement

I could not even begin to talk about my Ph.D thesis without acknowledging all the institutions, funding bodies and people who helped throughout the journey by supporting professionally and personally. I am greatly obliged to University of Hyderabad which has been my home for past several years and contributed to my professional and personal growth immensely. I came to this city with little experience of outside world and it completely transformed me as a person. I owe that to the University of Hyderabad and the people I had the fortune to meet.

I want to express my deep gratitude to my supervisor Prof. B.V.R Tata whose constant guidance and support in all the stages of my research work. I always admired depth of his knowledge in almost all fields of physics. His attention to detail and the uncompromised sense of perfection helped me to increase the quality of work. I would like to extend the gratitude to my Co-supervisor Dr. Ramachandrarao Yalla for always providing useful feedbacks and guidance. I thank my DRC members Prof. Surajith Dhara and Prof. Sharath Ananthamoorthy for providing right feedbacks for me all the time. I'm grateful to Prof. Dhara for allowing me to use his laboratory facilities. I cannot thank enough Prof. Soma Venugopal Rao for the collaborative work we had. He completely included me in his lab and gave the freedom to work in the lab and use the Raman spectrometer. I could not finish my thesis work without his constant support and the right feedbacks. I thank Prof. Sriram Gopal for allowing me to use the UV-Visible spectroscopy. I also thank Prof. K.C. James Raju, Dean School of Physics and the past Deans, Prof. A Bindu Bamba, Prof. Ashok Chatterjee, and Prof. V. Seshu Bai.

I would like to thank Dr. Pratyasha Sahani for her collaboration. She has been an important part of my thesis journey, always available to share doubts and answer questions without making me feel foolish. She was the perfect teammate. Additionally, I would like to thank the other research associates who worked in our lab: Dr. Chandu Byram and Dr. Nisha Gautham. I also extend my gratitude to Dr. Nishant Shankwar for being available to discuss anything related to COMSOL Multiphysics and modeling. I thank Jagannath Rathod for teaching me how to operate the Raman spectrometer and for assisting with my initial measurements and sample preparation. I greatly acknowledge Dr. Reshma Beeram and Dipanjan Banarjee, experts in SERS studies, for all the valuable discussions. I received my initial training in COMSOL Multiphysics in Prof.

Anantharamakrishna's lab at IIT Kanpur. I am grateful to him for his generosity and for helping me understand the software. Additionally, I thank Dr. Abhinav Bharadwaj for further training me in COMSOL Multiphysics. I cannot thank enough my two wonderful labmates, Dr. Saisavadas M.V and Mr. Vintha Sivaram, who have made my PhD journey much easier with their presence. I am greatly thankful for their companionship and for all the discussions we had on all the topics under the sky. I am really grateful to Saisav for all the assistance he has provided during the synthesis and sample preparation stages. I am very much thankful to Mrs. P. V. Rajamani for her meticulous proofreading, which greatly improved the thesis. Her constant support, warmth and appreciation for even the little things helped me to voyage through these years.

I would like to express my sincere thanks to many people from SoP who helped me during this journey. I thank Devika V.S. and Abhinash Bharthankur for helping me use the spin coater facility. I would like to thank Mr. Sajin Ponnan and Ms. Shilpa M. for helping me use the UV-Visible spectrometer and for all the help Sajin has provided, which contributed to my thesis. I also thank Mr. Poly Rose for making sample holders and cutting samples. I also thank all the office staffs in SoP and the staffs from sanitation department for making my life in UoH easier. And I thank all my friends for all the support and companionship they generously given throughout the years.

The development of laser diffraction setup was supported by the Science and Engineering Research Board (SERB), Core Grant Project (CRG) of the Department of Science and Technology (Project number: DST-SERB/CRG/2019/003714) with Prof. B.V.R Tata as PI and Prof. Soma Venugopal Rao as Co-PI. I was supported by the DST-INSPIRE fellowship for a tenure of 5 years (2018 to 2023). I greatly acknowledge the support of DST, India.

Last but not the least, I want to thank my family. I thank my mother, Mrs. Santha, for all the unconditional love and care she showered upon me, even when she had doubts. Thank you for believing in me. I thank my father, Mr. Narayanan B.K, for all the love he left in my heart. I wouldn't have finished the thesis if it wasn't for you. Thank you for always being proud of me. I want to thank my brother for being there for me. Thank you for making my life the best and for making me feel safe, knowing that I can always come back to you. And finally, I want to thank my favorite soul in the whole world, my grandmother, for unconditionally loving me all along.

Saranya Narayanan

Contents	Page No.
Synopsis	XIII
List of Figures	XX
List of Tables	XXIX
List of Symbols	XXX
List of Abbreviations	XXXII
Chapter 1	1
Introduction	1
1.1 Photonic crystals	2
1.1.1 The History of Photonic Crystals	3
1.2 Electromagnetic waves through Photonic crystals	4
1.3 Fabrication of Photonic crystals	6
1.3.1 Hybrid approach	6
1.3.2 Bottom-up approach	9
1.4 Colloidal Photonic crystals (CPhCs)	12
1.4.1 Charged colloidal photonic crystals	12
1.4.2 Colloidal Opal Photonic crystals	13
1.4.3 Photonic Band Structure (PBG) in CPhCs	15
1.5 Surface Enhanced Raman Scattering (SERS)	16
1.5.1 Plasmonic Resonance	18
1.5.2 SERS Enhancement Mechanisms	19
1.6 Applications of PhCs	21
1.6.1 Applications of CPhCs	22
1.6.2 CPhC Assisted Sensing	24
1.7 Motivation	27
References	29
Chapter 2	44
Experimental and Simulation Techniques	44
2.1 Introduction	44
2.2 Synthesis and Purification of Colloidal particles	45

2.2.1 Synthesis of Polystyrene colloidal particles	45
2.2.2 Purification of colloidal particles	49
2.3 Fabrication of different types of CPhCs	52
2.3.1 CPhC with bcc and fcc ordering in aqueous medium	52
2.3.2 Opal type CPhC	52
2.3.3 CPhC monolayer	53
2.4 Experimental Techniques	54
2.4.1 Development of Laser Diffraction Setup	54
2.4.2 Dynamic light Scattering (DLS) Technique	61
2.4.3 UV-visible spectroscopy	65
2.4.4 Field emission scanning electron microscopy (FESEM)	67
2.4.5 Raman Spectroscopy	69
2.5 Simulation techniques	75
2.5.1 Finite Element Method (FEM)	75
2.5.2 Plane Wave Method (PWM)	83
References	84
Chapter 3	87
Understanding Photonic Crystals through Band structure and	
3.1 Introduction	
3.2 Theory	
3.3 Simulation details	
3.3.1 Band structure calculations	90
3.3.2 Reflectance calculations	91
3.4 Results and discussion	93
3.4.1 Square lattice	93
3.4.2 Hexagonal lattice	99
3.5 Summary	103
References	104
Chapter 4	
Numerical Simulation of Internal Electric Field Distribution in Crystal Thin Films	
C1 y5ta1 1 HH I HHI5	······································

4.1 Introduction	107
4.2 Computational details	108
4.3 Results and discussion	110
4.3.1 Reflectance spectra	110
4.3.2. Internal electric field distribution	112
4.3.3 Comparison of internal electric field distribution in PSPhC	
4.4 Summary	120
References	
Chapter 5	123
Raman Signal Enhancement of Molecules by Thin Colloid	_
5.1 Introduction	123
5.2 Experimental and simulation details	125
5.2.1 PSPhC monolayer template	125
5.2.2 AuNP SERS substrate	126
5.2.3 Simulation details	126
5.3 Results and discussion	128
5.3.1 Raman spectroscopic measurements	128
5.3.2 Electromagnetic simulations	130
5.4 Summary	133
References	134
Chapter 6	136
Thin Colloidal Photonic Crystal Template Decorated with Detection	_
6.1 Introduction	
6.2 Experimental details	
6.2.1 PSPhC monolayer SERS template	
6.2.2 UV-Visible spectroscopic studies	
6.2.3 Surface enhanced Raman spectroscopic studies	
6.2.4 Simulation details	
6.3 Results and discussion	

6.3.1. Surface enhanced Raman spectroscopic studies	142
6.3.2. Electromagnetic simulations on PSPhC monolayer template	146
6.4. Summary	149
References	150
Chapter 7	152
Summary and Future Work	152
7.1 Summary and Conclusions	152
7.2 Key Findings of the Thesis	157
7.3 Scope for Future studies	159
Publications Related to Thesis	160
Workshops/Conferences attended	160

Synopsis

Different types of photonic crystals (PhCs), which are structures with periodicity in refractive index at length scales of wavelength of visible light, are used in many fields to control light matter interactions. Colloidal photonic crystals (CPhCs), are extensively studied because of the excellent periodicity that can be achieved by the efficient and inexpensive method of self- assembly. Monodisperse colloidal particles of variety of dielectric materials including organic (polymers) and inorganic materials (eg:TiO₂, SiO₂, etc) can be synthesized effectively. The ease and control over synthesis procedure enables one to synthesis useful monodisperse particles of definite size, which is tunable by changing the synthesis conditions, and it enables the fabrication of a self-assembled CPhC with tunable stopbands. The light guiding mechanism in PhCs can provide several technological applications: CPhC thin films of monolayer and/or multilayer dielectric nanospheres (combined with metal nanoparticles) have emerged as ideal for enhancing the local electric field (known popularly as hot spots). Such CPhC structures expect to serve excellent template for sensing applications using Surface Enhanced Raman Spectroscopy (SERS). The excitation wavelength that lies inside the stop band is of fundamental and practical importance as is expected to enhance the light matter interaction manifold. Understanding the distribution of electric field (E-field) at different excitation wavelengths in PhCs and the mechanism of enhancement in E-field is expected to pave the way for design novel PhC temples for different applications.

Charge stabilized suspensions of monodisperse polystyrene (PS) colloidal particles can be synthesized through conventional emulsion polymerization method. These colloidal particles can be self-assembled to CPhCs (bulk as well as 2D films) through different evaporation techniques, or by controlling the electrostatic interaction in aqueous medium.

Since the length scales are in the wavelength of visible light (~ size of colloidal particles), these self-assembled CPhCs exhibit structural colors due to the Bragg diffraction of visible light, and possess photonic stopband in the visible region. The presence of stopband has been utilized in several sensing applications, where the change in effective refractive index or lattice constant due to external stimuli, viz. chemical or physical stimuli results in the shift in the position of the stopband. In turn, the wavelengths within the stop band can enhance the light matter interaction drastically, which can be used for sensing applications using SERS. The major focus of the thesis is on understanding of enhancement of light matter interaction in CPhCs at different excitation wavelengths, that are within or outside the stop bands, and fabricating CPhCs that can enhance E-field and there by using them for detection of different analyte molecules through SERS.

The thesis is structured in the following way. First chapter of the thesis, introduces to the fundamental concepts of PhC and photonic band structures and their applications. The experimental details including the synthesis of colloidal particles, different fabrication methods of CPhCs, development of laser light diffraction setup, other experimental techniques, and the electromagnetic (EM) simulation details are presented in Chapter 2. The numerical studies to understand PhCs through bandstructure, reflectance spectra and E- field distributions are presented in Chapter 3. Chapter 4 describes the FEM simulations on polystyrene colloidal photonic crystal (PSPhC) thin films for E-field distribution at on-resonance and off-resonance conditions. The experimental studies of Raman signal enhancement of dye molecules using PSPhC monolayer template are presented in Chapter 5. The SERS study of various dye molecules using PSPhC monolayer combined with AuNPs are presented in Chapter 6. Chapter 7 discusses the summary and conclusions of the investigations that have been carried out using EM simulations, and experimental studies using SERS. The key findings and directions for future work are also presented in Chapter 7.

Chapter 1. Introduction

A detailed introduction of the fundamental concepts and history of PhCs are provided in the first part of this chapter. The principle of propagation of electromagnetic waves through periodic dielectric structures are described using Maxwell's equations and the origin of bandgap is described. Different types of CPhCs and the existence of stopband are detailed. Various applications of CPhCs are also briefly described in the chapter. The basic concepts and enhancement mechanisms in SERS including the plasmonic resonance are described in detail in this chapter. Finally, chapter 1 concludes with the motivation and general outline of the thesis.

Chapter 2. Experimental and Simulation Techniques

The experimental details including the synthesis of colloidal particles, fabrication and characterization of CPhCs, and the EM simulation details are presented in chapter 2. Synthesis details of PS colloidal particles using emulsion polymerization method and purification of the freshly synthesized suspension through dialysis, ultrafiltration and using mixed bed of ion exchange resins are also described in detail. The fabrication of different types of CPhCs with PS colloidal particles are presented. The development of a laser light diffraction setup for the structural characterization of different types of CPhC samples is presented in chapter 2. The synthesized colloidal particles are characterized for its size and size polydispersity using dynamic light scattering technique. The fabricated PSPhC monolayers are characterized for the ordering using scanning electron microscopy and its working principled is described. The reflectance/ absorption spectra of the fabricated photonic crystals are recorded using UV-visible spectroscopy. The basic theory of Raman spectroscopy and the working of Raman spectrometer are presented in detail. Finally, the simulation techniques, including finite element method (FEM), and plane wave method (PWM) are described in this chapter.

Chapter 3. Understanding Photonic crystals through Band structure and Reflectance calculations

Understanding PhCs requires knowledge about the photonic band structure, which depends on the symmetry and structural parameters of the PhC. One of the simplest types of PhCs to start with is a two-dimensional photonic crystal (2D PhC), where the periodicity is along only two directions (one plane). It is easy to model and simulate such a system since the computational time and memory requirements are lesser compared to other complicated structures, such as those found in three-dimensional (3D) PhCs. Understanding the band structure for different lattice symmetries and tuning the structural parameters to achieve band gap in specific wavelength ranges is fundamentally important for utilizing PhCs in various applications. In chapter 3, we investigate the band structure of 2D PhC with different symmetry (square and hexagonal), and dependance of band gap on the structural parameters for attaining optimum band gap in the visible region. The lattice structures we have chosen are with square and hexagonal structures of amorphous titania rods of infinite length. Additionally, we present effect of defects in the reflectance spectra and E-field distributions of these 2D PhCs. The effect of dielectric contrast on the position of defect modes within the bandgap is also discussed. The bandstructure calculations are carried out using MIT photonic bandgap (MPB) software employing the PWM and the reflectance calculations are carried out using COMSOL multiphysics software using FEM.

Chapter 4. Numerical Simulation of Internal Electric Field Distribution in Colloidal Photonic Crystal Thin Films

Colloidal photonic crystal (CPhC) thin films of monolayer and/or multilayer dielectric nanospheres have been reported using surface-enhanced Raman spectroscopy. However, the internal E- field distributions in mono and/or multilayered CPhC thin films have not been well studied in the literature. The internal E- field distribution in the monolayer, and top layers of bilayer and trilayer CPhC films is investigated in detail in this chapter using COMSOL

Multiphysics software with wave optics module. The monolayer, bilayer, and trilayer PhC films consist of one-, two-, and three- layers of hexagonally close-packed spherical PS colloidal particles. We have extended our investigation to include the dependency of E- field distribution on incident wavelengths (lying at different spectral regimes of the CPhC films; in particular the on-resonance and off-resonance wavelengths). On-resonance wavelength means that lies inside the stop band of the CPhC films and off-resonance wavelength lies outside the forbidden photonic band. These simulations reveal that at on-resonance condition the E-filed gets localized and enhanced at the air void regions of the close packed CPhC. Whereas at off-resonance condition, the maximum E-field is localized and enhanced inside the colloidal particle. Our calculations reveled that the choice of incident wavelength plays an important role in better E- field enhancement at specific CPhC sites, and shows that CPhC films can serve as templates for sensing applications.

Chapter 5. Raman Signal Enhancement of Molecules on Thin Colloidal Photonic Crystal Template

In this chapter we investigate the effect of thin PSPhC template in the enhancement of Raman signal of some analyte molecules. This is to verify the simulation work carried out in Chapter 4. At on-resonance wavelength, where the excitation wavelength falls inside the stop band of the PSPhC, the E- field is redistributed on the surface of the PSPhC in such a way that the maximum E- field is localized and enhanced at the void regions of the particle array. In this chapter we experimentally verify it by conducting the Raman spectroscopic studies on the methylene blue (MB) dye, which is taken as a test molecule, on a bare glass substrate vs. on a PSPhC monolayer template. Additionally, we perform EM simulations specifically at the excitation wavelength used in the experiments and compared it with the E-filed distribution on a glass substrate as well as on the template of gold nanoparticles (AuNP) distributed on a glass substrate. The results show that there is a significant enchantment in the Raman signal of the

analyte molecules when a bare glass substrate is replaced with a PSPhC monolayer template, hence the PSPhC monolayer template can serve as an alternative to AuNP on a glass substrate.

Chapter 6. Thin Colloidal Photonic Crystal Template for SERS Detection

The investigations in Chapter 5 shed light on the effect of thin PSPhC template in enhancing the Raman signal of analyte molecules. In this chapter, the combined effect of PSPhC and AuNPs is investigated. While there are studies in the literature on CPhC templates assisted SERS, the concept of on-resonance excitation, a property induced by the PhC structure, has not been investigated in detail experimentally. Limited studies have reported on monolayer colloidal particle arrays as templates, which can enhance the distribution and accessibility of hotspots generated by plasmonic nanoparticles or nanofilms. However, on-resonance excitation has been the primary focus in only a few of these studies, where the emphasis was on combining plasmonic nanoparticles with bulk PhCs. Here, we have investigated the effect of the PSPhC monolayer template on the Raman signal enhancement of some dye molecules under on-resonance excitation. In addition to the excellent control of the distribution of the AuNPs, we probe the on-resonance excitation, increasing the light-matter interaction. We also present EM simulations for PSPhC templates with AuNPs to study the E- field distribution to identify the enhanced E- field regions that are potential hot spots for improved SERS signals. The results show a significant enhancement in the Raman signal of the analyte molecules with the PSPhC monolayer- AuNPs template compared to a randomly distributed AuNPs on glass substrate. In Chapter 5, it is experimentally proved that the PSPhC monolayer serve as an alternative to a randomly distributed AuNPs SERS template in enhancing the Raman signal of analyte molecules. In this Chapter we showed that, AuNPs together with PSPhC monolayer serve as a better template than just AuNPs in detecting the analyte molecules.

Chapter 7. Summary and Future Work

This chapter covers the summary and conclusions from the investigations carried out in CPhCs by employing EM simulations and the experimental studies using SERS. Additionally, the key findings and the scope for future research are discussed here. Important findings of the thesis are as follows. From our simulations, it has been found that at onresonance excitation the E- field mainly localized and enhanced at the air void- wedge region of the hexagonally close packed array of the CPhC thin film, whereas at the off-resonance wavelength, the maximum field is localized inside the colloidal particles. This result has importance in the application in SERS where the E-field enhancement is the major contributor in the Raman signal enhancement. Raman signal of different dye molecules with and without the PSPhC monolayer template is recorded. It has been observed that, the thin PSPhC templates enhance the Raman signal of the molecules significantly. Furthermore, the PSPhC templates are combined with AuNPs resulted in achieving lower detection limits. The AuNPs trapped inside the void regions of the PSPhC monolayer template where the E- field is localized and enhanced at on resonance excitation. The combined effect of plasmonic resonance and photonic modes at on-resonance excitation enhances the E- field furthermore and produce stronger hotspots which helps in detecting the analyte molecules to very lower concentrations.

List of Figures

Figure No.	Figure Caption	Page No.
Fig. 1.1	Schematic representation of (a) 1D PhC (b) 2D PhC (c) 3D	2
	PhC. The red arrows represent the direction(s) of periodicity.	
Fig. 1.2	Flow chart of different PhC fabrication techniques.	7
Fig. 1.3	(a) Iridescence due to the Bragg reflection from the CPhC of	13
	charged polystyrene colloidal particles in aqueous medium of	
	volume fraction, 0.022. (b) the UV- Visible spectrum showing	
	the stop band centered around 555 nm.	
Fig. 1.4	(a) the iridescence from the opal type CPhC fabricated through	14
	inward growing self-assembly method with PS colloidal	
	particle of diameter 287nm. (b) the SEM image of the	
	hexagonal array of the PS particles (c) reflectance spectra of the	
	CPhC showing the stop band around 613 nm.	
Fig. 1.5	schematic representation of localised surface plasmon in a	19
	plasmonic NP with E- field hot pot on the poles of the NP along	
	the direction of E- field.	
Fig. 1.6	Diagram showing the applications of PhCs.	21
Fig. 2.1	The schematic representation of the emulsion polymerisation	47
	process of the monomer in the presence of a surfactant with a	
	concentration higher than CMC.	
Fig. 2.2	The polymerisation rate with respect to the time indication	47
	three stages, viz. initiation (I), propagation (II) and termination	
	(III)	
Fig. 2.3	Schematic illustration of synthesis set-up for PS colloidal	48
	particles through emulsion polymerisation.	
Fig. 2.4	(a) The dialysis tubing cellulose membrane filled with PS	50
	suspension and kept immersed in MilliQ water. (b) The	
	conductivity of the surrounded milliQ water as a function of	
	time (in units of days).	

Fig 2.5	schematic representation of purification using an ultra-filtration	51
	system under applied gas pressure.	
Fig 2.6	Schematic representation of fabrication of CPhC monolayer.	54
	(a) PS colloidal suspension drying on the spin coater (b)	
	Dispersing unstable monolayer on the water surface and	
	picking up using a pre-cleaned glass substrate (c) Hexagonally	
	close-packed PS colloidal particle monolayer formed on the	
	glass substrate after drying	
Fig 2.7	The schematic illustration of laser light diffraction setup.	57
Fig. 2.8	The photograph of the diffraction setup in the laboratory.	58
Fig 2.9	Schematics of scattering geometry. D: sample-to-detector	59
	distance, θ_i : scattering angle of i^{th} reflection, r_i : radial distance	
	from the centre to i^{th} reflection.	
Fig. 2. 10	(a) Diffraction pattern of the CPhC sample PS1. (b) ring pattern	59
	obtained from the diffraction pattern by distributing the total	
	intensity to the area of the ring with diameter r and width Δr	
	for further processing.	
Fig. 2.11	(a) Intensity as a function of q , and (b) structure factor as a	60
	function of q of the sample PS-1 indicating the peaks fitting	
	with planes of fcc lattice.	
Fig. 2.12	(a) The hexagonal diffraction pattern indicating the hexagonal	61
	symmetry of the CPhC of sample PS-2 (b) FESEM image of	
	the hexagonal arrangement of colloidal particles.	
Fig. 2.13	Schematic representation of Dynamic light scattering technique	64
Fig 2.14	Schematic representation of UV-visible spectroscopic	66
	technique.	
Fig 2.15	Schematic representation of field emission scanning electron	68
	microscopic technique.	
Fig. 2.16	The FESEM image of to the PSPhC monolayer (a) surface	69
	view, and (b) cross- sectional view, showing a single layer.	
Fig. 2.17	The Schematic representation of light scattering illustrates the	71
	incident light of frequency v and its scattering behavior.	

	D 1 1 4 4 1 1 1 1	
	Rayleigh scattering occurs when the scattered light has the	
	same frequency as the incident light. Stokes scattering refers to	
	the scattered light with a lower frequency than the incident	
	light, while anti-Stokes scattering is the scattered light with a	
	higher frequency than the incident light.	
Fig. 2.18	Schematic illustration of Raman scattering, showing the	72
	excitation and de-excitation of molecular vibrational states	
	resulting in Stokes and anti-Stokes lines and comparing the	
	Raman spectral lines with the Rayleigh spectral line.	
Fig. 2.19	Schematic representation of Raman spectroscopic technique.	75
Fig. 2.20	Mesh elements generated using Comsol Multiphysics software	77
	for (a) a straight line in one-dimensional geometry with line	
	segments as mesh elements (b) a two-dimensional geometry	
	with triangular shapes as mesh elements. (c) a three-	
	dimensional geometry with mesh elements of shape	
	tetrahedrons.	
Fig. 2.21	Basic mesh elements with number of nodes for one-	78
	dimensional, two dimensional and three-dimensional cases.	
Fig. 3.1	(a) The square array of dielectric cylinders by periodically	91
	repeating the unit cell, shown as the shaded square region (b)	
	the Brillouin and irreducible Brillouin zone (orange color	
	shaded region) of square lattice with the symmetry points Γ , X ,	
	and M along which the band structure is calculated. (c) The	
	hexagonal array of dielectric cylinders by periodically	
	repeating the unit cell (shown as the shaded rhombus). (d) the	
	Brillouin and irreducible Brillouin zone of hexagonal lattice	
	with the symmetry points Γ , K and M along which the band	
	structure is calculated.	
Fig. 3.2	(a) Schematic representation of computational domain of the	92
	square array of amorphous titania rods in air matrix. The wave	
	excitation is along y-direction with port boundary conditions	
	and they have been backed by perfectly matched layer (PML)	
	conditions and the lateral boundaries have been set to periodic	

Fig. 2.2	boundary condition (PBC) (b) computational domain with the defect, created by replacing the central lattice point with different materials keeping all the other parameters same. The array size has been varied to optimize the bandgap and the square lattice is replaced with hexagonal lattice to simulate the reflection spectra for hexagonal 2D PhC.	02
Fig. 3.3	(a) Optimization of band gap of the square 2D PhC for TE polarization. The maximum band gap of 36.6% is obtained for $r/a = 0.23$. (b) Band structure corresponding to $r/a = 0.23$ giving band gap between first and second TE bands shown in the shaded region. The Y-axis is represented in a/λ in units of c/a .	93
Fig. 3.4	(a) Reflectance spectra of the square lattice of titania cylinders for different array sizes. (b) Band gap for different array sizes.	95
Fig. 3.5	(a) Reflectance spectrum showing the defect mode corresponding to the air defect by a dip in the reflectance spectrum at 470.6 nm. (b) the plot of E-field distribution at 470.6 nm showing the localized monopole with the color label indicating the magnitude of the relative E-field. (c) the line plot of E-field along the vertical line $(x = 6a)$ passing through the center of the defect as shown in the inset.	95
Fig. 3.6	The effect of doping with different dielectric materials in the defect in a square 2D PhC (a) defect modes for Δn_d from 0.27 to 1.67 showing hole- type nature (b) variation of defect mode wavelength with respect to Δn_d of the hole- type defect (c) defect modes for Δn_d from 0.53 to 2.53 (d) variation of defect mode wavelength with respect to the Δn_d of the rod- type defect.	97
Fig. 3.7	(a) Reflectance spectra for $\Delta n_d = 1.33$, showing the defect mode as a dip in the reflectance spectrum at central wavelength 472.601 nm. (b) The contour plot of the defect mode showing a dipole nature with one nodal plane at the center of the defect	98

	with maximum relative E-field as 900. (c) The line graph of the	
	E-field values along the vertical line (x= 6a, white vertical line	
	as shown in the inset) passing through the center of the defect.	
Fig. 3.8	(a) Optimization of band gap for the hexagonal 2D PhC for TE	99
	polarization. The maximum band gap of 36.6% is obtained for	
	r/a = 0.21. (b) Band structure corresponding to $r/a = 0.21$	
	giving band gap between first and second TE bands shown in	
	the shaded region. The Y-axis is represented in α/λ in units of	
	c/a.	
Fig. 3.9	.Reflection spectrum for normal incidence (corresponding to	100
	ΓM direction) for TE polarization, showing band gap from 459	
	nm to 699 nm identified by the wavelength range in which the	
	reflectance is maximum.	
Fig 3.10	The effect of doping with different dielectric materials in the	101
	defect in a hexagonal 2D PhC. (a) defect modes for Δn_d from	
	0.27 to 1.67 showing hole- type nature (b) variation of defect	
	mode wavelength with respect to the Δn_d of the hole-type	
	defect, where the pink color band at the bottom indicates the air	
	band and the blue band at the top indicates the dielectric band	
	(c) defect modes for Δn_d from 0.33 to 2.53 showing rod-type	
	nature. (d) variation of defect mode wavelength with respect to	
	the Δn_d of the rod- type defect, where the pink color band at	
	the bottom indicates the air band and the blue band at the top	
	indicates the dielectric band.	
Fig. 3.11	(a) Reflectance spectrum showing the defect mode	102
	corresponding to the air defect by a dip in the reflectance	
	spectrum at 532.11 nm. (b) the contour plot of E-field	
	distribution at 532.111 nm showing the localized monopole	
	with the color label indicating the magnitude of the relative E-	
	field. (c) the line plot of E-field along the vertical line $(x = 6a)$	
	passing through the center of the defect as shown in the inset.	
Fig. 3.12	(a) Reflectance spectrum showing the defect mode	102
	corresponding to the air defect by a dip in the reflectance	

	spectrum at 559.609 nm. (b) the contour plot of E-field	
	distribution at 559.609 nm showing the localized monopole	
	with the color label indicating the magnitude of the relative E-	
	field. (c) the line plot of E-field along the vertical line ($x = \frac{1}{2}$	
	6a) passing through the center of the defect as shown in the	
	inset.	
Fig. 4.1	Schematic of the computational domain of monolayer PSPhC	110
	on a glass substrate. Bilayer and trilayer PSPhC films replace	
	the monolayer one-by-one in the same computation domain	
	while the vertical height of the domain can be adjusted. Light	
	is incident from the air region along -Z direction.	
Fig 4.2	Simulation results of reflection spectra of monolayer, bilayer,	111
	and trilayer PSPhC films. The vertical dashed lines R1 and R2	
	corresponds to the wavelength under consideration in the	
	following sections.	
Fig 4.3	Contour plot of normalized E- field in the monolayer PSPhC	113
	film at (a) $\lambda_{\text{on-res}} = 653$ nm, and (b) $\lambda_{\text{off-res}} = 360$ nm. The	
	sampling plane is at $Z = Z_1 = \alpha/2$. The black circles indicate	
	the circumference of the colloidal spheres in the sampling	
	plane. The color bars provide the strength of the E- field	
	represented by relative E- field values ($ E/E_{inc} $).	
Fig. 4.4	The line plots of normalized E- field at both λ_{on-res} and $\lambda_{off-res}$	114
	across the linear regions defined as (a) $y = 0.49 a$,(b) $y =$	
	-0.37 a, (c) $x = -0.49 a$, and (d) $x = 0$ in connection with	
	Fig. 4.3(a) and Fig. 4.3(b). The insets in (a-d) show the	
	positions of the chosen lines in monolayer PSPhC regime as	
	indicated by the red horizontal/vertical lines in the contour	
	plots.	
Fig. 4.5	Contour plot of normalized E- field in top layer of bilayer	115
	PSPhC at (a) $\lambda_{\text{on-res}} = 653$ nm, and (b) $\lambda_{\text{off-res}} = 360$ nm. The	
	sampling plane is at $Z = Z_1 + \sqrt{2a/\sqrt{3}}$.	
Fig. 4.6	The line plots of E-field values at both λ_{on-res} and $\lambda_{off-res}$ are	116
	plotted across the lines (a) $y = 0.66a$, (b) $y = -0.21a$, (c)	

	x = -0.49a, and (d) $x = 0$ in connection with Fig. 4.5 (a) and	
	(b). The insets in (a-d) show the positions of the chosen lines in	
	the top layer of bilayer as indicated by the red	
	horizontal/vertical lines in the contour	
Fig. 4.7	Contour plot of normalized E- field in top layer trilayer PSPhC	117
	at (a) $\lambda_{\text{on-res}} = 653$ nm, and (b) $\lambda_{\text{off-res}} = 360$ nm. The sampling	
	plane is at $Z = Z1 + 2\sqrt{2a}/\sqrt{3}$.	
Fig. 4.8	The line plots of E-field at both $\lambda_{on\text{-res}}$ and $\lambda_{off\text{-res}}$ across the	117
	linear regions (a) $y = 0.21a$, (b) $y = -0.65a$, (c) $x =$	
	-0.49a, and (d) $x = 0$ in connection with Fig. 4.7 (a) and (b).	
	The insets in (a-d) show the positions of the chosen lines in the	
	top layer of trilayer as indicated by the red horizontal/vertical	
	lines in the contour plots.	
Fig. 5.1	(a) FESEM image of PSPhC monolayer showing the highly	125
	close-packed hexagonal array. (b) The reflectance spectrum of	
	the fabricated PSPhC monolayer. The vertical dashed line	
	indicates the excitation wavelength chosen for the Raman	
	measurements which lies within the stopband (shown as shaded	
	region) of the PSPhC monolayer. Inset shows the photographic	
	image of red iridescence from the PSPhC monolayer for visible	
	light.	
Fig. 5.2	(a) The TEM image of AuNPs, indicating the morphology and	126
	spherical shape of the non-aggregated particles. (b) Extinction	
	spectra of AuNPs having SPR wavelength at 528 nm (dashed	
	line).	
Fig. 5.3	The schematic illustration of the computational domains of (a)	127
	a bare glass substrate (b) PSPhC monolayer (c) randomly	
	distributed AuNPs on a glass substrate.	
Fig. 5.4	Raman spectra of MB with 5 mM concentration detected on a	128
	bare glass substrate (black line) Vs. on PSPhC monolayer	
	template (red line).	
Fig. 5.5	Raman spectral measurements of different concentrations of	129
	MB on a (a) bare glass substrate. The lowest concentration of	

	MB detected on this substrate is 500 μM (b) PSPhC monolayer	
	template. The lowest concentration of MB detected on this	
	template is 50 μM	
Fig. 5.6	Raman spectral measurements of different concentrations of	130
	MB on AuNPs- glass SERS substrate. The lowest concentration	
	of MB detected on this substrate is 50 μM	
Fig. 5.7	The contour plots of normalised E- field distribution on a (a)	130
	bare glass substrate (b) PSPhC monolayer on glass substrate,	
	and (c) a AuNP on glass substrate.	
Fig. 5.8	The line graph of the normalized E-field distributions in glass	131
	substrate, AuNP on a glass substrate and PSPhC monolayer on	
	a glass substrate along the line (eq. $y = -8.5x + 16.5a$) on (i)	
	bare glass substrate (ii) PSPhC monolayer, and (ii) AuNP on	
	glass substrate.	
Fig. 5.9	The maximum E- field enhancement Vs. number density, np of	132
	AuNPs on a glass substrate	
Fig. 6.1	The schematic representation of SERS active PSPhC	138
	monolayer -AuNPs template created by drop casting AuNPs on	
	the PSPhC monolayer template and drying it.	
Fig. 6.2	(a) SEM image of PSPhC monolayer showing the highly close-	139
	packed hexagonal array. (b) SEM image of the drop casted	
	AuNPs on the PSPhC monolayer showing the AuNPs trapped	
	inside the voids of the PS spheres arranged in hexagonal array.	
	The inset shows a schematic representation of AuNPs (red-	
	colored tiny spheres) trapped inside the hexagonal array of PS	
	colloidal particles (white spheres).	
Fig. 6.3	The reflectance spectrum of the fabricated PSPhC monolayer	140
1 -5. 0.0	(red line) and extinction spectra of AuNPs (green) having SPR	1.0
	wavelength at 528 nm (green line). The red colour dashed line	
	indicates the excitation wavelength chosen for the Raman	
	spectroscopy which lies inside the stopband of the PSPhC	
	specialistics with the most of the 151 he	

	monolayer. Inset shows the photographic image of red	
	iridescence from the PSPhC monolayer for visible light.	
Fig. 6.4	(a) Schematic representation of the computational domain of	141
	PSPhC monolayer on a glass substrate. Direction of incident	
	light is shown as -ve Z- direction and perpendicular to the X-Y	
	plane of the PSPhC monolayer indicated by red color arrow. (b)	
	The top view of the PSPhC monolayer with close-packed	
	hexagonal array of PS colloidal particles placed on a glass	
	substrate at z=0. P1, P2 and P3 are the PS particles chosen to	
	represent a void region under touching configuration. (c)	
	Schematic of magnified wedge region formed by PS particles	
	P1, P2 and P3 of the PSPhC monolayer with a AuNP which is	
	shown in red colour.	
Fig. 6.5	(a) Raman spectra of 5 mM concentration of methylene blue	143
	(MB) dye on a bare glass substrate and (b) Raman spectra of 5	
	mM concentration of MB molecules on different SERS	
	substrates, viz. AuNPs drop casted on a bare glass plate and	
	AuNPs drop casted on a PSPhC monolayer template.	
Fig. 6.6	(a) Raman spectral measurements of different concentrations	144
	of MB on Glass -AuNPs SERS template. The lowest	
	concentration of MB detected on this substrate is 50 µM. (b)	
	Raman spectral measurements of different concentrations of	
	MB on PSPhC monolayer -AuNPs template. The lowest	
	concentration of MB detected on this substrate is 500 nM.	
Fig. 6.7	(-) P	145
	(a) Raman spectral measurements of different concentrations	
	of R6G on PSPhC monolayer -AuNPs template. The lowest	
	concentration of R6G detected on this substrate is 500 nM (b)	
	Raman spectral measurements of different concentrations of	
	MG on PSPhC monolayer -AuNPs template. The lowest	
	concentration of MG detected on this substrate is 50 nM.	

Fig. 6.8.	Linear dependence of SERS intensity (I) vs. analyte	146
	concentration (C) for the principal modes of MB, R6G and MG	
	molecule on PSPhC-AuNP template.	
Fig. 6.9	Contour plot of normalized E- field distribution in (a) PSPhC	147
	monolayer upon excitation by 633 nm wavelength shows the	
	redistribution of the electric field with E- field localized and	
	enhanced at the wedge regions of the touching PS colloidal	
	particles. (b) Normalized E- field distribution in the wedge	
	region of PSPhC monolayer with AuNP, and E- field shows	
	significant enhancement around AuNP. (c) The line plots of	
	electric field along the line defined by $y = -1.79x - 0.52a$.	
	The inset shows the line (red) passing through the wedge	
	region, W1(with AuNP) and wedge region, W2 (without the	
	AuNP). (d) The maximum E- field enhancement vs. number	
	density, np of AuNPs on a glass substrate (blue) and void	
	regions of PSPhC monolayer template (red). Simulations for	
	different substrates were carried out under identical conditions	
	of AuNP arrangement.	

List of Tables

Table No.	Table Caption	Page No.
Table 2.1	Details of reagents used in synthesis of Polystyrene (PS) colloidal particles along with the hydrodynamic diameter, d _h of PS particles at 25 ⁰ C and corresponding size polydispersity (SPD).	49

List of Symbols

Electric field	E
Magnetic field	$ec{H}$
Position vector	$ec{r}$
Dielectric constant	arepsilon
Volume fraction	ϕ
Effective charge	Ze
Surface charge density,	σ
Inverse Debye screening length	κ
Number density	n_p
Salt concentration	C_s
Effective refractive index	n_{eff}
Interplanar spacing	d_{hkl}
Lattice constant	a
scattering angle	heta
Bragg peak wavelength	λ_B
Scattered intensity	$I_s(q,t)$
Intensity autocorrelation function	$g^{(2)}(q,t)$
Electric field autocorrelation function	$g^{(1)}(q,t)$
Coherence factor	β
Magnitude of scattering wave vector	q

Incident wave vector	$\overrightarrow{k_{\iota}}$
Scattered wave vector	$\overrightarrow{k_{\scriptscriptstyle S}}$
Wavelength of the incident light	λ
Scattering angle	heta
Intermediate scattering function	f(q,t)
Dynamic structure factor	F(q,t)
Static structure factor	S(q)
Mean square displacement (MSD)	$< r^{2}(t) >$
Free diffusion coefficient	D_0
Boltzmann constant	k_B
Absolute temperature	T
Viscosity of the solvent	η
Hydrodynamic diameter	d_H
Decay constant	Γ
Glancing angle	$ heta_g$
Refractive index of the solution	$\mu_{\scriptscriptstyle \mathcal{S}}$
Initial energy of the molecule	E_i
Final energy of the molecule	E_s
Frequency of the incident radiation	$ u_i$
Frequency of scattered radiation	$ u_{\scriptscriptstyle S}$
Plank's constant	h
Polarizability	α
Induced dipole moment	μ_i
Raman shift	$\Delta ar{ u}$

Basis function N_j^e On-resonance wavelength $\lambda_{on\text{-}res}$ Off-resonance wavelength $\lambda_{off\text{-}res}$ Incident electric field E_{inc} Percentage enhancement %E

List of Abbreviations

PhC Photonic Crystal

PBG Photonic Bandgap

1D PhC One-dimensional Photonic Crystal

2D PhC Two-dimensional Photonic Crystal

3D PhC Three-dimensional Photonic Crystal

CPhC Colloidal Photonic Crystal

fcc Face-Centered Cubic

bcc Body- Centered Cubic

PS Polystyrene

PMMA Poly-Methyl Methacrylate

PNIPAM Poly-N-isopropylacrylamide

SERS Surface Enhanced Raman Spectroscopy

AuNP Gold Nanoparticle

IO PhC Inverse Opal Photonic Crystal

LSPR Localized Surface Plasmon Resonance

SPR Surface Plasmon Resonance

EME Electromagnetic Enhancement

CE Chemical enhancement

PSPhC Polystyrene colloidal photonic crystal

FEM Finite Element Method

PWM Plane Wave Method

PML Perfectly Matched Layers

PBC Periodic Boundary Conditions

FWHM Full Width at Half Maximum

NS Nanostructures

NP Nanoparticles

GNR Gold Nanorod

Chapter 1

Introduction

"I mean it's not just beauty at this dimension, at one centimeter; there's also beauty at smaller dimensions, the inner structure, also the processes. The fact that the colors in the flower evolved in order to attract insects to pollinate it is interesting; it means that insects can see the color. It adds a question: does this aesthetic sense also exist in the lower forms? Why is it aesthetic? All kinds of interesting questions which the science knowledge only adds to the excitement, the mystery and the awe of a flower. It only adds."

-Richard P. Feynman

Ever since human civilization, we have been trying to manipulate the flow of light to make our lives easier. Devices using sophisticated control and manipulation of light are designed using cutting edge technologies like artificial intelligence (AI) and machine learning in optics and photonics. Scientist's quests to manipulate, control, and harness the properties of light both in the macroscopic scale and nanoscale has paved the way for novel materials. Here, we explore the possibility of controlling and manipulating light at mesoscopic scale through photonic crystals to investigate their potential applications in detection platforms. This thesis presents both experimental and simulation studies, beginning with the synthesis of colloidal particles for photonic crystal fabrication, and subsequently exploring their application in SERS-based detection platforms. Additionally, the work includes an investigation of photonic crystal modes through electromagnetic simulations.

1.1 Photonic crystals

Photonic crystals (PhCs) are ordered periodic structures with a periodically varying refractive index, where the periodicity is of the order of the wavelength light. If the wavelength of the incident light, that is incident on the PhCs satisfy the Bragg condition, the periodic arrangement reflects the light thus prevent the propagation of that wavelength through the crystal. When a band of frequencies are forbidden to propagate in all three directions and for all polarizations of light, the periodic structure is said to have a complete photonic bandgap (PBG), and such structures are referred to as photonic bandgap crystalsA refractive index contrast (Δ n) greater than 2.7 is often necessary for achieving a complete photonic band gap in a three-dimensional PhC with a fcc structure [1-3].

Depending on the dimensionality of periodicity, PhCs are classified into three types: one-dimensional (1D PhC), two-dimensional (2D PhC), and three-dimensional (3D PhC) photonic crystals. In 1D PhCs, as seen in Bragg reflectors or multilayered films, the periodicity in refractive index exists along a single direction. The periodicity is only two directions in the case of 2D PhCs, such as 2D PhC slabs. If the refractive index exhibits periodicity along all three directions, the PhCs are referred to as 3D PhCs, as observed in structures like opals, inverse opals, wood pile structures, etc. The schematic representation of the 1D, 2D and 3D

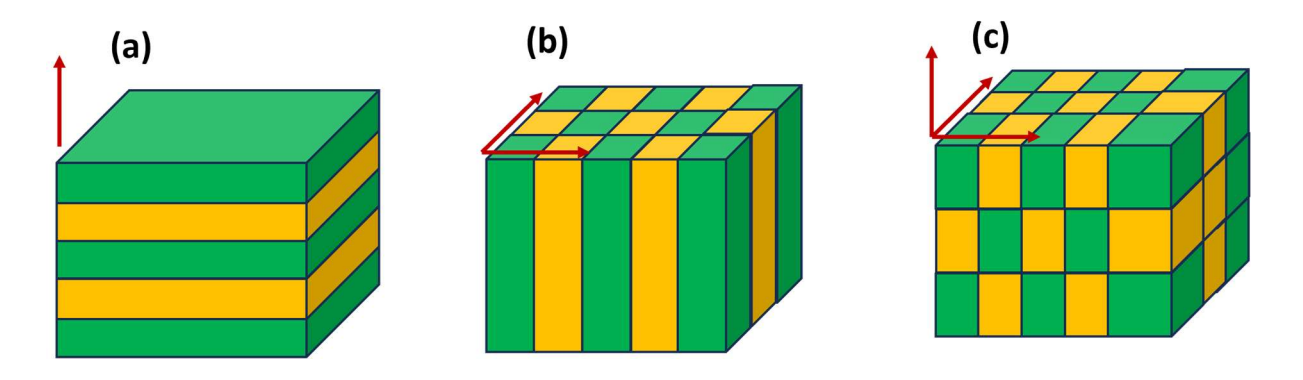


Fig. 1.1 schematic representation of (a) 1D PhC (b) 2D PhC (c) 3D PhC. The red arrows represent the direction(s) of periodicity

PhCs are given in Fig. 1.1. where the red arrows in each figure indicates the direction(s) of periodicity.

1.1.1 The History of Photonic Crystals

The idea of a one-dimensional stopband dates back to 1887 when Lord Rayleigh first derived it. In his paper [4], Rayleigh provided a formula for the edges of the forbidden gap in terms of the modulation period, and of the relative strength of the periodic density modulation. His proposal focused on 1D periodic structures, where even a small refractive index contrast would lead to the formation of a forbidden band gap. The notion of two- and three-dimensionally periodic crystals, along with their respective band gaps, was introduced only a century after Rayleigh's work, in 1987, by Eli Yablonovitch [5] and Sajeev John [6].

In the 1980s, Yablonovitch, noticed that losses in semiconductor lasers and similar devices due to light emitted at undesirable frequencies might be prevented by using a medium that prevents the transmission of these frequencies. He suggested fabricating a structure using transparent material that has air holes, resembling a crystal lattice, where the material and holes have distinct refractive indices. Yablonovitch predicted that the concept of a "band gap" in semiconductors, which limits certain electron energies, might also be applied to light frequencies in a photonic band gap. This would effectively remove such frequencies from the structure being considered. The existence of a periodic structure, in both scenarios, leads to the occurrence of destructive wave interference, whether it be electron waves or electromagnetic fields. This interference ultimately gives rise to the formation of the band gap. Coincidentally, at approximately the same time, Sajeev John from Princeton University put forth a comparable proposition on his own. They mutually agreed to designate structures that possess a band gap for electromagnetic waves as 'Photonic Crystals'.

In 1991 paper [7], Yablonovitch along with T.J. Gmitter, claimed to have the first photonic band gap structure, consisting of holes in a block of plastic with a fcc lattice structure.

Instead of infrared or visible light wavelengths, he worked with microwaves, which allowed him to make hole in milli meter size. It took again years for the fabrication of PhCs in optical wavelengths [8]. Since the first prediction of PhCs, they have been the subject of extensive research for various applications, including optical fibers [9], waveguides [10- 12], sensors[13- 16], optical switches [17], transducers [18], filters[19- 21], and display devices[22], etc.

1.2 Electromagnetic waves through Photonic crystals

Since, the electromagnetic wave propagation in any medium is governed by Maxwell's equations, let's start with the four Maxwell's equations, including two divergence equations and two curl equations:

$$\vec{\nabla}.\vec{H}(\vec{r},t) = 0$$

$$\vec{\nabla}.\left[\varepsilon(\vec{r})\vec{E}(\vec{r},t) = 0\right]$$
(1.1)

$$\vec{\nabla} \times \vec{E}(\vec{r}, t) + \mu_0 \frac{\partial \vec{H}(\vec{r}, t)}{\partial t} = 0$$

$$\vec{\nabla} \times \vec{H}(\vec{r}, t) - \varepsilon_0 \varepsilon(\vec{r}) \frac{\partial \vec{E}(\vec{r}, t)}{\partial t} = 0$$
(1.2)

Typically, the electric field (\vec{E}) and magnetic field (\vec{H}) are complex functions that depend on space (position vector, \vec{r}) and time (t), μ_0 is the permeability of free space, ε_0 is permittivity of free space, and $\varepsilon(\vec{r})$ is the position dependent permittivity. However, due to the linearity of Maxwell's equations, the time dependence can be separated from the spatial dependence by expanding the fields into a series of harmonic modes. A harmonic mode can then be expressed as the product of a spatial pattern and a complex exponential;

$$\vec{H}(\vec{r},t) = \vec{H}(\vec{r})e^{-i\omega t} \tag{1.3}$$

$$\vec{E}(\vec{r},t) = \vec{E}(\vec{r})e^{-i\omega t} \tag{1.4}$$

To derive the governing equations of the mode profiles at a specific frequency, we substitute these equations (1.3 & 1.4) into the set of Maxwell's equations. Then, the following conditions can be derived from the two divergence equations.

$$\vec{\nabla} \cdot \vec{H}(\vec{r}) = 0, \qquad \vec{\nabla} \cdot \left[\varepsilon(\vec{r}) \vec{E}(\vec{r}) \right] = 0$$
 (1.5)

This imposes a transversality condition on $\vec{H}(\vec{r})$ and $\varepsilon(\vec{r})\vec{E}(\vec{r})$. Now, we can focus only on the other two curl equations derived from the Maxwell's equations keeping these transversality conditions. The curl equations will take the form;

$$\vec{\nabla} \times \vec{E}(\vec{r}) - i\omega\mu_0 \vec{H}(\vec{r}) = 0$$

$$\vec{\nabla} \times \vec{H}(\vec{r}) + i\omega\varepsilon_0 \varepsilon(\vec{r}) \vec{E}(\vec{r}) = 0$$

$$(1.6)$$

Here, by dividing the equation of (1.4) by $\varepsilon(\vec{r})$ and substituting the equation (1.3) to eliminate $\vec{E}(\vec{r})$, the equations can be decoupled and expressed in the form of;

$$\vec{\nabla} \times \left(\frac{1}{\varepsilon(\vec{r})} \vec{\nabla} \times \vec{H}(\vec{r})\right) = \left(\frac{\omega}{c}\right)^2 \vec{H}(\vec{r}) \tag{1.7}$$

This Eigenvalue equation is called the Master equation with operator $\vec{V} \times \frac{1}{\varepsilon(\vec{r})} \vec{V}$ acting on the vector $\vec{H}(\vec{r})$ giving the Eigen value of $\left(\frac{\omega}{c}\right)^2$ where the speed of light $c = \frac{1}{\sqrt{\mu_0 \varepsilon_0}}$. This is the Master equation for a medium with position-dependent dielectric constant. By solving the above equation (1.7) one can get the dispersion characteristics of the propagating electromagnetic waves in the PhCs. For a particular structure, $\varepsilon(\vec{r})$ the Master equation can be solved to get the modes, $\vec{H}(\vec{r})$ and the corresponding frequencies, together with the divergence equations. After solving the equation (1.7) for $\vec{H}(\vec{r})$, we can recover the electric field modes through the equation;

$$\vec{E}(\vec{r}) = \frac{i}{\omega \varepsilon_0 \varepsilon(\vec{r})} \vec{\nabla} \times \vec{H}(\vec{r})$$
 (1.8)

Since the divergence of a curl is always zero, the electric field transversality condition $\vec{\nabla} \cdot \left[\varepsilon(\vec{r}) \vec{E}(\vec{r}) \right] = 0$ is also preserved here [23].

1.3 Fabrication of Photonic crystals

Different techniques have been used to PhCs depending on their intended applications. The fabrication techniques of PhCs can be broadly classified into bottom- up approach, or hybrid approaches (includes the combination of bottom- up and top-down approaches). The hybrid approach typically begins with a bulk material, from which the desired structure is carved out or patterned to achieve the final PhC structure. Techniques such as lithography, ion beam milling, and chemical etching fall under the hybrid approach category. These methods are effective for creating precise structures with controlled dimensions and periodicity in the micro wave region. On the other hand, the bottom-up approach, which is useful in the optical region, involves starting with fundamental building blocks, such as nanoparticles or molecules, and assembling them into the desired PhC structure through self-assembly or controlled growth processes. Examples of bottom-up techniques include self-assembly using block copolymers, colloidal crystal templating, and sol-gel processing. This approach offers advantages in creating complex structures at the nanoscale and can lead to novel optical properties based on the arrangement of the building blocks. A brief description about these two techniques are given below.

1.3.1 Hybrid approach

The fabrication of PhCs through hybrid approach involves three main stages: deposition of the film, definition of the pattern, and transfer of the pattern. Several methods used for film deposition include chemical vapor deposition (CVD) [24], molecular beam epitaxy (MBE) [25], and sputtering [26]. Different lithographic techniques [27] have been used to define

desired pattern on the deposited substrate. Figure 1.2 provides an overview of the primary lithographic techniques used for the fabrication of PhCs.

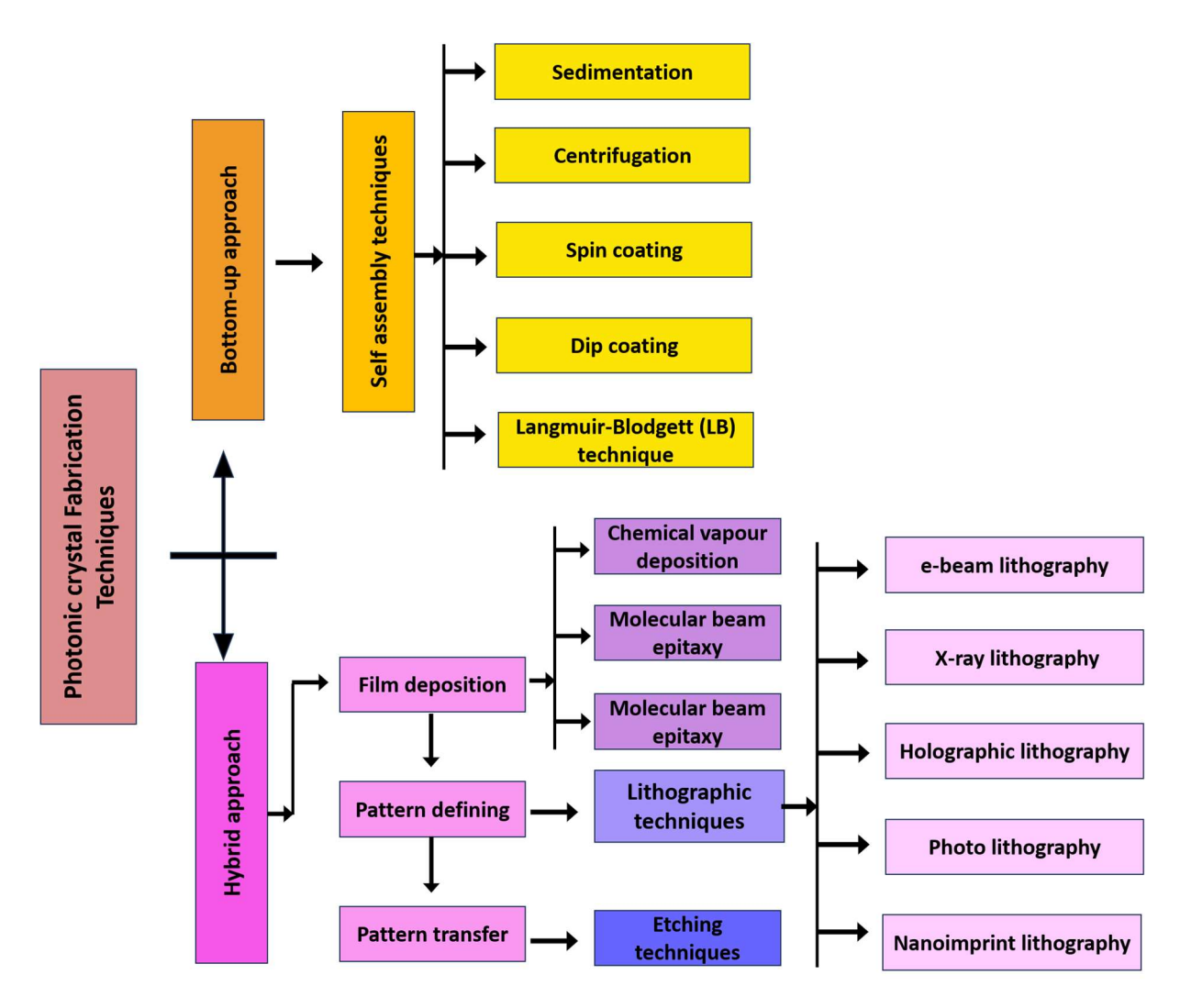


Fig. 1.2. Flow chart of different PhC fabrication techniques.

Electron beam lithography (EBL) utilizes a focused electron beam to pattern a resist layer deposited on a substrate. This resist layer, composed of an organic polymer material, is sensitive to the e-beam and which is categorized into two types: positive resist and negative resist [28]. In positive resist, exposure to the electron beam renders the resist soluble in the developer solution. Conversely, in negative resist, the exposed areas become insoluble in the developer. X-ray lithography [29] involves defining a pattern using a specialized mask with different local x-ray absorption. The design of the mask is then reproduced on a x-ray-sensitive

resist. Based on the chemical properties of the resist, exposure to x-rays can induce crosslinking (in the case of negative resists) or bond breaking (in positive resists). After exposure to x-rays, the whole structure is immersed in a specific solvent. The solvent interacts with the resist based on its nature: it either dissolves the exposed regions, revealing the desired pattern, or conversely, dissolves the unexposed areas, leaving the pattern intact on the resist surface. This process results in a precisely defined pattern on the resist, ready for further processing steps in fabrication. Holographic lithography [30] relies on the optical interference of multiple laser beams during a single light exposure. It offers a rapid and cost-effective method of fabrication by using the optical interference generated from laser beams to expose a photoresist material. This technique involves two phases of exposure: underexposed and overexposed, resulting from the duration of light exposure. Following exposure, one of the two exposed phases is selectively removed by applying a developer material to the photoresist. The resulting structure from the development step serves as a template for creating PBG materials. Photolithography, also referred to as optical lithography is a method used to create patterns on substrate through microfabrication techniques [31]. In this method, a defined geometric pattern is transferred using light from an optical mask onto a chemical photoresist applied to the substrate. This technique excels in generating very small and precisely controlled patterns, offering a cost-effective means of fabrication. Despite its advantages, photolithography has certain limitations. It requires a flat substrate and is less effective for shaping non-flat surfaces. Additionally, a highly clean operating environment is essential for successful implementation. Nanoimprint lithography (NIL) is a cost-effective technique for fabricating high-resolution nano-scale patterns [32]. Unlike optical lithography methods that rely on photons or electrons to alter the resist layer's properties, NIL achieves patterning through direct mechanical deformation of the resist. This approach allows NIL to achieve resolutions surpassing those limited by light diffraction or beam scattering.

1.3.2 Bottom-up approach

Hybrid techniques, while offering excellent precision and resolution in PhC structure, are typically expensive and time-consuming for fabricating in larger areas. Further, hybrid approach pose difficulty to make 3D structures. Conversely, bottom-up approaches depend on the self-assembly of particles to form ordered periodic structures, offering faster, more cost-effective fabrication on a larger scale compared to hybrid methods. Bottom- up approach have advantages over hybrid approach as it offer flexibility in fabricating 3D structures with desirable size of the crystals. However, bottom-up techniques may slightly compromise on the level of control and precision achievable compared to the hybrid approaches. Nevertheless, the affordability and ease of fabrication associated with bottom-up approaches make them a practical and competitive alternative to hybrid methods.

Bottom-up approaches for fabricating colloidal PhCs commonly utilize spherical beads, typically made of silica or polystyrene (PS) latex due to their effective synthesis to monodisperse particles. The self-driven assembly of colloidal PhCs is governed by colloidal forces that bring these tiny building blocks together. Within colloidal assembly, it's important to highlight three key types of forces at play. Firstly, intrinsic driving forces for ordering arise from the entropically favourable packing of monodisperse colloidal particles into periodic arrays. The monodispersity of particle size and shape is crucial for this process. Secondly, external forces with long-range effects, such as gravity or centrifugation, aid in bringing the particles closer together. Thirdly, electrostatic interactions [33] between the particles play a crucial role in preventing aggregation against. Van der Waals interaction [34] between the particles. Depending on the type of building block and intended structures (2D monolayers or 3D bulk PhCs) and the applications, there are several assembly methods available and some of which are listed in Fig. 1.2.

One of the most straightforward methods for self-assembly onto a substrate is sedimentation, mirroring the natural formation of opals where gravity acts on individual particles to form the opal structure [35]. Another approach is drop-casting, involving the deposition of a colloidal suspension onto a substrate surface followed by evaporation [36]. Particles are drawn together by the retreating meniscus of evaporating water, which causes them to reorganise into a form with the lowest surface energy. Adjusting variables including temperature, humidity regulation, suspension concentration, and substrate selection might improve the quality of colloidal crystals developed with this technique. Two techniques that make use of centrifugal forces to close-pack particles within a colloidal suspension are centrifugation and spin-coating. Centrifugation compacts the particles to produce bulk colloidal crystals of higher quality by spinning the colloidal suspension in a centrifuge at high speeds [37]. Conversely, spin coating is used to fabricate colloidal PhC monolayers or thin films on planar substrates [38], [39]. Still, the resulting colloidal PhC films may show nonuniformity throughout the substrate because of the varying forces that the suspension experiences at different points during spinning. Jiang et al. have created a reliable, affordable spin-coating technique that can be scaled up and integrated with conventional microfabrication processes [40]. Furthermore, they have shown that spin-coating can be used to create nonclose-packed 2D colloidal PhC arrays [41]. The process of vertical deposition involves driving the convective assembly of a colloidal PhC onto a substrate by evaporating the liquid phase of a colloidal suspension. This process involves holding the substrate vertically, or at a slight inclination, and partially immersing it in a colloidal suspension, unlike to drop casting, in which the substrate is horizontal [42]. This technique demands precise control over deposition conditions and environmental factors such as suspension concentration, solvent type, temperature, humidity, as well as minimizing disturbances like ground vibrations or air movement. The deposition process typically spans several days to allow complete evaporation

of the liquid (usually water). Any disruptions during drying can significantly compromise the quality of the resulting colloidal PhC. However, when executed correctly, this method can yield exceptionally high-quality colloidal PhCs. In the dip coating process, a substrate is carefully withdrawn from a colloidal suspension [43]. One end of the substrate is immersed in the colloidal suspension while it is positioned vertically. Convective assembly, which is similar to what is seen in vertical deposition, takes place at the contact between the substrate surface and the air/liquid interface when the substrate is gradually raised out of the suspension. One way to control the thickness of the formed colloidal PhC is to adjust the speed at which the substrate is withdrawn from the suspension. The Langmuir-Blodgett (LB) technique differs from the previously mentioned methods in its approach. Instead of directly fabricating colloidal PhCs onto substrates, a 2D colloidal PhC monolayer is initially formed on a water surface and subsequently transferred to a substrate in the two-step LB method [44]. To create the monolayer, a colloidal suspension is spread on the water surface and the particles are compacted using movable arms while monitoring the surface pressure to achieve a closepacked monolayer. This method is different from the direct interfacial self-assembly approach, in which particles are dispersed across a water surface and, without the need for moveable arms or physical compression, self-assemble into closed-packed arrays by modifying the surface tension using a surfactant [45], [46].

Self-assembled colloidal PhCs can be modified after development to modify them for particular uses. One method is nanosphere lithography, where the assembled colloidal crystal is infiltrated with additional materials and then the spheres are etched away to create a patterned surface. Similarly, by infiltrating the colloidal PhCs with a suitable material and then removing the template, inverse opals can be produced.

1.4 Colloidal Photonic crystals (CPhCs)

The advances in the synthesis of submicron- sized, highly monodisperse (Polydispersity < 10%) charged colloids [47], hard sphere colloids[36] and soft sphere (Thermo– responsive and pH responsive) colloids [48] enabled the self-assembly of the particles into the colloidal crystalline arrays, which are known as colloidal photonic crystals (CPhCs) [49]. These colloidal particles in aqueous suspension self-assemble into different crystal structures depending upon the volume fraction. For higher volume fractions (ϕ), it will crystallize to a face-centered-cubic (fcc) structure, whereas charge-stabilized aqueous suspensions of silica and polystyrene nanospheres self-assemble into body-centered cubic (bcc) at low volume fractions (ϕ < 0.15), and fcc at higher volume fractions (ϕ > 0.15) [50], [51]. Since the periodicity (lattice constant) of these CPhCs are in the visible range, they exhibit iridescence due to Bragg diffraction of visible light. Due to the long-range ordering of colloidal particles, CPhCs exhibit several unique characteristics, such as diffraction of light, photonic band gaps, structural colors, and high surface/volume ratio etc. [50], [52-56].

1.4.1 Charged colloidal photonic crystals

Monodisperse, charged colloidal particles suspended in aqueous medium interacts electrostatically and exhibit different structural ordering depending on the strength and range of these interactions. The coulomb repulsive interaction potential between the charged colloidal particles is given by;

$$U(r) = \frac{Z^2 e^2}{\varepsilon} \left[\frac{e^{\kappa a}}{1 + \kappa a} \right]^2 \frac{e^{-\kappa r}}{r}$$
 (1.9)

where, Ze is the effective charge and is related to surface charge density, $\sigma = Ze/\pi d^2$, α is the radius of the particle, ε the dielectric constant of the medium and κ is the inverse Debye screening length defined as;

$$\kappa^2 = \frac{4\pi e^2}{\varepsilon k_B T} (n_p Z + C_s) \tag{1.10}$$

The interaction potential can be modified by varying the particle number density, n_p , the surface charge density, σ , and salt concentration C_s . Under very low values of C_s , and moderate σ , the charge stabilized suspension will self-assemble to either fcc or bcc crystal structures depending upon the volume fraction. By deionizing (removing the salt ions in the

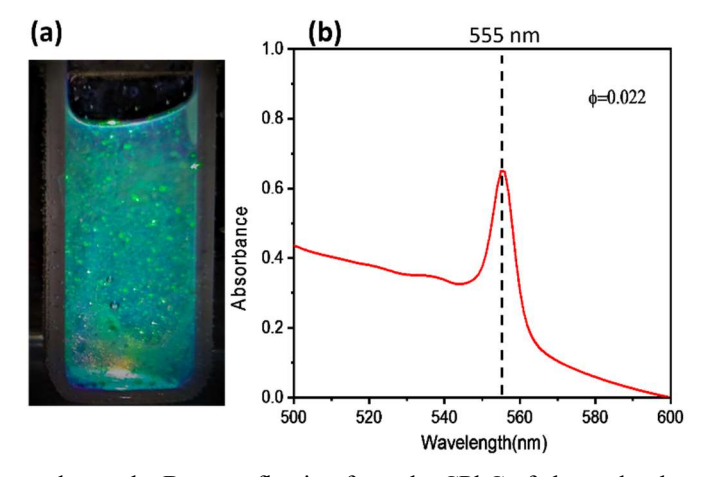


Fig. 1.3 (a) Iridescence due to the Bragg reflection from the CPhC of charged polystyrene colloidal particles in aqueous medium of volume fraction, 0.022. **(b)** the UV- Visible spectrum showing the stop band centered around 555 nm.

solvent) the suspensions using a mixed bed of ion-exchange resins, CPhCs of charged colloidal polystyrene and silica in aqueous suspension can be fabricated [57], [58]. Further, the surface charge of colloidal silica can be increased by adding small amounts of Sodium hydroxide (NaOH) or Pyridine, which enhances the dissociation of weakly acidic silanol groups [59].

1.4.2 Colloidal Opal Photonic crystals

An alternative method for fabricating CPhCs through colloidal self-assembly to opal structure. In this process, monodisperse colloidal particles spontaneously self-assemble into a closely packed face-cantered cubic (fcc) structure upon the evaporation of the water content.

Natural opal is a CPhC of periodically arranged amorphous silica particles of size in hundreds of nanometres. The silica colloidal particles form a fcc structure with volume fraction of 0.74 (74% Silica particles and 26% air)[60]. Due to the periodicity, which is in hundreds of nanometres, the Bragg diffraction of visible light from the array of silica particles results in visually appealing colours known as opalescence. We can grow similar opal structures using monodisperse colloidal polystyrene (PS) particles of similar diameters. The iridescence of the opal CPhC, fabricated through inward growing self-assembly of PS particles, is depicted in Fig.

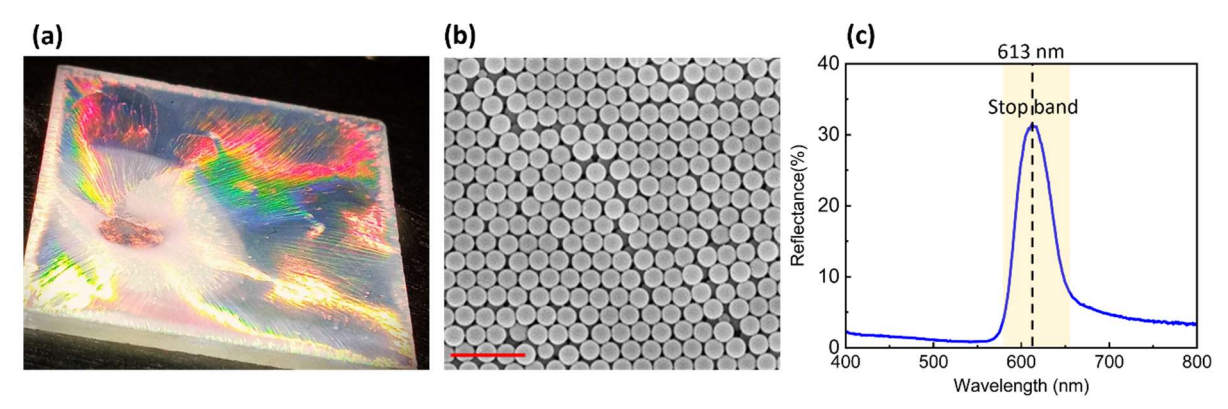


Fig. 1.4 (a) the iridescence from the opal type CPhC fabricated through inward growing self-assembly method with PS colloidal particle of diameter 287nm. **(b)** the SEM image of the hexagonal array of the PS particles **(c)** reflectance spectra of the CPhC showing the stop band around 613 nm.

1.4 (a). The SEM image in Fig. 1.4 (b) displays the periodic close-packed array of PS particles. The stop band, recorded with a UV-Visible spectrometer and shown in Fig. 1.4 (c), is centered around 613 nm.

Several research groups have used opal based CPhCs fabricated though the natural or assisted sedimentation of silica or latex colloidal particles onto flat substrates to fabricate CPhCs. This technique results in the formation of free-standing, millimetre-sized polycrystalline samples, where the packing is close to fcc structure. The analysis of the optical properties of these structures has contributed to a deeper understanding of PhCs[61]. Additionally, CPhCs have been employed as templates to fabricate inverse opal PhCs with higher index materials such as, silicon [62], [63] and germanium [64], titania [65], [66] etc.

Opal PhCs can be fabricated through different methods such as vertical deposition [42], inward growing method [67], dip coating [68], Langmuir -Blodgett method [69], spin coating [70], [71] etc.

1.4.3 Photonic Band Structure (PBG) in CPhCs

Attaining a full photonic bandgap in PhCs often requires a high threshold of refractive index contrast. Artificial opals, composed of colloidal particles such as polystyrene (PS), polymethyl methacrylate (PMMA), and silica[72], [73], create a low refractive index contrast when surrounding medium is air, typically resulting in the formation of a stopbands [1], [74]. For inverse opal structures, in which the particle positions in an opal structure are replaced with air spheres in a high refractive index medium, the threshold refractive index contrast for opening a PBG is predicted to be 2.8 for an fcc structure [75], [76]. PBG in opal CPhC structure is achievable with a refractive index contrast of 2.7 or higher by employing colloidal particles of higher refractive index $(n \ge 3.7)$ [77]. Despite the absence of a complete photonic bandgap, CPhCs have been found to be highly versatile in various applications. This is attributed to the easily attainable structural order and the existence of stopbands in the visible region. The stopband for CPhCs can be calculated using the modified Bragg's law [78];

$$m\lambda_B = 2d_{hkl}\sqrt{n_{eff}^2 - \sin^2\theta}$$
 (1.11)

Where, $n_{eff} = \sqrt{\phi_1 n_1^2 + \phi_2 n_2^2}$, with n_1 and n_2 being the refractive indices and ϕ_1 and ϕ_2 are the volume fractions of the constituent dielectric media respectively. For a cubic lattice, $d_{hkl} = \frac{a}{\sqrt{h^2 + k^2 + l^2}}$, where a is the lattice constant and h, k, and l are the miller indices of the plane. The electromagnetic wave with wavelength, λ_B can undergo Bragg diffraction satisfying the Eq. 1.11 (for a particular scattering angle, θ) at which the scattered waves add up coherently resulting in in a peak in the reflection geometry.

PhCs are popular choices for developing optical sensors, where variations in refractive contrast and periodicity lead to changes in the stopband position [79], [80]. Various fields, including medical [81-83], biological [84], and chemical research [85-87] have effectively employed the optical stopband of PhCs as sensors to detect a diverse range of substances. Apart from the optical sensing applications, stop band in tunable wavelength regions can be used in fabrication of waveguides [88], [89]. The light- matter interaction can be enhanced through a property known as the band edge effect [90-92]. This effect occurs when the group velocity of photons at the photonic band edge decreases significantly (slow photons [93]), leading to an increased interaction time of the photons with the material.

1.5 Surface Enhanced Raman Scattering (SERS)

Analyzing the information from molecular vibrational spectrum provides a potent method for evaluating the characteristics, dynamics, and distinct interactions of molecules. Raman spectroscopy, a form of vibrational spectroscopy, has been widely used in various fields, including chemistry, physics, biology, and material science, for applications such as analyzing chemical compositions, studying biological samples, and monitoring phase transitions in materials. It is a non-destructive technique and can be applied to both solids and liquids, making it a versatile tool in scientific research and industrial applications [94-97]. Raman scattering can also be used in molecular detection; however, the overall sensitivity is constrained due to the typically weaker signal compared to Rayleigh scattering. Surface-enhanced Raman spectroscopy (SERS) exploits the amplification of signals in Raman scattering when molecules are situated close to metallic surfaces. SERS predominantly arises from the confinement of electromagnetic energy by nanostructures hosting localized surface plasmon resonances (LSPRs)[98], [99]. This phenomenon leads to signal enhancement, enabling the detection and measurement of molecules down to single molecular concentrations[100]. The combination of Raman spectroscopy's direct molecular identification

capability with the enhanced sensitivity of SERS has established it as a highly effective analytical technique.

The initial observation of SERS phenomena was accidental, made by Fleischmann in 1974 during the examination of pyridine adsorbed on a roughened silver electrode [101]. The enhancement was then attributed to a greater adsorption surface area accessible to the molecules. The true origin of this enhancement was only understood by further investigations conducted independently in 1977 by two research groups: Jeanmaire and van Duyne [102] and Albrecht and Creighton [103]. Now it is widely recognized that the primary contributors to enhancement are the two mechanisms: electromagnetic enhancement (EME) and chemical enhancement (CE). The Raman signal enhancement due to the CE mechanism is due to the chemical interaction between the adsorbed molecule and the surface. It can alter the molecular polarizability and induce the charge transfer leading to the enhancement [104]. The amplified electromagnetic field on the metal nanostructures, due to the plasmonic resonances results in the electric field (E- field) enhancement. These resonances arise from the collective oscillations of conduction band electrons, known as plasmons when exposed to incident light. The increased electromagnetic fields thus generated have the capacity to stimulate Raman-active molecules, resulting in the enhancement of the Raman signals [105]. The scattering intensity of the molecule is expected to experience a substantial increase, potentially by multiple orders of magnitude, due to the combined effects of the two enhancements, as indicated by their product [106]. It is important to understand the effect of different parameters such as, shape, size, and material of the nanoparticles (NPs), including the experimental parameters to maximize the SERS enhancement [107]. This understanding is essential for translating research findings into practical applications.

1.5.1 Plasmonic Resonance

To improve the factors affecting SERS, it is crucial to comprehend the plasmonic resonance mechanism. The majority of SERS-active substrates rely on gold (Au) or silver (Ag) metals, due to the capability of metal nanostructures to sustain surface plasmons which are the collective oscillations of conduction electrons at metal/dielectric interfaces [123], [124]. Materials that can sustain surface plasmons are known as plasmonic materials[125], [126]. Surface plasmons are commonly categorized into two types: (i) localized surface plasmons (LSP), where electrons collectively oscillate in a localized fashion within and around a nanostructure, and (ii) propagating surface plasmons or surface-plasmon polaritons (SPPs), wherein the coherent electron oscillation travels as a longitudinal wave along the metal surface [124-128]. The energy is concentrated at the nanoscale features such as edges, tips or, crevices of the plasmonic materials due to LSP excited by far field incident light. It enhances the local field intensity to 2 to 5 orders of magnitudes. When the incident frequency matches with the plasmonic frequency the plasmonic resonance occurs. The resonance in LSP is called localized surface plasmon resonance (LSPR).

Some studies have explored the combined utilization of Surface Plasmon Resonance (SPR) and Localized Surface Plasmon Resonance (LSPR) for dual-mode enhancement in SERS[129-131]. However, the research conducted in this thesis has focused on LSPR. This can be treated as an electrostatic problem since the size of the metal NP is smaller than the excitation wavelength. Upon irradiation with electromagnetic radiation, the conduction electrons within the metal NP undergo displacement from the positive ions, leading to polarization of the system. However, the Columbic attraction between the seperated negative and positive charges brings them together, creating a restoring force. In reaction to the periodic electric field and the restoring force resulting from Columbic attraction, the conduction electrons within the NP engage in coherent oscillation (which can be imagine as a mass spring

problem), which is known as LSPR. These are spatially localized three dimensions. Figure 1.5 shows the 5 schematic representation of localised surface plasmon in a plasmonic NP with electric field hot pot on the poles of the NP along the direction of E- field.

1.5.2 SERS Enhancement Mechanisms

It is important to understand the mechanisms behind the SERS enhancement to

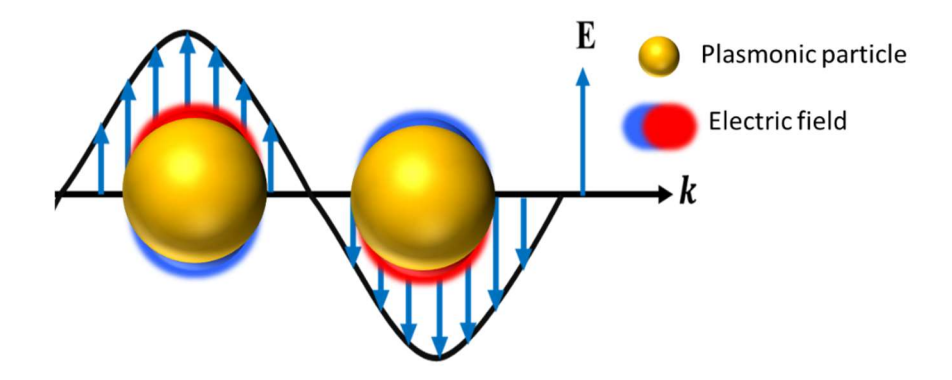


Fig. 1.5 schematic representation of localised surface plasmon in a plasmonic NP with E- field hot pot on the poles of the NP along the direction of E- field.

optimize the factors detects molecules with concentration lowest as possible. The enhancement mechanisms are classified into two;

i) Electromagnetic mechanism

The Electromagnetic Enhancement (EME) observed in SERS is primarily linked to the characteristics of LSPR and its impact on the presence of probe molecules in the surrounding area. Similar to any LSPR technique, it constitutes a near-field enhancement and is contingent upon various factors that affect LSPR. The enhancement is determined by solving the electric field around these probe molecules in the presence of the metal NPs/NSs.

When the incident E- field becomes localized and enhanced at the vicinity of the NP, is called the local field enhancement (LFE). These regions of dense electric field are known as hotspots. The field enhancement in this scenario can be comprehended through the classical

dipole approximation, that the power of dipole radiation from the oscillating Raman dipole (P_{Raman}) is defined as,

$$P_{Raman} = \frac{\omega^4}{12\pi\varepsilon_0 c^3} |p_{induced}|^2 = \frac{\omega^4}{12\pi\varepsilon_0 c^3} |\propto E_{inc}|^2$$
 (1.12)

, where, $p_{induced}$ is the induced dipole moment which is proportional to the incident E- field (E_{inc}) , which means that the Raman power is proportional to the square if incident E- field. So, we can define the local field intensity enhancement (LEF) factor as,

$$LEF = \left| \frac{E_{loc}(\omega_i)}{E_{inc}(\omega_i)} \right|^2 \tag{1.13}$$

Where, ω_i is the incident light frequency, E_{loc} is the local electric field and E_{inc} is the incident electric field. The local field enhancement depends on the type of plasmonic nanostructure.

ii) Chemical enhancement

The origin of Chemical enhancement (CE) in SERS is attributed to changes in the polarizability of a molecule resulting from chemical or physical changes following its interaction with a plasmonic material. The magnitude of this enhancement varies depending on the combination of the molecule and metal involved. While the contribution is generally less compared to EME, it has a vital role in SERS by causing notable effects such as shifts in anticipated Raman modes and the amplification of certain modes while suppressing others. Broadly, this is known as 'charge transfer mechanisms,' wherein the electronic charge distribution around the molecule is subtly influenced in the presence of the plasmonic NS.

1.6 Applications of PhCs

PhCs have become integral in a variety of scientific and technological applications due to their unique ability to control and manipulate the propagation of light based on periodic nanostructures. One significant area of application is in optical filters and reflectors, where PhCs are employed to selectively transmit or reflect specific wavelengths of light, enabling the development of advanced optical filtering and mirror technologies [132]. In the field of photonics, PhCs play a pivotal role in photonic integrated circuits [133], allowing for the miniaturization and integration of optical components such as waveguides, splitters, and switches. These circuits are essential for optical communication systems and signal processing applications. PhCs also contribute to laser technologies [134] by enhancing laser performance, enabling low-threshold lasing, and controlling emission characteristics. Moreover, PhCs are instrumental in sensor technologies [135], serving as the core sensing element in various applications including biosensors for label-free molecular detection, environmental gas

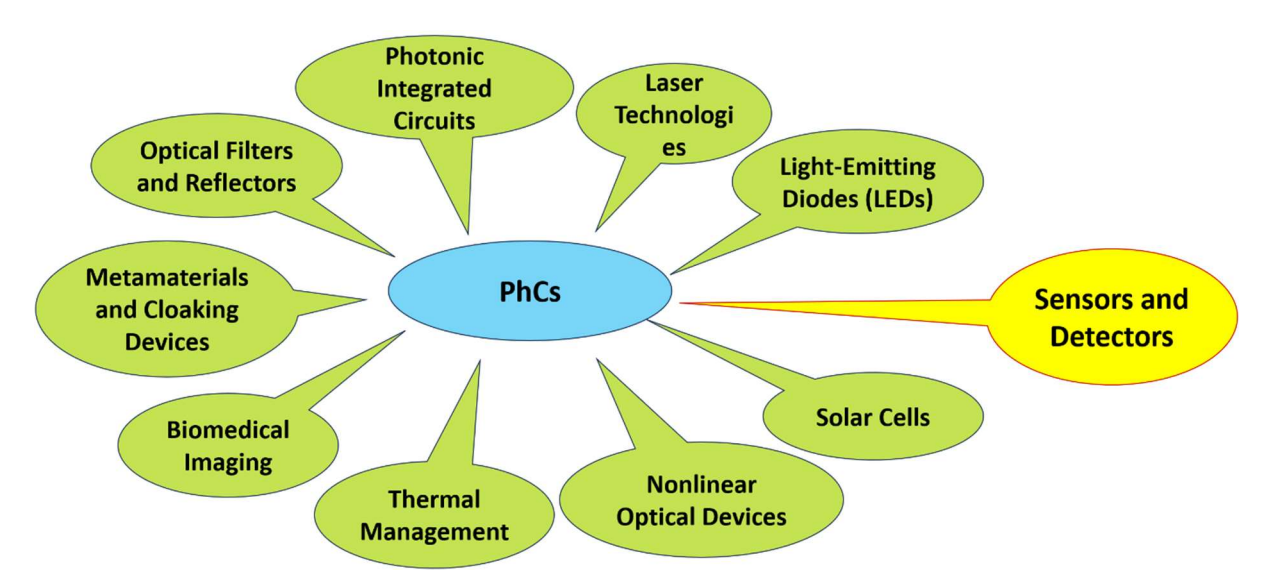


Fig. 1.6 Diagram showing the applications of PhCs.

sensors, and precise PhC fibers for sensing applications. In the realm of light-emitting devices, PhCs enhance the efficiency and directionality of LEDs, leading to advancements in display technology, lighting, and optical communications [136]. In renewable energy, PhCs are

being explored to improve solar cell efficiency by enhancing light absorption and trapping [137]. They also find utility in nonlinear optical devices for generating and manipulating nonlinear optical effects, essential in optical signal processing and quantum optics [138]. Additionally, PhCs contribute to thermal management by controlling thermal radiation properties, offering potential applications in thermal insulation and heat manipulation [139]. In biomedical engineering, PhCs enable advanced optical imaging techniques like superresolution microscopy and optical coherence tomography (OCT), as well as biosensing platforms for biomarker detection and cellular interaction studies [140]. Furthermore, integrating PhCs with metamaterials allows for the creation of novel structures with exotic optical properties, paving the way for innovative optical devices and even electromagnetic cloaking technologies.

These diverse applications underscore the versatility and significance of PhC in advancing optical technologies across various fields, encompassing telecommunications, electronics, biomedicine, renewable energy and beyond. In the following sections we focus mainly on the applications offered by CPhCs.

1.6.1 Applications of CPhCs

The self-assembly of CPhCs has gained growing attention owing to its broad range of fundamental and practical applications. Numerous sophisticated self-assembly methods have been developed to meet the requirements of these applications [141] such as, optical waveguides [23], laser resonators and filters, optical cavities, LEDs, solar photovoltaics, biomedical engineering, drug delivery, SERS sensors etc. to name a few. Some of the applications are described below.

In the age of information, there is a growing need for the advancement of dynamic display technologies. Utilizing structural colors from PhCs in displays enables clear visibility even under intense daytime lighting conditions. Furthermore, there is a significant reduction in

energy consumption, as these devices leverage ambient light as their light source, eliminating the need for back-lit lights. Consequently, numerous researchers have explored the development of CPhC-based color pigments for a wide range of display devices [22], [142], including portable devices, signboards, and billboards. Three main strategies have been investigated: CPhCs can be pixelated to replace traditional optical filter patterns; PhCs' lattice constants can be used to dynamically adjust reflection colours; and photonic microparticles with anisotropic optical properties can be used to create rotation-based displays [142].

The use of CPhCs in the photonic devices is pioneered by Shkunov et al. [143], presenting CPhCs lasers fabricated with silica opals. In this study, sedimentation was used to fabricate a millimeter-thick opal, which was then submerged in a liquid media with a dissolved dye. A directional laser beam is produced by optical pumping when the dye's spontaneous emission spectrum matches up with the CPhCs' band-edge position. This beam generation arises from stimulated emission at the band edge of the CPhC, where the density of states is high and the group velocity of light is low. By immersing an opal in two different dyes, two distinct wavelengths of lasing can be produced based on the crystal direction, corresponding to different band-edge positions. Various research groups have used CPhC opal structures such resonators[144], [145]. Lasing with CPhCs can also be accomplished with the defect mode. Furumi et al. [146] devised CPhCs that incorporated planar defects. CPhC of PS particles was infiltrated with polydimethylsiloxane, and the defect layer was gel-doped with dye molecules. The CPhC films, demonstrated laser emission at a wavelength corresponding to the defect mode rather than from the band edge.

CPhCs can find valuable applications in the biomedical field due to their distinctive structural and optical characteristics. In addition to providing mechanical supports for cell growth, the 3D or 2D porous structures of CPhCs are effective tools for tracking cell viability, identifying relevant medications, and facilitating drug transport to biological targets [141]. A

controllable drug delivery system was developed using a CPhCs. The drug delivery process was monitored through their structural color [147]. In drug delivery systems, inverse opal CPhCs are frequently used for enhancing the total drug loading capacity. Their high surface-to-volume ratios and porous frameworks are the main factors behind this choice. The unique optical characteristics and micro/nanostructures of CPhCs make them an attractive choice for "intelligent" materials in cell research. Cell capture, cell culture, and organ-on-a-chip platforms are the three main uses of CPhCs in cell research. In such applications, CPhCs serve as real-time sensors that can track changes in the microenvironment or cell behaviours, in addition to serving as substrates with ordered and tunable micro/nanostructures. Furthermore, CPhCs are suitable materials for high-throughput bioassays in cell research because of their tunable structural colours.

Due to the increasing demand for sensing devices, CPhCs have emerged as a potential tool in various fields such as healthcare, physical parameter monitoring, defense, food quality control, aerospace etc.

1.6.2 CPhC Assisted Sensing

PhCs with properties in controlling the flow of light facilitate the fabrication of diverse high-performance sensors. One way of achieving PhC sensors focuses on incorporating functional materials into PhCs and manipulating the PBG by gaining control over structures, symmetry, and refractive index contrast. PhC sensors can be largely categorized based on the types of external stimuli they respond to. Physically stimuli-responsive sensors, including those sensitive to temperature, humidity, magnetic fields, electric fields, and mechanical forces, are one category. Another category comprises chemically stimuli-responsive sensors that react to stimuli such as organic solvents and their vapors, ions, pH levels, and some analytical substances. Additionally, there are biologically stimuli-responsive sensors designed to detect biological elements like enzymes, nucleic acids, antibodies, and biomacromolecules.

Polymers with temperature-sensitive characteristics are extensively employed in physically responsive sensors, and polymer-based thermo-sensitive PhCs have gained widespread application for this purpose [148-150]. Poly(N-isopropylacrylamide (PNIPAM) is recognized for its thermo-sensitive properties, exhibiting a reversible transition between hydrophilic and hydrophobic states near the critical temperature, approximately 32°C [48]. At higher temperatures, the polymer undergoes deswelling, leading to a reduction in the particle size which results in the change in diffraction peak of the CPhC. Humidity-responsive CPhC sensor based on the structural color changes has been reported with CPhC immobilized on hydrogel matrix [151]. In response to an increase in environmental humidity, the CPhC hydrogel absorbs water and undergoes swelling. This swelling, changes the Bragg diffraction peak of the CPhC. On the other hand, the CPhC hydrogel slowly revert to its starting state as the humidity drops. When exposed to varying humidity conditions, the CPhC-based humidity sensor demonstrates structural color changes within the visible light spectrum, transitioning from transparency to various colors [152]. Mechano-responsive CPhC sensors have been reported by directly and efficiently manipulating the structural characteristics of PhCs through compression and stretching [153], [154]. CPhC sensors that respond to electrical stimuli exhibit noticeable optical features when subjected to an applied electric field. The materials associated with these electrically responsive PhCs include those based on CPhC infiltrated in liquid crystals [155], [156]. Magnetically responsive PhCs use magnetic-responsive materials as the basic units, in contrast to other responsive CPhCs that need the coupling of PhC with responsive materials. Magnetic fields can be applied to these magnetic CPhCs without requiring additional treatment [157-159].

Another important application of CPhCs is in chemically stimuli responsive CPhC sensors. For the volatile organic components, the vapor interacts with CPhC and changes the effective refractive index resulting in shift in the Bragg peak [160].

Incorporating pH-responsive materials into a CPhC facilitates the fabrication of pH-responsive CPhC sensors. As the external environment's acidity or alkalinity changes, the pH-responsive material undergoes swelling/ deswelling indicated by the change in structural colour and the change in stop band position [161-163]. Gas-responsive CPhC sensors typically feature a substantial pore volume to enhance gas absorption capacity. The effective refractive index of the system changes when gas molecules diffuse into the sensor, which causes a shift in the CPhC's diffraction peak. Consequently, qualitative and quantitative gas identification is made possible by the shift in the diffraction peak. As of now, a lot of CPhC-based gas detecting devices make use of an inverse opal CPhCs. This choice is attributed to the larger specific surface area of the inverse opal structure compared to the opal structure, effectively improving the diffusion rate of gas molecules in the material [164-167].

Apart from functionalizing and labeling CPhCs to make them responsive to specific materials, combining with SERS techniques enables the use of CPhCs as label-free detection platforms. Plasmonic NPs are extensively used in LSPR or SPR based sensing applications [122]. The sensitivity of LSPR-based sensors, has limitations, and controlling the distribution and accessibility of plasmonic NP "hot spots" (which are crucial for SERS) [171] is challenging. This challenge contributes to performance shortcomings in practical applications. In such cases, the integration of plasmonic NPs with CPhC can be highly beneficial. The CPhC efficiently adjusts the distribution and accessibility of "hot spots." Additionally, CPhC can regulate the local density of states with its bandgap, offering to enhance the interaction between light and plasmonic materials[172]. The utilization of the electromagnetic field enhancement in the CPhC at wavelengths falling inside the photonic bandgap (PBG) or stopband to enhance the Raman signal, in combination with plasmonic enhancement is the major focus of this thesis.

1.7 Motivation

Understanding PhCs requires knowledge about the photonic band structure, which depends on the symmetry and structural parameters of the PhC. One of the simplest types of PhCs to start with is a 2D PhC, where the periodicity is along only one plane and uniform along the direction perpendicular to it. It is easy to model and simulate such a system since the computational time and memory expense are less compared to other complicated structures, such as those found in 3D PhC. Understanding the band structure for different symmetries and tuning the structural parameters to achieve band gap in specific wavelength ranges, particularly in the visible range is fundamentally important for utilizing PhCs in various applications. Analyzing the reflectance spectra, both with and without defects, and understanding the electromagnetic field distribution are also crucial from an application point of view. We have systematically investigated the band structures of a 2D array of amorphous titania rods placed in an air matrix with both square and hexagonal symmetries. The band structures were optimized by adjusting the structural parameters to achieve a maximum band gap and to tune the band gap into the visible range. Additionally, we investigated the effect of doping on the defects, considering hole-type and rod-type defects in both square and hexagonal symmetries, and analyzed their electric field distribution. These results are summarized in Chapter 3.

PhCs self-assembled via a colloidal route have attracted the interest of the research community for years due to their ease of fabrication, cost-effectiveness, and easy-to-engineer properties. The light guiding mechanism in PhCs can offer several technological applications: CPhC thin films of monolayer and/or multilayer dielectric nanospheres (combined with metal NPs) have emerged as very good templates for SERS applications. While near-field and far-field studies on PhC thin films have been reported [179-181], the internal E-field distributions in mono- and multilayered CPhC thin films have not been extensively studied in the literature. Both near-field and far-field microscopic techniques have been utilized for sensing applications

and imaging the structural colors resulting from Bragg diffraction of visible light by PhC thin films. These studies have motivated us to conduct detailed investigations into the internal E-field distribution of light in CPhC films with appreciable refractive index contrast and explore their application in SERS.

We investigated the internal E- field distribution in the monolayer, as well as the top layers of bilayer and trilayer PhC films, using numerical simulations with the wave optics module in COMSOL Multiphysics software. The monolayer, bilayer, and trilayer PhC films consist of one, two, and three layers of hexagonally close-packed spherical colloids, respectively. Additionally, we examined the dependency of the E- field distribution on incident wavelengths, focusing on those at different spectral regimes of the PhC films, particularly at on-resonance and off-resonance wavelengths. On-resonance wavelength means that lies inside the forbidden frequency of the photonic band of the CPhC films and off-resonance wavelength lies outside the forbidden photonic band. These numerical simulation results are presented in Chapter 4, which can provide the knowledge of E- field localization and enhancement in specific CPhC regimes which can be further utilized in several CPhC-based applications.

We have verified the simulation studies using SERS. Although there are studies in the literature on CPhC templates, the concept of on-resonance excitation for SERS studies, a property induced by the PhC structure, has not been thoroughly investigated experimentally. A few studies have explored monolayer colloidal particle arrays as templates to enhance the distribution and accessibility of hotspots generated by plasmonic NPs or nanofilms[182], [183]. However, only a limited number of these studies [172], [184], have focused primarily on on-resonance excitation, emphasizing the combinations of plasmonic NPs with bulk PhCs. Here, we have investigated the effect of the monolayer CPhC template on the Raman peak enhancement of some dye molecules under on-resonance excitation. In addition to the excellent control of the distribution of the gold NPs, we probe the on-resonance excitation, increasing

the light-matter interaction. We also present finite element method (FEM) EM simulations for CPhC templates with gold NPs to study the E- field distribution to identify the enhanced E-field regions that are potential hot spots for improved SERS signals. These results are presented in Chapter 5 & 6.

The thesis is structured in the following way. The experimental details including the synthesis of colloidal particles, fabrication and characterization of CPhC thin films, development of laser diffraction setup, and the electromagnetic simulation details are presented in Chapter 2. The studies to understand PhCs through bandstructure, reflectance and electromagnetic field distributions are presented Chapter 3. Chapter 4 describes the electromagnetic simulations on CPhC thin films. The experimental verification of plasmon free SERS on CPhC thin film template for dye molecules are presented in Chapter 5. The SERS of various dye molecules on the template of CPhC thin film combined with gold NPs are presented in Chapter 6. Chapter 7 discusses the summary and conclusions of the investigations that have been carried out using the electromagnetic simulations and the experimental investigations of PhC templates using Raman scattering experiments and using them for sensing applications. The key findings of these investigations and directions of future work are also presented.

References

- [1] Y. A. Vlasov, V. Astratov, O. Karimov, A. Kaplyanskii, V. Bogomolov, and A. Prokofiev, "Existence of a photonic pseudogap for visible light in synthetic opals," *Phys Rev B Condens Matter Phys*, vol. 55, no. 20, 1997
- [2] M. N. Shkunov, Z. V. Vardeny, M. C. DeLong, R. C. Polson, A. A. Zakhidov, and R. H. Baughman, "Tunable, gap-state lasing in switchable directions for opal photonic crystals," *Adv Funct Mater*, vol. 12, no. 1, 2002
- [3] R. Biswas, M. Sigalas, G. Subramania, C. Soukoulis, and K. Ho, "Photonic band gaps of porous solids," *Phys Rev B Condens Matter Mater Phys*, vol. 61, no. 7, 2000
- [4] Lord Rayleigh, "XVII. On the maintenance of vibrations by forces of double frequency, and on the propagation of waves through a medium endowed with a periodic structure

- ," The London, Edinburgh, and Dublin Philosophical Magazine and Journal of Science, vol. 24, no. 147, 1887
- [5] E. Yablonovitch, "Inhibited spontaneous emission in solid-state physics and electronics," *Phys Rev Lett*, vol. 58, no. 20, 1987
- [6] S. John, "Strong localization of photons in certain disordered dielectric superlattices," *Phys Rev Lett*, vol. 58, no. 23, 1987
- [7] E. Yablonovitch, T. J. Gmitter, and K. M. Leung, "Photonic band structure: The face-centered-cubic case employing nonspherical atoms," *Phys Rev Lett*, vol. 67, no. 17, 1991
- [8] S. Y. Lin *et al.*, "A three-dimensional photonic crystal operating at infrared wavelengths," *Nature*, vol. 394, no. 6690, 1998
- [9] J. Broeng, D. Mogilevstev, S. E. Barkou, and A. Bjarklev, "Photonic Crystal Fibers: A New Class of Optical Waveguides," *Optical Fiber Technology*, vol. 5, no. 3, 1999
- [10] M. Lončar, T. Doll, J. Vučković, and A. Scherer, "Design and fabrication of silicon photonic crystal optical waveguides," *Journal of Lightwave Technology*, vol. 18, no. 10, 2000
- [11] Y. Zhang and B. Li, "Photonic crystal-based bending waveguides for optical interconnections," *Opt Express*, vol. 14, no. 12, 2006
- [12] A. Bertoncini and C. Liberale, "3D printed waveguides based on photonic crystal fiber designs for complex fiber-end photonic devices," *Optica*, vol. 7, no. 11, 2020
- [13] O. Frazão, J. L. Santos, F. M. Araújo, and L. A. Ferreira, "Optical sensing with photonic crystal fibers," *Laser Photon Rev*, vol. 2, no. 6, 2008
- [14] J. Hou, M. Li, and Y. Song, "Recent advances in colloidal photonic crystal sensors: Materials, structures and analysis methods," *Nano Today*, vol. 22. 2018
- [15] D. Men, D. Liu, and Y. Li, "Visualized optical sensors based on two/three-dimensional photonic crystals for biochemicals," *Science Bulletin*, vol. 61, no. 17. 2016.
- [16] F. Qi, Z. Meng, M. Xue, and L. Qiu, "Recent advances in self-assemblies and sensing applications of colloidal photonic crystals," *Analytica Chimica Acta*, vol. 1123. 2020.
- [17] K. Nozaki *et al.*, "Sub-femtojoule all-optical switching using a photonic-crystal nanocavity," *Nat Photonics*, vol. 4, no. 7, 2010
- [18] S. Amrehn, X. Wu, and T. Wagner, "Tungsten Oxide Photonic Crystals as Optical Transducer for Gas Sensing," *ACS Sens*, vol. 3, no. 1, 2018
- [19] M. Zamani, "Photonic crystal-based optical filters for operating in second and third optical fiber windows," *Superlattices Microstruct*, vol. 92, 2016

- [20] R. Sathyadevaki, A. S. Raja, and D. S. sundar, "Photonic crystal-based optical filter: a brief investigation," *Photonic Network Communications*, vol. 33, no. 1, 2017
- [21] H. S. Lee, T. S. Shim, H. Hwang, S. M. Yang, and S. H. Kim, "Colloidal photonic crystals toward structural color palettes for security materials," *Chemistry of Materials*, vol. 25, no. 13, 2013
- [22] A. C. Arsenault, D. P. Puzzo, I. Manners, and G. A. Ozin, "Photonic-crystal full-colour displays," *Nat Photonics*, vol. 1, no. 8, 2007
- [23] J. D. Joannopoulos, S. G. Johnson, J. N. Winn, and R. D. Meade, *Photonic crystals: Molding the flow of light.* 2011.
- [24] M. Duneau, F. Delyon, and M. Audier, "Holographic method for a direct growth of three-dimensional photonic crystals by chemical vapor deposition," *J Appl Phys*, vol. 96, no. 5, 2004
- [25] M. Nishimoto, K. Ishizaki, K. Maekawa, K. Kitamura, and S. Noda, "Air-hole retained growth by molecular beam epitaxy for fabricating gaas-based photonic-crystal lasers," *Applied Physics Express*, vol. 6, no. 4, 2013
- [26] F. Scotognella *et al.*, "Metal oxide one dimensional photonic crystals made by RF sputtering and spin coating," *Ceram Int*, vol. 41, no. 7, 2015
- [27] F. Hua, J. Shi, Y. Lvov, and T. Cui, "Patterning of Layer-by-Layer Self-Assembled Multiple Types of Nanoparticle Thin Films by Lithographic Technique," *Nano Lett*, vol. 2, no. 11, 2002
- [28] D. V. Nicolau, T. Taguchi, H. Taniguchi, and S. Yoshikawa, "Negative and positive tone protein patterning on e-beam/deep-UV resists," *Langmuir*, vol. 15, no. 11, 1999
- [29] G. Feiertag *et al.*, "Fabrication of photonic crystals by deep x-ray lithography," *Appl Phys Lett*, vol. 71, no. 11, 1997
- [30] M. Campbell, D. N. Sharp, M. T. Harrison, R. G. Denning, and A. J. Turberfield, "Fabrication of photonic crystals for the visible spectrum by holographic lithography," *Nature*, vol. 404, no. 6773, 2000
- [31] M. D. Levenson, N. S. Viswanathan, and R. A. Simpson, "Improving Resolution in Photolithography with a Phase-Shifting Mask," *IEEE Trans Electron Devices*, vol. 29, no. 12, 1982
- [32] L. J. Guo, "Nanoimprint lithography: Methods and material requirements," *Advanced Materials*, vol. 19, no. 4, 2007
- [33] D. A. Walker, B. Kowalczyk, M. O. De La Cruz, and B. A. Grzybowski, "Electrostatics at the nanoscale," *Nanoscale*, vol. 3, no. 4, 2011

- [34] K. J. M. Bishop, C. E. Wilmer, S. Soh, and B. A. Grzybowski, "Nanoscale forces and their uses in self-assembly," *Small*, vol. 5, no. 14. 2009
- [35] K. E. Davis, W. B. Russel, and W. J. Glantschnig, "Disorder-to-order transition in settling suspensions of colloidal silica: X-ray measurements," *Science* (1979), vol. 245, no. 4917, 1989
- [36] P. N. Pusey and W. Van Megen, "Phase behaviour of concentrated suspensions of nearly hard colloidal spheres," *Nature*, vol. 320, no. 6060, 1986
- [37] C. Ma *et al.*, "Centrifugation-induced water-tunable photonic colloidal crystals with narrow diffraction bandwidth and highly sensitive detection of SCN-," *ACS Appl Mater Interfaces*, vol. 5, no. 6, 2013
- [38] Y. G. Ko, D. H. Shin, G. S. Lee, and U. S. Choi, "Fabrication of colloidal crystals on hydrophilic/hydrophobic surface by spin-coating," *Colloids Surf A Physicochem Eng Asp*, vol. 385, no. 1–3, 2011
- [39] G. Arutinov, S. B. Brichkin, and V. F. Razumov, "Self-Assembling of polystyrene microsphere monolayers by spin-coating," *Nanotechnol Russ*, vol. 5, no. 1–2, 2010
- [40] Y. Fang, B. M. Phillips, K. Askar, B. Choi, P. Jiang, and B. Jiang, "Scalable bottom-up fabrication of colloidal photonic crystals and periodic plasmonic nanostructures," *J Mater Chem C Mater*, vol. 1, no. 38, 2013
- [41] P. Jiang, T. Prasad, M. J. McFarland, and V. L. Colvin, "Two-dimensional nonclose-packed colloidal crystals formed by spincoating," *Appl Phys Lett*, vol. 89, no. 1, 2006
- [42] Z. Zhou and X. S. Zhao, "Flow-Controlled Vertical Deposition Method for the Fabrication of Photonic Crystals," *Langmuir*, vol. 20, no. 4, 2004
- [43] E. Armstrong, W. Khunsin, M. Osiak, M. Blömker, C. M. S. Torres, and C. O'Dwyer, "Ordered 2D colloidal photonic crystals on gold substrates by surfactant-assisted fast-rate dip coating," *Small*, vol. 10, no. 10, 2014
- [44] S. Reculusa and S. Ravaine, "Synthesis of colloidal crystals of controllable thickness through the Langmuir-Blodgett technique," *Chemistry of Materials*, vol. 15, no. 2, 2003
- [45] N. Vogel, S. Goerres, K. Landfester, and C. K. Weiss, "A convenient method to produce close- and non-close-packed monolayers using direct assembly at the air-water interface and subsequent plasma-induced size reduction," *Macromol Chem Phys*, vol. 212, no. 16, 2011
- [46] Z. Lu and M. Zhou, "Fabrication of large scale two-dimensional colloidal crystal of polystyrene particles by an interfacial self-ordering process," *J Colloid Interface Sci*, vol. 361, no. 2, 2011

- [47] P. S. Mohanty, B. V. R. Tata, A. Toyotama, and T. Sawada, "Gas-solid coexistence in highly charged colloidal suspensions," *Langmuir*, vol. 21, no. 25, 2005
- [48] M. V. Saisavadas, S. Dhara, R. G. Joshi, and B. V. R. Tata, "Large amplitude oscillatory shear studies on dense PNIPAM microgel colloidal glasses," *Colloid Polym Sci*, vol. 301, no. 6, 2023
- [49] B. V. R. Tata, R. G. Joshi, D. K. Gupta, J. Brijitta, and B. Raj, "Crystalline arrays of submicron-sized particles through colloidal route," *Curr Sci*, vol. 103, no. 10, pp. 1175–1184, 2012.
- [50] B. V. R. Tata and S. S. Jena, "Ordering, dynamics and phase transitions in charged colloids," *Solid State Commun*, vol. 139, no. 11–12, 2006
- [51] J. Chakrabarti, H. R. Krishnamurthy, and A. K. Sood, "Density functional theory of laser-induced freezing in colloidal suspensions," *Phys Rev Lett*, vol. 73, no. 21, 1994
- [52] Y. Iwayama *et al.*, "Optically tunable gelled photonic crystal covering almost the entire visible light wavelength region," *Langmuir*, vol. 19, no. 4. 2003
- [53] D. J. Norris and Y. A. Vlasov, "Chemical approaches to three-dimensional semiconductor photonic crystals," *Advanced Materials*, vol. 13, no. 6, 2001
- [54] J. E. G. J. Wijnhoven and W. L. Vos, "Preparation of photonic crystals made of air spheres in titania," *Science* (1979), vol. 281, no. 5378, 1998
- [55] G. Pan, R. Kesavamoorthy, and S. A. Asher, "Optically nonlinear bragg diffracting nanosecond optical switches," *Phys Rev Lett*, vol. 78, no. 20, 1997
- [56] J. H. Holtz and S. A. Asher, "Polymerized colloidal crystal hydrogel films as intelligent chemical sensing materials," *Nature*, vol. 389, no. 6653, 1997
- [57] T. Kanai, T. Sawada, and J. Yamanaka, "Fabrication of large-area silica colloidal crystals immobilized in hydrogel film," *Journal of the Ceramic Society of Japan*, vol. 118, no. 1377, 2010
- [58] C. E. Reese, C. D. Guerrero, J. M. Weissman, K. Lee, and S. A. Asher, "Synthesis of highly charged, monodisperse polystyrene colloidal particles for the fabrication of photonic crystals," *J Colloid Interface Sci*, vol. 232, no. 1, 2000
- [59] M. Murais *et al.*, "Unidirectional crystallization of charged colloidal silica due to the diffusion of a base," *Langmuir*, vol. 23, no. 14, 2007
- [60] V. Mizeikis, S. Juodkazis, A. Marcinkevičius, S. Matsuo, and H. Misawa, "Tailoring and characterization of photonic crystals," *Journal of Photochemistry and Photobiology C: Photochemistry Reviews*, vol. 2, no. 1. 2001

- [61] H. Míguez *et al.*, "Photonic crystal properties of packed submicrometric SiO2 spheres," *Appl Phys Lett*, vol. 71, no. 9, 1997
- [62] A. Blanco *et al.*, "Large-scale synthesis of a silicon photonic crystal with a complete three-dimensional bandgap near 1.5 micrometres," *Nature*, vol. 405, no. 6785, 2000
- [63] Y. A. Vlasov, X. Z. Bo, J. C. Sturm, and D. J. Norris, "On-chip natural assembly of silicon photonic bandgap crystals," *Nature*, vol. 414, no. 6861, 2001
- [64] H. Míguez *et al.*, "Photonic bandgap engineering in germanium inverse opals by chemical vapor deposition," *Advanced Materials*, vol. 13, no. 21, 2001
- [65] L. Wang, T. R. Mogan, K. Wang, M. Takashima, B. Ohtani, and E. Kowalska, "Fabrication and Characterization of Inverse-Opal Titania Films for Enhancement of Photocatalytic Activity," *ChemEngineering*, vol. 6, no. 3, 2022
- [66] J. Yu, J. Lei, L. Wang, J. Zhang, and Y. Liu, "TiO2 inverse opal photonic crystals: Synthesis, modification, and applications A review," *Journal of Alloys and Compounds*, vol. 769. 2018
- [67] R. V. Nair and R. Vijaya, "Structural and optical characterization of photonic crystals synthesized using the inward growing self-assembling method," *Appl Phys A Mater Sci Process*, vol. 90, no. 3, pp. 559–563, Mar. 2008
- [68] C. Deleuze, B. Sarrat, F. Ehrenfeld, S. Perquis, C. Derail, and L. Billon, "Photonic properties of hybrid colloidal crystals fabricated by a rapid dip-coating process," *Physical Chemistry Chemical Physics*, vol. 13, no. 22, 2011
- [69] M. Parchine, J. McGrath, M. Bardosova, and M. E. Pemble, "Large Area 2D and 3D Colloidal Photonic Crystals Fabricated by a Roll-to-Roll Langmuir-Blodgett Method," *Langmuir*, vol. 32, no. 23, 2016
- [70] H. Wang, K. P. Yan, J. Xie, and M. Duan, "Fabrication of ZnO colloidal photonic crystal by spin-coating method," *Mater Sci Semicond Process*, vol. 11, no. 2, 2008
- [71] T. T. H. Nguyen, H. H. Nguyen, Y. S. Kim, and Y. S. Cho, "Rapid fabrication of colloidal crystal films by spin coating using polymeric particles synthesized by dispersion polymerization," *Particulate Science and Technology*, 2023
- [72] Y. Xia, B. Gates, Y. Yin, and Y. Lu, "Monodispersed colloidal spheres: Old materials with new applications," *Advanced Materials*, vol. 12, no. 10, 2000
- [73] A. Stein and R. C. Schroden, "Colloidal crystal templating of three-dimensionally ordered macroporous solids: Materials for photonics and beyond," *Curr Opin Solid State Mater Sci*, vol. 5, no. 6, 2001

- [74] F. Galisteo-López, E. Palacios-Lidón, E. Castillo-Martínez, and C. López, "Optical study of the pseudogap in thickness and orientation controlled artificial opals," *Phys Rev B Condens Matter Mater Phys*, vol. 68, no. 11, 2003
- [75] K. Busch and S. John, "Photonic band gap formation in certain self-organizing systems," Phys Rev E Stat Phys Plasmas Fluids Relat Interdiscip Topics, vol. 58, no. 3, 1998
- [76] J. S. King, D. Heineman, E. Graugnard, and C. J. Summers, "Atomic layer deposition in porous structures: 3D photonic crystals," in *Applied Surface Science*, 2005
- [77] H. S. Sözer, J. W. Haus, and R. Inguva, "Photonic bands: Convergence problems with the plane-wave method," *Phys Rev B*, vol. 45, no. 24, 1992
- [78] A. Reynolds, F. López-Tejeira, D. Cassagne, F. J. García-Vidal, C. Jouanin, and J. Sánchez-Dehesa, "Spectral properties of opal-based photonic crystals having a Sio2 matrix," *Phys Rev B Condens Matter Mater Phys*, vol. 60, no. 16, 1999.
- [79] Y. Liu and H. W. M. Salemink, "Photonic crystal-based all-optical on-chip sensor," *Opt Express*, vol. 20, no. 18, 2012.20.019912.
- [80] S. Amrehn, X. Wu, C. Schumacher, and T. Wagner, "Photonic crystal-based fluid sensors: Toward practical application," *Physica Status Solidi (A) Applications and Materials Science*, vol. 212, no. 6, 2015
- [81] H. Xu *et al.*, "A multifunctional wearable sensor based on a graphene/inverse opal cellulose film for simultaneous, In situ monitoring of human motion and sweat," *Nanoscale*, vol. 10, no. 4, 2018
- [82] W. S. Lee, T. Kang, S. H. Kim, and J. Jeong, "An antibody-immobilized silica inverse opal nanostructure for label-free optical biosensors," *Sensors (Switzerland)*, vol. 18, no. 1, 2018
- [83] N. J. Nicolas, M. A. Duffy, A. Hansen, and J. Aizenberg, "Inverse Opal Films for Medical Sensing: Application in Diagnosis of Neonatal Jaundice," *Adv Healthc Mater*, vol. 10, no. 4, 2021
- [84] T. Cassagneau and F. Caruso, "Inverse opals for optical affinity biosensing," *Advanced Materials*, vol. 14, no. 22, 2002
- [85] C. Y. Kuo, S. Y. Lu, S. Chen, M. Bernards, and S. Jiang, "Stop band shift based chemical sensing with three-dimensional opal and inverse opal structures," *Sens Actuators B Chem*, vol. 124, no. 2, 2007
- [86] H. Li, J. Wang, L. Yang, and Y. Song, "Superoleophilic and superhydrophobic inverse opals for oil sensors," *Adv Funct Mater*, vol. 18, no. 20, 2008

- [87] Y. Zhang *et al.*, "A visual and organic vapor sensitive photonic crystal sensor consisting of polymer-infiltrated SiO2 inverse opal," *Physical Chemistry Chemical Physics*, vol. 17, no. 15, 2015
- [88] V. Lousse and S. Fan, "Waveguides in inverted opal photonic crystals," *Opt Express*, vol. 14, no. 2, 2006
- [89] S. A. Rinne, F. García-Santamaría, and P. V. Braun, "Embedded cavities and waveguides in three-dimensional silicon photonic crystals," *Nat Photonics*, vol. 2, no. 1, 2008
- [90] S. Edappadikkunnummal *et al.*, "Impact of Photonic Band Edge Enabled Slow Light Effect on Optical Limiting Activity of Graphene Quantum Dots in All Polymer 1-D Photonic Crystals," *ACS Appl Polym Mater*, vol. 5, no. 8, 2023
- [91] F. Bordas, M. J. Steel, C. Seassal, and A. Rahmani, "Confinement of band-edge modes in a photonic crystal slab," *Opt Express*, vol. 15, no. 17, 2007
- [92] V. V. Vipin, P. R. Chandran, A. M. Ramachandran, A. P. Mohamed, and S. Pillai, "Photonic band gap effect and dye-encapsulated cucurbituril-triggered enhanced fluorescence using monolithic colloidal photonic crystals," *New Journal of Chemistry*, vol. 43, no. 41, 2019
- [93] J. I. L. Chen, G. Von Freymann, S. Y. Choi, V. Kitaev, and G. A. Ozin, "Slow photons in the fast lane in chemistry," *J Mater Chem*, vol. 18, no. 4, 2008
- [94] P. Hildebrandt, T. Heimburg, D. Marsh, P. Hildebrandt, T. Heimburg, and G. L. Powell, "Conformational Changes in Cytochrome c and Cytochrome Oxidase upon Complex Formation: A Resonance Raman Study," *Biochemistry*, vol. 29, no. 6, 1990
- [95] A. Rygula, K. Majzner, K. M. Marzec, A. Kaczor, M. Pilarczyk, and M. Baranska, "Raman spectroscopy of proteins: A review," *Journal of Raman Spectroscopy*, vol. 44, no. 8. 2013
- [96] R. C. Spiker and I. W. Levin, "Phase transitions of phospholipid single-wall vesicles and multilayers. Measurement by vibrational raman spectroscopic frequency differences," *BBA Biomembranes*, vol. 433, no. 3, 1976
- [97] R. R. Brenner, "Effect of unsaturated acids on membrane structure and enzyme kinetics," *Progress in Lipid Research*, vol. 23, no. 2. 1984
- [98] S. Y. Ding, E. M. You, Z. Q. Tian, and M. Moskovits, "Electromagnetic theories of surface-enhanced Raman spectroscopy," *Chemical Society Reviews*, vol. 46, no. 13. 2017

- [99] N. De Acha, D. López-Torres, A. Delgado-Camón, V. Elía-Lorente, C. Elosúa, and F. J. Arregui, "Self-Assembled Gold Nanoparticle Cluster Array Onto Seeded Optical Fiber for Chemical Sensors," ECS Meeting Abstracts, vol. MA2020-01, no. 33, 2020
- [100] A. B. Zrimsek *et al.*, "Single-Molecule Chemistry with Surface- and Tip-Enhanced Raman Spectroscopy," *Chemical Reviews*, vol. 117, no. 11. 2017
- [101] M. Fleischmann, P. J. Hendra, and A. J. McQuillan, "Raman spectra of pyridine adsorbed at a silver electrode," *Chem Phys Lett*, vol. 26, no. 2, 1974
- [102] D. L. Jeanmaire and R. P. Van Duyne, "Surface raman spectroelectrochemistry. Part I. Heterocyclic, aromatic, and aliphatic amines adsorbed on the anodized silver electrode," *Journal of Electroanalytical Chemistry*, vol. 84, no. 1, 1977
- [103] M. G. Albrecht and J. A. Creighton, "Anomalously Intense Raman Spectra of Pyridine at a Silver Electrode," *J Am Chem Soc*, vol. 99, no. 15, 1977
- [104] D. T. Nurrohman and N. F. Chiu, "A review of graphene-based surface plasmon resonance and surface-enhanced raman scattering biosensors: Current status and future prospects," *Nanomaterials*, vol. 11, no. 1. 2021
- [105] J. Homola, "Sebastian Schlücker (Ed.): Surface enhanced Raman spectroscopy: analytical, biophysical and life science applications," *Anal Bioanal Chem*, vol. 401, no. 8, 2011
- [106] E. C. Le Ru and P. G. Etchegoin, *Principles of Surface-Enhanced Raman Spectroscopy*. 2009
- [107] N. D. Israelsen, C. Hanson, and E. Vargis, "Nanoparticle properties and synthesis effects on surface-enhanced Raman scattering enhancement factor: An introduction," *Scientific World Journal*, vol. 2015. 2015
- [108] S. Fateixa, H. I. S. Nogueira, and T. Trindade, "Surface-Enhanced Raman Scattering Spectral Imaging for the Attomolar Range Detection of Crystal Violet in Contaminated Water," *ACS Omega*, vol. 3, no. 4, 2018
- [109] R. Beeram and V. R. Soma, "Ultra-trace detection of diverse analyte molecules using femtosecond laser structured Ag–Au alloy substrates and SERRS," *Opt Mater (Amst)*, vol. 137, 2023
- [110] D. Banerjee, M. Akkanaboina, S. Ghosh, and V. R. Soma, "Picosecond Bessel Beam Fabricated Pure, Gold-Coated Silver Nanostructures for Trace-Level Sensing of Multiple Explosives and Hazardous Molecules," *Materials*, vol. 15, no. 12, 2022

- [111] R. Beeram, D. Banerjee, L. M. Narlagiri, and V. R. Soma, "Machine learning for rapid quantification of trace analyte molecules using SERS and flexible plasmonic paper substrates," *Analytical Methods*, 2022
- [112] K. Kneipp *et al.*, "Single molecule detection using surface-enhanced raman scattering (SERS)," *Phys Rev Lett*, vol. 78, no. 9, 1997
- [113] H. Lin *et al.*, "Biosensors: On-line SERS Detection of Single Bacterium Using Novel SERS Nanoprobes and A Microfluidic Dielectrophoresis Device (Small 22/2014)," *Small*, vol. 10, no. 22, 2014
- [114] J. Wu, L. Zhang, F. Huang, X. Ji, H. Dai, and W. Wu, "Surface enhanced Raman scattering substrate for the detection of explosives: Construction strategy and dimensional effect," *Journal of Hazardous Materials*, vol. 387. 2020
- [115] F. Zapata, M. López-López, and C. García-Ruiz, "Detection and identification of explosives by surface enhanced Raman scattering," *Applied Spectroscopy Reviews*, vol. 51, no. 3, 2016.
- [116] A. Hakonen, P. O. Andersson, M. Stenbæk Schmidt, T. Rindzevicius, and M. Käll, "Explosive and chemical threat detection by surface-enhanced Raman scattering: A review," *Analytica Chimica Acta*, vol. 893. 2015.
- [117] V. S. Vendamani, R. Beeram, M. M. Neethish, S. V. S. N. Rao, and S. V. Rao, "Wafer-scale silver nanodendrites with homogeneous distribution of gold nanoparticles for biomolecules detection," *iScience*, vol. 25, no. 8, 2022.
- [118] C. Byram, S. S. Bharathi Moram, and S. Venugonal Rao, "Femtosecond Laser-patterned and Au-coated Iron Surfaces as SERS Platforms for Multiple Analytes Detection," in 2019 Workshop on Recent Advances in Photonics, WRAP 2019, 2019.
- [119] D. Zhang *et al.*, "Rapid field trace detection of pesticide residue in food based on surface-enhanced Raman spectroscopy," *Microchimica Acta*, vol. 188, no. 11. 2021.
- [120] R. M. Jarvis and R. Goodacre, "Characterisation and identification of bacteria using SERS," *Chem Soc Rev*, vol. 37, no. 5, 2008.
- [121] P. H. B. Aoki, L. N. Furini, P. Alessio, A. E. Aliaga, and C. J. L. Constantino, "Surface-enhanced Raman scattering (SERS) applied to cancer diagnosis and detection of pesticides, explosives, and drugs," *Rev Anal Chem*, vol. 32, no. 1, 2013.
- [122] R. Beeram, K. R. Vepa, and V. R. Soma, "Recent Trends in SERS-Based Plasmonic Sensors for Disease Diagnostics, Biomolecules Detection, and Machine Learning Techniques," *Biosensors*, vol. 13, no. 3, 2023.
- [123] M. Moskovits, "Surface-enhanced spectroscopy," 1985.

- [124] H. Raether, G. Hohler, and E. A. Niekisch, "Surface Plasmons on Smooth and Rough Surfaces and on Gratings," *Springer Tracts in Modern Physics*, vol. 111. 1988.
- [125] A. Boltasseva and H. A. Atwater, "Low-loss plasmonic metamaterials," *Science*, vol. 331, no. 6015. 2011.
- [126] G. V. Naik, V. M. Shalaev, and A. Boltasseva, "Alternative plasmonic materials: Beyond gold and silver," *Advanced Materials*, vol. 25, no. 24. 2013.
- [127] S. A. Maier, Plasmonics: Fundamentals and applications. 2007.
- [128] K. A. Willets and R. P. Van Duyne, "Localized surface plasmon resonance spectroscopy and sensing," *Annu Rev Phys Chem*, vol. 58, 2007
- [129] S. A. Meyer, E. C. Le Ru, and P. G. Etchegoin, "Combining Surface Plasmon Resonance (SPR) spectroscopy with surface-enhanced Raman scattering (SERS)," *Anal Chem*, vol. 83, no. 6, 2011
- [130] Y. H. Jang *et al.*, "Configuration-controlled Au nanocluster arrays on inverse micelle nano-patterns: Versatile platforms for SERS and SPR sensors," *Nanoscale*, vol. 5, no. 24, 2013
- [131] C. Chen, Z. Liu, C. Cai, and Z. M. Qi, "Facile fabrication of nanoporous gold films for surface plasmon resonance (SPR) sensing and SPR-based SERS," *J Mater Chem C Mater*, vol. 9, no. 21, 2021
- [132] N. Kumar and S. P. Ojha, "Photonic crystals as infrared broadband reflectors with different angles of incidence: A comparative study," *Progress in Electromagnetics Research*, vol. 80, 2008
- [133] L. Thylén, M. Qiu, and S. Anand, "Photonic crystals A step towards integrated circuits for photonics," *ChemPhysChem*, vol. 5, no. 9. 2004.
- [134] M. A. Butt, S. N. Khonina, and N. L. Kazanskiy, "Recent advances in photonic crystal optical devices: A review," *Optics and Laser Technology*, vol. 142. 2021.
- [135] T. Li, G. Liu, H. Kong, G. Yang, G. Wei, and X. Zhou, "Recent advances in photonic crystal-based sensors," *Coordination Chemistry Reviews*, vol. 475. 2023.
- [136] K. Wang, X. Dong, Y. Bu, and X. Wang, "Design of photonic crystals for light-emitting diodes," *Journal of the American Ceramic Society*, vol. 106, no. 12. 2023
- [137] W. Liu, H. Ma, and A. Walsh, "Advance in photonic crystal solar cells," *Renewable and Sustainable Energy Reviews*, vol. 116. 2019.
- [138] J. Vučković, "Quantum optics and cavity QED with quantum dots in photonic crystals Jelena Vučković, Stanford University," *Note*, vol. 2013, no. August, 2013.

- [139] G. X. Li *et al.*, "High-Performance Photonic Crystal Films for Thermal Management and Wound Healing," *ACS Appl Polym Mater*, vol. 4, no. 8, 2022
- [140] H. Inan *et al.*, "Photonic crystals: Emerging biosensors and their promise for point-of-care applications," *Chemical Society Reviews*, vol. 46, no. 2. 2017.
- [141] Z. Cai et al., "From colloidal particles to photonic crystals: Advances in self-assembly and their emerging applications," *Chemical Society Reviews*, vol. 50, no. 10. 2021
- [142] S. H. Kim, S. J. Jeon, W. C. Jeong, H. S. Park, and S. M. Yang, "Optofluidic synthesis of electroresponsive photonic janus balls with isotropic structural colors," *Advanced Materials*, vol. 20, no. 21, 2008
- [143] S. G. Romanov and A. V. Fokin, "Variation of spontaneous emission in the opal stopband with an enhanced refractive-index contrast," *Physics of the Solid State*, vol. 45, no. 3, 2003
- [144] H. Yamada, T. Nakamura, Y. Yamada, and K. Yano, "Colloidal-crystal laser using monodispersed mesoporous silica spheres," *Advanced Materials*, vol. 21, no. 41, 2009,
- [145] S. H. Kim, S. H. Kim, W. C. Jeong, and S. M. Yang, "Low-threshold lasing in 3D dye-doped photonic crystals derived from colloidal self-assemblies," *Chemistry of Materials*, vol. 21, no. 20, 2009
- [146] S. Furumi, H. Fudouzi, H. T. Miyazaki, and Y. Sakka, "Flexible polymer colloidalcrystal lasers with a light-emitting planar defect," *Advanced Materials*, vol. 19, no. 16, 2007
- [147] J. Liao, C. Ye, P. Agrawal, Z. Gu, and Y. S. Zhang, "Colloidal Photonic Crystals for Biomedical Applications," *Small Structures*, vol. 2, no. 5. 2021.
- [148] Y. Takeoka and M. Watanabe, "Tuning Structural Color Changes of Porous Thermosensitive Gels through Quantitative Adjustment of the Cross-Linker in Pre-gel Solutions," *Langmuir*, vol. 19, no. 22, 2003
- [149] K. Matsubara, M. Watanabe, and Y. Takeoka, "A thermally adjustable multicolor photochromic hydrogel," *Angewandte Chemie International Edition*, vol. 46, no. 10, 2007
- [150] F. Liu, S. Zhang, X. Jin, W. Wang, and B. Tang, "Thermal-Responsive Photonic Crystal with Function of Color Switch Based on Thermochromic System," *ACS Appl Mater Interfaces*, vol. 11, no. 42, 2019
- [151] E. Tian, J. Wang, Y. Zheng, Y. Song, L. Jiang, and D. Zhu, "Colorful humidity sensitive photonic crystal hydrogel," *J Mater Chem*, vol. 18, no. 10, 2008

- [152] D. Kou, W. Ma, S. Zhang, J. L. Lutkenhaus, and B. Tang, "High-Performance and Multifunctional Colorimetric Humidity Sensors Based on Mesoporous Photonic Crystals and Nanogels," ACS Appl Mater Interfaces, vol. 10, no. 48, 2018
- [153] P. Escudero, J. Yeste, C. Pascual-Izarra, R. Villa, and M. Alvarez, "Color tunable pressure sensors based on polymer nanostructured membranes for optofluidic applications," *Sci Rep*, vol. 9, no. 1, 2019
- [154] T. Han, Y. Liu, Z. Wang, Z. Wu, S. Wang, and S. Li, "Simultaneous temperature and force measurement using Fabry-Perot interferometer and bandgap effect of a fluid-filled photonic crystal fiber," *Opt Express*, vol. 20, no. 12, 2012
- [155] Y. Shimoda, M. Ozaki, and K. Yoshino, "Electric field tuning of a stop band in a reflection spectrum of synthetic opal infiltrated with nematic liquid crystal," *Appl Phys Lett*, vol. 79, no. 22, 2001
- [156] S. Kubo, Z. Z. Gu, K. Takahashi, A. Fujishima, H. Segawa, and O. Sato, "Tunable photonic band gap crystals based on a liquid crystal-infiltrated inverse opal structure," J Am Chem Soc, vol. 126, no. 26, 2004
- [157] J. Ge and Y. Yin, "Magnetically tunable colloidal photonic structures in alkanol solutions," *Advanced Materials*, vol. 20, no. 18, 2008
- [158] W. Luo, H. Ma, F. Mou, M. Zhu, J. Yan, and J. Guan, "Steric-repulsion-based magnetically responsive photonic crystals," *Advanced Materials*, vol. 26, no. 7, 2014
- [159] Y. Zhang, Y. Wang, Y. Wen, Q. Zhong, and Y. Zhao, "Self-Healable Magnetic Structural Color Hydrogels," *ACS Appl Mater Interfaces*, vol. 12, no. 6, 2020
- [160] T. Endo, Y. Yanagida, and T. Hatsuzawa, "Colorimetric detection of volatile organic compounds using a colloidal crystal-based chemical sensor for environmental applications," *Sens Actuators B Chem*, vol. 125, no. 2, 2007
- [161] K. Lee and S. A. Asher, "Photonic crystal chemical sensors: pH and ionic strength," *J Am Chem Soc*, vol. 122, no. 39, 2000
- [162] X. Xu, A. V. Goponenko, and S. A. Asher, "Polymerized polyHEMA photonic crystals: pH and ethanol sensor materials," *J Am Chem Soc*, vol. 130, no. 10, 2008
- [163] H. Jiang *et al.*, "Photonic crystal pH and metal cation sensors based on poly(vinyl alcohol) hydrogel," *New Journal of Chemistry*, vol. 36, no. 4, 2012
- [164] C. Li, L. Li, S. Yu, X. Jiao, and D. Chen, "High Performance Hollow Metal–Organic Framework Nanoshell-Based Etalons for Volatile Organic Compounds Detection," *Adv Mater Technol*, vol. 1, no. 7, 2016

- [165] Y. Zhang *et al.*, "Fluoral-p infiltrated SiO2 inverse opal photonic crystals as fluorescent film sensors for detecting formaldehyde vapor," *J Mater Chem C Mater*, vol. 4, no. 41, 2016
- [166] J. Liu, Y. Zhang, R. Zhou, and L. Gao, "Volatile alcohol-responsive visual sensors based on P(HEMA-: Co -MA)-infiltrated SiO2 inverse opal photonic crystals," *J Mater Chem C Mater*, vol. 5, no. 24, 2017
- [167] W. Hong *et al.*, "Full-color CO2 gas sensing by an inverse opal photonic hydrogel," *Chemical Communications*, vol. 49, no. 74, 2013
- [168] B. Cunningham, J. Qiu, B. Lin, P. Li, and J. Pepper, "A Plastic Colorimetric Resonant Optical Biosensor for Multiparallel Detection of Label-Free Biochemical Interactions," *Proceedings of IEEE Sensors*, vol. 1, no. 1, 2002
- [169] Y. Tan, E. Sutanto, A. G. Alleyne, and B. T. Cunningham, "Photonic crystal enhancement of a homogeneous fluorescent assay using submicron fluid channels fabricated by E-jet patterning," *J Biophotonics*, vol. 7, no. 3–4, 2014
- [170] B. Liu, H. Monshat, Z. Gu, M. Lu, and X. Zhao, "Recent advances in merging photonic crystals and plasmonics for bioanalytical applications," *Analyst*, vol. 143, no. 11. 2018.
- [171] S. Y. Ding *et al.*, "Nanostructure-based plasmon-enhanced Raman spectroscopy for surface analysis of materials," *Nature Reviews Materials*, vol. 1, no. 6. 2016
- [172] Z. Mu, X. Zhao, Y. Huang, M. Lu, and Z. Gu, "Photonic Crystal Hydrogel Enhanced Plasmonic Staining for Multiplexed Protein Analysis," *Small*, vol. 11, no. 45, 2015
- [173] D. Wang, X. Zhao, X. Liu, Z. Mu, and Z. Gu, "Rapid identification of electricigens via silver-plated photonic crystal filters," *Nano Res*, vol. 9, no. 9, 2016
- [174] S. V. Gaponenko *et al.*, "Raman scattering enhancement using crystallographic surface of a colloidal crystal," *JETP Lett*, vol. 74, no. 6, 2001
- [175] L. Lu *et al.*, "Controlled fabrication of gold-coated 3D ordered colloidal crystal films and their application in surface-enhanced raman spectroscopy," *Chemistry of Materials*, vol. 17, no. 23, 2005
- [176] S. Kubo, Z. Z. Gu, D. A. Tryk, Y. Ohko, O. Sato, and A. Fujishima, "Metal-coated colloidal crystal film as surface-enhanced Raman scattering substrate," *Langmuir*, vol. 18, no. 13, 2002
- [177] S. Guddala, S. A. Kamanoor, A. Chiappini, M. Ferrari, and N. R. Desai, "Experimental investigation of photonic band gap influence on enhancement of Raman-scattering in metal-dielectric colloidal crystals," *J Appl Phys*, vol. 112, no. 8, 2012.

- [178] H. Wang, Y. Wu, and H. Song, "Synergistic effects of photonic crystal and gold nanostars for quantitative SERS detection of 3-Phenoxybenzoic acid," *Appl Surf Sci*, vol. 476, 2019.
- [179] T. Yamasaki and T. Tsutsui, "Fabrication and optical properties of two-dimensional ordered arrays of silica microspheres," *Japanese Journal of Applied Physics, Part 1: Regular Papers and Short Notes and Review Papers*, vol. 38, no. 10, 1999.
- [180] G. T. Ayenew *et al.*, "Photonic properties of two-dimensional photonic crystals based on monolayer of dielectric microspheres," in *Nanophotonics IV*, SPIE, Apr. 2012.
- [181] H. T. Miyazaki, H. Miyazaki, K. Ohtaka, and T. Sato, "Photonic band in two-dimensional lattices of micrometer-sized spheres mechanically arranged under a scanning electron microscope," *J Appl Phys*, vol. 87, no. 10, pp. 7152–7158, May 2000.
- [182] X. Zhao, J. Xue, Z. Mu, Y. Huang, M. Lu, and Z. Gu, "Gold nanoparticle incorporated inverse opal photonic crystal capillaries for optofluidic surface enhanced Raman spectroscopy," *Biosens Bioelectron*, vol. 72, 2015.
- [183] Z. Yi *et al.*, "Ordered array of Ag semishells on different diameter monolayer polystyrene colloidal crystals: An ultrasensitive and reproducible SERS substrate," *Sci Rep*, vol. 6, 2016.
- [184] D. Qi, L. Lu, L. Wang, and J. Zhang, "Improved SERS sensitivity on plasmon-free TiO2 photonic microarray by enhancing light-matter coupling," *J Am Chem Soc*, vol. 136, no. 28, 2014.

Experimental and Simulation Techniques

The study of PhCs requires the use of both experimental techniques and numerical simulation techniques to understand their optical properties and design novel photonic devices. These techniques provide valuable insights that CPhCs can be used to design templates with unique optical properties for various applications.

2.1 Introduction

The fabrication of photonic crystals (PhCs) through colloidal self-assembly routes [1-5] requires a range of experimental techniques to characterize photonic bandstructures and other optical properties accurately. The monodisperse colloidal polystyrene (PS) particles of different sizes can be synthesized through emulsion polymerization method. An indigenously developed laser light diffraction setup can be used to characterize the crystal structure of the fabricated PhC. Apart from that, the size and polydispersity of the colloidal particles can be measured using Dynamic Light Scattering (DLS) technique. The stop band of the fabricated PhCs, both in bulk and as thin films, can be identified through Bragg peak analysis [6], [7], which can be measured using UV-visible spectroscopy. To further characterize the PhC thin films, the morphology, periodicity of the particle array, particle size, and number of layers Field Emission Scanning Electron Microscopy (FESEM) and light scattering technique can be used. The Raman spectroscopic technique is used to study the effect of PhC templates on the detection of molecules.

In addition to experimental techniques, numerical techniques have been employed to understand the band structure and the optical properties of PhCs [8], [9]. The Finite Element

Method (FEM) have been used to analyze the reflection spectra and electric field distributions within the PhC structure. At the same time, the band structure is calculated using the Plane Wave Method (PWM). These numerical techniques provide valuable insights into the propagation and electromagnetic field distribution of light within the PhC. These properties can be used to optimize the design of PhC devices for various sensing applications. The above mentioned experimental and simulation techniques and their corresponding working principles have been explained in detail in the following sections.

2.2 Synthesis and Purification of Colloidal particles

2.2.1 Synthesis of Polystyrene colloidal particles

Polystyrene (PS) colloidal particle synthesis uses the conventional emulsion polymerization technique[10]. The synthesis procedure involves the formation of emulsion of the liquid monomer in water. The emulsion of monomer in water can be prepared by vigorous stirring of the solution. But it would separate into layers immediately after stopping the agitation. It is common to use surfactants to form a stabilized emulsion. Emulsion polymerization method typically involves four main ingredients, monomer, dispersion medium, surfactant and initiator. Other auxiliary components such as buffers, chain transfer agents, bases, acids and anti-aging agents are added based on the requirement.

The selection of monomers that can be polymerized through emulsion polymerization is based on their ability to form free radicals. Water is typically used as the dispersion medium for the polymer particles and monomer droplets due to its low viscosity and good heat transmission. It also acts as solvent for initiator, surfactant, and other agents. Surfactants are the components which serve multiple roles in the emulsion polymerization process [11]. It reduces the interfacial tension between the monomer water and helps to form a stable emulsion through agitation. When the surfactant concentration is greater than the critical micelle

concentration (CMC), spherical micelles are formed with the hydrophobic tail towards the monomer droplet and hydrophilic head in the water. Micelles help in controlling the particle size and shape. Increasing the amount of surfactant reduces the particle size [12]. Monomer chains, inside the core of micelles leads to nucleation of seed particles. The polymerization process starts upon adding the initiator into the reaction chamber, which is kept at a constant temperature of $70^{\circ}\text{C} \pm 0.1^{\circ}\text{C}$. The thermally decomposable initiator forms free radicals at this elevated temperature and starts the polymerization reaction. These free radicals react with the monomers and form highly reactive monomer radicals known as oligomers which will start growing. Buffers are usually added to the system to regulate the pH. The schematic representation of the step-by-step process leading to the initiation of polymerization is shown in Fig. 2.1. Initially, the larger monomer droplets are dispersed in the dispersion medium by adding a surfactant and then stirring. The spherical micelles formed around these smaller monomer droplets when the surfactant concentration used is greater than CMC. In the next step the initiator decomposes and form free radicals which react with monomer molecules in the micelles to form monomer radicals (oligomers) which initiate the polymerization process.

In general, emulsion polymerization takes place in three steps; i) initiation, ii) propagation, and iii) termination. Figure 2.2 is the schematic plot of the polymerization rate vs. time. At the initial stage, the free radicals are formed by decomposing the initiator, react with the monomer molecules to initiate the polymerization. By reacting with another monomer molecule, these free radicals function as active centres for the polymerization, extending the chain. After the propagation stage, the reaction gets terminated by reacting with another free radical molecule or an oligomer. A turbid suspension of polymer colloidal particles dispersed in the water medium (also known as latex) is collected at the end of the reaction.

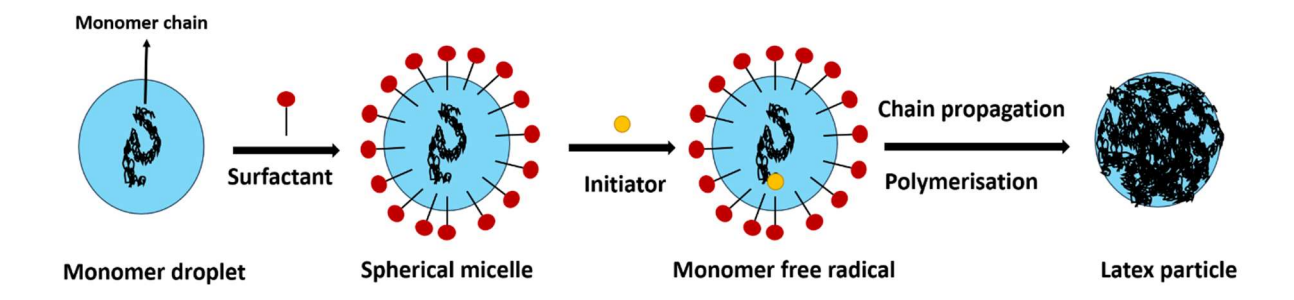


Fig 2.1 The schematic representation of the emulsion polymerisation process of the monomer in the presence of a surfactant with a concentration higher than CMC.

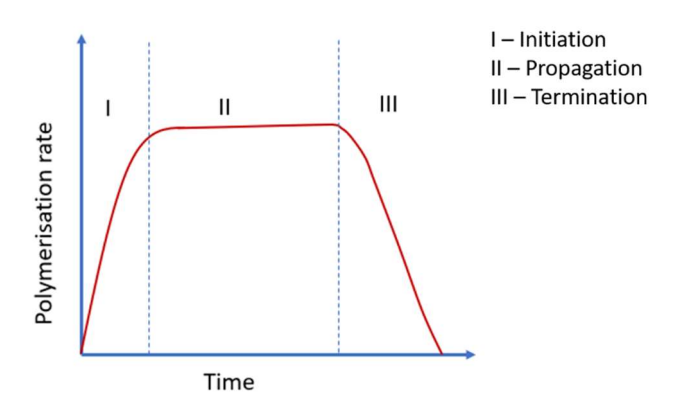


Fig. 2.2 The polymerisation rate with respect to the time indication three stages, viz. initiation (I), propagation (II) and termination (III)

PS colloidal particles with different particle sizes are synthesized using the method reported by Fu. *Et al.*[13]. The main components in the synthesis constitute, monomer (Styrene), initiator (Potassium persulfate (KPS)), surfactant (sodium dodecyl sulfate (SDS)), and buffer (Sodium bicarbonate (NaHCO₃)). All the chemicals of analytical grade (AR) are purchased from Sigma Aldrich. Styrene is preserved with an added inhibitor, which is removed using 1M sodium hydroxide (NaOH) solution. The cleaning process is carried out by washing with NaOH solution and MilliQ water consecutively a minimum of three times. Initially, the monomer solution is prepared by mixing the styrene, SDS and NaHCO₃. These constituents are mixed thoroughly with the help of a magnetic stirrer. The monomer solution is filtered through a syringe filter with 0.22 μm to remove any dust particles present in the solution, which

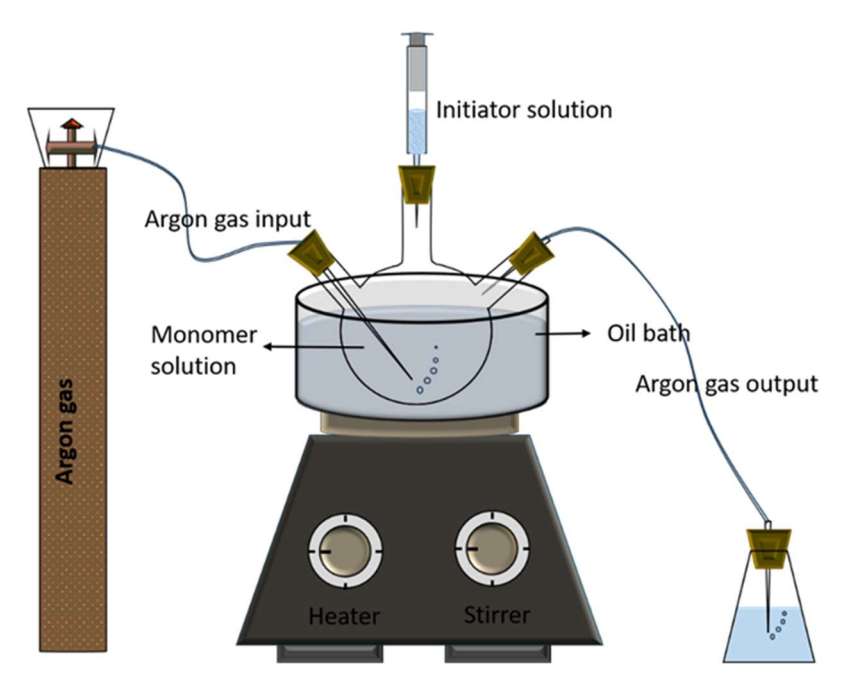


Fig. 2.3 Schematic illustration of synthesis set-up for PS colloidal particles through emulsion polymerisation.

will act as nucleation centers during the polymerization. The filtered monomer solution is transferred to the three-neck round bottom flask (RB flask), which is housed inside an oil bath to keep the reaction chamber's temperature constant. The monomer solution is degassed through the Argon gas purging under vigorous stirring to remove the dissolved oxygen in the monomer solution. During the purging process, the monomer solution is heated up to 70° C and is maintained at this temperature. The initiator solution is separately prepared in MilliQ water 70^{0} \mathbf{C} which introduced at and filtered, the monomer to solution to start the polymerization. Polymerization is kept for 13 hours under constant argon purging and stirring. Any fluctuations in the gas purging rate, stirring speed and temperature can result in polydispersity of particles during synthesis. After completing the reaction, the turbid solution is cooled back to room temperature and transferred for purification and further processing. The schematic representation of the synthesis setup is shown in Fig. 2.3. Differentsized particles can be synthesized by varying the amount of different components, which is shown in table. 2.1. The colloidal suspension thus synthesized has been characterized to the particle size and size poly dispersity using dynamic light scattering (DLS), which is discussed in latter part of this chapter.

Table 2.1: Details of reagents used in synthesis of PS colloidal particles along with the hydrodynamic diameter, d_h of PS particles at 25 0 C and corresponding SPD.

Sample	Styrene (M)	SDS (mM)	KPS (mM)	NaHCO ₃ (mM)	d _h (nm)	SPD (%)
PS-1	1.9	4.69	11.5	9.3	72	5.7
PS-2	1.02	0.1	1.95	6.9	528	2
PS-3	1.05	3	1.63	6.9	287	4.3

2.2.2 Purification of colloidal particles

As synthesized PS particles are purified by subjecting the suspension to purification methods such as: dialysis, ultrafiltration and using ion-exchange resins.

i) Dialysis

Subjecting the synthesized suspension to dialysis removes the unreacted monomers, ionic impurities etc. The dialysis process uses semipermeable membrane. The process of purification of colloidal suspension is based on the osmotic pressure difference across the semipermeable membrane. Depending on the pore size of the membrane, unreacted monomer molecules and ions pass through the membrane leaving the polymer particles inside the dialysis bag. The colloidal suspension is filled in the dialysis bag and kept inside the MilliQ water bath. The conductivity of the MilliQ water is recorded every day, and the process is continued till the water conductivity reaches the conductivity of the MilliQ water used for dialysis. The dialysis tubing cellulose membrane (purchased from Sigma Aldrich) with a molecular weight

cut-off (MWC) of 14,000 g/mol is used. Figure. 2.3 (a) shows the photographic image of PS colloidal suspension under dialysis and Fig. 2.4 (b) gives the graph of conductivity of the water outside the dialysis bag as the function of the time kept for dialysis. The conductivity is found to reduce exponentially as a function of time during dialysis.

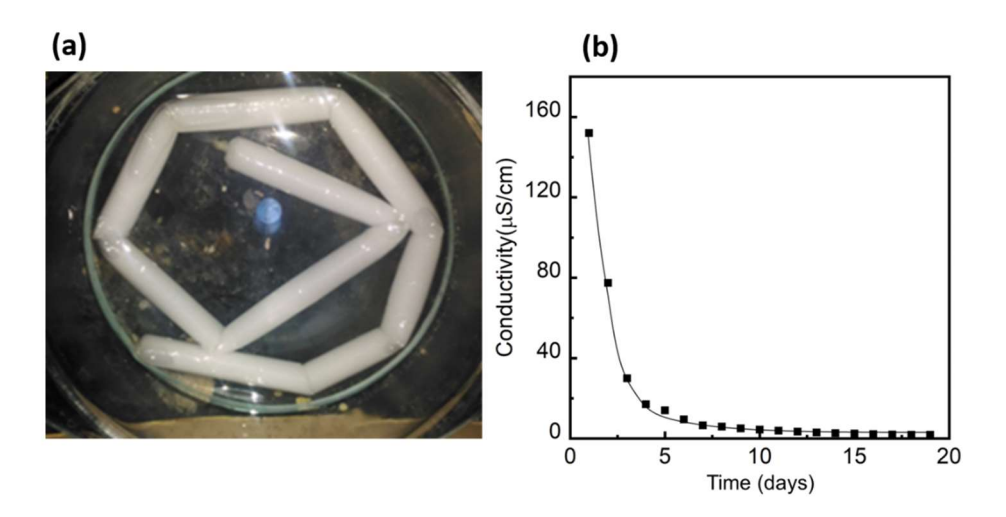


Fig. 2.4 (a) The dialysis tubing cellulose membrane filled with PS suspension and kept immersed in MilliQ water. **(b)** The conductivity of the surrounded milliQ water as a function of time (in units of days).

ii) Ultrafiltration

After the dialysis process, the purified suspension is concentrated by the ultrafiltration technique. Argon gas pressure is applied to the ultrafiltration cell filled with the suspension. The solutes below the MWC of the filter membrane and water will pass through the membrane while the rest of the particles are retained in the cell. The filtration process is carried out under gentle stirring to minimize the concentration polarization and shear denaturation. The schematic representation of the ultrafiltration process is given in Fig. 2.5. The ultrafiltration unit(M/s Axiva Sichem Pvt-Ltd) with Millipore filters of MWC of 1kDa.

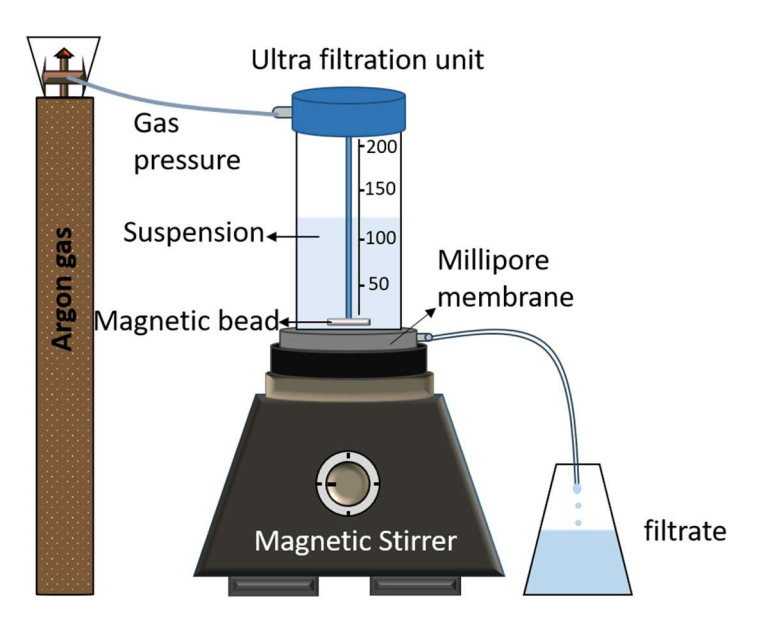


Fig 2.5 schematic representation of purification using an ultra-filtration system under applied gas pressure.

iii) Deionization using ion exchange resins

The concentrated suspension (also referred to as mother suspension) is further purified for removing ionic impurities by keeping the colloidal suspensions in contact with a mixed bed of ion-exchange resins (AmberLite® MB20 Mixed Ion Exchange resin, Sigma Aldrich). Ions originating from dissolved CO₂ molecules in the air and leached-out ions, from the sample cell walls, contribute to the impurity content. The mixed bed of ion exchange resins facilitates the exchange of positive and negative ions with H⁺ and OH⁻ ions, respectively, thereby reducing the overall impurity ion concentration in the suspension. If the concentration of colloidal particles are high and concentration of impurity is are low in the charged colloidal suspension such as a suspension of PS particles, results in the formation of spontaneous crystalline order, which are popularly known as colloidal crystals. Thus, a low impurity concentration in the suspension is essential to achieve stable colloidal suspension with charged colloidal particles interaction through Coulomb repulsion [14], [15].

2.3 Fabrication of different types of CPhCs

2.3.1 CPhC with bcc and fcc ordering in aqueous medium

Several methods have been devised for the fabrication of CPhCs, such as developing artificial opals by close-packing spherical colloidal particles. Another approach is to use colloidal particles that, under low ionic strength, self-assemble into a non-close-packed crystal structure. This particular procedure relies on the self-assembly of charged colloidal particles, which assumes a minimum energy configuration due to electrostatic repulsion, typically forming an fcc lattice structure with (111) planes aligning along the surfaces of the container. The number density (n_p) and the strength of the repulsive interactions of colloidal particles in the solution can be tuned to fabricate CPhCs with specific lattice constants with bcc or fcc ordering. Thus, self-assembly method allows for the customization of CPhCs to achieve with bcc or fcc ordering desired lattice constants [5]. Samples with varying volume fractions can be prepared by diluting the stock suspensions with MilliQ water of conductivity of less than 1 μS/cm. The scattering cell, or sample cuvette, is made up of quartz and has dimensions of 1 x 4.5 cm with a path length of 1 mm. The cuvette is cleaned with chromic acid and rinsed thoroughly with multiple organic solvents followed by washing with MilliQ water. The colloidal suspension is introduced into the cuvette, and ion exchange resins are added. Gravity causes these resins, which are about a 4:1 ratio to the sample, to settle to the bottom of the cell. Subsequently, the cuvette is sealed using a clean, airtight Teflon stopper. Bright iridescence appears signalling the crystallisation of PS particles in a aqueous medium.

2.3.2 Opal type CPhC

Different types of convective self-assembly methods are available for the fabrication of close- packed opal type CPhCs such as vertical self-assembly, which is limited by the particle size. Here we are using an inward growing self-assembly method [16] for fabricating the CPhC (opal type) multilayer (around 15 layers). In this method, initially a glass substrate of

dimension 2.5 cm x 2.5 cm is thoroughly cleaned. After treating the glass substrates with chromic acid overnight, they are rinsed with ethanol and MilliQ water and then dried in an oven. The colloidal suspension of known concentration and volume is then added to the center of the glass substrate using a micro pipette. The drop is spread using a 1 mm pipette tip for a uniformity and left it for drying under ambient temperature (25 ± 2^{-0} C). Within a minute, vibrant colors began to emerge, gradually moving towards the film's center as growth progressed. Crystallization is completed within three hours, yielding a uniformly coated substrate, except for a small central void measuring a few millimeters. The method's efficacy was notably sensitive to factors such as solution concentration, volume (ranging from 0.05 ml to 0.1 ml), temperature, and ambient air flow conditions. Air currents in the room were found to influence the directionality of crystallization, which in turn alters the uniformity of film growth.

2.3.3 CPhC monolayer

The CPhC monolayer can be fabricated using the air-water self-assembly method [17]. Figure 2.5 provides a schematic illustration of the step-by-step fabrication process. First, 20 µl of aqueous colloidal suspension is deposited on a glass substrate and dried using a spin coater, resulting in an unstable monolayer of individually separated colloidal spheres on the substrate. This spin coated substrate is then slowly immersed in Milli-Q water in a petri dish. By adding a surfactant solution (SDS), the surface tension of the water is reduced, resulting in the formation of a large monolayer with highly ordered areas. The highly ordered monolayer is picked up by the glass substrate, multiple organic solvents and water. The schematic illustration of step-by step fabrication of CPhC monolayers are shown in Fig. 2.6 ((a) to (c)). The fabricated CPhC monolayers are characterized using scanning electron microscope (SEM) and the details are given in the latter section of this chapter.

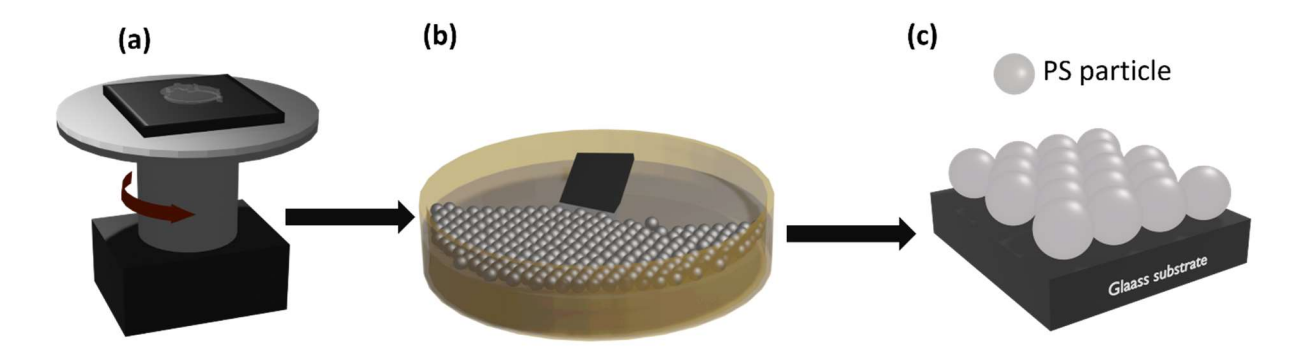


Fig. 2. 6 Schematic representation of fabrication of CPhC monolayer. (a) PS colloidal suspension drying on the spin coater (b) Dispersing unstable monolayer on the water surface and picking up using a pre-cleaned glass substrate (c) Hexagonally close-packed PS colloidal particle monolayer formed on the glass substrate after drying

2.4 Experimental Techniques

2.4.1 Development of Laser Diffraction Setup

The light scattering techniques were extensively used in the characterisation of PhCs for its symmetry and structural ordering. In these techniques, the measurement involves the scattered intensity I(q) plotted against the scattering wave vector, q defined by;

$$q = (4\pi n/\lambda)\sin(\theta/2) \tag{2.1}$$

When the scattering angle, θ is fixed (i.e., position of the detector), then q is varied by changing the incident light wavelength, λ , referred to as energy dispersive method. Conversely, when λ is fixed and the angle is varied, known as angle resolved static light scattering (SLS). In SLS the scattering angle is changed by changing the position of the detector with respect to the incident direction of the laser light. Thus, SLS utilizes the angle resolved method, with the detector sweeping across scattering angle range from $\theta = 15^0$ to 160^0 .

We have developed a laser diffraction setup to characterise the CPhC templates for its structural ordering and symmetry, by using area detector (screen with CCD camera). The process involves collecting Bragg spots at various q values. This is achieved by capturing the

diffraction pattern, analyzing it, and converting it into a intersity pattern. This method is particularly well-suited for thin samples which are not opaque to light. Beyond its cost-effectiveness in terms of components and fabrication, this setup offers the flexibility of changing the incident wavelength manually by changing the laser light source.

i) Theory

Since the interparticle separation is of the order of wavelength of light, laser light scattering is ideal to investigate the structural ordering in the colloidal PhCs. The analysis involves examining the scattered intensity, denoted as I(q), to derive the static structure factor, S(q).

Assume the scattering of light from a volume V containing N spherical colloidal particles. When compared to the quasi-elastic scattering by the particles, the light scattered by the solvent contributes significantly less. Using Rayleigh-Gans approximation, the time-averaged intensity can be expressed as expressed by [5], [14], [15];

$$I(q) = AP(q)S(q) \tag{2.2}$$

Here, q is the scattering wave vector defined by Eq. 2.1 The particle-scattering form factor or particle structure factor P(q) of a spherical particle of radius a is given by;

$$P(q) = \left(\frac{3(\sin(qa) - (qa)\cos(qa))}{(qa)^3}\right)^2$$
 (2.3)

The interparticle structure factor, S(q) is defined by;

$$S(q) = 1 + \frac{1}{N} \sum_{m>n=1}^{N} \exp[iq.(r_m - r_n)]$$
(2.4)

where r_m is the position of the centre of mass of the m^{th} particle. The constant, A, for a polarized scattered light is given by;

$$A = \frac{16\pi^4 N a^6}{\lambda^4} \left(\frac{\mu^2 - 1}{\mu^2 + 2}\right) \frac{I_0}{D^2}$$
(2.5)

Here, $\mu = \frac{\mu_p}{\mu_m}$, the relative refractive index, where μ_p is the particle refractive index and μ_m is the refractive index of the medium. I_0 is the incident intensity and D is the distance between the sample and the detector.

S(q) is determined by measuring I(q) with respect to q and subsequently correcting for P(q) using Eq. 2.2, i.e., $S(q) = \frac{I(q)}{AP(q)}$. The resulting S(q) is used to characterize structural ordering in the sample.

ii) Development of the laser diffraction instrument and measurements

A new and simple setup for laser light diffraction measurements on PhCs is indigenously developed by procuring the individual components (laser, CCD camera, optical components, anti-vibration optical table, XY, and XYZ translation stages). The setup consists of a He-Ne laser source of maximum power 10 mW and of wavelength 633 nm with a beam diameter of 0.68 mm (Lumentum He-Ne laser, M/S Infrared Optics). The schematic illustration of the development of diffraction setup is given in Fig. 2.7. S(q) can be measured by varying the scattering wave vector, which is related to the scattering angle, θ by Eq. 2.1. Intensity at all scattering angles in a 2D plane can be captured from 0 to 70^{0} in a 2D translucent screen / detector as shown in Fig. 2.7. If the sample is colloidal photonic crystal, one observes Bragg diffraction from the crystallites with interplanar spacing (d) that satisfies the Bragg condition, $n\lambda = 2dsin\theta$. The most important feature of this light diffraction setup is that, it does not require the rotation of either the detector or the laser source for changing the scattering angle.

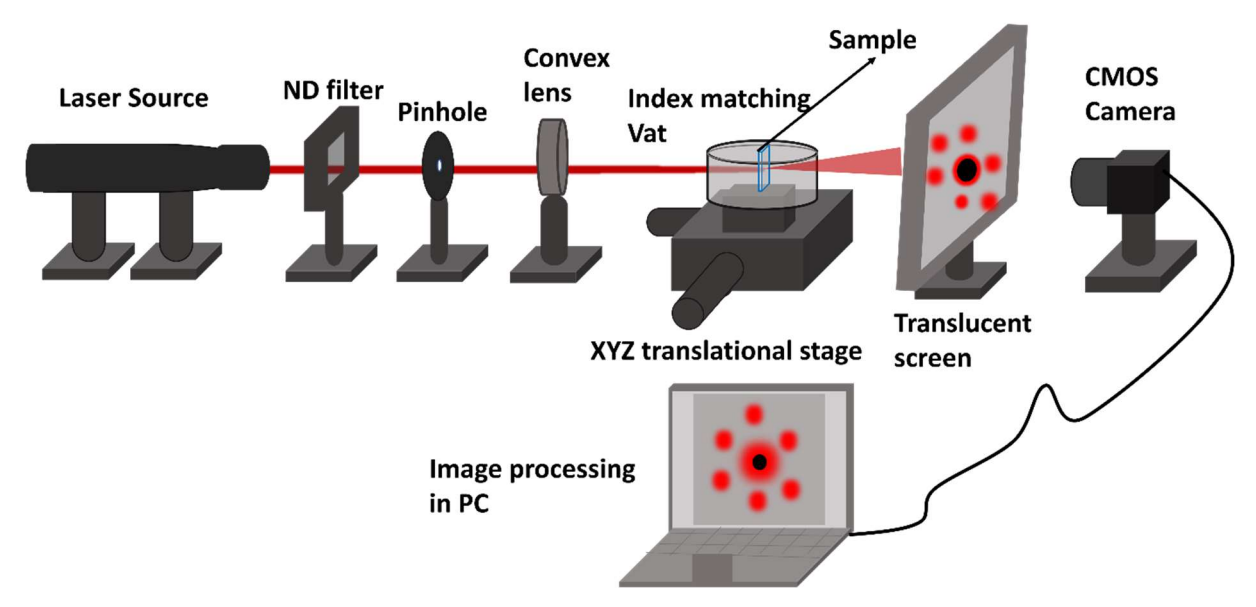


Fig. 2.7 The schematic illustration of laser light diffraction setup.

The entire diffraction pattern is captured on a translucent screen, with each diffraction spot corresponding to different q values. To control the incident light intensity, a series of neutral density (ND) filters are employed. These filters reduce the intensity by; $I_T = I_0 \times 10^{-0D}$, where I_T is the transmitted intensity, I_0 is the incident intensity, and OD is the optical density of the ND filter. The laser beam undergoes further refinement by passing through a pinhole to block any stray reflections, and then the beam is focused onto the sample using a convex lens with a focal length of 15 cm. The PhC sample is positioned on an XYZ stage capable of moving the sample in all three directions. This movement ensures that all crystallites are exposed to the incident beam, enabling the collection of all possible diffraction patterns. Additionally, the sample is housed within an index-matching vat, where the container is filled with a liquid (glycerin) with refractive index matches with the material of the sample cuvette (quartz). The vat with glycerin also serve as a temperature bath. This arrangement is designed to minimize unwanted reflections from the sample surface. The reflections from the vat surface are effectively scattered away, preventing interference with the scattered diffraction pattern from the sample. The sample is prepared according to the method given in section 2.3.1.The diffraction pattern scattered from the sample is recorded on a translucent screen, positioned at

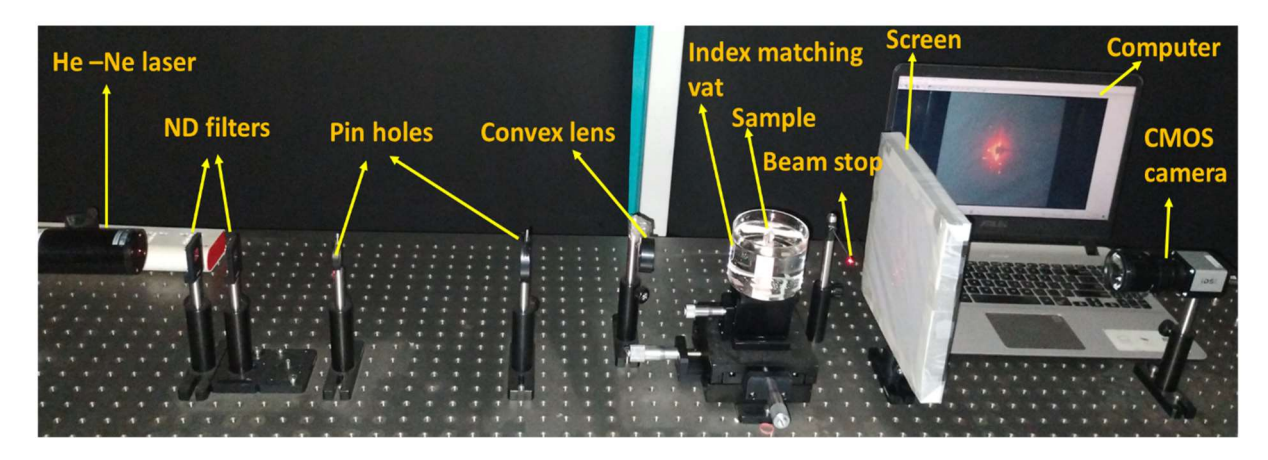


Fig. 2.8 The photograph of the diffraction setup in the laboratory.

an optimum distance from the sample to encompass the maximum possible q range. The central laser spot is blocked using a beam stopper (diameter 7 mm) to further reduce the screen illumination. The diffraction pattern is then captured using a CMOS camera (IDS- uEye SE, M/S Infrared optics) for subsequent processing. The camera features a sensor with an area of 14.2 x 7.5 mm and a pixel size of 3.45 x 3.45 μ m. Equipped with a fixed focal length lens of 12 mm and a minimum working distance of 100 mm, the camera is connected to a computer. The captured diffraction pattern is digitized through computer programming developed in Python. The resulting I(q) versus q diffraction data is further converted into structure factor data to obtain the information on the structural ordering and the symmetry of the PhC sample. The photographic image of the diffraction setup is given in Fig. 2.8.

The Python code consists of mainly three parts. 1) Averaging a set of diffraction images and subtracting the background. The image captured for the beam passing through the non-crystallized sample is taken as the background. This part of the code is dedicated to noise reduction. 2) Converting the Bragg spots to rings. This involves adding the pixel intensities along the ring of radius r and width Δr and equally distributing the sum across the area of the ring. 3) Structure factor calculation. In this step, the ring pattern is converted to the I(q) versus q and with r related to scattering angle θ by, $\tan \theta_i = \frac{r_i}{D}$, where, θ_i is the scattering angle of ith diffraction spot and D is the distance between sample and screen (see Fig. 2.9). The scattering

angle, θ_i of i^{th} Bragg spot is related to the scattering wave vector, q_i through the relation Eq. 2.1. The intensity of diffraction pattern is then converted to S(q) versus q by employing the equations described in section 2.4.1 (Eq. 2.1 to Eq. 2.5).

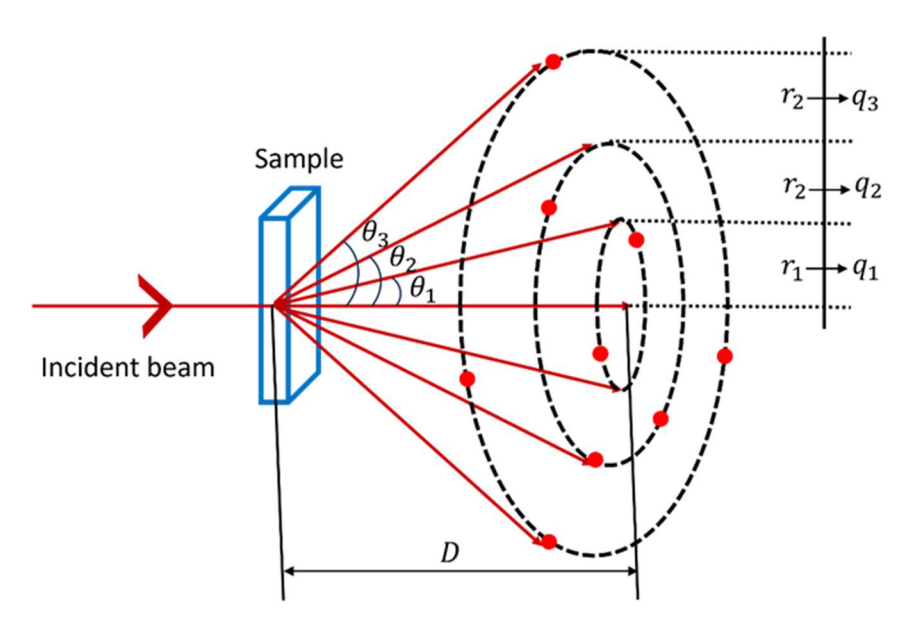


Fig. 2.9 Schematics of scattering geometry. D: sample-to-detector distance, θ_i : scattering angle of i^{th} reflection, r_i : radial distance from the centre to i^{th} reflection.

To characterize the structural ordering of the PhC samples, the diffraction pattern is recorded and analysed. The diffraction pattern of sample PS1, with ϕ , 0.0037 (calculated using the method described in section 2.5.2) is reordered and given in Fig. 2.10(a). The diffraction pattern is then converted into rings, with the total intensity at diameter r and width Δr

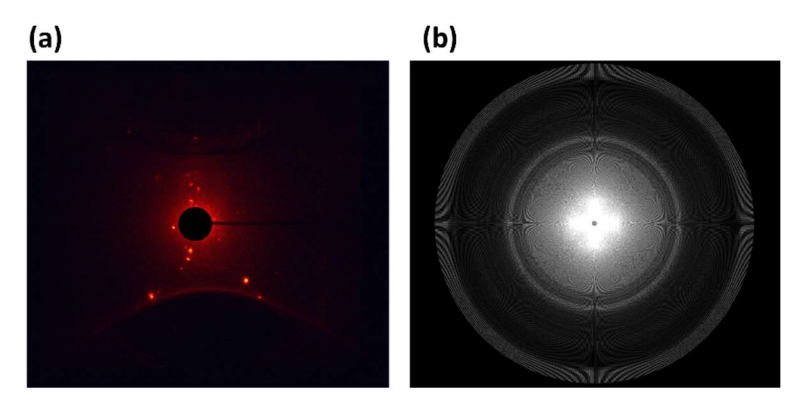


Fig. 2.10 (a) Diffraction pattern of the CPhC sample PS1. (b) ring pattern obtained from the diffraction pattern by distributing the total intensity to the area of the ring with diameter r and width Δr for further processing.

distributed uniformly around the area of the ring (Fig. 2.10(b)), to facilitate conversion of the diffraction pattern into a 1D plot of I(q) vs. q.

The recorded diffraction pattern is then converted to a plot of I(q) vs. q to extract the crystal structure. I(q) versus q graphs are smoothened and corrected for baseline. The peaks are fitted for an fcc crystal structure, with the first peak of diffraction originating from the (111) plane, and subsequent planes are calculated satisfying the ratio, $\frac{q_1}{q_2} = \sqrt{\frac{h_1^2 + k_1^2 + l_1^2}{h_2^2 + k_2^2 + l_2^2}}$, where the h, k and l are the miller indices. The I(q) versus q is given in Fig. 2.11, hence obtaining the crystal structure of the CPhC under study.

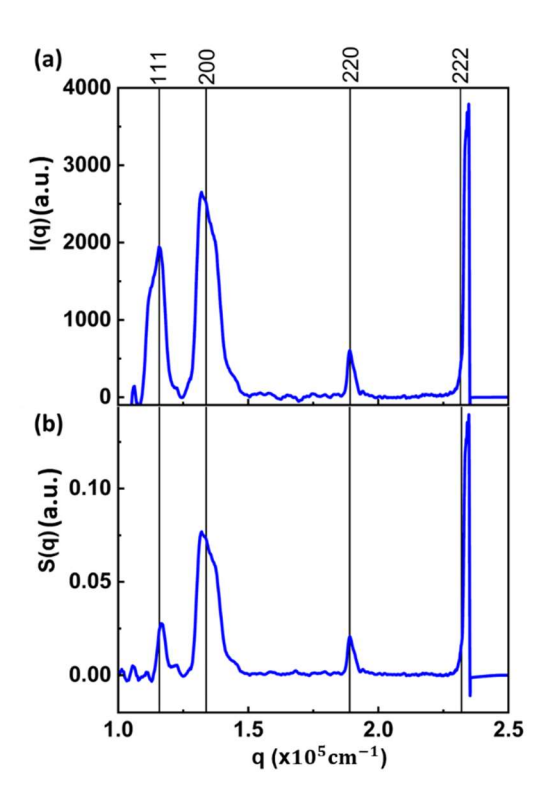


Fig. 2.11 (a) Intensity as a function of q, and (b) structure factor as a function of q of the sample PS-1 indicating the peaks fitting with planes of fcc lattice.

The diffraction pattern of PSPhC multilayer of sample PS-2, fabricated using inward growing self-assembly method (described in section 2.3.2), is recorded using a blue light source. The sample is no longer placed inside a vat, since the it is a film coated on a glass surface. Instead, it is placed on a sample holder as shown in Fig. 2.12 (a). The diffraction spots

(see Fig. 2.12 (b)) show a hexagonal pattern indicating the hexagonal symmetry of the CPhC. The hexagonal symmetry is further confirmed using the SEM image of the sample (Fig. 2.12 (b)).

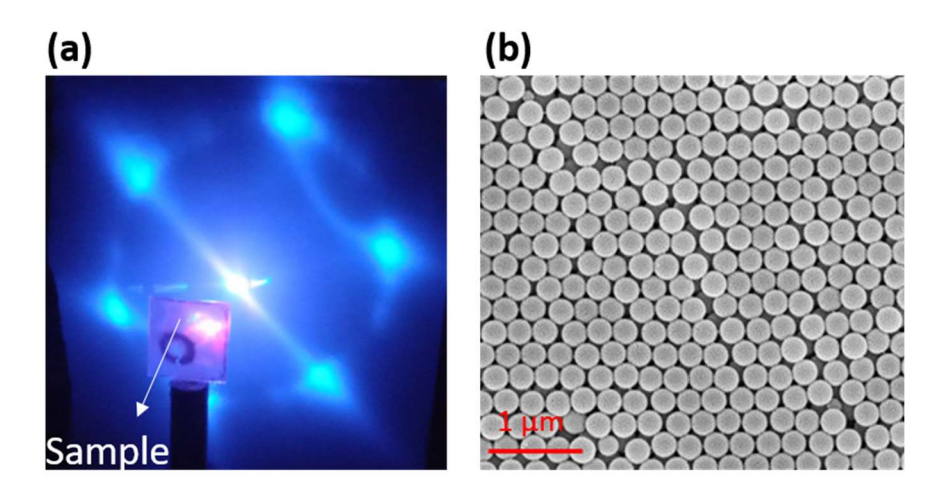


Fig. 2.12 (a) The hexagonal diffraction pattern indicating the hexagonal symmetry of the CPhC of sample PS-2 **(b)** FESEM image of the hexagonal arrangement of colloidal particles.

2.4.2 Dynamic light Scattering (DLS) Technique

Dynamic light scattering (DLS) measures the equilibrium fluctuations in density states of particles or scatterers in a medium. By analyzing the time-correlation function of these fluctuations in scattering intensity, one obtains the information on the decay time of the correlation function which is related to the diffusion of particles suspended in a medium and their size [18]. Here, the measurement involves analyzing the time-dependent scattered light at a particular scattering angle by calculating the intensity-intensity autocorrelation function of the scattered light, typically using a digital correlator. The sample concentration is prepared in such a way that the light that reaches the detector is single scattered and multiple scattering events are negligible.

The scattered intensity $I_s(q,t)$, fluctuates in time around a time-averaged intensity $\langle I_s(q) \rangle$. The resulting normalized intensity autocorrelation function of the scattered intensity is given by [18], [19],

$$g^{(2)}(q,t) = \frac{\langle I_s(q,t)I_s(q,0) \rangle}{\langle I_s(q,0) \rangle^2}$$
(2.6)

The, auto correlation function of the scattered electric field is defined as,

$$g^{(1)}(q,t) = \frac{\langle E_s(q,t)E_s(q,0) \rangle}{\langle E_s(q,0) \rangle^2}$$
(2.7)

In the notation, $g^{(1)}(q,t)$, the superscript in brackets indicates that it is a first-order correlation function (electric field auto correlation function), whereas the intensity autocorrelation function is a second-order correlation function. The electric field autocorrelation function can be related to the intensity autocorrelation function through the equation known as Siegert relation [20], given by,

$$g^{(2)}(q,t) = 1 + \beta |g^{(1)}(q,t)|^2$$
(2.8)

 $\beta \approx 1$, is the coherence factor which depends on the experimental geometry [1] and q, is the magnitude of scattering wave vector given by Eq. 2.1.

The electric field autocorrelation function is commonly known as the intermediate scattering function denoted as f(q,t). This term is often used because, in DLS, we measure the intensity correlation function. f(q,t) is described by the equation;

$$g^{(1)}(q,t) = f(q,t) = \frac{F(q,t)}{S(q)}$$
 (2.10)

Where F(q,t) dynamic structure factor and S(q) is the static structure factor. At dilute conditions $S(q) \to 1$. Then f(q,t) can be written as,

$$f(q,t) = \exp(-q^2 < r^2(t) > /6) = \exp(-D_0 q^2 t)$$
 (2.11)

,where, $\langle r^2(t) \rangle$ is the mean square displacement (MSD) which used to study the dynamics of the particle. For a three-dimensional system, MSD related to the free diffusion coefficient, D_0 , by,

$$\langle r^2(t) \rangle = 6D_0 t$$
 (2.12)

The free diffusion coefficient and the particle diameter are related through the Stokes-Einstein relation,

$$D_0 = \frac{k_B T}{3\pi n d_B} \tag{2.13}$$

Here, k_B , T and η are the Boltzmann constant, absolute temperature and viscosity of the solvent respectively. d_h is the hydrodynamic diameter of the particle. Now, for a very dilute (non-interacting system) and monodisperse sample, the Eq. 2.8 becomes,

$$g^{(2)}(q,t) = 1 + \beta exp(-2\Gamma t)$$
 (2.14)

, where $\Gamma = q^2 D_0$, is the decay constant, i.e., the decaying part of the signal contains the information regarding the diffusivity of the particle being studied. Now, from the intensity autocorrelation function, the particles' free diffusion coefficient and, *via* the Stokes-Einstein relation [20], their hydrodynamic diameter can be obtained.

If the colloidal particles are polydisperse in diameter, the decay constant, Γ has a distribution, $G(\Gamma)$. Then the intermediate autocorrelation function can be written as,

$$f(q,t) = \int_0^\infty G(\Gamma) \exp(-\Gamma t) d\Gamma$$
 (2.15)

The particle size distribution can be determined by calculating the Laplace inversion f(q, t) of with the distribution $G(\Gamma)$. However, finding the precise functional form for the distribution requires complex calculations. An alternative, simpler method to extract information about the particle size and size polydispersity (SPD) from the DLS data is to use the method of cumulants [13]. This approach involves expressing $\ln [f(q,t)]$ as a cumulant expansion, which has the form,

$$\ln[f(q,t)] = -\bar{\Gamma}t + \frac{\kappa_2}{2!}t^2 - \frac{\kappa_3}{3!}t^3 + \cdots$$
 (2.16)

, where the first cumulant, denoted as $\bar{\Gamma}$, is related to the average diffusion coefficient \bar{D} through, $\bar{\Gamma}=\bar{D}q^2$. This is used to determine the average diameter of the colloidal particles using the Stokes-Einstein relation mentioned earlier. The second cumulant, denoted as κ_2 , provides information about the variance of the size distribution relative to the average diameter.

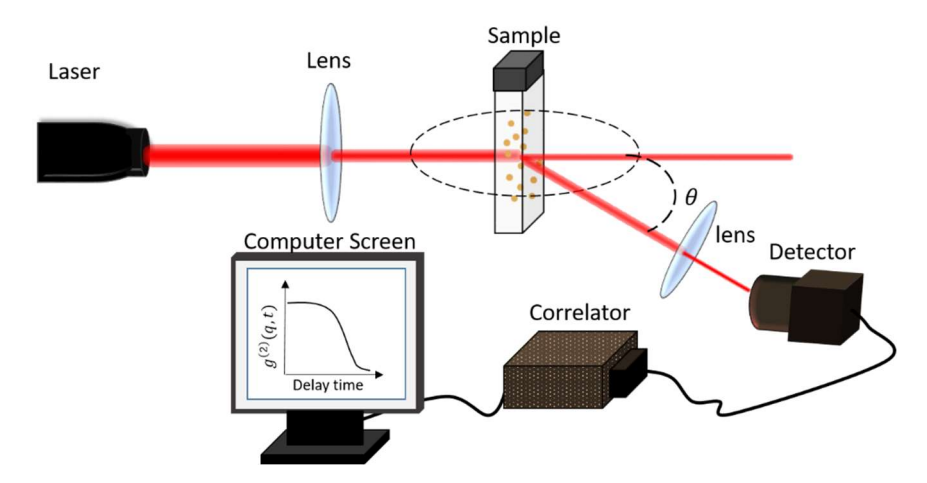


Fig. 2.13 Schematic representation of Dynamic light scattering technique

The square root of κ_2 gives the SPD, defined as the standard deviation divided by the average diameter.

We have used a particle size analyzer (M/s Litesizer™ 500, Anton Paar, Austria) that employs DLS technique. Figure 2.13 shows the schematic representation of the DLS setup. A diode laser with a wavelength 658 nm, and power of 40 mW is used as the light source. This setup can measure particle sizes can within the range of 0.3 nm to 10 µm.

2.4.3 UV-visible spectroscopy

As mentioned earlier in laser diffraction setup, one sweeps scattering angle, θ by keeping λ fixed to record the Bragg diffraction pattern. In the case of UV-visible spectroscopy, one sweeps λ by keeping the incident angle fixed to record the Bragg diffraction from PhCs. This technique is similar to energy dispersive X-ray scattering used for characterizing atomic and molecular systems [21], [22]. Here, the wavelength of the incident light is varied from ultraviolet to visible and to near-infrared regions, while maintaining a constant angle of measurement. The light incident on the sample gets attenuated due to absorption and scattering.

UV-visible spectroscopy is an effective tool for characterizing the structural ordering [5] in colloidal PhCs. Peaks in the absorption/reflection spectrum of the PhCs are due to Bragg diffraction of the wavelength λ that satisfies the Bragg diffraction condition,

$$n\lambda = 2d_{hkl}\mu_m \sin\left(\theta_g\right) \tag{2.17}$$

,where θ_g is the Bragg angle(90° for normal incidence), d_{hkl} is the interplanar distance between crystal planes with (hkl) miller indices, and n is the order of diffraction [23]. For normal incidence, the Bragg's condition will be,

$$n\lambda = 2d_{hkl}\mu_m \tag{2.18}$$

The major peaks in the absorption spectra for fcc and bcc correspond to the plane (111) and (110) respectively. The number density, n_p of the colloidal PhC can be calculated from the peak position using the formula;

For fcc,
$$n_p = \frac{4}{3\sqrt{3}} \left(\frac{2\mu_m}{\lambda_B}\right)^3 \tag{2.19}$$

And for bcc,
$$n_p = \frac{1}{\sqrt{2}} \left(\frac{2\mu_m}{\lambda_B}\right)^3 \tag{2.20}$$

Here, λ_B is the Bragg peak position.

We have used a UV-visible spectrometer (M/s JASCO-V670 spectrophotometer, Japan), a double beam spectrophotometer in our studies. The schematic representation of the UV-visible spectrometer is given in Fig. 2.14. The spectrometer employs a single monochromator design that covers a wavelength range of 190nm to 2500nm. The monochromator is equipped with dual gratings (automatically exchanged) - 1200 grooves/mm for the UV/VIS region and 300 grooves/mm for the NIR region (see Fig. 2.14). The UV/VIS region employs a photomultiplier tube (PMT) detector, while the NIR region employs a Peltier-

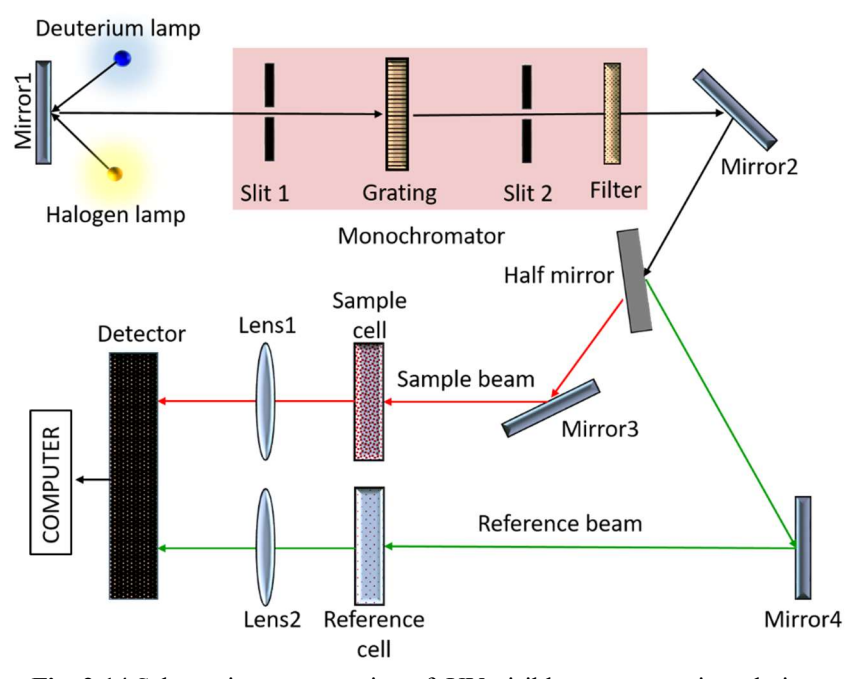


Fig. 2.14 Schematic representation of UV-visible spectroscopic technique.

cooled PbS detector. The gratings and detectors are automatically exchanged within the user-selectable wavelength range 750nm to 900nm range. For the wavelength range of 190nm to 350nm, a deuterium lamp is used as the source, and for the wavelength range of 330nm to 2500nm range, a halogen lamp is employed.

2.4.4 Field emission scanning electron microscopy (FESEM)

The Field Emission Scanning Electron Microscope (FESEM) is widely used to study the ordering of CPhC, hence study structure [24] and defects [25] in real space. The FESEM operates by utilizing the principles of electromagnetism and quantum mechanics. Electrons, are generated by a field emission source and accelerated by a high electrical field gradient within the high vacuum column of the microscope. As these primary electrons travel towards the object being scanned, they are focused and deflected by electrostatic/ electromagnetic lenses, resulting in a narrow beam that hits the surface of the sample. The electrons that collide with the surface of the sample cause the emission of secondary electrons, which are ejected from the sample at different angles and velocities depending on the surface structure of the sample. The detector detects the emission of secondary electrons and generates an electrical signal. Subsequently, the signal is amplified and converted into a video scan-image, which can be displayed on a screen or stored as a digital image for further processing. The motion of electrons with energy $E_e = h\nu$ (h is Planck's constant, and ν is the frequency of the wave associated with the electron) in the microscope can be described by the Lorentz force equation: $\overrightarrow{F} = q_e(\overrightarrow{E} + \overrightarrow{v} \times \overrightarrow{B})$, where \overrightarrow{F} is the force on the electron, q_e is the charge of the electron, \vec{E} is the electric field, \vec{v} is the velocity of the electron, and \vec{B} is the magnetic field.

In order to image, the sample must be conductive in nature. If the samples are dielectric/insulators, it should made conductive by coating them with a thin layer (1.5 - 3.0 nm) of gold or gold–palladium (using a sputtering system). The sample must also be able to maintain the high vacuum and not interfere with it in any way, such as by releasing water

molecules, gases or vapours. The sample is placed on a sample holder once it has been made conductive. The sample is placed into the high vacuum port of the microscope, which has a built in moveable (XYZ) stage, via an exchange chamber.

We have used Zeiss Ultra⁵⁵ FESEM instrument (Germany) for our study and given schematically in Fig. 2.15. The FESEM employs a Schottky field-emission electron gun as a source

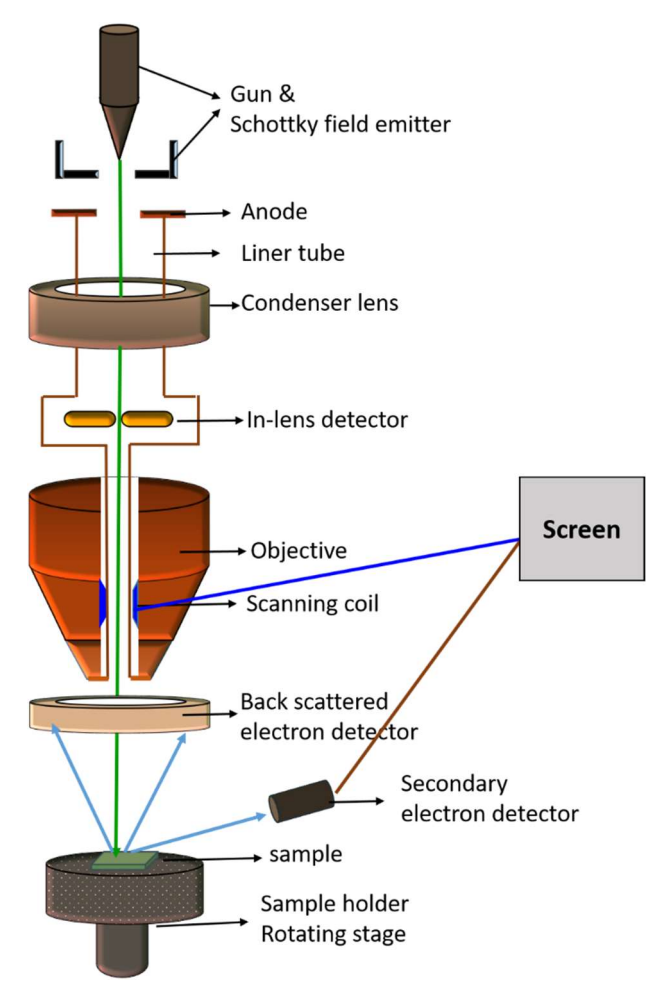


Fig. 2.15 Schematic representation of field emission scanning electron microscopic technique.

of primary electrons, produces high-intensity electron beams with very low energy spread, making it ideal for high-resolution imaging. A variety of detectors are included with the microscope, such as secondary electron detector, a backscattered electron detector, and an incolumn energy-selective backscatter detector, which allow for imaging of surface topography,

material composition, and crystallographic orientation, respectively. The Ultra⁵⁵ FESEM also features a range of focusing lenses, including electrostatic and electromagnetic lenses, used for focusing and scanning coils for scanning the electron beam, allowing for precise control of the imaging process. The Ultra⁵⁵ FESEM is suitable for imaging a wide range of samples at the nanoscale, including PhC thin films. Figure. 2.16 shows the SEM image of the close packed hexagonal array of PSPhC monolayer recorded using the instrument, at a magnification of 50 kX, at a voltage of 5 kV. Figure 2.16 (a) shows the top view of the sample, while Fig. 2.16 (b) presents the cross-sectional view. The cross-sectional view indicates a single layer, as the thickness matches the average diameter of one PS particle, which is 287 nm.

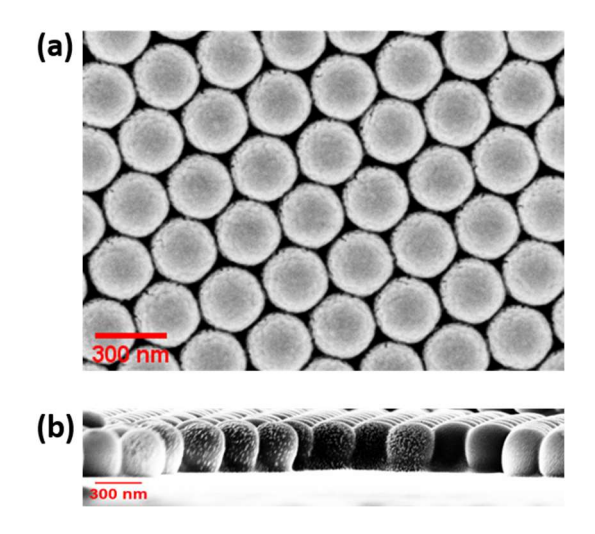


Fig. 2.16 The FESEM image of to the PSPhC monolayer (a) surface view, and (b) cross-sectional view, showing a single layer.

2.4.5 Raman Spectroscopy

Raman spectroscopy is a method of characterization that involves using scattered light to study the vibrational energy modes of a substance. The technique is named after C.V. Raman, an Indian physicist, first observed inelastic scattering of light by molecules in liquids in 1928 [26]. Raman spectroscopy can provide valuable chemical and structural information, and hence one can identify substances by their unique Raman "fingerprint". When a monochromatic light interacts with the sample, both elastic and inelastic scattering of light

occurs. The majority of the scattered light has the same energy as the incident photons (elastic scattering), known as Rayleigh scattering. However, a small fraction of the scattered light has higher or lower energy (inelastic) than the incident light referred to as Raman scattering [27]. During Raman scattering, the interaction between light and matter causes the molecules to gain or loss energy. According to the energy conservation law;

$$E_i + h\nu_i = E_s + h\nu_s \tag{2.21}$$

$$\Delta E = E_i - E_s = h(\nu_s - \nu_i) \tag{2.22}$$

Where E_i , E_s , v_i , v_s and h are initial energy of the molecule, final energy of the molecule, frequency of the incident light, frequency of scattered light, and plank's constant respectively. Based on the frequency of the scattered light, we can consider three cases as shown in Fig. 2.17;

 $v_s = v_i \Rightarrow \Delta E = 0$ (Elastic scattering), Rayleigh scattering

- i) $v_s < v_i \Rightarrow \Delta E < 0$ (Inelastic scattering), Stokes line
- ii) $v_s > v_i \Rightarrow \Delta E > 0$ (Inelastic scattering), Antistokes line

When light is incident on the sample, the molecule gets excited to a higher energy state by absorbing the energy of the photons. In most cases, the excited molecule returns to the ground state by emitting the photons with the energy same as the energy of the incident photon. This is the predominant process and is known as elastic scattering of light, also known as Rayleigh scattering. The considerably rarer process of Raman scattering, which is an inelastic scattering process involving an energy transfer between the scattered photon and molecule, happens in around 1 in 10 million photons. If a small fraction of the molecules which are in the ground state (see Fig. 2.18) is excited to a short-lived vibrational virtual state and returns to a higher vibrational state than the

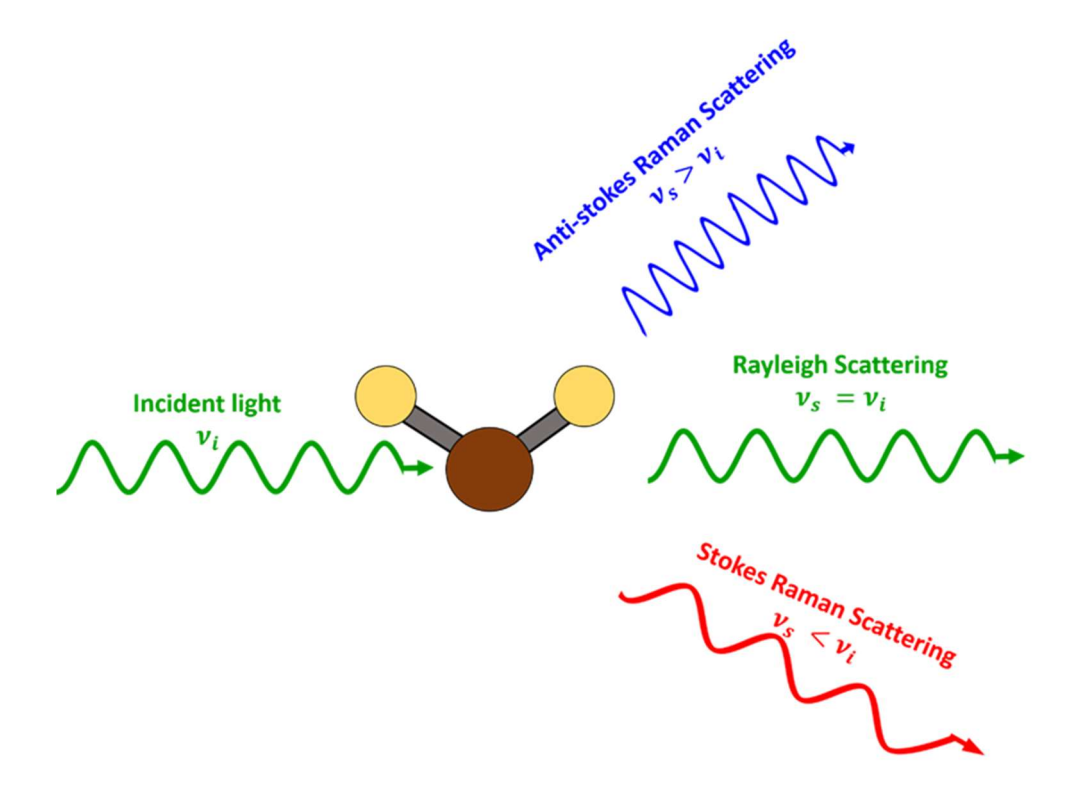


Fig. 2.17. The Schematic representation of light scattering illustrates the incident light of frequency v and its scattering behavior. Rayleigh scattering occurs when the scattered light has the same frequency as the incident light. Stokes scattering refers to the scattered light with a lower frequency than the incident light, while anti-Stokes scattering is the scattered light with a higher frequency than the incident light.

ground state by emitting photons having energy lower than the incident energy, then it is called Stokes scattering, and the anti-Stokes scattering occurs when the molecule already exists in a higher vibrational level than the ground state and absorbs energy from the incident photon to reach a virtual state. The molecules then return to the ground state by emitting a photon with energy higher than the incident photon (see Fig. 2.18). Therefore, the emitted photon has more energy than the absorbed photon (Fig. 2.18). From a quantum mechanical standpoint, both Stokes and anti-Stokes scattering are equally likely phenomena. Nevertheless, in a collection of molecules, the majority of molecules will exist in the lowest energy state at normal temperatures, as dictated by the Boltzmann distribution. Thus, the likelihood of Stokes scattering is statistically higher than that of anti-Stokes scattering. Consequently, the Stokes

line is generally have higher intensity than the anti-Stokes line. Hence, in a Raman scattering experiment, usually the stoke line is measured.

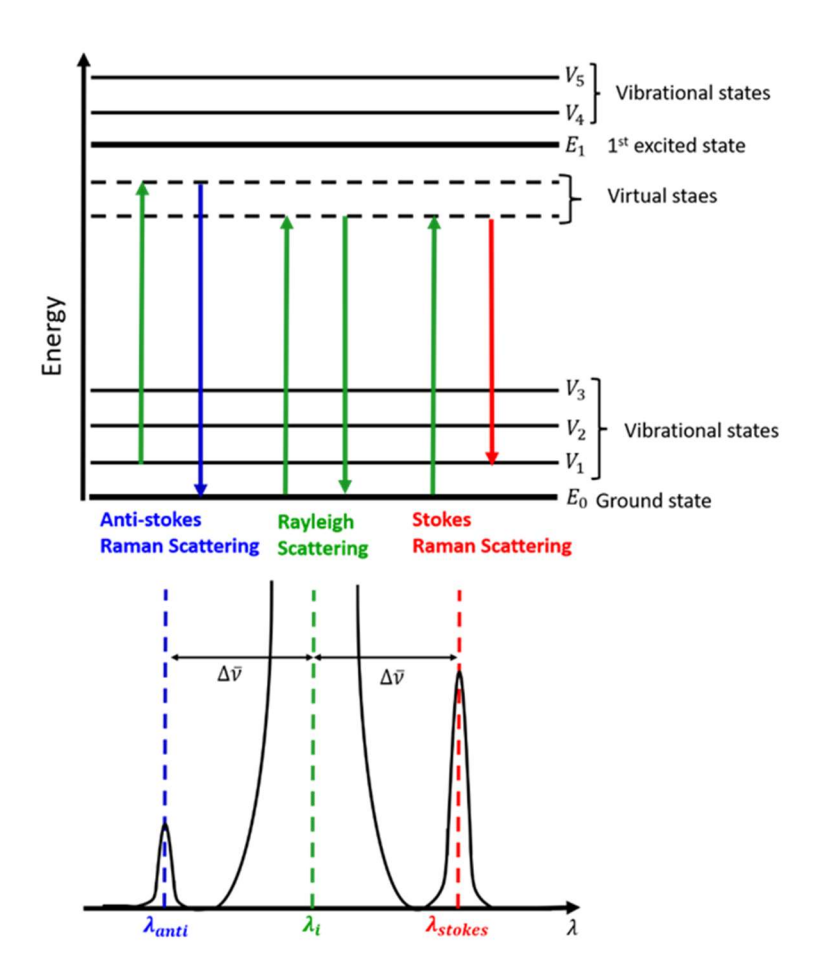


Fig. 2.18 Schematic illustration of Raman scattering, showing the excitation and de-excitation of molecular vibrational states resulting in Stokes and anti-Stokes lines and comparing the Raman spectral lines with the Rayleigh spectral line.

The classical theory of Raman scattering provides insights into the occurrence of stokes and anti-stokes lines, which is fundamentally based on a molecule's polarizability. When a molecule is subjected to a static electric field, it experiences some deformation due to the attraction of the electronic cloud to the positive pole of the field and the positively charged nuclei to the negative pole. This charge separation creates an induced dipole moment, denoted by μ_i , and the molecule is said to be polarized. The magnitude of μ_i depends on the intensity of the electric field, E, and the ease of deformation or polarizability, α , of the molecule, i.e.,

$$\mu_i = \alpha \vec{E} \tag{2.23}$$

It can be re-written for an oscillating electric field of light with frequency, v_i

$$\mu_i = \alpha E_0 \sin(2\pi \nu_i t) \tag{2.24}$$

Here the incident electric field of light is given by $\vec{E} = E_0 \sin{(2\pi v_i t)}$ with amplitude, E_0 . The dipole (oscillating with the frequency of the applied field) will be superimposed on its vibrational motion of the molecules. For example, let us consider the frequency of vibration of the molecule v_v , which changes the polarizability to;

$$\alpha = \alpha_0 + \beta \sin(2\pi \nu_\nu t) \tag{2.25}$$

, where α_0 is the polarizability at the equilibrium position and β represents the change in polarization during the vibration. Then the induced dipole moment can be written as;

$$\mu_i = (\alpha_0 + \beta \sin(2\pi \nu_\nu t)) E_0 \sin(2\pi \nu_i t)$$
 (2.26)

$$\mu_{i} = \alpha_{0} E_{0} \sin(2\pi \nu_{i} t) + \frac{1}{2} \beta E_{0} \cos 2\pi (\nu_{i} - \nu_{\nu}) t$$

$$+ \frac{1}{2} \beta E_{0} \cos 2\pi (\nu_{i} + \nu_{\nu}) t$$
(2.27)

Thus, the induced dipole moment (μ_i) of a molecule has three components, with component 1 changing at the same frequency as the incident light wave (ν_i) . Components 2 and 3 change at frequencies which are the difference and the sum of the exciting frequency (ν_i) and the vibrational frequency (ν_v) of the molecule respectively. That implies the three frequencies observed in the scattered light: ν_i , $\nu_i \pm \nu_v$. The Rayleigh line appears at the exciting frequency (ν_i) , while the Raman lines appear at frequencies $\nu_i \pm \nu_v$. The line that appears on the low frequency side of the Rayleigh line $(\nu_i - \nu_v)$ is called the Stokes line, while

the line on the high frequency side $(v_i + v_v)$ is called the anti-Stokes line. So, the fundamental selection rule for the molecule to be Raman active is that the molecular vibration should create a change in the polarizability, i.e., the derivative of polarizability with respect to its position coordinate should be non-zero.

The wavelength of the Raman scattered light, as we have seen, is dependent on the excitation wavelength, which makes it difficult to compare Raman spectra obtained with different lasers. Therefore, the Raman scattered wavelength is converted to a Raman shift $(\Delta \bar{\nu})$ value expressed in units of cm^{-1} with respect to the excitation wavelength (λ_i) and Raman scattered wavelength (λ_s) which is given by;

$$\Delta \bar{v}(cm^{-1}) = \left(\frac{1}{\lambda_i(nm)} - \frac{1}{\lambda_s(nm)}\right) x \frac{(10^7 nm)}{(cm)}$$
(2.28)

We have used Raman spectrometer (M/s Horiba LabRam Raman Spectrometer, Japan) instrument with confocal Raman microscope with a single-stage spectrometer that uses an 800 mm focal length Czerny-Turner type spectrograph with mirrors. The schematic of the Raman spectrometer is given in Fig. 2.19 .The software-controlled motorized optical paths can switch between lasers, detectors, and exits. The visible version of the instrument covers the 440-1100 mm wavelength range and has multiple laser sources (532nm, 633nm, and 785nm). The laser power on the sample can be decreased using a filter wheel with nine neutral density filters (100%, 50%, 25%, 10%, 5%, 3%, 1%, 0.1%, and 0.01%). The instrument with tunable light intensity and an internal white light illuminator is supplied with an Abbe condenser. A revolving turret with achromatic objectives (10x, 20x, 45x 50x, and 100x) is also included. The instrument has a camera for simultaneous visualization of the sample under white light illumination and the laser spot using the LabSpec software. The 800 mm focal length achromatic flat field monochromator features two 76 mmx76 mm gratings, 1800 gr/mm and

600 gr/mm, mounted on a motorized turret controlled by software to vary both spectral resolution and spectral coverage in one shot. The instrument uses a multichannel air-cooled CCD detector with a pixel size of 1024x256 pixels (26x26 microns) in the 200-1050nm spectral range.

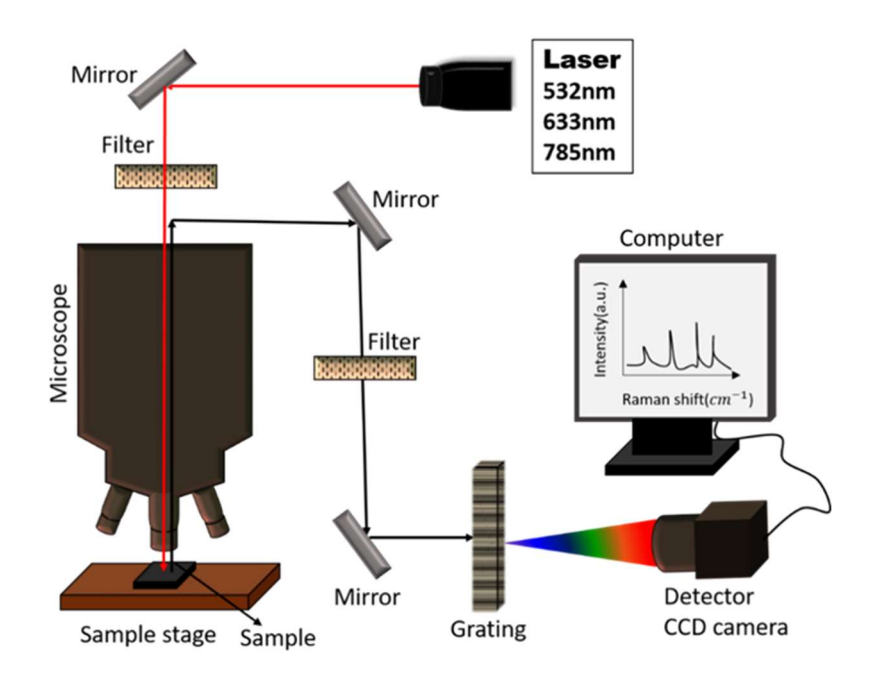


Fig. 2.19 Schematic representation of Raman spectroscopic technique.

2.5 Simulation techniques

2.5.1 Finite Element Method (FEM)

To describe the laws of physics for space-time dependent problems, it is usually necessary to express them in terms of partial differential equations (PDEs). Analytical methods are generally insufficient to solve these PDEs for most geometries and problems. Instead, one can construct an approximation of the equations by employing various types of discretization. hese discretization methods employ numerical model equations to determine the PDEs, which can subsequently be solved numerically. The actual solution to the PDEs is usually approximated by solving the numerical model equations. The method employed to calculate these approximations is the finite element method (FEM) [28]. FEM is extensively employed

as a computer-aided analysis technique in numerous physical and engineering domains, such as structural analysis, fluid mechanics, vibration analysis, heat transfer, and electromagnetics.

The fundamental principle of FEM involves dividing the total continuous domain into multiple subdomains. The unknown function is represented within each subdomain using interpolation functions with unknown coefficients. This process enables the approximation of the solution within each subdomain. Therefore, the infinite number of degrees of freedom in the original boundary value problem are reduced to a finite number in the new problem. Put differently, a finite number of unknown coefficients approximate the solution of the entire system. Subsequently, the Galerkin procedure[28] is applied to obtain the system of algebraic equations, then the solution to the boundary value problem is obtained by solving this system of equations numerically. So, FEM analysis of any problem involves the following four steps [29]:

- i) Dividing the solution domain into finite number of subdomains or mesh elements
- ii) Deriving the governing equation for a mesh element
- iii) Combining all elements in the domain and formulating the system of equations
- iv) Solving the system of equations

i) Domain discretization

The first and crucial step in any finite element analysis (FEA) is the discretization of the domain, denoted as Ω . Domain discretization significantly impacts various aspects of the simulation, including computer storage requirements, computation time, and the accuracy of numerical results. Here, the total domain Ω is divided into multiple smaller domains denoted as Ω^e (e = 1,2,3,...,m), where m represents the total number of subdomains. For one-dimensional domains, such as straight or curved lines (as shown in Fig. 2.20 (a)) the elements are typically line segments that are connected to approximate the actual line. In 2D domains, triangular and rectangular elements are commonly used (Fig. 2.20 (b)). Rectangular elements

are well-suited for rectangular regions, where triangular elements are suitable for irregular regions. In three-dimensional problems, the domain can be subdivided into tetrahedral (Fig. 2.20 (c)), triangular prisms, or rectangular bricks, depending on the specific requirements of the problem.

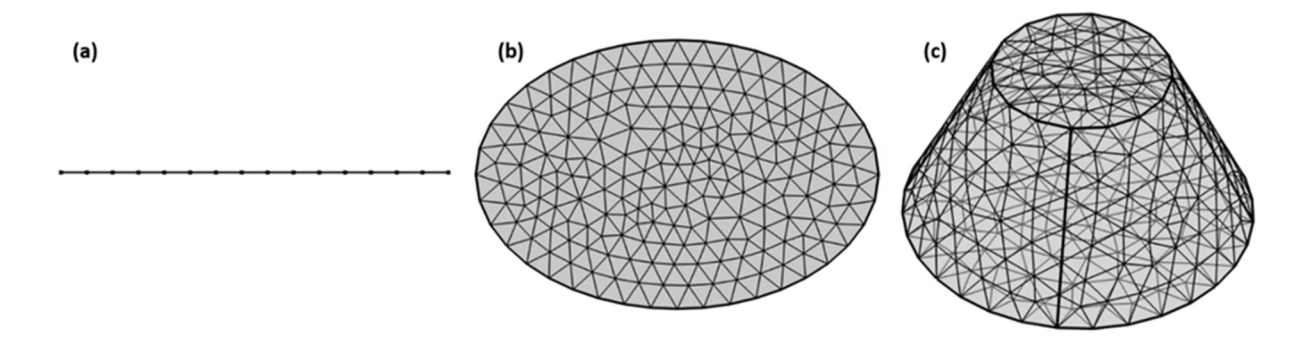


Fig. 2.20 Mesh elements generated using Comsol Multiphysics software for **(a)** a straight line in one-dimensional geometry with line segments as mesh elements **(b)** a two-dimensional geometry with triangular shapes as mesh elements. **(c)** a three-dimensional geometry with mesh elements of shape tetrahedrons.

The problem is usually expressed in terms of the unknown function ϕ at nodes corresponding to the elements in finite element solutions. The number of nodes depends on the type of element used. For instance, a linear line element has two nodes located at its endpoints, while a triangular element has three nodes at its vertices. Similarly, a tetrahedron has four nodes positioned at the corners. Figure 2.21 indicates the schematic representation of nodes in the basis mesh elements. To facilitate implementation, nodes need to be described in detail. This includes specifying their coordinate values, local numbers, and global numbers. The coordinate values indicate the position of the node in space, which can be determined easily. However, the numbering of nodes and elements needs a strategic approach. The aim is to minimize the bandwidth of the resulting banded matrix, determined by the maximum difference between the global numbers of any two nodes within an element. The nodes should be numbered properly to minimize the bandwidth, and to reduce the storage and computational costs significantly when employing a banded matrix solution method to solve the final matrix equation.

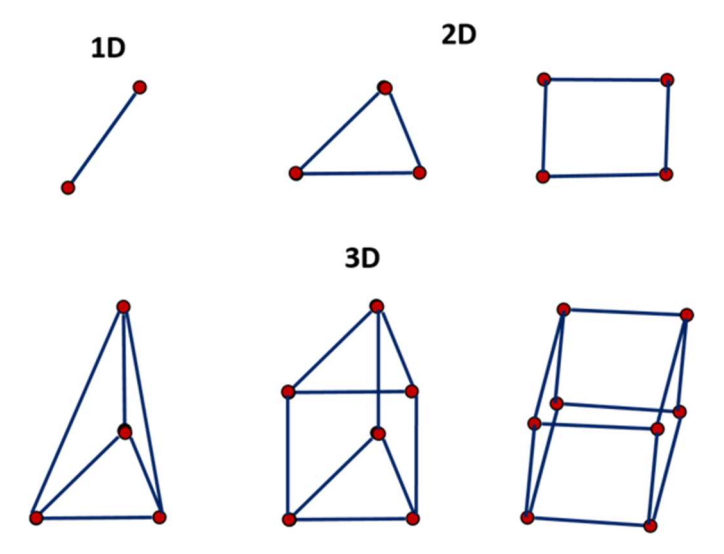


Fig. 2.21 Basic mesh elements with number of nodes for one-dimensional, two dimensional and three-dimensional cases.

The meshing of the computational domain is typically regarded as a preprocessing step as it can be performed independently of the other following steps. Advanced finite element software packages often offer tools for subdividing arbitrarily shaped lines, surfaces, and volumes into appropriate elements. These packages also include optimized methods for assigning global numbers to the elements, facilitating the process of domain discretization

i) Selection of interpolation functions

The second step in FEA involves selecting an interpolation function that approximates the unknown solution within an element. Typically, interpolation functions are chosen as polynomials of first (linear), second (quadratic), or higher order. While higher order polynomials provide increased accuracy, but often lead to more complex formulations than lower order polynomials. As a result, linear interpolation remains largely used. Once the polynomial order is determined, we can express the unknown element *e* as a summation of basis functions multiplied by their respective values at each node within the element. This expression takes the form:

$$\varphi^e = \sum_{j=1}^n N_j^e \, \varphi_j^e = \{N^e\}^T \{\varphi^e\} = \{\varphi^e\}^T \{N^e\}$$
(2.29)

Here, n represents the number of nodes in the element, φ_j^e denotes the value of φ at node j, and N_j^e refers to the interpolation function also known as the basis function or the expansion function. The highest order of the basis functions N_j^e within a given element determines the element's order. Let's say, if the N_j^e functions are linear, the element e is considered linear. A major characteristic of the basis functions N_j^e is that they are nonzero only within the element and vanish outside of it, ensuring that they capture the behavior of the unknown function specifically within the element.

ii) Formulation of the system of equations

Although analytical solutions to boundary value problems are ideal, they are only attainable in a limited number of exceptional situations. Finding an analytical solution is typically the exception rather than the rule. Most of the problems of practical significance lack analytical solutions. Various approximate methods have been developed to address this challenge, and Galerkin method has been used widely among the other methods. These methods offer effective approaches to approximate the solutions of boundary value problems where analytical solutions are not readily available.

A boundary value problem is defined by a governing differential equation within a domain Ω :

$$\mathcal{L}\varphi = f \tag{2.30}$$

along with the boundary conditions specified on the boundary Γ surrounding the domain. In Eq. 2.30, \mathcal{L} represents the differential operator, f denotes the excitation or forcing function, and φ represents the unknown quantity sought.

Galerkin's method belongs to the class of weighted residual methods, that aim to find a solution by weighting the residual of the differential equation. Let's consider, $\bar{\varphi}$ is an approximate solution to Eq. 2.30. Substituting $\bar{\varphi}$ for φ in the equation yields a non-zero residual:

$$r = \mathcal{L}\bar{\varphi} - f \neq 0 \tag{2.31}$$

The most optimal approximation for $\bar{\varphi}$ is the one that minimizes the residual r at all points in Ω . Hence, the weighted residual integral can be expressed as follows:

$$R_i = \int \omega_i \, r \, d\Omega = 0 \tag{2.32}$$

Here, ω_i are chosen weighting functions. Then, Eq. 2.32 can be re-written as;

$$R_i^e = \int N_i^e \left(\mathcal{L}\bar{\varphi}^e - f\right) d\Omega \qquad i = 1, 2, 3, \dots, n$$
 (2.33)

Substituting Eq. 2.29 into Eq. 2.33 gives;

$$R_{i}^{e} = \int N_{i}^{e} \mathcal{L}\{N^{e}\}^{T}\{\varphi^{e}\}d\Omega - \int f N_{i}^{e} d\Omega \qquad i = 1, 2, 3, ..., n$$
 (2.34)

this can be re-written in the matrix form as;

$$\{R^e\} = [K^e]\{\varphi^e\} - \{b^e\}$$
 (2.35)

where, $\{R^e\} = [R_1^e, R_2^e, ..., R_n^e]^T$ and the matrix elements where $[K^e]$ is an $n \times n$ matrix and $\{b^e\}$ an $n \times 1$ with their elements given by

$$K_{ij}^e = \int N_i^e \, \mathcal{L} N_j^e \, d\Omega \tag{2.36}$$

And

$$b_i^e = \int f N_i^e \, d\Omega \tag{2.37}$$

Prior to solving the system of equations for a particular solution, it is necessary to implement the relevant boundary conditions. The formulation of the system of equations involves three sub-steps. First, we create the elemental Eq. 2.35 for each element. Then, these elemental equations are summed over all elements to assemble the system of equations. This step is known as assembly. Thirdly, the boundary conditions are imposed to get the final form of the system of equations. In computer execution, these three sub-steps are typically intertwined and not strictly divided. During the assembly process, the formation of elemental matrices and the application of boundary conditions frequently take place concurrently.

iii) Solution of the system of equations

The final step in the FEM method is solving the system of equations. The resulting system can take one of two following forms:

$$[K]\{\varphi\} = \{b\}$$
 (2.38)

Or

$$[A]\{\varphi\} = \lambda[B]\{\varphi\} \tag{2.39}$$

Equation (2.33) represents a deterministic system which arises from an inhomogeneous differential equation, an inhomogeneous boundary condition, or both. Equation (2.34) corresponds to an eigenvalue system, which arises from homogeneous differential equations and homogeneous boundary conditions. Eigenvalue systems in electromagnetics usually occur in source-free problems like cavity resonances and wave propagation in waveguides. In such cases, the known vector $\{b\}$ is zero, and the matrix [K] can be expressed as $[A] - \lambda[B]$, where λ represents the eigenvalue.

After obtaining the solution vector $\{\varphi\}$ by solving the system of equations, we can proceed to calculate the required parameters. These computed parameters provide valuable insights and can be presented in various forms, such as curves, plots, or color pictures. This final stage of analyzing and presenting the results is commonly referred to as post-processing. It is worth noting that post-processing can be treated as a distinct and separate step independent of the other stages of the finite element analysis.

iv) COMSOL Multiphysics Software

We have employed the wave optics module of the commercially available COMSOL Multiphysics software package for the electromagnetic simulations based on FEM. COMSOL Multiphysics is an interactive simulation environment widely employed for modelling and solving various scientific and engineering problems. This software offers a comprehensive, integrated desktop with a Model Builder, providing a complete overview of their models and access to all available functionalities. With COMSOL Multiphysics, we can expand conventional models for a single type of physics into multiphysics models that address coupled phenomena from various disciplines.

The Wave Optics Module of COMSOL Multiphysics is designed to solve electromagnetic wave problems, specifically at optical frequencies. The Wave Optics Module

is applicable in simulating and designing optical applications across various areas that involve electromagnetic waves. These include optical fibers, photonic waveguides, PhCs, nonlinear optics, laser resonator design, active devices in photonics, and more. It is a versatile module that can be employed in virtually any field where electromagnetic waves play a significant role in optical phenomena.

2.5.2 Plane Wave Method (PWM)

The plane wave method (PWM) is mainly employed to study the bandstructre of PhCs using MIT Photonic Band gap software. This method originates from solid-state physics, where electronic wave functions are scalar while electromagnetic fields are vectors. A scalar approximation of fields is insufficient for describing the band structure accurately. To address this, the PWM is modified to consider the vectorial nature of the fields.

MIT photonic bandgap (MPB) is an open-source software works on Unix based operating systems[31]. It gives a fully vectorial analysis of three-dimensional Bloch wave functions. MPB uses a frequency domain approach where it calculates the Eigen modes and Eigen values directly form the Maxwell's equations. Here it uses an iterative Eigen solver, where it iteratively improves the approximate solutions. MPB analyzes a periodic dielectric structure to determine its eigenmodes, which represent the electromagnetic waves capable of propagating through the structure at specific frequencies. This corresponds to solving an eigenvalue problem $MH = \left(\frac{\omega}{c}\right)^2 H$, where H is the magnetic field, ω is the frequency, and M is the Maxwell operator $\nabla \times \frac{1}{\varepsilon(r)} \nabla \times$. We also have an additional constraint, that $\nabla \cdot H$ be zero (H must be "transverse"). Given the periodic nature of the structure, Bloch's theorem can be applied, expressing the states as $e^{i kx}$ multiplied by a periodic function, where k represents the Bloch wavevector. Consequently, for each k point (Bloch wavevector), a discrete set of eigenstates, known as the photonic bands of the structure, must be determined. To

computationally solve for these eigenstates, the H needs to be expanded using a chosen basis, with the basis truncated to a finite number of points for problem discretization. For instance, a conventional finite element basis could be employed, where the field is sampled at a finite number of mesh points and linearly interpolated between them. However, enforcing the transversality constraint in this basis is computationally expensive. Instead, a Fourier (spectral) basis is utilized, where the periodic part of the field is expanded using e^{iGx} plane waves. In this basis, maintaining the transversality constraint is straightforward, as it simply implies that the plane wave amplitudes must be orthogonal to k + G, where G is the reciprocal lattice vector. To determine the eigenfunctions, one approach is to explicitly compute the elements of the matrix M within our chosen basis and then utilize LAPACK or a similar library to find the eigenvectors and eigenvalues. However, for a three-dimensional calculation, this could involve finding the eigenvectors of a matrix with hundreds of thousands of elements on each side, which is challenging both in terms of storage and computation. Since we are interested in only a few eigenvectors, less expensive iterative methods can be employed that do not necessitate the explicit storage of M.

References

- [1] R. V. Nair and R. Vijaya, "Structural and optical characterization of photonic crystals synthesized using the inward growing self-assembling method," *Appl Phys A Mater Sci Process*, vol. 90, no. 3, pp. 559–563, Mar. 2008.
- [2] Y. Masuda, T. Itoh, and K. Koumoto, "Self-assembly patterning of silica colloidal crystals," *Langmuir*, vol. 21, no. 10, pp. 4478–4481, May 2005.
- [3] S. Wong, V. Kitaev, and G. A. Ozin, "Colloidal Crystal Films: Advances in Universality and Perfection," *J Am Chem Soc*, vol. 125, no. 50, pp. 15589–15598, Dec. 2003.
- [4] H. Ge, Y. Song, L. Jiang, and D. Zhu, "One-step preparation of polystyrene colloidal crystal films with structural colors and high hydrophobicity," *Thin Solid Films*, vol. 515, no. 4, pp. 1539–1543, Dec. 2006.

- [5] B. V. R. Tata, R. G. Joshi, D. K. Gupta, J. Brijitta, and B. Raj, "Crystalline arrays of submicron-sized particles through colloidal route," *Curr Sci*, vol. 103, no. 10, pp. 1175–1184, 2012.
- [6] T. S. Deng, J. Y. Zhang, K. T. Zhu, Q. F. Zhang, and J. L. Wu, "Controlled tuning of the stop band of colloidal photonic crystals by thermal annealing," *Opt Mater (Amst)*, vol. 32, no. 9, pp. 946–949, 2010.
- [7] D. Rout and R. Vijaya, "Role of Stopband and Localized Surface Plasmon Resonance in Raman Scattering from Metallo-Dielectric Photonic Crystals," *Plasmonics*, vol. 12, no. 5, pp. 1409–1416, Oct. 2017.
- [8] M. Maldovan, C. K. Ullal, W. C. Carter, and E. L. Thomas, "Exploring for 3D photonic bandgap structures in the 11 f.c.c. space groups," *Nat Mater*, vol. 2, no. 10, pp. 664–667, 2003.
- [9] S. G. Johnson, S. Fan, P. R. Villeneuve, J. D. Joannopoulos, and L. A. Kolodziejski, "Guided modes in photonic crystal slabs," *Phys Rev B*, vol. 60, no. 8, pp. 5751–5758, 1999.
- [10] H. Berber, "Emulsion Polymerization: Effects of Polymerization Variables on the Properties of Vinyl Acetate Based Emulsion Polymers," in *Polymer Science*, 2013.
- [11] I. A. Penboss, "Emulsion Polymerization Theory," in *Surface Coatings*, Springer, Dordrecht, 1993, pp. 294–302.
- [12] J. Herrera-Ordonez, R. Olayo, and S. Carro, "The kinetics of emulsion polymerization: Some controversial aspects," *Journal of Macromolecular Science Polymer Reviews*, vol. 44, no. 3. 2004.
- [13] Y. Fu, Z. Jin, Z. Liu, and W. Li, "Preparation of ordered porous SnO2 films by dip-drawing method with PS colloid crystal templates," *J Eur Ceram Soc*, vol. 27, no. 5, 2007
- [14] B. V. R. Tata and S. S. Jena, "Ordering, dynamics and phase transitions in charged colloids," *Solid State Commun*, vol. 139, no. 11–12, 2006.
- [15] A. K. Arora and B. V. R. Tata, "Interactions, structural ordering and phase transitions in colloidal dispersions," *Adv Colloid Interface Sci*, vol. 78, no. 1, 1998.
- [16] R. V. Nair and R. Vijaya, "Structural and optical characterization of photonic crystals synthesized using the inward growing self-assembling method," *Appl Phys A Mater Sci Process*, vol. 90, no. 3, pp. 559–563, Mar. 2008.
- [17] Y. Rag and J. M. Chem, "Themed issue: Materials Chemistry of Nanofabrication," vol. 21, no. 37, 2011.

- [18] B. J. Berne and R. Pecora, *Dynamic Light Scattering With applications to Chemistry, Biology* , and *Physics*, vol. 1st edition. 2003.
- [19] Victor A. Bloomfield et al., Dynamic Light Scattering Applications of Photon Correlation Spectroscopy, vol. 1st edition. Boston, MA: Springer US, 1985.
- [20] E. Eiser, "Dynamic Light Scattering," in *Multi Length-Scale Characterisation*, Wiley, 2014, pp. 233–282.
- [21] L. A. Lyon, J. D. Debord, S. B. Debord, C. D. Jones, J. G. McGrath, and M. J. Serpe, "Microgel colloidal crystals," *Journal of Physical Chemistry B*, vol. 108, no. 50, pp. 19099–19108, Dec. 2004.
- [22] R. G. Joshi, D. K. Gupta, P. Amesh, P. K. Parida, and T. R. Ravindran, "Microgel-hydrogel composite photonic crystals to monitor and extract uranyl ions in aqueous solutions," *Microporous and Mesoporous Materials*, vol. 319, May 2021.
- [23] C. Kittel, *Introduction to Solid State Physics*, 8th edition. 2005.
- [24] Y. Li, F. Piret, T. Léonard, and B.-L. Su, "Rutile TiO2 inverse opal with photonic bandgap in the UV–visible range," *J Colloid Interface Sci*, vol. 348, no. 1, pp. 43–48, Aug. 2010.
- [25] O. Painter *et al.*, "Two-Dimensional Photonic Band-Gap Defect Mode Laser," *Science* (1979), vol. 284, no. 5421, pp. 1819–1821, 1999.
- [26] C. V. Raman and K. S. Krishnan, "A New Type of Secondary Radiation," *Nature*, vol. 121, pp. 501–502, 1928.
- [27] E. Smith and G. Dent, *Modern Raman Spectroscopy-A Practical Approach*, 1st ed. John Wiley & Sons Ltd, 2004.
- [28] J.-M. Jin, *The Finite Element Method in Electromagnetics*, 2nd ed. John Wiley & Sons Inc., 2002.
- [29] M. N. O. Sadiku, Numerical techniques in electromagnetics, 2nd ed. CRC Press LLC, 2001.
- [30] L. Oyhenart and V. Vignéras, "Overview of Computational Methods for Photonic Crystals," in *Photonic Crystals Introduction, Applications and Theory*, 1st ed., A. Massaro, Ed., IntechOpen, 2012, pp. 267–290.
- [31] S. Johnson and J. Joannopoulos, "Block-iterative frequency-domain methods for Maxwell's equations in a planewave basis," *Opt Express*, vol. 8, no. 3, p. 173, 2001.

Understanding Photonic Crystals through Band structure and Reflectance calculations

We present the band structure and reflectance spectra calculations of different 2D PhCs in this chapter. Additionally, we investigate how doping in photonic crystal defects can improve the light-matter interaction.

3.1 Introduction

In two-dimensional photonic crystals (2D PhC) the refractive index is periodic along only two directions. 2D PhCs are one of the simplest types of PhCs which can be fabricated though different lithography techniques such as e-beam lithography[1], [2], nano-imprint lithography [3], [4], photo lithography [5], [6], holographic lithography [7], [8] etc. In recent decades, extensive research has been carried out on the band structure and E-field distributions of 2D PhC with and without defects [9]- [13]. The band structure of the PhC provides information on the position and magnitude of the band gap and gives the possibility to tune by varying the structural parameters according to the need/interest. Unlike other type of PhCs, in 2D PhCs, for light propagating in the plane of periodicity, the harmonic modes can be divided into two independent polarizations, each with its own band structure. The polarizations being transverse electric (TE) modes where the E- field normal to the plane and transverse magnetic (TM) where the E- field parallel to the plane. The band structures for TE and TM modes can exhibit significant differences, potentially resulting in the existence of a photonic bandgap for one polarisation but not for the other. TE band gaps are generally preferred in lattices of isolated high refractive index regions, while TM band gaps are preferred in connected lattices [14].

When the in-plane periodicity in a 2D PhC is perturbed by a single defect, we can acheive a single localized mode or a group of localized modes whose frequency lies within the band gap. These are called defect mode(s). The E- field associated with a defect mode is maximum inside the defect and decays exponentially away from it. As a result, E- field remains confined to the defect and is unable to penetrate into the rest of the crystal [15], [16]. Analogous to doped semiconductor crystals, one can fabricate doped PBG crystals either by creating vacancy or by addition of higher or lower dielectric material at the particular lattice point. The defects thus created serves as localized modes within the photonic band gap of PhC [17]. E-field confinement and enhancement in PhC defects are essential for tailoring the light matter interaction in various applications. These structures facilitate precise control over the propagation and manipulation of light, resulting in enhanced performance and novel functionalities in photonic and optoelectronic devices.

Here, we have investigated the band structure of 2D PhCs with different lattice symmetries and explored the dependence of the band gap on the structural parameters to optimize the band gap/stop band in the visible region. The 2D PhCs investigated in this study consist of square and hexagonal lattices of dielectric rods made of amorphous titania of infinite length. The effect of doped 2D PhC defects in the reflectance spectra and the E- field distribution is studied. Additionally, the effect of dielectric contrast on the position of defect modes within the bandgap is also discussed. The bandstructure calculations are carried out using plane wave method (PWM) implementation of MIT photonic bandgap (MPB) software and the reflectance calculations are carried out using finite element method (FEM) implementation of COMSOL Multiphysics Software.

3.2 Theory

Maxwell's equations describe how an electromagnetic wave travels through a medium. For a 2D PhC, it can always be described as a linear combination of a transverse E- field (TE) and a transverse magnetic field (TM). Maxwell's equations in the absences of sources are reduced to a Helmholtz equation for the electric field is given by;

$$\nabla^2 \vec{E_z}(\vec{r}) + \left(\frac{\omega}{c}\right)^2 \varepsilon_r(\vec{r}) = 0 \tag{3.1}$$

, when the magnetic field is confined in XY plane and the electric field is perpendicular to it (TE). Here, $E_z(\vec{r})$ is the z-component of the electric field at the position \vec{r} , $\varepsilon_r(\vec{r})$ is the relative dielectric constant of the PhC, ω is the angular frequency of the incident wave, and c is the speed of light in free space. Eq. 3.1 represents the PhC which is non-conducting ($\sigma = 0$) and non-magnetic ($\mu_r = 1$). The time dependant harmonic solution of the Eq. 3.1 is;

$$\vec{E}(\vec{r},t) = \vec{E}_z(\vec{r}) \exp(-i\omega t)\hat{z}$$
(3.2)

The application of suitable boundary conditions at the interfaces of the computational domains is a crucial step in any electromagnetic simulation. It is important to apply periodic boundary conditions that imitate an infinite simulation domain along with the periodicity of the PhC lattice for the photonic band structure calculations. Bloch's theorem is applied at the boundaries of the PhC unitcell to guarantee the periodicity of the lattice i.e., the electric (magnetic) field only experiences a change in phase when it travels from one point in the PhC to another point in the PhC that is separated by a lattice vector, \vec{R} .

$$\overrightarrow{E_z}(\vec{r} + \vec{R}) = \exp(i\vec{k}.\vec{R})\overrightarrow{E_z}(\vec{r})$$
(3.3)

, where \vec{k} is the wave vector of the electromagnetic wave.

On the other hand, finite size in the direction parallel to the incoming wave vector is employed for the reflectance calculations, whereas the PhC structure is extended infinitely in the perpendicular direction. Due to the finite size of the PhC at the entrance and exit of the EM wave, it is crucial to avoid unphysical reflections at the interfaces. This is achieved by using perfectly matched layer (PML) conditions at these interfaces. PML for a TE polarization is defined by;

$$\hat{z}.\hat{n} \times (\vec{\nabla} \times \vec{E_z}\hat{z}) - i\beta \vec{E_z} = -2i\beta \vec{E_{0Z}}$$
(3.4)

, where E_{0Z} is the initial value of electric field at the boundary and $\beta = k_0$, the propagation constant.

3.3 Simulation details

A two-dimensional (2D) square and hexagonal lattice of dielectric nano-rods is chosen as the 2D PhC. The dielectric rods have been assigned with a refractive index of amorphous titania (2.67) and are placed in an air matrix, hence giving refractive index contrast ($\Delta n = n_h - n_l$, n_h - higher refractive index material, n_l - lower refractive index material) of 1.67.

3.3.1 Band structure calculations

The photonic band structure calculations have been carried out using MIT Photonic Band (MPB) software, using plane wave method (PWM) to find the frequency eigenstates of Maxwell's equation in periodic dielectric structures. More details of PWM are presented in chapter 2, section 2.6.2. The band structure is calculated for the out-of-plane polarization (TE) of E- field, assuming E- field to be oriented perpendicular to the plane of periodicity (i.e. $E_x = E_y = 0$, $E_z \neq 0$), since TE band gaps are favored in a lattice of isolated high refractive index regions as in the case of periodic dielectric rods in an air matrix. In this study, we have considered two lattice structures; square lattice and hexagonal lattice of dielectric cylinders in

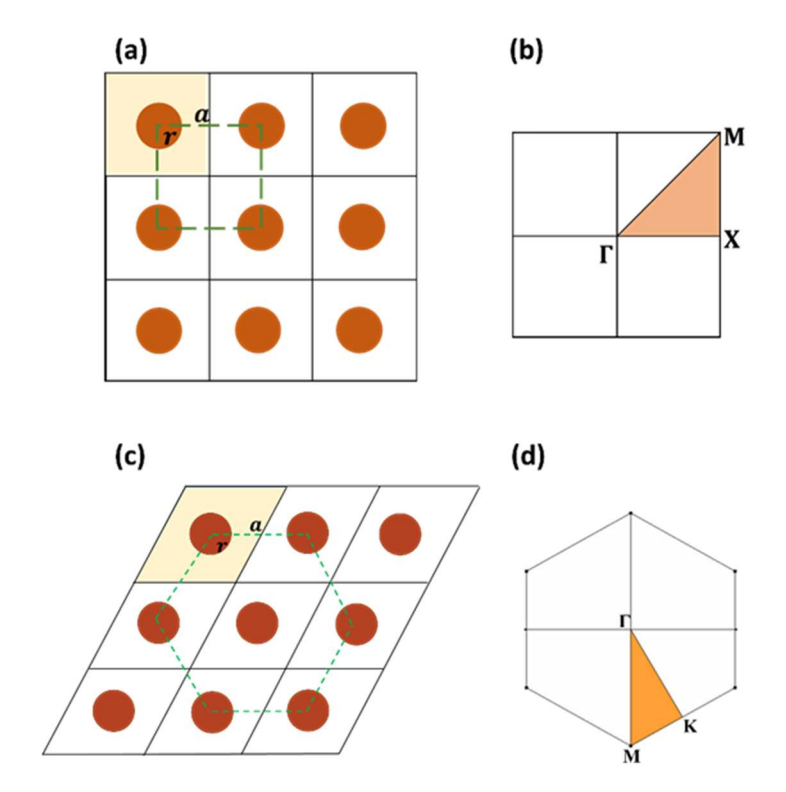


Fig 3.1 (a) The square array of dielectric cylinders by periodically repeating the unit cell, shown as the shaded square region (b) the Brillouin and irreducible Brillouin zone (orange color shaded region) of square lattice with the symmetry points Γ , X, and M along which the band structure is calculated. (c) The hexagonal array of dielectric cylinders by periodically repeating the unit cell (shown as the shaded rhombus). (d) the Brillouin and irreducible Brillouin zone of hexagonal lattice with the symmetry points Γ , K and M along which the band structure is calculated.

air matrix. The reciprocal lattices corresponding to square and hexagonal symmetries are also square and hexagonal respectively. The unit cell, and the corresponding Brillouin zone of square (Fig.3.1(a) and (b)) and hexagonal lattice (Fig.3.1(c) and (d)) are shown in Fig. 3.1. The band structure is calculated along the boundary of the irreducible Brillouin zone, given by shaded area in Fig. 3.1(b) and (d).

3.3.2 Reflectance calculations

The reflectance spectra and the corresponding E- field distributions are simulated using the finite element method (FEM) implementation of COMSOL Multiphysics software. The working principles of FEM are explained in chapter 2, section 2.6.1. The reflectance calculations have been carried out for a two-dimensional model of a square lattice and

hexagonal lattice of dielectric rods placed in an air matrix. The computational domain of a square lattice without and with defect are provided in Fig. 3.2 (a,b). A z-polarized (out-of-plane/TE) plane wave is incident along Y- direction using the port boundary conditions. A perfectly matched layer (PML) boundary condition is implemented at the top of the input port and the bottom of the output port to absorb undesired reflections from non-physical boundaries and to limit the computational domain [18]. The Floquet periodic boundary condition (PBC) is applied at the left and right of the computational domain along X- direction to ensure the hexagonal periodicity. The top boundary of the top PML and the bottom boundary of the bottom PML are applied with perfect electric conductor (PEC) boundary condition. The array size has been varied from 5x5 to 13x13 to optimize the band gap in reflectance spectra. The band gap is found to saturated for 13x13 array and beyond. The square lattice in Fig.3.2 is replaced with hexagonal lattice to simulate the reflectance spectra of a hexagonal 2D PhC. Point defects in the 2D PhCs are created by replacing the central lattice point (defect site) with

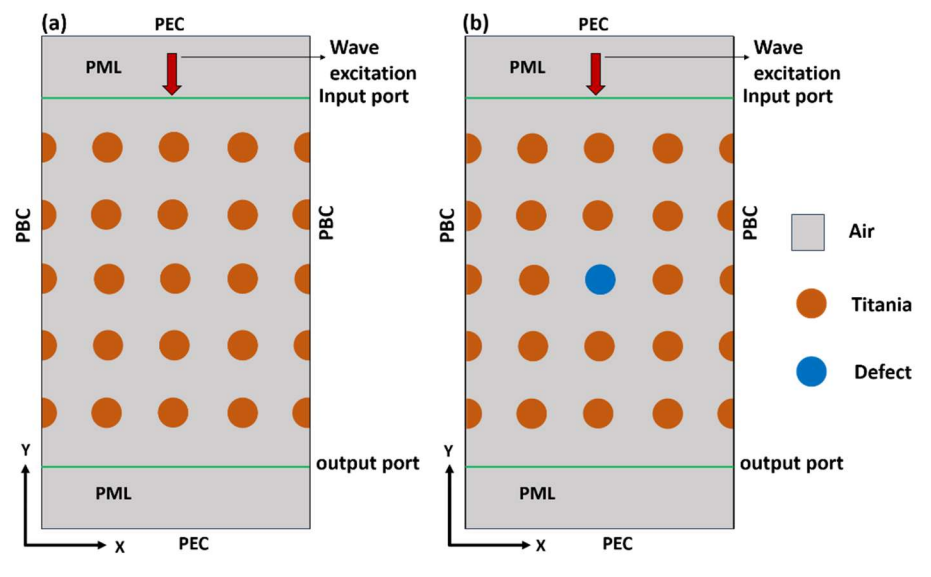


Fig 3.2. (a) Schematic representation of computational domain of the square array of amorphous titania rods in air matrix. The wave excitation is along y-direction with port boundary conditions and they have been backed by perfectly matched layer (PML) conditions and the lateral boundaries have been set to periodic boundary condition (PBC) (b) computational domain with the defect, created by replacing the central lattice point with different materials keeping all the other parameters same. The array size has been varied to optimize the bandgap and the square lattice is replaced with hexagonal lattice to simulate the reflection spectra for hexagonal 2D PhC.

different dielectric material. This can be achieved either by removing the dielectric material from the defect site (hole- type) or by adding dielectric material to the defect site (rod- type). The refractive index contrast of the defect (Δn_d) is defined as; $\Delta n_d = |n_r - n_d|$, where n_r is the refractive index of the surrounding rods and n_d is the refractive index of the defect. For a hole- type defect, n_d is less than n_r , and for rod- type defect, n_d is greater than n_r .

3.4 Results and discussion

3.4.1 Square lattice

i) Band structure calculations

The structural parameters of the 2D PhC, a being the nearest neighbor distance (lattice constant) and r being the radius of the rod, have been optimized to the maximum band gap. The band gap is quantified by gap-midgap ratio, $\frac{\Delta \omega}{\omega_m}$ expressed in percentage, where $\Delta \omega$ is the width of the band gap and ω_m is the central frequency of the band gap. Figure 3.3(a) shows the

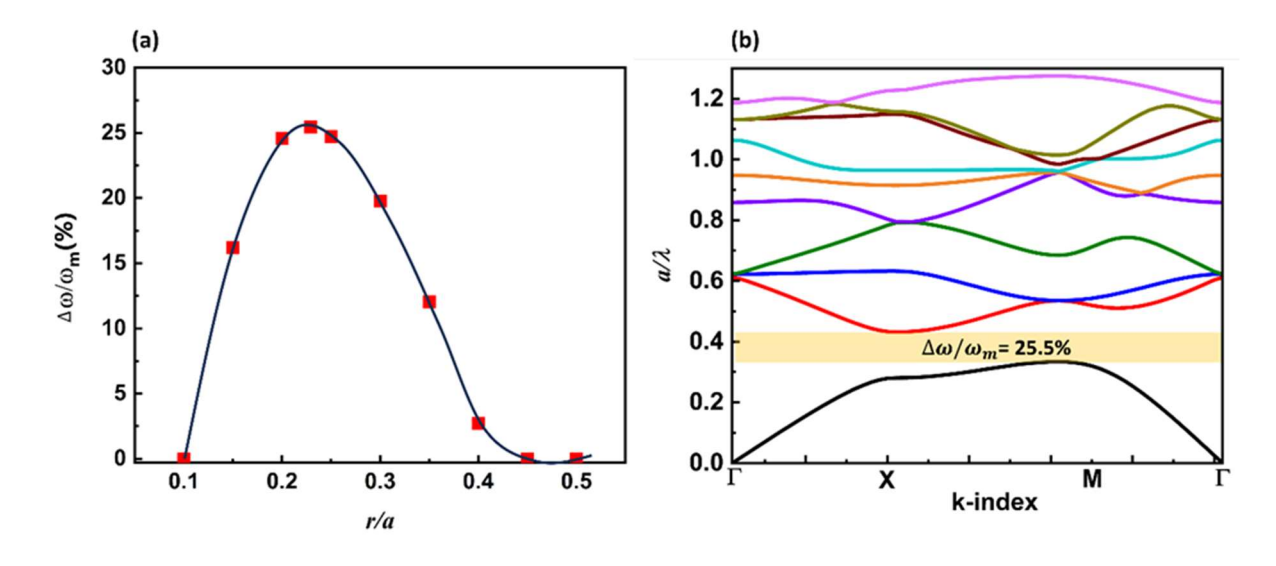


Fig 3.3 (a) Optimization of band gap of the square 2D PhC for TE polarization. The maximum band gap of 36.6% is obtained for r/a = 0.23. (b) Band structure corresponding to r/a = 0.23 giving band gap between first and second TE bands shown in the shaded region. The Y-axis is represented in a/λ in units of c/a.

change in the bandgap w.r.t. the r/a ratio, a maximum band gap of 25.5% % is opened for r/a = 0.21. The same is reflected in the band structure shown in Fig. 3.3(b), the band gap of 25.5% between the first and the second TE bands.

ii) Reflectance spectra

The corresponding reflection spectrum is calculated by keeping the same r/a, and it has been tuned to the visible range, with radius, r = 43nm and lattice constant, a = 187 nm. The system size (array size) effect on the band gap is studied by varying the array size and it has been observed that the band gap is broader for lower array size and becomes rectangular as array size increases (Fig. 3.4(a)) and expected to saturate for higher array sizes from 13x13. Hence, here onwards the array size of the lattice for reflection studies are fixed as 13x13. The band gap vs array size is plotted in Fig. 3.4 (b). The bandgap is identified as the region of maximum reflectance and it is found between to be 431 nm to 678 nm for a 13x 13 array. This has been verified with the position of band-gap in the band-structure where 1st band gap appears in ΓX direction (corresponds to normal incidence) between the frequency range; $0.28 \, c/a \, to \, 0.43 \, c/a \, (434 \, \text{nm} \, \text{to} \, 667 \, \text{nm})$. Thus, the frequencies falling within bandgap region are forbidden for propagation within the PhC. Thus, the wavelength region, 434 nm to 667 nm represents the photonic band gap in 2D PhC of dielectric rods. It may be mentioned here that the oscillations observed in the reflection spectra (see Fig. 3.4 (a)) at lower and higher wavelengths of the band gap region is due to the finite size of the PhC. Notice that, the oscillations around the band gap region, do depend on the array size.

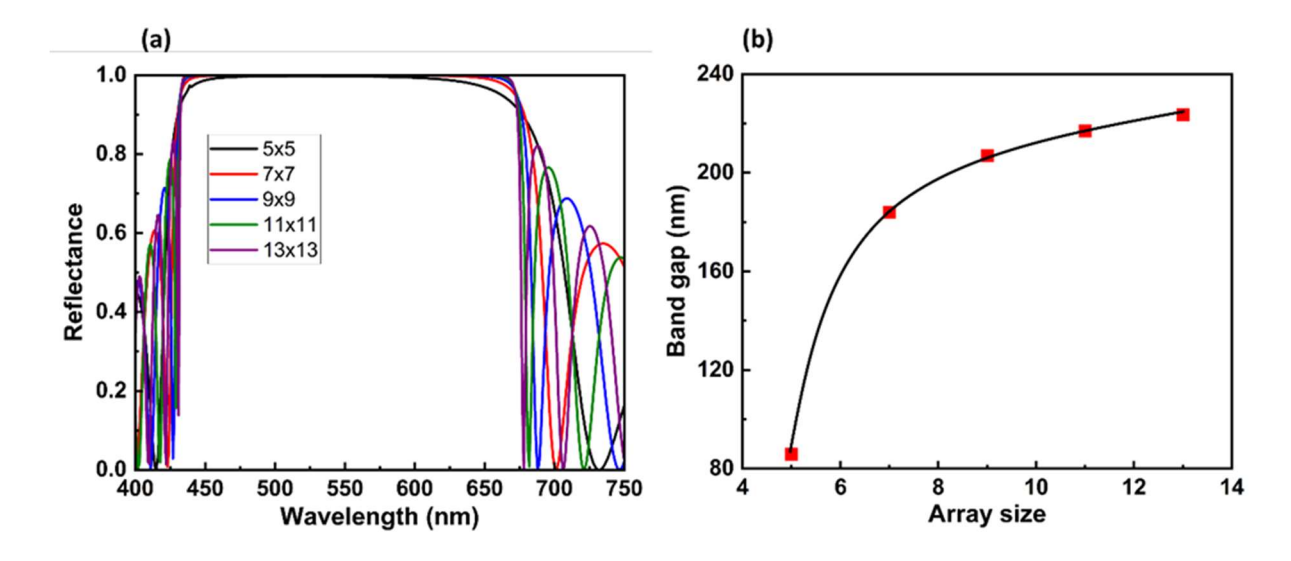


Fig. 3.4 (a) Reflectance spectra of the square lattice of titania cylinders for different array sizes. (b) Band gap for different array sizes.

A point defect is created at the center of the lattice by removing a rod from otherwise perfectly periodic array (Fig. 3.2 (b)). This small perturbation in the periodicity creates a point defect which is identified by a dip in the reflectance spectrum. There now exists a frequency within the bandgap corresponding to a defect mode for which the E- field is confined in the defect region and decays exponentially away from it, or in other words, cannot pass though the

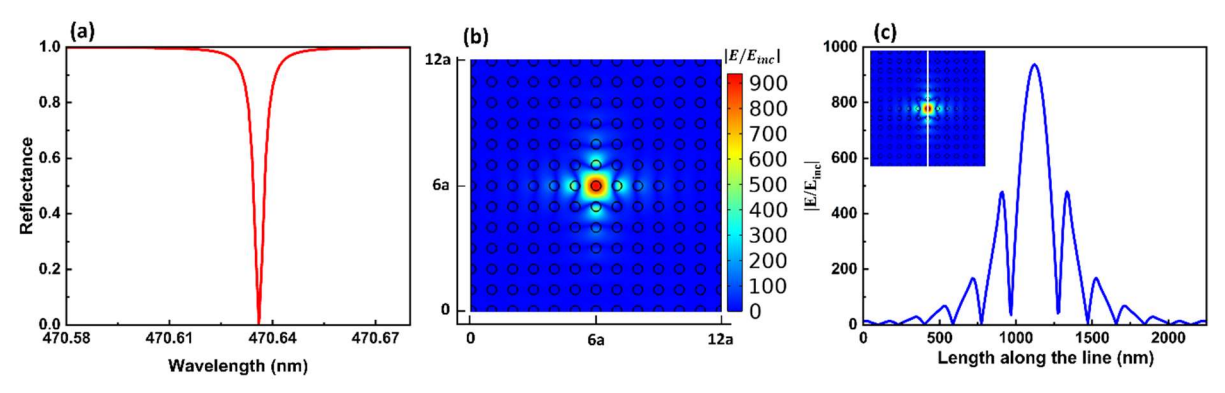


Fig 3.5 (a) Reflectance spectrum showing the defect mode corresponding to the air defect by a dip in the reflectance spectrum at 470.6 nm. (b) the plot of E-field distribution at 470.6 nm showing the localized monopole with the color label indicating the magnitude of the relative E-field. (c) the line plot of E-field along the vertical line (x = 6a) passing through the center of the defect as shown in the inset.

rest of the crystal. Since we are considering a 2D PhC, the defect mode is localized in the XY plane but extends in the Z-direction. Figure. 3.5(a) shows a dip in the reflection spectrum

indicating the existence of a defect mode at a wavelength 470.6 nm for . The Quality factor (Q) of the defect mode is calculated from the reflection spectrum, $Q = \frac{\lambda_0}{4\lambda}$ where λ_0 is the defect mode wavelength (wavelength at the center of the reflection dip) and $\Delta\lambda$ is the full width half maximum (FWHM) of the reflection dip with a Gaussian approximation. For $\Delta n_d = 1.67$, where the rod at the defect site is replaced with air, $Q = 1.18 \times 10^5$. The contour plot of normalized E- field distribution at the defect mode wavelength of 470.63 nm is illustrated in Fig.3.5 (b). From Fig. 3.5(b), it is evident that the maximum E- field is localized at the center of the defect. The magnitude of the relative E- field (normalized for the incident field (E_{inc}) , $(|E/E_{inc}|)$ is shown in the color bar. The E- field values presented in this chapter are the unitless relative E-field w.r.t to the incident E-field $(|E/E_{inc}|)$. For a better mathematical insight, a linear plot showing the variation of E- field values along a vertical line (x = 6a) passing through the center of the defect is shown in Fig. 3.5 (c). It can be observed that the E- field is highly localized in the defect region with the maximum value of $|E_{max}/E_{inc}| = 937.6$ at the center and decays away from its center.

The hole- type and rod- type defects in analogy with p-type and n-type semiconductors respectively, are created by varying the refractive index at the defect site. For hole- type defect, Δn_d is varied from 0.27 to 1.67. The defect mode shows a blue shift with increasing Δn_d and is shown in Fig. 3.6 (a). The mid band wavelength, λ_m is indicated by black dashed line. The defect mode appears nearer to dielectric band and moves towards the air band and disappear into the air band as the Δn_d increases for the hole- type defect and is shown in Fig. 3.6 (b). The pink color band at the bottom starts from 434 nm below which is the air band and the blue band at the top starts from 667 nm above which is the dielectric band (same for Fig. 3.6 (d) as well).

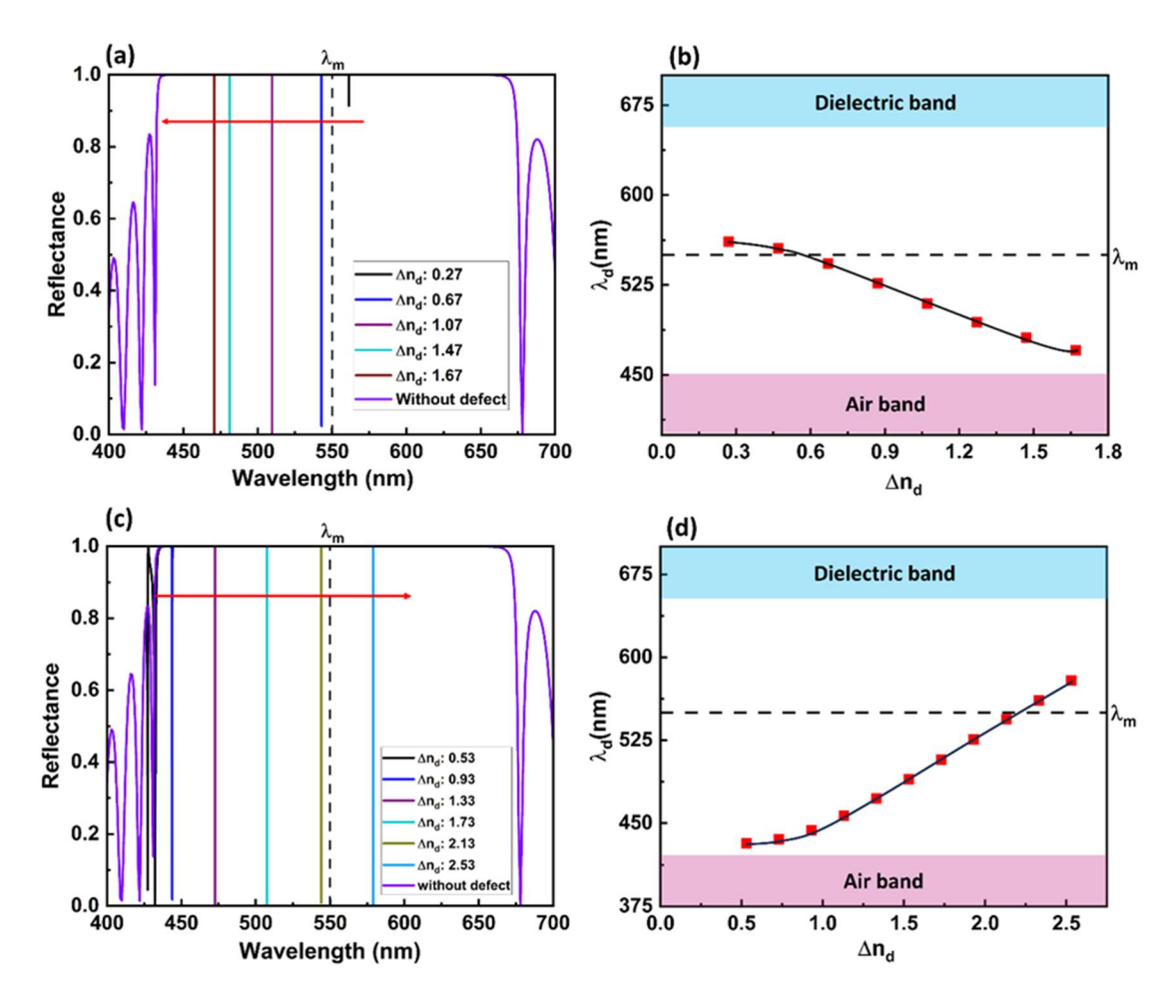


Fig 3.6 The effect of doping with different dielectric materials in the defect in a square 2D PhC (a) defect modes for Δn_d from 0.27 to 1.67 showing hole- type nature (b) variation of defect mode wavelength with respect to Δn_d of the hole- type defect (c) defect modes for Δn_d from 0.53 to 2.53 (d) variation of defect mode wavelength with respect to the Δn_d of the rod- type defect.

For a rod-type defect, Δn_d is varied from 0.53 to 2.53. Here the defect mode shows a red shift as Δn_d increases as shown in Fig. 3.6 (c). This has been illustrated in Fig. 3.6(d), where the defect mode appears nearer to the air band and moves towards dielectric band and disappear. The nature of the defect modes for rod-type defects are plotted for $\Delta n_d = 1.33$ ($n_d = 4$) is given in Fig. 3.7. The reflectance spectrum (Fig. 3.7(a)) shows the dip indicating a localized mode with central wavelength, 472.6 nm which lies within the band gap. The Q-factor calculated for the defect, $\Delta n_d = 1.33$, is $Q = 1.19 \times 10^5$. The E-field distribution of the defect mode shows a dipole nature with one nodal plane at the center of the defect as shown

in Fig. 3.7 (b). The line graph of the E-field values along the vertical line, x = 6a, passing through the center of the defect (inset of Fig. 3.7 (c)) is shown in the Fig. 3.7 (c). The maximum E- field value is 900 at the two poles of the dipole and it damps down to zero through rest of the line.

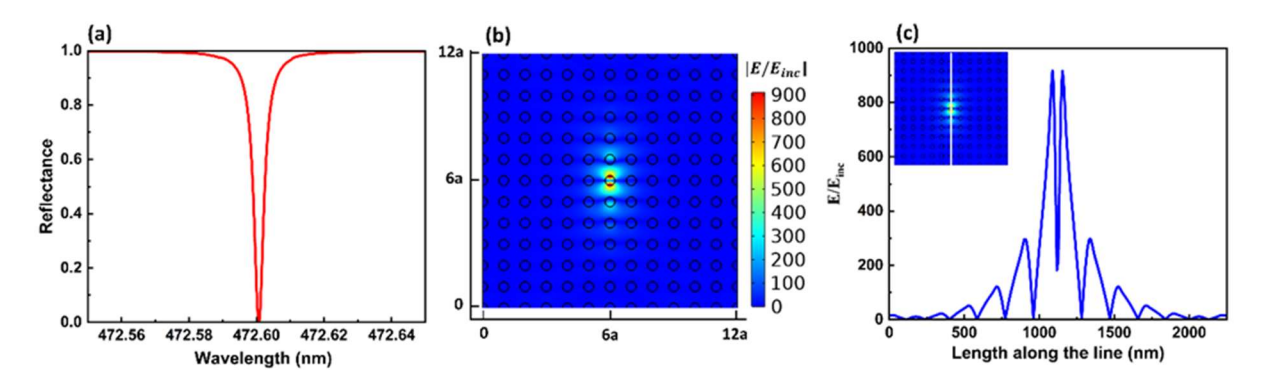


Fig. 3.7 (a) Reflectance spectra for $\Delta n_d = 1.33$, showing the defect mode as a dip in the reflectance spectrum at central wavelength 472.601 nm. (b) The contour plot of the defect mode showing a dipole nature with one nodal plane at the center of the defect with maximum relative E-field as 900. (c) The line graph of the E-field values along the vertical line (x=6a, white vertical line as shown in the inset) passing through the center of the defect.

In summary, the hole- type, and rod- type defects are created in the square lattice of 2D PhC. For hole- type defects, the defect mode appears nearer to dielectric band and moves towards the air band and disappear into the air band as the Δn_d increases, whereas, for the rod-type defects show the opposite trend, the defect mode appears nearer to the air band and moves towards dielectric band and disappear as Δn_d increases. E- filed distribution shows a monopole nature in a hole- type defect, whereas it has dipole nature in rod- type defects. The magnitude of the E- field maximum $|E_{max}/E_{inc}|$ is almost same for both type of defects. Q- factor showed a slight increase in rod- type defect compared to the hole type defect.

3.4.2 Hexagonal lattice

i) Band structure calculations

The bandgap is optimized with r/a ratio for the hexagonal lattice of amorphous titania rods in the similar way explained in section 3.3.1 for a square lattice. Figure 3.8 (a) shows the

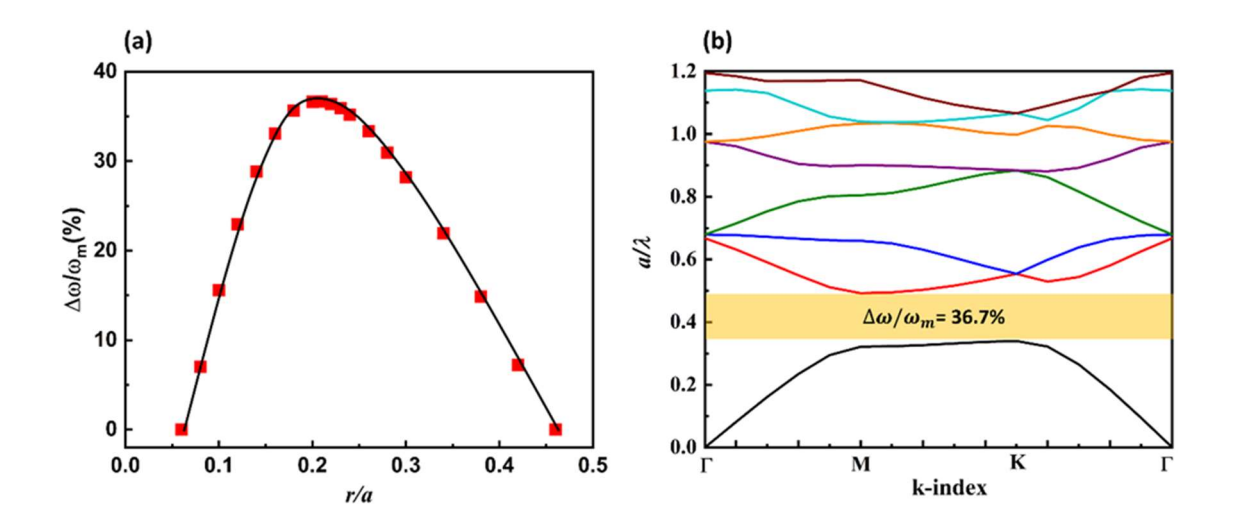


Fig. 3.8 (a) Optimization of band gap for the hexagonal 2D PhC for TE polarization. The maximum band gap of 36.6% is obtained for r/a = 0.21. (b) Band structure corresponding to r/a = 0.21 giving band gap between first and second TE bands shown in the shaded region. The Y-axis is represented in a/λ in units of c/a.

variation of the size of the bandgap w.r.t. the r/a ratio, a maximum band gap of 36.6% is opened for r/a = 0.21. The same is reflected in the band structure shown in Fig. 3.8 (b), the band gap of 36.6% between the first and the second TE bands.

ii) Reflectance spectra

The corresponding reflection spectrum is calculated keeping the same r/a and it has been tuned to the visible range, with radius,r=47nm and lattice constant, a=225nm and is shown in Fig. 3.9. The bandgap is identified as the region of maximum reflectance and it is found between 459 nm to 699 nm. This has been verified with the position of band-gap in the band-structure where band gap appears between 0.32 (c/a) to 0.49 (c/a) (corresponds to the

wavelength region, 459 nm to 703 nm). The reflectance spectrum for the normal incidence along Y-direction is corresponding to the band gap along the ΓM direction along the irreducible Brillouin zone.

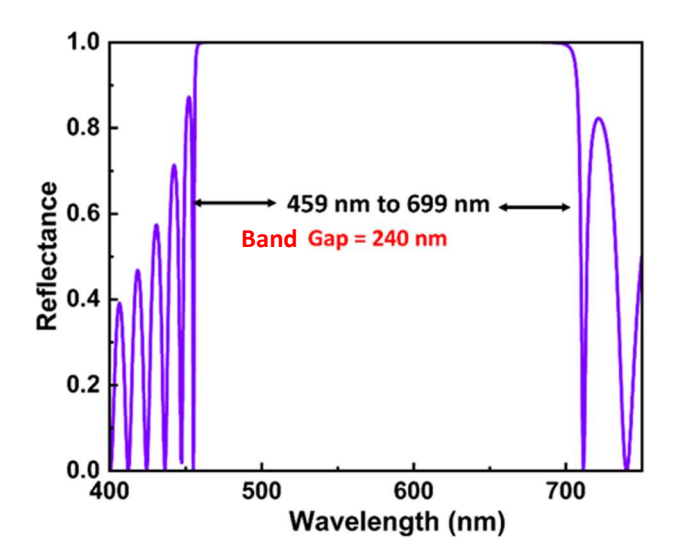


Fig. 3.9 Reflection spectrum for normal incidence (corresponding to ΓM direction) for TE polarization, showing band gap from 459 nm to 699 nm identified by the wavelength range in which the reflectance is maximum.

Hole- type and rod- type defects are created at the center of the hexagonal lattice and the defect modes are studied by varying Δn_d for both type of defects. For hole- type defects , Δn_d is varied from 0.27 to 1.67. It is observed that, the defect mode appears nearer to dielectric band for lower Δn_d and move toward lower wavelength region and disappears in the air band as Δn_d increases and is shown in Fig. 3.10 (a). The variation of λ_d with respect to Δn_d (from 0.27 to 1.67) is shown in Fig. 3.10 (b). The pink color band at the bottom starts from 459 nm below which is the air band and the blue band at the top starts from 699 nm above which is the dielectric band (same for Fig. 3.10 (d) as well). For rod- type defects, the Δn_d is varied from 0.33 to 2.53 and is given in Fig. 3.10 (c). The defect modes show a red shift as Δn_d increases. This variation of λ_d corresponds to Δn_d is shown in Fig. 3.10 (d). The defects modes start appearing near the air band and move towards the dielectric band as Δn_d increases and

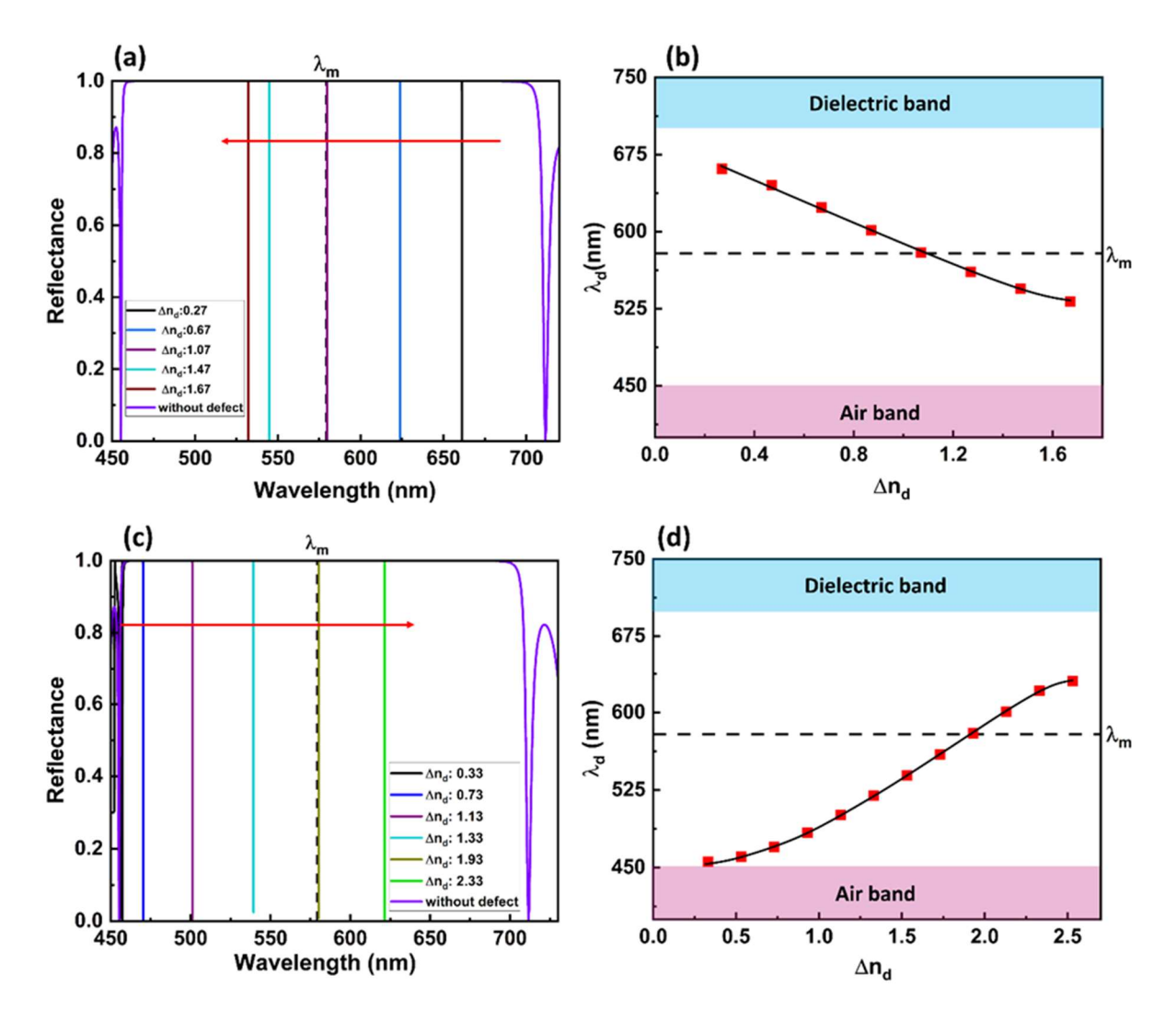


Fig 3.10 The effect of doping with different dielectric materials in the defect in a hexagonal 2D PhC. (a) defect modes for Δn_d from 0.27 to 1.67 showing hole- type nature (b) variation of defect mode wavelength with respect to the Δn_d of the hole- type defect, where the pink color band at the bottom indicates the air band and the blue band at the top indicates the dielectric band (c) defect modes for Δn_d from 0.33 to 2.53 showing rod- type nature. (d) variation of defect mode wavelength with respect to the Δn_d of the rod- type defect, where the pink color band at the bottom indicates the air band and the blue band at the top indicates the dielectric band.

disappear into the air band. The mid band wavelength $\lambda_m(579 \text{ nm})$ is shown as vertical dashed line in Fig. 3.10 (a) and (c) and horizontal dashed line in Fig. 3.10 (b) and (d). The nature of the E-field distribution of both type of defects is studied. For hole- type defect with Δn_d of 1.67 the reflectance spectrum (Fig. 3.11 (a)) shows a dip at 532.11 nm. The Q- factor is calculated for the defect, $\Delta n_d = 1.67$ is $Q = 3.62 \times 10^5$. The E- field distribution shows a

monopole nature at the center of the defect (Fig. 3.11 (b)). The E- field values along the vertical line (inset of Fig. 3.11 (c)) passing through the center of the defect is shown in Fig. 3.11 (c). The maximum relative E- field, $|E_{max}/E_{inc}| = 1788$ is concentrated at the center of the defect

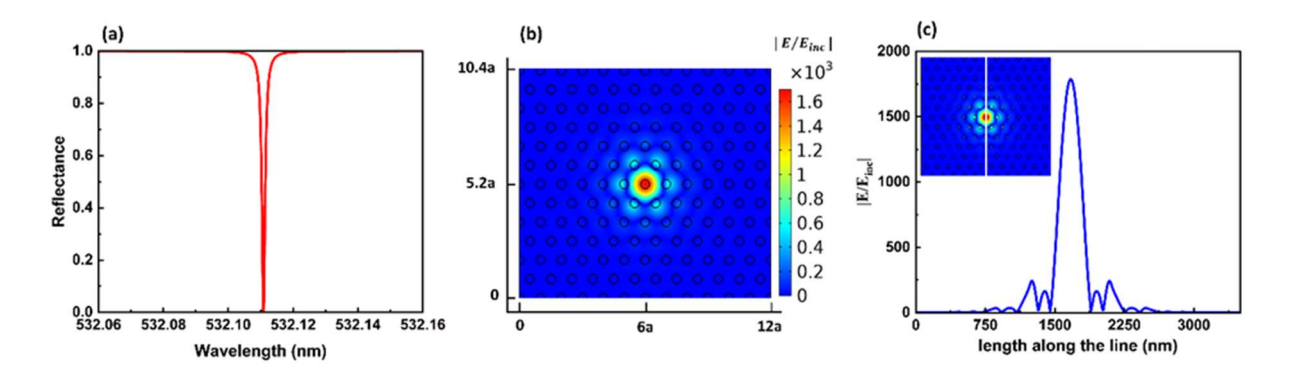


Fig. 3.11 (a) Reflectance spectrum showing the defect mode corresponding to the air defect by a dip in the reflectance spectrum at 532.11 nm. (b) the contour plot of E-field distribution at 532.111 nm showing the localized monopole with the color label indicating the magnitude of the relative E-field. (c) the line plot of E-field along the vertical line (x = 6a) passing through the center of the defect as shown in the inset.

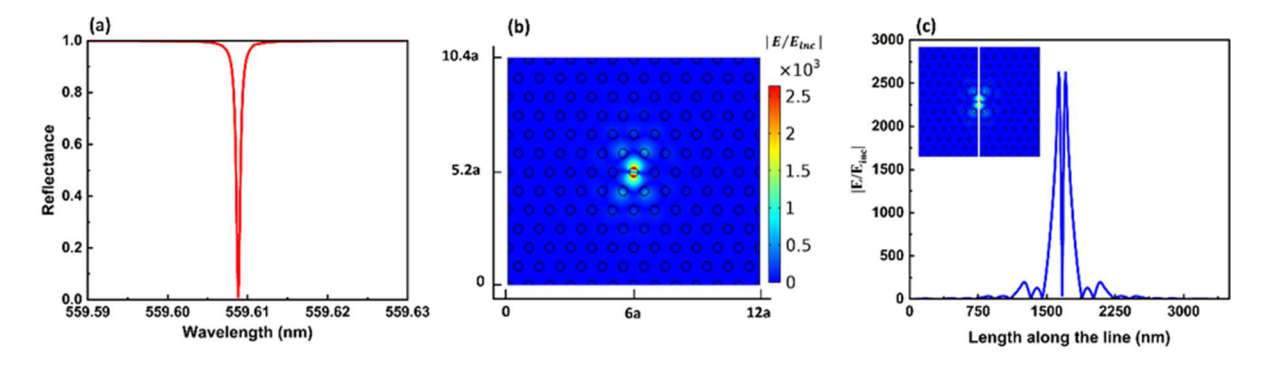


Fig. 3.12 (a) Reflectance spectrum showing the defect mode corresponding to the air defect by a dip in the reflectance spectrum at 559.609 nm. (b) the contour plot of E-field distribution at 559.609 nm showing the localized monopole with the color label indicating the magnitude of the relative E-field. (c) the line plot of E-field along the vertical line (x = 6a) passing through the center of the defect as shown in the inset.

and it decays away from the defect as we go up and down on the line. The nature of the defect modes for rod- type defects are plotted for $\Delta n_d = 1.73$ ($n_d = 4.4$) is given in Fig. 3.11. The reflectance spectrum (Fig. 3.12 (a)) shows a dip at a central wavelength, 559.609 nm indicating a localized mode at this wavelength. The Q- factor is calculated for the defect, $\Delta n_d = 1.67$ is $Q = 7.8 \times 10^5$. The contour plot of the E-filed distribution is provided in Fig. 3.12 (b). The

E-field distribution shows a dipole nature with one nodal plane at the center of the defect. The maximum E-field is localized on each pole of the defect site. The quantitative analysis of the E-filed values along a vertical line passing through the defect is given as a line graph in Fig. 3.12 (c). It shows two sharp peaks of same height of 2625 at the two poles of the defect site with E-field value approximately equal to zero at the center of the defect site.

In summary, the hole- type, and rod- type defects are created in the hexagonal lattice of 2D PhC. For hole- type defects, the defect mode appears nearer to dielectric band and moves towards the air band and disappear into the air band as the Δn_d increases, whereas, for the rod-type defects show the opposite trend, the defect mode appears nearer to the air band and moves towards dielectric band and disappear as Δn_d increases, similar to the nature showed for the defects in a square lattice of 2D PhC. E- filed distribution shows a monopole nature in a hole-type defect, whereas it has dipole nature in rod- type defects. The magnitude of the E- field maximum $|E_{max}/E_{inc}|$ is higher for the rod- type of defect compared to hole- type defect. This is reflected in the Q- factor as well, where it showed a higher value in rod- type defect compared to the hole type defect.

3.5 Summary

2D PhCs made up of a square/hexagonal lattice of infinitely long dielectric rods is modeled and studied using finite element method (FEM). The band structure for both type of 2D PhCs is calculated through plane wave method using MIT Photonic band gap package. The reflection spectra of 2D PhCs are optimized with array size of 13x13. The bandgap saturates above this array size. The reflection spectra of 2D PhCs with and without defects are studied. The effect of doping in the defect is systematically studied for both type of 2D PhCs. Hole-type defects are created by removing the dielectric material from the defect i.e., refractive index of the defect is less than the refractive index of rest of the rods. Rod-type of defects are created

by adding dielectric material to the defect, where the refractive index of the material is higher than the refractive index of rest of the rods. In hole- type defect, the defect modes appear nearer to the dielectric band and moves towards the air band and disappear into the air band as the refractive index contrast of the defect increases for both square and hexagonal 2D PhCs. In rod- type defects, the defect mode appears nearer to the air band and moves towards the dielectric band as the refractive index contrast of the defect increases and disappears into the dielectric band. The E- field distribution shows a monopole nature in the hole- type defect and a dipole nature in the rod- type defect for both square and hexagonal 2D PhCs. The E- field strength is more in the hexagonal lattice in which rod- type defect has higher maximum E-field value than the hole- type defect. The Q- factor showed higher value for the defects in hexagonal 2D PhC, in which the rod- type defects have higher Q- factor compared to the hole- type defects. These quantitative calculations of defect modes and electric field enhancement through electromagnetic simulations can possibly be used in PhC-based applications such as sensing with SERS technique.

References

- [1] J. Stodolka, D. Nau, M. Frommberger, C. Zanke, H. Giessen, and E. Quandt, "Fabrication of two-dimensional hybrid photonic crystals utilizing electron beam lithography," *Microelectron Eng*, vol. 78–79, no. 1–4, pp. 442–447, 2005
- [2] R. Jannesary, I. Bergmair, S. Zamiri, and K. Hingerl, "Design and fabrication of Sibased photonic crystal stamps with electron beam lithography (EBL)," *Alternative Lithographic Technologies II*, vol. 7637, p. 763720, 2010.
- [3] a Chen, S. Chua, C. F. Jr, B. Wang, and O. Wilhelmi, "Two-dimensional Photonic Crystals Fabricated by Nanoimprint Lithography," *Singapore-MIT Alliance (SMA)*, no. December, pp. 1–5, 2005.
- [4] K. J. Byeon, S. Y. Hwang, and H. Lee, "Fabrication of two-dimensional photonic crystal patterns on GaN-based light-emitting diodes using thermally curable monomer-based nanoimprint lithography," *Appl Phys Lett*, vol. 91, no. 9, 2007.

- [5] K. H. Choi *et al.*, "One-step combined-nanolithography-and-photolithography for a 2D photonic crystal TM polarizer," *Micromachines (Basel)*, vol. 5, no. 2, pp. 228–238, 2014.
- [6] P. Yao, G. J. Schneider, D. W. Prather, E. D. Wetzel, and D. J. O'Brien, "Fabrication of three-dimensional photonic crystals with multilayer photolithography," *Opt Express*, vol. 13, no. 7, p. 2370, 2005.
- [7] K. C. Lo, Y. S. Lan, and M. L. Hsieh, "Fabrication and characterization of two-dimensional photonic crystal using holographic lithography technology," *Proceedings of the 9th Joint Conference on Information Sciences, JCIS 2006*, vol. 2006, no. 2, pp. 2–5, 2006.
- [8] G. Q. Liang, W. D. Mao, Y. Y. Pu, H. Zou, H. Z. Wang, and Z. H. Zeng, "Fabrication of two-dimensional coupled photonic crystal resonator arrays by holographic lithography," *Appl Phys Lett*, vol. 89, no. 4, pp. 2004–2007, 2006.
- [9] S. G. Johnson, S. Fan, P. R. Villeneuve, J. D. Joannopoulos, and L. A. Kolodziejski, "Guided modes in photonic crystal slabs," *Phys Rev B*, vol. 60, no. 8, pp. 5751–5758, 1999.
- [10] K. M. Ho, C. T. Chan, and C. M. Soukoulis, "Existence of a photonic gap in periodic dielectric structures," *Phys Rev Lett*, vol. 65, no. 25, pp. 3152–3155, 1990.
- [11] F. Wen, S. David, X. Checoury, M. El Kurdi, and P. Boucaud, "Two-dimensional photonic crystals with large complete photonic band gaps in both TE and TM polarizations," *Opt Express*, vol. 16, no. 16, p. 12278, 2008.
- [12] S. Narayanan and B. V. R. Tata, "Effect of doping on defect modes of 2D photonic band gap crystals," *AIP Conf Proc*, vol. 2269, no. October, 2020.
- [13] O. Painter *et al.*, "Two-Dimensional Photonic Band-Gap Defect Mode Laser," *Science* (1979), vol. 284, no. 5421, pp. 1819–1821, 1999.
- [14] J. D. Joannopoulos, S. G. Johnson, J. N. Winn, and R. D. Meade, *Photonic crystals: Molding the flow of light*. 2011.
- [15] A. M. Zheltikov, S. A. Magnitskiĭ, and A. V. Tarasishin, "Two-dimensional photonic crystals with a lattice defect: Spectrum of defect modes, localization of light, and formation of evanescent waves," *Journal of Experimental and Theoretical Physics*, vol. 90, no. 4, pp. 600–608, 2000.
- [16] E. Yablonovitch, T. J. Gmitter, R. D. Meade, A. M. Rappe, K. D. Brommer, and J. D. Joannopoulos, "Rod- and hole- modes in photonic band structure," *Phys Rev Lett*, vol. 67, no. 24, pp. 3380–3383, 1991.

- [17] G. Guida, A. de Lustrac, and A. Priou, "An introduction to photonic band gap (PBG) materials," *Progress in Electromagnetics Research*, vol. 41. 2003.
- [18] I. Andonegui and A. J. Garcia-Adeva, "The finite element method applied to the study of two-dimensional photonic crystals and resonant cavities," *Opt Express*, vol. 21, no. 4, p. 4072, 2013.

Numerical Simulation of Internal Electric Field Distribution in Colloidal Photonic Crystal Thin Films

CPhCs, characterized by their periodic arrangement of dielectric colloidal particles, exhibit remarkable optical properties, including photonic bandgap effects and structural coloration. In this chapter, we'll take a closer look at the nature of internal E-field distribution that play a crucial role in their application in sensing platforms.

4.1 Introduction

Thin films of CPhC with monolayer or multilayer dielectric nanospheres have emerged as excellent templates for applications in SERS, fluorescence, and biosensing [1-4]. While extensive near-field and far-field studies on CPhC thin films have been conducted [5-8]; the internal E- field distributions in the mono and multilayered CPhC structures remain underexplored in the literature. Both near-field and far-field microscopic techniques have been utilized for sensing applications and imaging the structural colors generated by the Bragg diffraction of visible light in CPhC thin films. Some of these studies have motivated us for detailed investigations of the internal E- field distribution in CPhC films with appreciable refractive index contrast. These studies are crucial as they provide valuable information and insights into the interaction of light with CPhC thin films, which have numerous practical applications [1-9].

In this chapter, a detailed numerical investigation of the internal E-field distribution in the plane of monolayer, bilayer, and trilayer CPhC films have been presented. Though there have been some studies on the E-field distribution in monolayer CPhCs [9]–[11], detailed studies on the effect of addition of CPhC layers (bi and tri layers) on E- filed

distributions are lacking. The study of bilayer and trilayer CPhC films was carried out by adding periodic layers in the orthogonal direction. The internal E- field distribution in a monolayer CPhC was theoretically analyzed by Kurokawa *et al.* [9] using the vector Korringa-Kohn-Rostoker (KKR) method, and the effect of dielectric contrast on the E- field intensity distribution was examined. Additionally, the effect of semi-infinite and finite substrates on the transmission spectrum of a 2D monolayer CPhC and the consequent field distribution in the crystal plane were studied [10]. Numerical simulations based on the finite-difference time-domain (FDTD) method in a monolayer CPhC film at different relevant incident wavelengths were reported by Farcau *et al.* [11].

In this chapter, we report the investigation on the internal E- field distribution in the monolayer, and top layers of bilayer and trilayer CPhC thin films by performing numerical simulations using COMSOL Multiphysics software with a wave optics module. The monolayer, bilayer, and trilayer CPhC thin films consist of one-, two-, and three layers of (hexagonal) close-packed spherical colloids. We also discuss the dependency of E- field distribution on incident wavelengths (lying at different spectral regimes of the PhC thin films; in particular the on-resonance and off-resonance wavelengths). On-resonance wavelength lies within the stop band of the CPhC thin films, and the off-resonance wavelength lies outside the stop band. The numerical simulation results reported in this chapter can provide insights to the E- field localization and enhancement at specific CPhC regimes which can be further utilized in several PhC-based applications.

4.2 Computational details

The monolayer, bilayer, and trilayer CPhC films consist of monodisperse spherical polystyrene (PS) colloids (n = 1.59) of colloidal diameter of d = 287 nm. The lattice constant, a, in such close-packed structures is taken to be same as the colloidal diameter i.e., a = d = 287

nm. In simulation, we consider PS colloids as these are readily available commercially with different colloidal diameters and these can be easily synthesized using the emulsion polymerization technique [12]. In practice, the CPhC films of monolayer and multilayer can be fabricated by using the convective self-assembly method and the subsequent layers can clearly be distinguished from each other by recording microscopy images [[13]. In this work, the numerical simulations based on PSPhC films are performed by using commercial software, COMSOL Multiphysics with wave optic module, which employs FEM [14]. The detailed description of FEM is given in Chapter 2, Section 2.6.1.

The schematic of the computation domain for monolayer PSPhC film is shown in Fig. 4.1. Bilayer and trilayer PSPhC are simulated by adding subsequent planes (layers) of periodic array of PS colloidal particles in a way similar to the conventional ABC stacking [15]. B layer of bilayer and trilayer is displaced by $(a/2, \sqrt{3}a/2, \sqrt{2}a/\sqrt{3})$, and C layer of trilayer is displaced by $(a, a/\sqrt{3}, 2\sqrt{2}a/\sqrt{3})$ from A layer. The vertical height of the computational domain can be adjusted depending on the number of layers (bilayer or trilayer) of the PSPhC film used for simulation. The lower edge of the monolayer is placed at the middle of the computation domain (Z=0) and is sandwiched between air (n=1.00) on the top and glass (n=1.56) at the bottom. The thickness of the glass substrate is taken as 2.5a (717.5 nm) in the simulation. A Y-polarized plane wave is incident on PSPhC films from the air-film interface at normal incidence along -Z-direction. The PBCs are applied on both the sides of the periodic plane (along X- and Y- directions) which assume the PSPhC films are infinitely extended in the plane of periodicity. PML conditions are applied on the planes normal to the direction of propagation of light which are there to absorb the unwanted reflections from the crystal planes and truncate the simulation domain [16]. The source plane (indicated by blue region) is placed right after the PML layer.

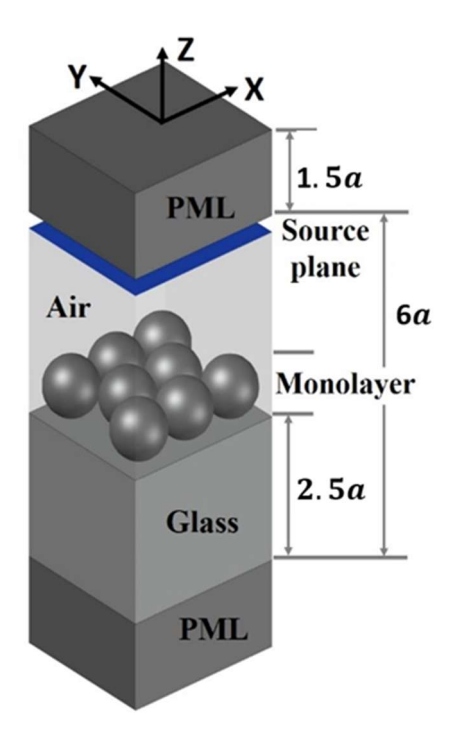


Fig. 4.1 Schematic of the computational domain of monolayer PSPhC on a glass substrate. Bilayer and trilayer PSPhC films replace the monolayer one-by-one in the same computation domain while the vertical height of the domain can be adjusted. Light is incident from the air region along -Z direction.

4.3 Results and discussion

4.3.1 Reflectance spectra

The choice of incident wavelengths used in further sections is obtained from the calculated reflection spectra of the PSPhC thin films as shown in Fig. 4.2. Figure. 4.2 gives the reflection spectra of monolayer, bilayer, and trilayer PSPhC films when light is incident from the air region at normal incidence as depicted in Fig. 4.1. The vertical solid lines (lines R_1 and R_2) in Fig. 4.2(a) correspond to the wavelengths which are taken into consideration in further sections. The wavelengths have been chosen such that the wavelength ($\lambda_{on-res} = 653$ nm) of R_1 satisfies the modified Bragg's law at normal incidence of light. In PSPhC films: $\lambda_{on-res} = 2d_{111}n_{eff}$, where $d_{111} = \sqrt{\frac{2}{3}}d$ is the interlayer distance for the close-packed hexagonal PhC films, n_{eff} is the effective refractive index (~ 1.44) of the PSPhC films provided, [111]- plane

is parallel to the substrate in the conventional ABC stacking [26]. The wavelength ($\lambda_{off-res}$ = 360 nm) of R₂ is chosen close to the product of colloidal diameter and effective refractive index of the PSPhC films. We address the R1 as on-resonance wavelength (λ_{on-res}) and R2 as off-resonance wavelength ($\lambda_{off-res}$).

We observe from Fig. 4.2 that the stop band of PSPhC monolayer at λ_{on-res} appears broad which can be due to the absence of out-of-plane periodicity along the direction of light propagation at normal incidence. The broad peak in monolayer can be attributed to the geometrical sum of Mie scattered waves from the colloidal spheres as reported by Inoue *et al.* [17]. However, the stop band becomes narrower around λ_{on-res} in bilayer and trilayer PSPhC films with gradual increase in reflectance value as a consequence of the addition of periodic layers along the light propagation direction. A further increase in the number of layers along

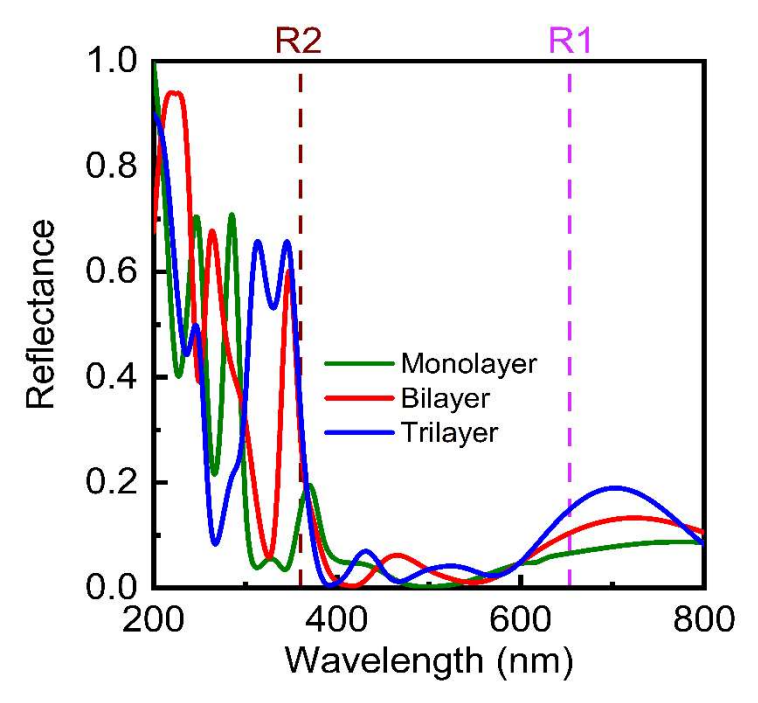


Fig 4.2 Simulation results of reflection spectra of monolayer, bilayer, and trilayer PSPhC films. The vertical dashed lines R1 and R2 corresponds to the wavelength under consideration in the following sections.

the vertical direction results in a further pronounced stop band of higher reflectance value and a small photonic band. From application perspective, the advantage of the presence of such reflection band is that at the wavelengths lying inside the band or at the band edge, the group velocity of light can be reduced drastically which can result in field localization and enhancement in PhC films. On the other hand, a sharp band appears in PSPhC films at $\lambda_{off-res}$ where the peak value changes with the addition of layers but the bandwidths don't get much affected by the number of layers. The sharp reflection peak at $\lambda_{off-res}$ corresponds to the resonant coupling of incident light with the bound Bloch-like states in the ordered plane as reported in the literature[18]. However, at short-wavelength regions, the incident light is likely to be attenuated due to huge scattering (incoherent) by the colloidal array[19].

4.3.2. Internal electric field distribution

i) PSPhC monolayer

Fig. 4.3(a) shows the contour plot of internal E- field distribution in PSPhC monolayer at on-resonance wavelength (λ_{on-res} = 653 nm) and that at off-resonance wavelength ($\lambda_{off-res}$ = 360 nm) is shown in Fig. 4.3(b). The sampling plane is parallel to XY-plane and is at Z = Z1 = a/2, considering the lower edge of the monolayer or the top surface of glass is at Z = 0. A glance at Fig. 4.3 infers that the E- field is getting redistributed in PSPhC regimes (in contrast to the expected uniform distribution of E- field in a homogeneous dielectric medium, glass substrate alone, for example). However, the redistribution of the E- field in PSPhC film depends on the choice of incident wavelength as evident from the contour plots in Fig. 4.3. We observe from Fig. 4.3(a) that the E- field is mainly localized and enhanced in the air void region between the spheres indicating the incident flux is not propagating. The enhancement of the field is attributed to the strong interaction between the dielectric spheres in a close-packed arrangement at wavelength λ_{on-res} as discussed earlier. On the other hand, Fig. 4.3(b) shows the crescent-shaped E- field distribution at the upper and lower edges of the dielectric spheres. This implies at wavelength $\lambda_{off-res}$, the E- field becomes localized within the dielectric spheres as the

spheres are non-interacting (or, weakly interacting) at this wavelength. The normalized E-field ($|E/E_{inc}|$) is the E- field relative to the incident field(E_{inc}). The E- field values presented in this chapter are the relative E- field values w.r.t the incident E-field. The magnitude of the maximum E- field value is different ($|E_{max}/E_{inc}| = 2.79$) at λ_{on-res} and ($|E_{max}/E_{inc}| = 6.66$) at $\lambda_{off-res}$ as observed from the color bar in Fig. 4.3(a,b) implying the extent of E- field redistribution is different in monolayer PSPhC film at both the wavelengths under consideration. The difference in maximum E- field values can be attributed to huge attenuation of the wave in the PSPhC monolayer at $\lambda_{off-res}$ as discussed under Fig. 4.2.

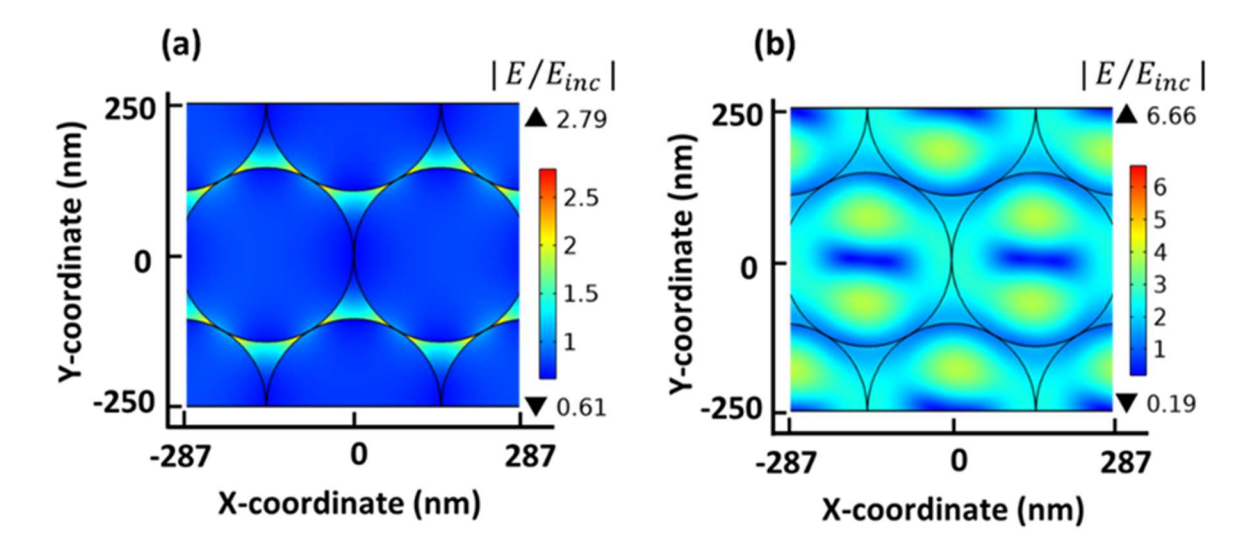


Fig 4.3 Contour plot of normalized E- field in the monolayer PSPhC film at (a) $\lambda_{\text{on-res}} = 653$ nm, and (b) $\lambda_{\text{off-res}} = 360$ nm. The sampling plane is at $Z = Z_1 = a/2$. The black circles indicate the circumference of the colloidal spheres in the sampling plane. The color bars provide the strength of the E- field represented by relative E- field values ($|E/E_{inc}|$).

For a better understanding of the observations under Fig. 4.3, a quantitative analysis of the E- field values at different linear regions of monolayer PSPhC film is provided by the line plots as shown in Fig. 4.4. Figures 4.4(a-d) show the normalized relative E- field ($|E/E_{inc}|$) values across the lines $y = 0.49 \, a$, $y = -0.37 \, a$, $x = -0.49 \, a$ and x = 0, respectively, as obtained from figures 4.3 (a, b). The red horizontal/vertical lines in the contour plots as

shown as the insets of figures 4.4(a-d) indicate the above-mentioned linear regions. The E-field values across the chosen lines in the plane of the monolayer PSPhC are obtained for both λ_{on-res} (green dashed curve) and $\lambda_{off-res}$ (blue solid curve) as shown in Fig. 4.4. A glance at Fig. 4.4 shows that the E-field distribution at λ_{on-res} has an opposite trend to that of $\lambda_{off-res}$ implying that there is an enhancement in the E- field at λ_{on-res} in the PSPhC regime where the field at $\lambda_{off-res}$ is suppressed and vice versa. Also, a higher value of E- field enhancement is observed in the high dielectric region of the PSPhC monolayer at $\lambda_{off-res}$ than at λ_{on-res} in the low dielectric region as seen from the scale bar (Fig. 4.3(a,b)). These observations help to use the PSPhC templates for sensing applications.

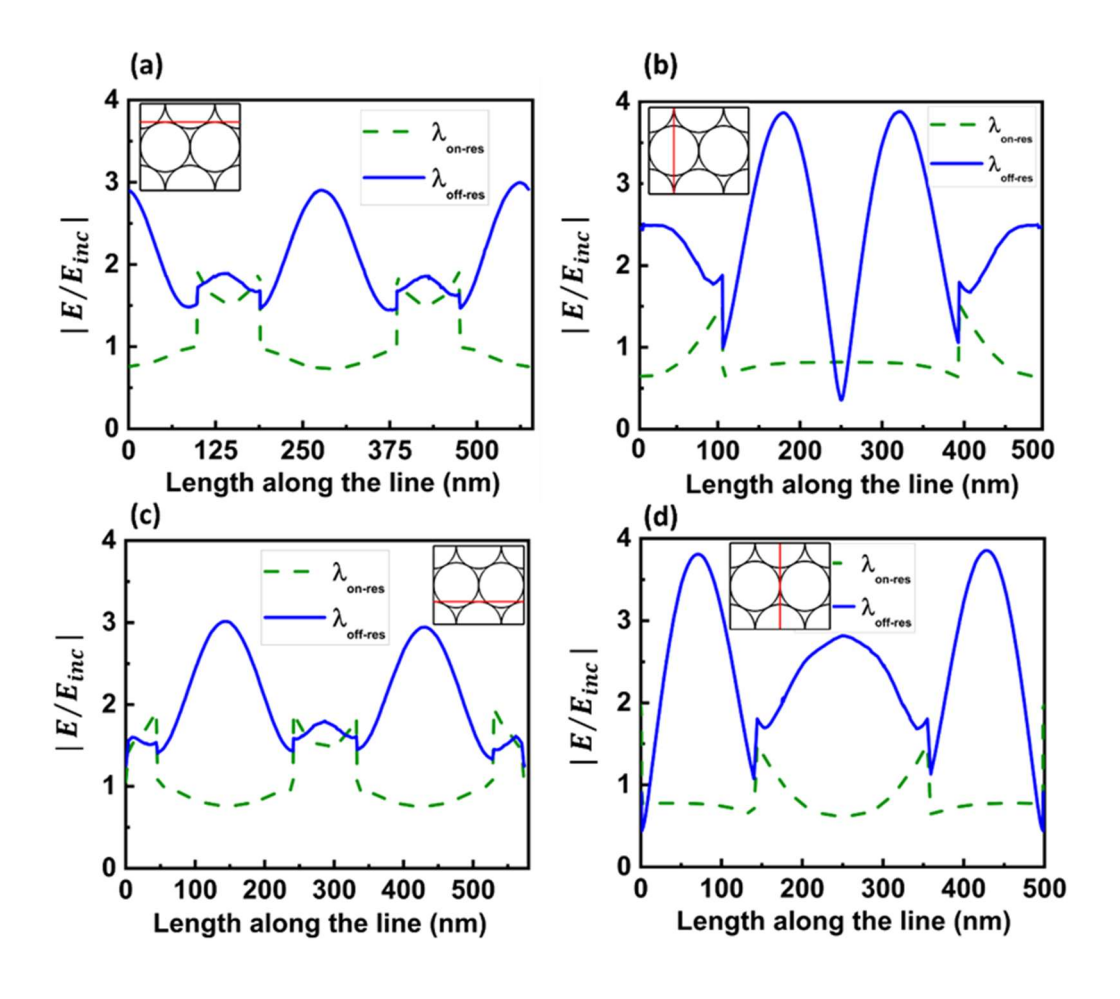


Fig. 4.4 The line plots of normalized E- field at both λ_{on-res} and $\lambda_{off-res}$ across the linear regions defined as (a) $y = 0.49 \ a$, (b) $y = -0.37 \ a$, (c) $x = -0.49 \ a$, and (d) x = 0 in connection with Fig. 4.3(a) and Fig. 4.3(b). The insets in (a-d) show the positions of the chosen lines in monolayer PSPhC regime as indicated by the red horizontal/vertical lines in the contour plots.

ii) PSPhC bilayer

The normalized E- field distribution is computed for the PSPhC bilayer and the E- field values across different linear regions in the crystal plane are evaluated as before. Fig. 4.5(a) and Fig. 4.5(b) show contour plots of normalized E- field values in PSPhC bilayer (top layer) at λ_{on-res} , and $\lambda_{off-res}$ respectively. Figures 4.6(a-d) show the line plots of E- field values across the lines defined as y=0.66a, y=-0.21a, x=-0.49a, and x=0 respectively. The red horizontal/vertical lines in the contour plots as shown as the insets of Fig. 4.6(a-d) indicate the above-mentioned linear regions. We observe from Fig. 4.5(a) that the E- field is mainly localized and enhanced in the air void region at λ_{on-res} whereas it becomes localized at the upper and lower edges within the dielectric spheres at $\lambda_{off-res}$, similar to what is observed in monolayer PSPhC. These observations are quantitatively verified from the line plots in Fig. 4.6 (a-d)

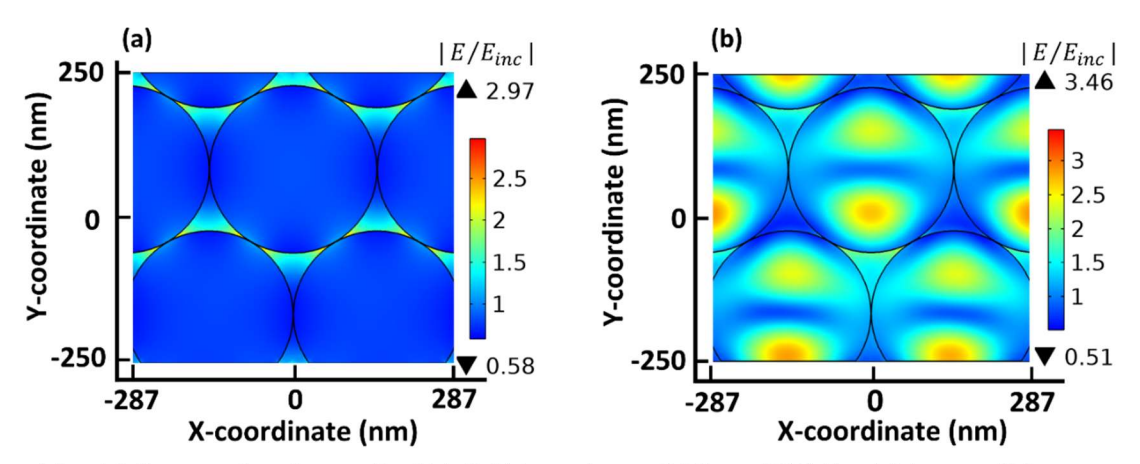


Fig. 4.5 Contour plot of normalized E- field in top layer of bilayer PSPhC at (a) $\lambda_{\text{on-res}} = 653$ nm, and (b) $\lambda_{\text{off-res}} = 360$ nm. The sampling plane is at $Z = Z_1 + \sqrt{2\alpha/\sqrt{3}}$.

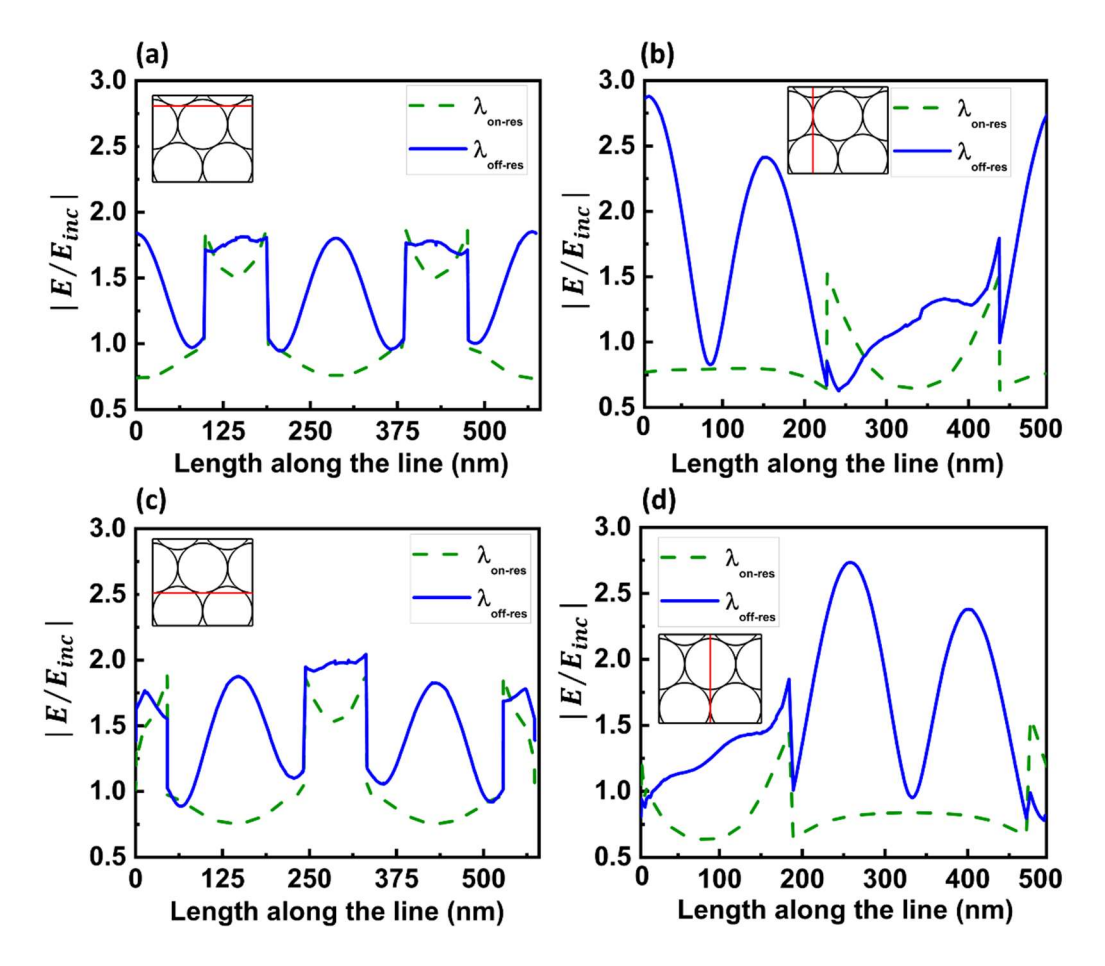


Fig. 4.6 The line plots of E-field values at both $\lambda_{\text{on-res}}$ and $\lambda_{\text{off-res}}$ are plotted across the lines (a) y = 0.66a, (b) y = -0.21a, (c) x = -0.49a, and (d) x = 0 in connection with Fig. 4.5 (a) and (b). The insets in (a-d) show the positions of the chosen lines in the top layer of bilayer as indicated by the red horizontal/vertical lines in the contour

showing E-field distribution in top layer of bilayer at λ_{on-res} has the opposite trend to that of $\lambda_{off-res}$ implying that there is a field enhancement in the PSPhC regime at the former wavelength whereas the field is suppressed at the latter wavelength and vice versa.

iii) PSPhC trilayer

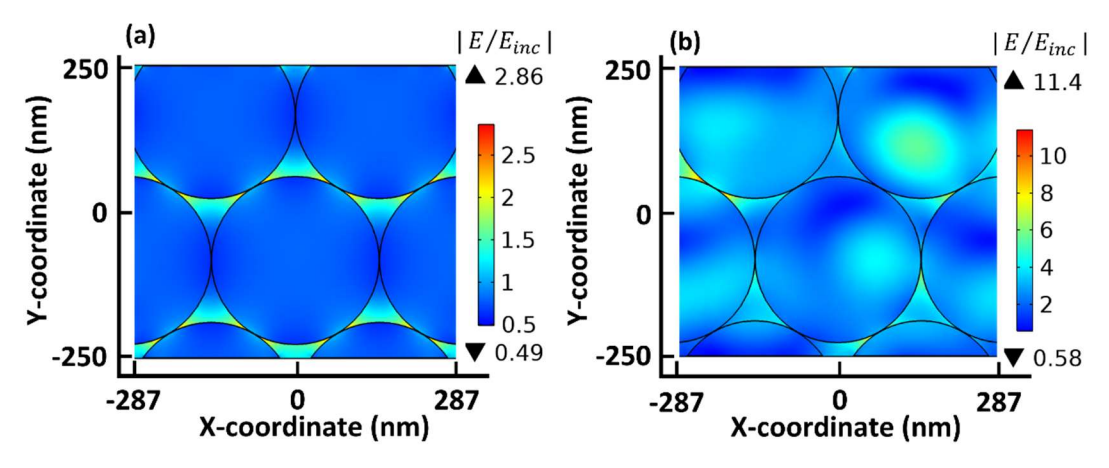


Fig. 4.7 Contour plot of normalized E- field in top layer trilayer PSPhC at (a) $\lambda_{\text{on-res}} = 653$ nm, and (b) $\lambda_{\text{off-res}} = 360$ nm. The sampling plane is at $Z = Z1 + 2\sqrt{2a/\sqrt{3}}$.

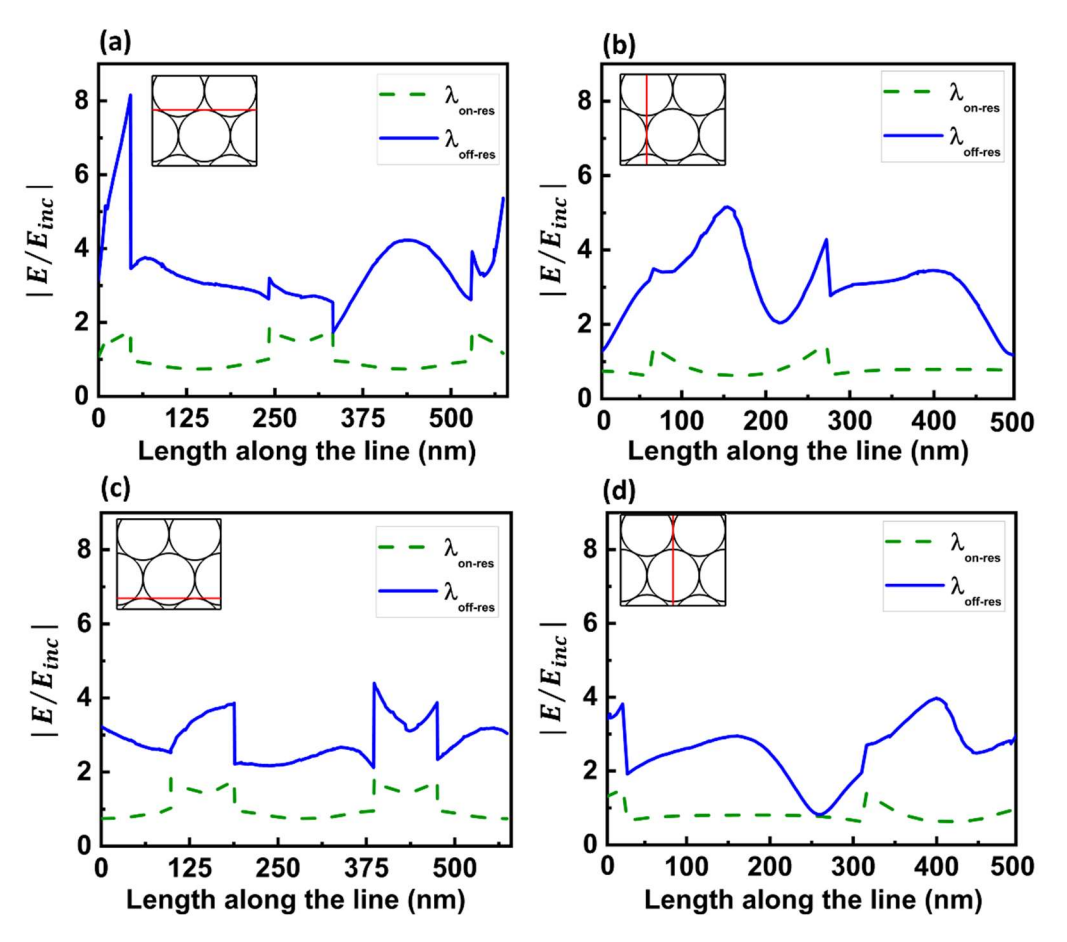


Fig. 4.8 The line plots of E-field at both $\lambda_{\text{on-res}}$ and $\lambda_{\text{off-res}}$ across the linear regions (a) y = 0.21a, (b) y = -0.65a, (c) x = -0.49a, and (d) x = 0 in connection with Fig. 4.7 (a) and (b). The insets in (a-d) show the positions of the chosen lines in the top layer of trilayer as indicated by the red horizontal/vertical lines in the contour plots.

Fig. 4.7(a) and Fig. 4.7(b) show the contour plots of E- field values in PSPhC trilayer (top layer) at $\lambda_{onr-res}$, and $\lambda_{off-res}$ respectively. Figures 4.8(a-d) show line plots of E- field values across the lines defined as y=0.21a, y=-0.65a, x=-0.49a, and x=0, respectively. The red horizontal/vertical lines in the contour plots as shown as the insets of figures 4.8(a-d) indicate the above-mentioned linear regions. We observe from Fig. 4.7(a) that the E- field is mainly localized and enhanced in the air void region at $\lambda_{onr-res}$ similar to what observed in monolayer and bilayer (top layer) PSPhC films. However, Fig. 4.7(b) shows the field profile in the top layer of the trilayer at $\lambda_{off-res}$ which forms a connecting network, as the field appears within both the air void and dielectric colloidal sphere regions, implying the propagation of E-field in the crystal plane (no well-defined field pattern is observed). The reason for this might be due to larger scattering by the trilayer at $\lambda_{off-res}$ (scattering increases with the subsequent addition of layers along the direction of propagation). It may be noted that the top layer of the trilayer is not showing a uniform field profile throughout the crystal plane at $\lambda_{off-res}$ implying that at some locations the field enhancement is drastically more as compared to the other sites.

4.3.3 Comparison of internal electric field distribution in monolayer, bilayer and trilayer PSPhC

A comparison of maximum E- field values in the top layer of bilayer with those in monolayer reveals the maximum E- field values are nearly the same in the PSPhC films at λ_{on-res} . Whereas, monolayer ($|E_{max}/E_{inc}| = 6.66$) has slightly larger maximum E- field value at $\lambda_{off-res}$ than the top layer of bilayer ($|E_{max}/E_{inc}| = 3.46$) as obtained from the scale bar in figures 4.3(a, b) and 4.5(a, b). It is noted that although the E- field is localized within the dielectric sphere regions in both monolayer and (top layer of) bilayer PSPhC films at $\lambda_{off-res}$, the maximum field values are different in both the structures. The reason for the difference in maximum field values at $\lambda_{off-res}$ might be due to the fact that at this wavelength the bilayer PSPhC scatters (and attenuates) the incident wave to a greater extent as compared to monolayer

PSPhC as discussed earlier under Fig. 4.2. As a result, the internal E- field localization can be reduced in the crystal plane of the bilayer than that in the monolayer. In fact, as a result of large scattering, the wave can propagate in all spatial directions of the crystal, hence reducing the internal E- field localization in the crystal plane.

Furthermore, we have obtained the E- field distribution in the (top layer of) PSPhC trilayer, by adding another periodic layer of close-packed colloidal spheres along the direction of propagation of light which is discussed in Fig. 4.7. A comparison of maximum E- field values in the top layer of trilayer at λ_{on-res} , and $\lambda_{off-res}$ with those in monolayer and (top layer of) bilayer reveals the PSPhC films show nearly the same field enhancement at λ_{on-res} whereas the top layer of trilayer has greater *E*- field value (11.4) at $\lambda_{off-res}$ than those in monolayer and bilayer PhC films. However, the maximum E- field value in the top layer of trilayer is observed at some random locations (not well defined) as indicated by the spikes in figures 4.8(a,b). The not-so-well-defined profile of field distribution in PSPhC trilayer is attributed to increased scattering at $\lambda_{off-res}$ with an increasing number of layers along the direction of propagation as discussed earlier.

The E- field distributions on (top layer of) bilayer and trilayer PSPhC thin films are important from an experimental perspective when CPhC thin films are coated/drop-casted with other materials (for example, metal films or metal NPs) to form hybrid structures. In such structures, the effective E- field enhancement is likely to arise from the interaction of light at the interface of external material-CPhC film. We believe such structures have impending applications in sensing using, for example, the technique of surface enhanced Raman scattering. However, in practice, the fabricated monolayer, bilayer, and trilayer PSPhC thin films consist of several uncontrollable defects arising during the fabrication process (widely used self-assembly method). As a result, there is a possibility that the external coated materials can escape to the bottom layers of bilayer and trilayer PSPhC thin films which can also

contribute to the field enhancement from these hybrid structures. The above discussion involves the PSPhC thin films whose structural parameters are close to the experimental conditions with the available Raman spectroscopy. However, PSPhC thin films of different structural parameters and with different lattice types need to be explored to know which structure gives better E-field distribution for employing it as potential PSPhC templates for sensing applications.

4.4 Summary

The internal E- field distribution was investigated in monolayer, bilayer, and trilayer PSPhC thin films. The influence of on-resonance and off-resonance incident wavelengths on the E- field distribution in PSPhC thin films was studied. It was found that at on-resonance wavelength, the E- field remains localized and is enhanced in the air void regions between the close-packed spheres in the PSPhC thin films, where the maximum E- field values remain nearly the same and become independent of the addition of layers along the direction of light propagation. In contrast, at off-resonance wavelength, the internal E- field distribution varies significantly in the crystal planes of monolayer, bilayer, and trilayer PSPhC thin films. The Efield remains localized within the dielectric sphere regions in monolayer and bilayer PSPhC thin films, while in the trilayer, the E- field propagates within the crystal plane at off-resonance wavelengths. E- Field enhancement mechanisms at the wavelengths under study are mainly due to changes in the photonic band structure and random scattering from colloidal spheres. At the off-resonance wavelength, the maximum E- field value is higher in the monolayer compared to the bilayer. In the trilayer PSPhC, the maximum E- field becomes significantly high, occurring at random sites rather than well-defined locations. The selection of the incident wavelength plays a crucial role in enhancing the E- field at specific CPhC sites, which can be utilized in designing CPhC-based templates for sensing applications.

References

- [1] B. Subramanian, G. Theriault, J. Robichaud, N. Tchoukanova, and Y. Djaoued, "Large-area crack-free Au–SiO2 2D inverse opal composite films: Fabrication and SERS applications," *Mater Chem Phys*, vol. **244**, (2020)
- [2] A. Yadav *et al.*, "State-of-art plasmonic photonic crystals based on self-assembled nanostructures," *J Mater Chem C Mater*, vol. **9**, no. 10, pp. 3368–3383, (2021)
- [3] P. Sahani and R. Vijaya, "Polarization state of transmitted and emitted light in homogeneous and inhomogeneous medium," *Appl Phys B*, vol. **127**, no. 2, (2021)
- [4] X. Huang and M. A. El-Sayed, "Gold nanoparticles: Optical properties and implementations in cancer diagnosis and photothermal therapy," *Journal of Advanced Research*, vol. 1, no. 1. (2010)
- [5] T. Yamasaki and T. Tsutsui, "Fabrication and optical properties of two-dimensional ordered arrays of silica microspheres," *Japanese Journal of Applied Physics, Part 1:*Regular Papers and Short Notes and Review Papers, vol. 38, no. 10, (1999)
- [6] G. T. Ayenew *et al.*, "Photonic properties of two-dimensional photonic crystals based on monolayer of dielectric microspheres," *Nanophotonics IV*, SPIE, (2012)
- [7] H. T. Miyazaki, H. Miyazaki, K. Ohtaka, and T. Sato, "Photonic band in two-dimensional lattices of micrometer-sized spheres mechanically arranged under a scanning electron microscope," *J Appl Phys*, vol. **87**, no. 10, pp. 7152–7158, (2000)
- [8] L. A. Dorado, R. A. Depine, D. Schinca, G. Lozano, and H. Míguez, "Experimental and theoretical analysis of the intensity of beams diffracted by three-dimensional photonic crystals," *Phys Rev B Condens Matter Mater Phys*, vol. **78**, no. 7, (2008)
- [9] Y. Kurokawa, Y. Jimba, and H. Miyazaki, "Internal electric-field intensity distribution of a monolayer of periodically arrayed dielectric spheres," *Phys Rev B Condens Matter Mater Phys*, vol. **70**, no. 15, (2004)
- [10] Y. Kurokawa, H. Miyazaki, and Y. Jimba, "Light scattering from a monolayer of periodically arrayed dielectric spheres on dielectric substrates," *Phys Rev B Condens Matter Mater Phys*, vol. **65**, no. 20, pp. 2011021–2011024, (2002)
- [11] C. Farcău, S. Astilean, and E. Vinţeler, "Experimental and theoretical investigation of optical properties of colloidal photonic crystal films", *J. Optoelectron. Adv. Mater*, Vol. **10**, No. 12, p. 3165 3168 (2008)

- [12] K. Tauer, R. Deckwer, I. Kühn, and C. Schellenberg, "A comprehensive experimental study of surfactant-free emulsion polymerization of styrene," *Colloid Polym Sci*, vol. **277**, no. 7, (1999)
- [13] J. R. Oh, J. H. Moon, S. Yoon, C. R. Park, and Y. R. Do, "Fabrication of wafer-scale polystyrene photonic crystal multilayers via the layer-by-layer scooping transfer technique," *J Mater Chem*, vol. **21**, no. 37, (2011)
- [14] D. H. Beckett, S. J. Cox, J. M. Generowicz, B. P. Hiett, M. Molinari and K. S. Thomas, "Application of finite element methods to photonic crystal modelling," The Fourth International Conference on Computation in Electromagnetics, CEM 2002 (Ref. No. 2002/063), Bournemouth, UK, (2002)
- [15] O. A. Castañeda-Uribe, J. C. Salcedo-Reyes, H. A. Méndez-Pinzón, and A. M. Pedroza-Rodríguez, "Fabrication and optical characterization of a high-quality fcc-opal-based photonic crystal grown by the vertical convective self-assembly method," *Univ Sci* (*Bogota*), vol. **15**, no. 2, (2010)
- [16] M. Li, X. Hu, Z. Ye, K.-M. Ho, J. Cao, and M. Miyawaki, "Perfectly matched layer absorption boundary condition in planewave based transfer-scattering matrix method for photonic crystal device simulation," *Opt Express*, vol. **16**, no. 15, (2008)
- [17] M. Inoue, K. Ohtaka, and S. Yanagawa, "Light scattering from macroscopic spherical bodies. II. Reflectivity of light and electromagnetic localized state in a periodic monolayer of dielectric spheres." *Phys. Rev. B* **25**, 689 (1982)
- [18] H. Miyazaki and K. Ohtaka, "Near-field images of a monolayer of periodically arrayed dielectric spheres." *Phys. Rev. B* **58**, 6920 (1998)
- [19] Y. Xu, "Electromagnetic scattering by an aggregate of spheres," *Appl Opt*, vol. **34**, no. 21, (1995)
- [20] B. V. R. Tata, R. G. Joshi, D. K. Gupta, J. Brijitta, and B. Raj, "Crystalline arrays of submicron-sized particles through colloidal route," *Curr Sci*, vol. **103**, no. 10, pp. 1175–1184, (2012)
- [21] V. N. Bogomolov *et al.*, "Photonic band gap in the visible range in a three-dimensional solid state lattice Rapid communication," *Appl Phys A Mater Sci Process*, vol. **63**, no. 6, (1996)

Raman Signal Enhancement of Molecules by Thin Colloidal Photonic Crystal Template

In this chapter, we present the Raman spectroscopic measurements of detection of molecules on a CPhC template by making use of the on-resonance excitation. The numerical simulations are presented to understand the E- field distribution and enhancement due to CPhC template.

5.1 Introduction

PhCs are extensively used in the field of detection by utilizing the tunable properties of structural colors [1], stopband/ photonic band gap [2],[3] and the frequency dependent E- field enhancement [4]. It is important to have increased light matter interaction for an efficient detection of molecules. The tunable stopband/ photonic band gap provides the route for increasing light matter interaction. Many refractive index sensors are based on the shift in the stopband position according to the change in the refractive index of the surrounding medium [5]. But in the case of SERS based detection platforms the E- field enhancement comes from the plasmonic substate is the major concern. In the case of colloidal photonic crystal (CPhC) templates, the E-field distribution and its enhancement at the on-resonance arises from the localized E-field at the void regions. CPhC offer flexibility in tuning the position of the stopband by changing the structural and material parameters which in turn helps to fine tune or choose the right excitation wavelength.

One of the methods to measure the E- field enhancement due to a PhC template, is by employing Raman spectroscopy. E- field enhancement is one of the mechanisms in which the

Raman signal enhancement occurs[6], which is also used in Surface Enhanced Raman spectroscopy (SERS) [7]. Employing PhC templates for Raman signal enhancement of analyte molecules are explored in few studies [8]- [10]. Qi. *et.al.* has investigated the effect of plasmonfree titania inverse opal PhC array in detecting the Raman signal enhancement [8]. It was shown that, by matching laser wavelength with band gap position, improves the detection sensitivity. However, a proper understanding of the enhancement of Raman signal due to PhC templates is still lacking.

Motivated by the above-mentioned studies, we investigate the effect of thin PSPhC template in the enhancement of Raman signal of some analyte molecules. This is to verify the simulation work reported in Chapter 4 on the E-field distribution on the PSPhC monolayer at different excitation wavelengths. At on-resonance wavelength, where the excitation wavelength falls within the stop band, the E- field is redistributed on the surface of the PSPhC in such a way that the maximum E- field is localized and enhanced at the void regions of the particle array [4]. Here, we experimentally verify it by carrying out the Raman spectroscopic studies on methylene blue (MB) dye, which is taken as a test molecule, on a bare glass substrate results are compared with a PSPhC monolayer template. Additionally, we perform EM simulations specifically at the excitation wavelength used in the experiments and compared it with the E-field distribution on a glass substrate as well as on the randomly distributed gold nanoparticles (AuNP) on a glass substrate. These results are reported in this chapter.

5.2 Experimental and simulation details

5.2.1 PSPhC monolayer template

The PS colloidal particles are synthesized using emulsion polymerization (chapter 2, section 2.2.1) and characterized for particle size (diameter, d=287 nm) and size polydispersity

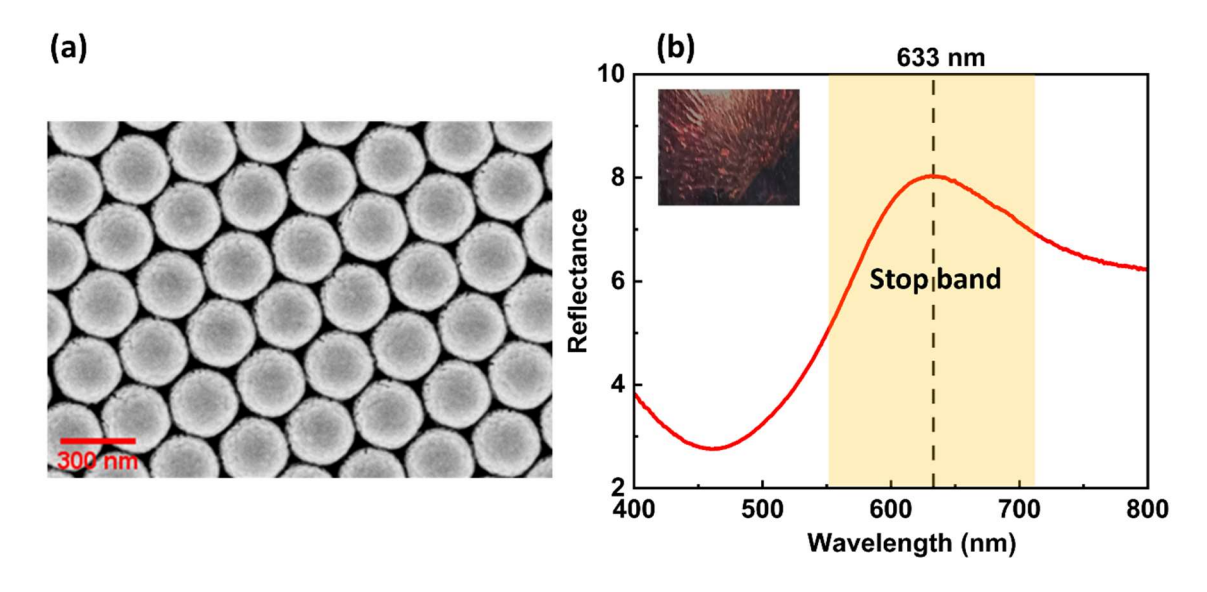


Fig. 5.1 (a) FESEM image of PSPhC monolayer showing the highly close-packed hexagonal array. **(b)** The reflectance spectrum of the fabricated PSPhC monolayer. The vertical dashed line indicates the excitation wavelength chosen for the Raman measurements which lies within the stopband (shown as shaded region) of the PSPhC monolayer. Inset shows the photographic image of red iridescence from the PSPhC monolayer for visible light.

(3%) using dynamic light scattering technique (DLS). The monolayer of PSPhC was fabricated using the technique described in chapter 2, section 2.3.3. The hexagonal ordering of the crystal is observed under SEM and it is shown in Fig. 5.1(a). The reflectance spectra of the PSPhC monolayer recorded using UV-Visible spectrometer is given in Fig. 5.1 (b) and shows the stop band with a peak centered around 629 nm (as expected from the numerical simulations (chapter 4, section 4.3.1,), which is also confirmed by observing red iridescence [see inset in Fig. 5.1 (b)] due to the Bragg diffraction by photonic crystalline order in the monolayer. The onresonance excitation wavelength (λ_{on-re}) used in the Raman spectroscopic studies is marked using a vertical dashed line which falls inside the stop band (see Fig. 5.1 (b)).

5.2.2 AuNP SERS substrate

To compare the Raman spectroscopic results with a SERS substrate, laser ablated AuNPs based substrate was used. AuNPs of diameter of 20 nm with a polydispersity of 9% were synthesized using femtosecond laser ablation of pure gold in water. This process employed a Ti-Sapphire laser of wavelength 800 nm, pulse duration of ~50 fs, and a repetition rate of 1 kHz [11]. The AuNPs are spherical in shape which is confirmed with the TEM image (Fig. 5.2(a)) and it indicates that they are individual particles without any aggregation. The suspension of these individual particles when dropped on the glass substrate is expected to spread in a random spatial configuration. Extinction spectra of the aqueous suspension of AuNPs are shown in Fig. 5.2 (b), indicating that the SPR peak of the AuNPs occurs at 528 nm.

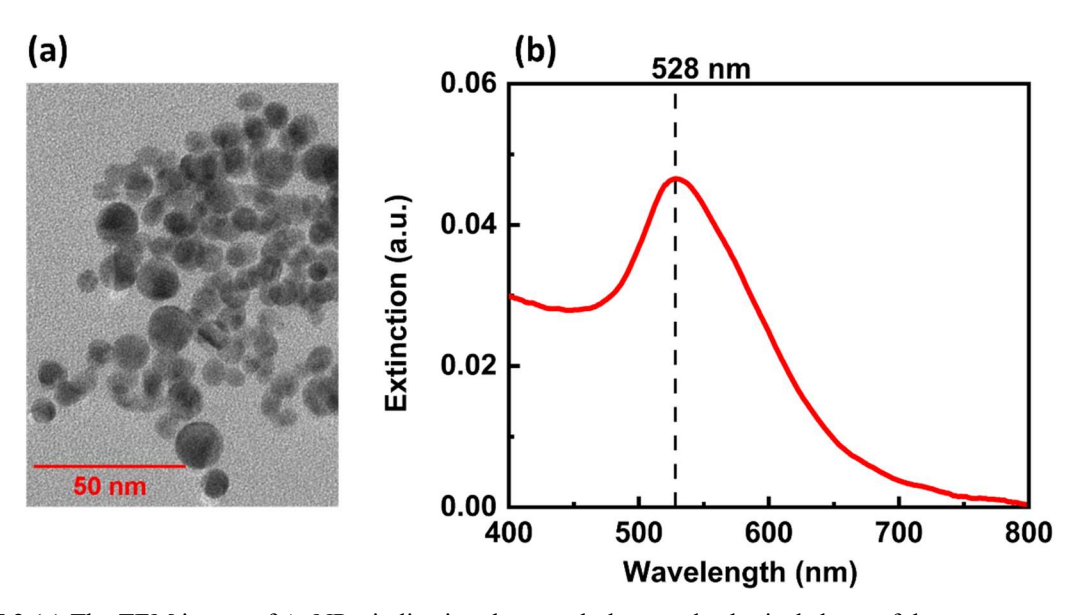


Fig. 5.2 (a) The TEM image of AuNPs, indicating the morphology and spherical shape of the non-aggregated particles. **(b)** Extinction spectra of AuNPs having SPR wavelength at 528 nm (dashed line).

5.2.3 Simulation details

Numerical simulation model explained in chapter 4, section 4.2 is used to simulate the E- field distribution at the excitation wavelength used in this study. To understand how a CPhC monolayer template helps enhance the SERS signal of the analyte molecules, FEM based electromagnetic simulations close to the experimental situation has been carried out using

COMSOL Multiphysics 5.6 software with wave optics module. The E- field distribution on the PSPhC monolayer is compared with that in a bare glass substrate by removing the PSPhC layer from the computational domain and with the randomly distributed AuNP by replacing the PhC layer. The schematic illustration of computational domains of a bare glass substrate, PSPhC monolayer and randomly distributed AuNPs are shown in Fig. 5.3. PSPhC monolayer consists of PS particles (with refractive index n_{PS} =1.59 and diameter d=287 nm) surrounded by air matrix (n_{air} =1) are assumed to have 2D-hexagonal order on a glass substrate (refractive index, n_g =1.56) as shown in Fig. 5.3(b). A Y-polarized plane wave is incident on the PSPhC monolayer/ bare glass substrate/ and AuNPs at normal incidence along the -ve Z-direction. PBCs are applied along the X- and Y-directions to simulate a 2D PhC array extending infinitely in the X-Y plane. PML are implemented at the top and bottom of the computational domain to

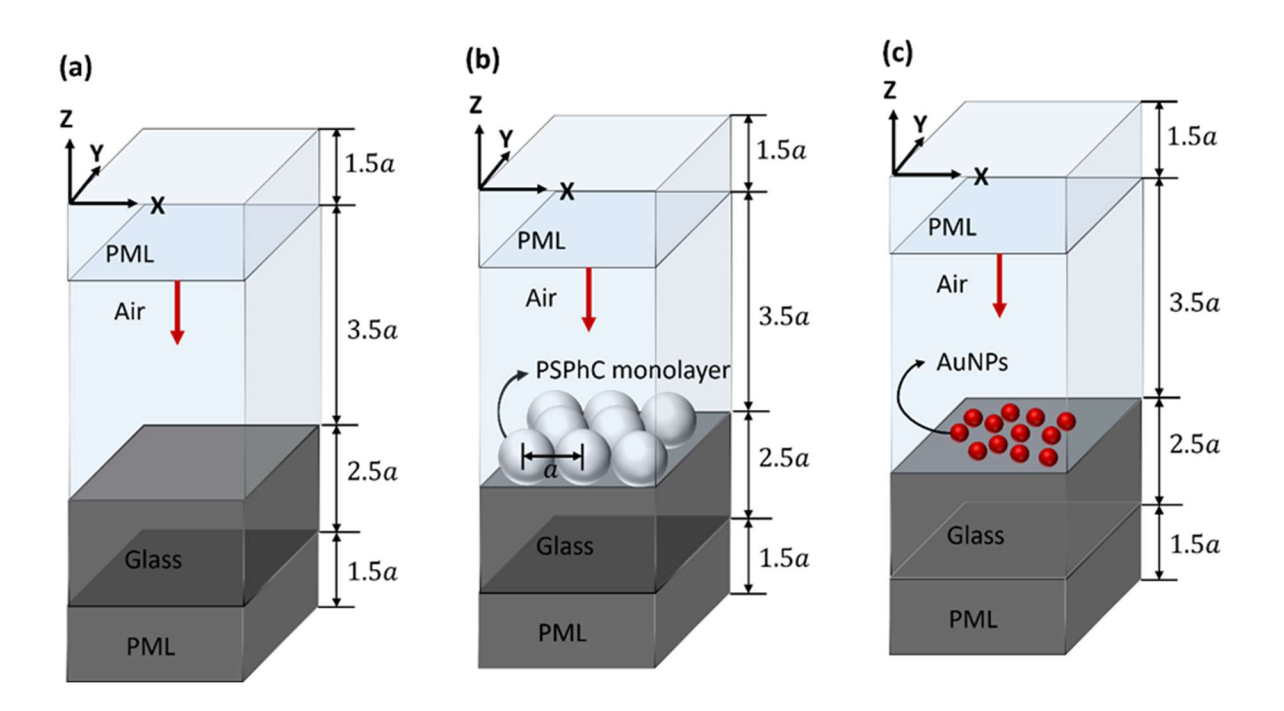


Fig. 5.3 The schematic illustration of the computational domains of (a) a bare glass substrate (b) PSPhC monolayer (c) randomly distributed AuNPs on a glass substrate.

absorb unwanted reflections from the non-physical boundaries [12]. The refractive index of the upper PML layer is chosen such a way that it matched that of the adjacent domain, which is air, while the refractive index of the lower PML layer is matched with that of the substrate (glass) of the PhC layer. The source plane is positioned below the upper PML layer. Highly refined mesh elements with a size of approximately 0.5 nm have been employed on the AuNP to ensure an optimal grid resolution for accurately capturing the E- field distribution from the AuNP surface.

5.3 Results and discussion

5.3.1 Raman spectroscopic measurements

To understand the effect of PSPhC monolayer on the enhancement of Raman signal, a systematic study with methylene blue (MB) dye has been carried out. Figure 5.4 provides a comparison of Raman spectra of MB molecules of concentration 5 mM on a bare glass substrate Vs. on a PSPhC monolayer template. From Fig. 5.4 it can be inferred that there is a significant enhancement in the Raman signal of MB detected on PSPhC monolayer template compared to the bare glass substrate. The percentage enhancement (%E) is calculated for two major peaks 448 cm⁻¹ (peak 1) and 1623 cm⁻¹ (peak 2) using the formula;

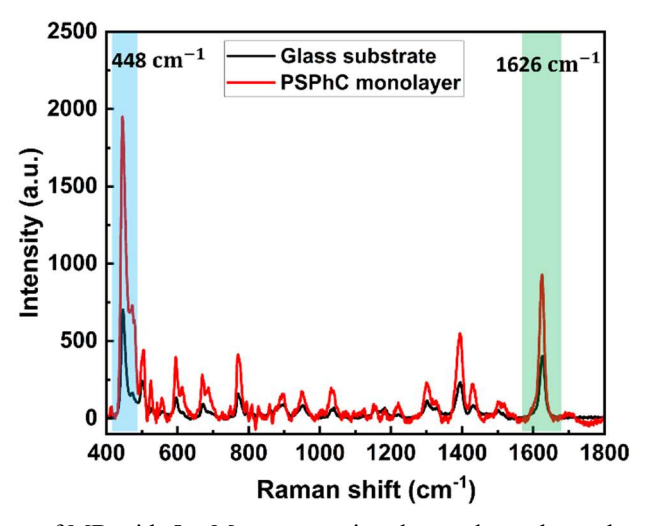


Fig. 5.4 Raman spectra of MB with 5 mM concentration detected on a bare glass substrate (black line) Vs. on PSPhC monolayer template (red line).

$$\%E = \frac{I_{PSPhC} - I_{Glass}}{I_{Glass}}$$

where, I_{PSPhC} and I_{Glass} are the Raman peak intensity of the respective peak under consideration detected on PSPhC monolayer template and bare glass substrate respectively. The %E for peak 1 and peak 2 is 186 % and 136% respectively.

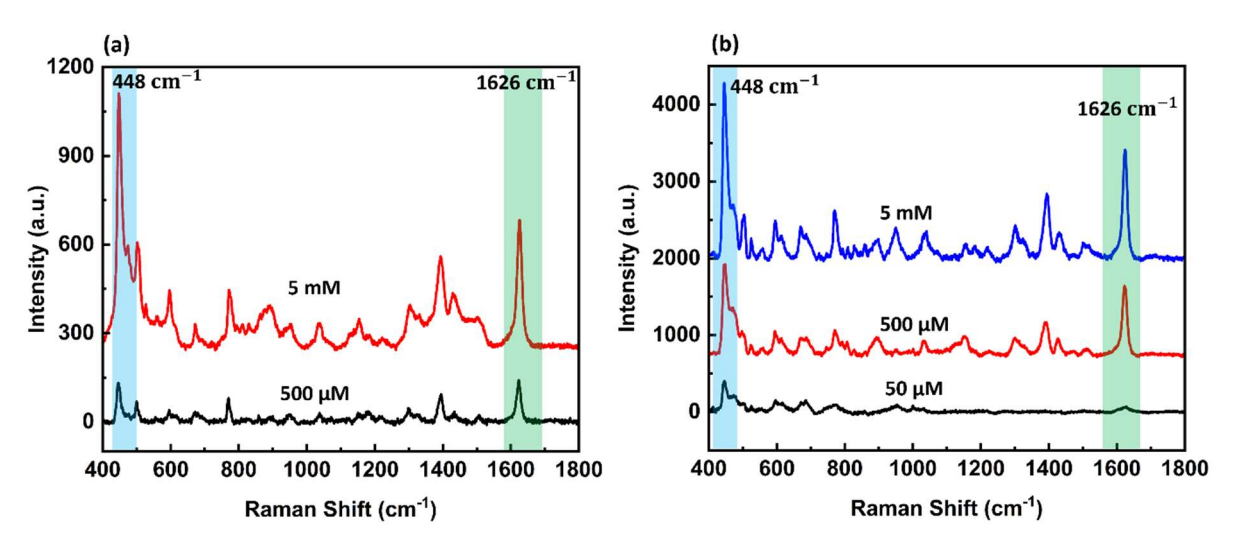


Fig. 5.5 Raman spectral measurements of different concentrations of MB on a (a) bare glass substrate. The lowest concentration of MB detected on this substrate is 500 μ M (b) PSPhC monolayer template. The lowest concentration of MB detected on this template is 50 μ M

Furthermore, the lowest concentration detected for a bare glass substrate and PSPhC monolayer template are compared by recording the Raman spectra of varying concentration of MB on respective templates and it is presented in Fig. 5.5. On the bare glass substrate, the lowest concentration detected is 500 µM (Fig. 5.5(a)) whereas, on PSPhC monolayer template it is 50 µM (Fig. 5.5(b)) The lowering in the detection concentration of MB while using PSPhC monolayer can be attributed to the E- field enhancement at on-resonance excitation condition (excitation wavelength within the stopband of PSPhC monolayer) which is discussed in detail in chapter 4, section 4.3.2. To further compare the enhancement in the PSPhC monolayer template with a SERS template, randomly distributed AuNPs on a glass substrate has been considered. Figure 5.6 shows the lowest concentration detected for MB on the AuNPs-glass

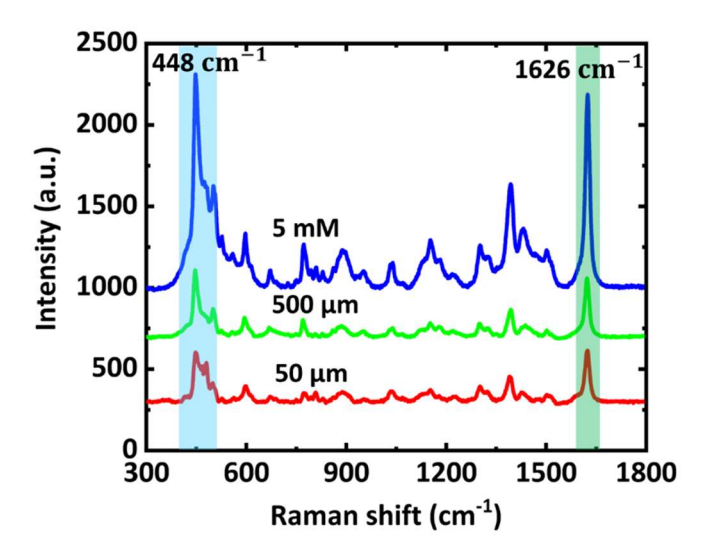


Fig. 5.6 Raman spectral measurements of different concentrations of MB on AuNPs- glass SERS substrate. The lowest concentration of MB detected on this substrate is $50 \, \mu M$

substrate. The lowest concentration detected on the AuNPs- glass substrate is $50 \mu M$ which is same as that of the lowest concentration detected on the PSPhC monolayer template.

5.3.2 Electromagnetic simulations

The normalized E- field distribution on a bare glass substrate, PSPhC monolayer template, and AuNP on a glass substrate are simulated. A quantitative comparison of the E-field enhancement on each substrate is performed at an incident wavelength of 633 nm, consistent with the wavelength used in our SERS studies. The contour plots of the E-field distribution in these substrates are given in Fig. 5.7. The E- field values presented here are the

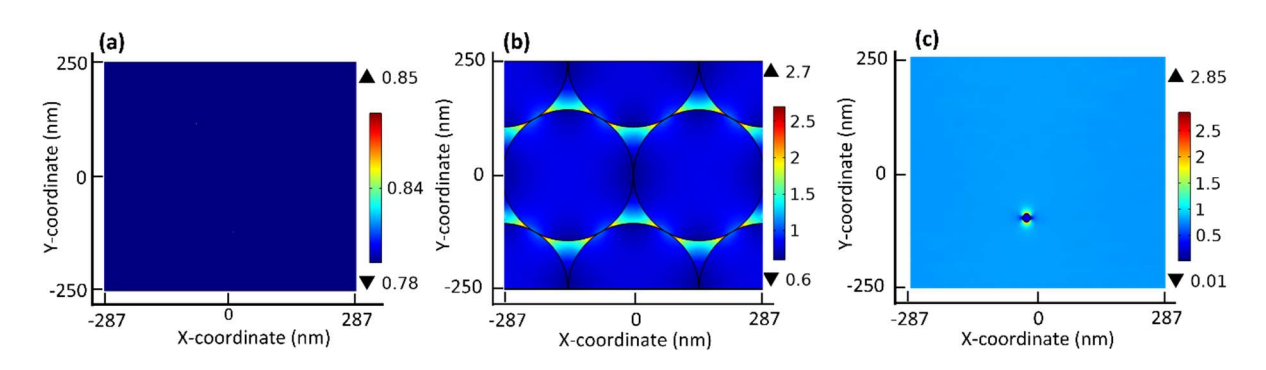


Fig. 5.7 The contour plots of normalised E- field distribution on a (a) bare glass substrate (b) PSPhC monolayer on glass substrate, and (c) a AuNP on glass substrate.

relative E-field values w.r.t the incident E-field ($|E/E_{inc}|$). The uniform glass substrate shows a uniform E- field distribution with a maximum E- field value, $|E_{max}/E_{inc}|=0.85$ (Fig. 5.7(a)). In the PSPhC monolayer, the E- field is redistributed on the surface of the monolayer with ($|E_{max}/E_{inc}|=2.7$, and is localized in the wedge region of the two touching particles (inside the void) as predicted by the simulations for an on-resonance excitation wavelength in chapter 4, section 4.3.2. The E-field on a AuNP placed on a glass substrate shows maximum field magnitude on the surface of the particle creating hotspots with $|E_{max}/E_{inc}|=2.85$, which is almost same as that on the PSPhC monolayer. The quantitative analysis of the E-field distribution is presented in Fig. 5.8 by plotting the E-field values along the line, y=-8.5x+16.5a, on a bare glass substrate, PSPhC monolayer and on a AuNP -glass substrate. The figures, Fig. 5.8 (i), (ii), and (iii) shows the line (white line) along which the E-field values are calculated for a glass substrate, PSPhC monolayer and AuNP- glass substrate respectively. The

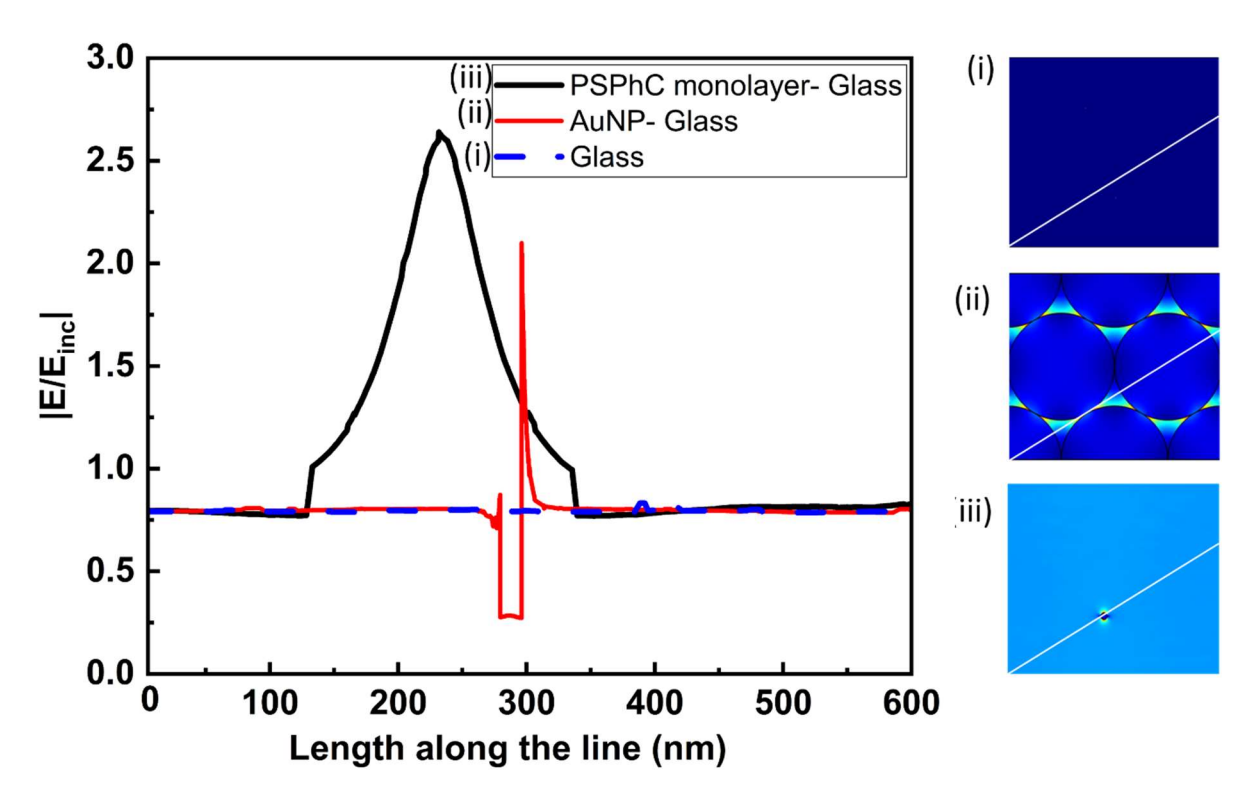


Fig. 5.8 The line graph of the normalized E-field distributions in glass substrate, AuNP on a glass substrate and PSPhC monolayer on a glass substrate along the line (eq. y = -8.5x + 16.5a) on (i) bare glass substrate (ii) PSPhC monolayer, and (ii) AuNP on glass substrate.

line graph on the glass substrate (blue spheres) shows a straight line parallel to the X-axis at E-field value of 0.8, showing the uniform field distribution.

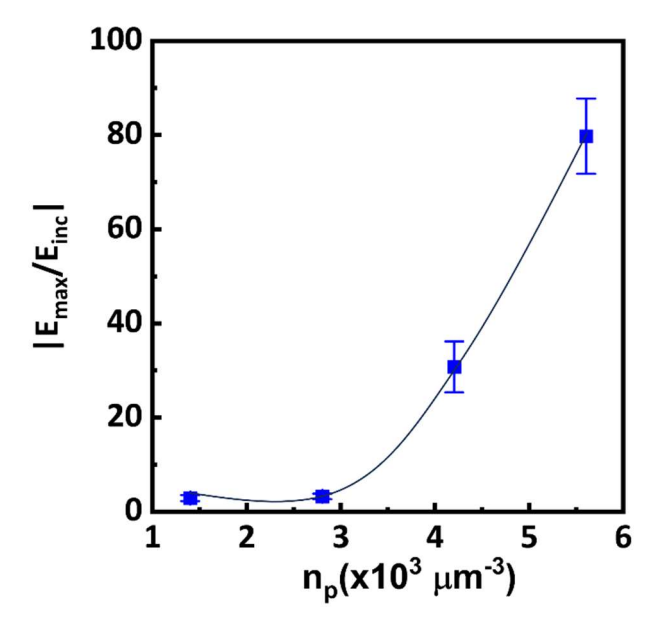


Fig. 5.9 The maximum E- field enhancement Vs. number density, np of AuNPs on a glass substrate

In the realistic scenario there will be several AuNPs on the glass substrate which are randomly distributed. This has been simulated assuming the particles are having a random distribution and they are non-touching. Figure 5.9 gives the plot of maximum E- field value for different values of number density (number of particles in unit volume) of AuNPs. It has been found that the E-field value increases as the number of particles increases in a fixed volume by coupling the plasmonic resonances of more than one particle and creating high intensity hotspots in between the particles. Combining the plasmonic resonances and the E- field enhancement in the PSPhC monolayer can enhance the E-field further and improve the detection limit to lower concentrations of the analyte. The detailed investigations of the combined effect of AuNPs on PSPhC monolayer template on the detection of different analyte molecules are discussed in the next chapter (Chapter 6).

5.4 Summary

The study on the effect of thin PSPhCs on the Raman signal enhancement is systematically carried out. Monolayer of PSPhC is fabricated though air-water self-assembly method and characterized using SEM for the structural ordering, and UV-Visble spectroscopy for the Reflectance spectrum. An on-resonance excitation wavelength of 633 nm is chosen for the Raman spectroscopic studies. MB dye molecules are used for the Raman studies. The Raman signal intensity of MB on a bare glass substrate and on a PSPhC template are compared and percentage enhancement (%E) is calculated. The %E for the peak 448 cm⁻¹ and 1626 cm⁻¹ are calculated as 186 % and 136% respectively for the PSPhC template compared to the bare glass substrate. The lowest concentration detected on the PSPhC monolayer template is 50 µM whereas on the bare glass substrate is 500 µM. The lowest concentration of MB detected on the PSPhC monolayer template is same as that detected on the randomly distributed AuNPs on a glass substrate. The EM simulations close to the experimental conditions are performed for the bare glass substrate, PSPhC monolayer and AuNP placed on a glass substrate. The relative E- field ($|E/E_{inc}|$) is plotted to understand the E- field distribution and enhancement in these templates. For the uniform glass substrate, a uniform E- field distribution is observed whereas the E- field is redistributed on the PSPhC monolayer in such a way that the maximum E-field is localized and enhanced in the wedge regions of the voids at on-resonance excitation. The analyte molecules when experience the higher E- field exhibit enhanced Raman signal intensity, hence favoring the detection of analyte molecules at lower concentrations. The AuNP shows plasmonic resonance at light excitation and hence forming hotspots on the surface of the AuNP on the opposite poles along the E-field polarization direction. The maximum E-field value on the AuNP hotspot is almost same as the maximum E-field value on the PSPhC monolayer. Hence, these investigations suggest that PSPhC template can replace the randomly

distributed AuNPs based SERS substrate. The effect of combining the plasmonic resonance and photonic crystal modes are investigated in detail in the next chapter (Chapter 6).

References

- [1] H. S. Lee, T. S. Shim, H. Hwang, S. M. Yang, and S. H. Kim, "Colloidal photonic crystals toward structural color palettes for security materials," *Chemistry of Materials*, vol. 25, no. 13, 2013.
- [2] Y. A. Vlasov, V. Astratov, O. Karimov, A. Kaplyanskii, V. Bogomolov, and A. Prokofiev, "Existence of a photonic pseudogap for visible light in synthetic opals," *Phys Rev B Condens Matter Mater Phys*, vol. 55, no. 20, 1997.
- [3] R. Biswas, M. Sigalas, G. Subramania, C. Soukoulis, and K. Ho, "Photonic band gaps of porous solids," *Phys Rev B Condens Matter Mater Phys*, vol. 61, no. 7, 2000.
- [4] P. Sahani, S. Narayanan, B. V. R. Tata, and S. V. Rao, "Numerical simulation of internal electric field distribution in colloidal photonic crystal thin films," *Opt Commun*, vol. 528, 2023.
- [5] J. Hou, M. Li, and Y. Song, "Recent advances in colloidal photonic crystal sensors: Materials, structures and analysis methods," *Nano Today*, vol. 22. 2018.
- [6] S. S. B. Moram, C. Byram, and V. R. Soma, "Gold-nanoparticle- and nanostar-loaded paper-based SERS substrates for sensing nanogram-level Picric acid with a portable Raman spectrometer," *Bulletin of Materials Science*, vol. 43, no. 1, 2020.
- [7] C. Byram, S. S. B. Moram, and V. R. Soma, "SERS based detection of multiple analytes from dye/explosive mixtures using picosecond laser fabricated gold nanoparticles and nanostructures," *Analyst*, vol. 144, no. 7, 2019.
- [8] D. Qi, L. Lu, L. Wang, and J. Zhang, "Improved SERS sensitivity on plasmon-free TiO2 photonic microarray by enhancing light-matter coupling," *J Am Chem Soc*, vol. 136, no. 28, 2014.
- [9] X. Zhu, W. Yan, P. Uhd Jepsen, O. Hansen, N. Asger Mortensen, and S. Xiao, "Experimental observation of plasmons in a graphene monolayer resting on a two-dimensional subwavelength silicon grating," *Appl Phys Lett*, vol. 102, no. 13, 2013.
- [10] I. Alessandri, "Enhancing raman scattering without plasmons: Unprecedented sensitivity achieved by TiO2 shell-based resonators," *J Am Chem Soc*, vol. 135, no. 15, 2013.

- [11] R. Beeram, D. Banerjee, L. M. Narlagiri, and V. R. Soma, "Machine learning for rapid quantification of trace analyte molecules using SERS and flexible plasmonic paper substrates," *Analytical Methods*, 2022.
- [12] M. Li, X. Hu, Z. Ye, K.-M. Ho, J. Cao, and M. Miyawaki, "Perfectly matched layer absorption boundary condition in planewave based transfer-scattering matrix method for photonic crystal device simulation," *Opt Express*, vol. 16, no. 15, 2008.

Thin Colloidal Photonic Crystal Template Decorated with Gold Nanoparticles for SERS Detection

In the realm of advanced analytical techniques, Surface-Enhanced Raman Spectroscopy (SERS) stands out as a powerful tool for detecting and characterizing molecules at very low concentrations. As researchers strive to enhance the sensitivity and efficiency of SERS-based detection methods, the utilization of PhC templates has emerged as a promising avenue. In the previous chapter we have explored the effect of thin CPhC templates in the enhancement of Raman signal of the analyte molecules. In this chapter we delve into the exploration of these thin CPhC templates combined with gold plasmonic NPs for SERS detection.

6.1 Introduction

The CPhCs can be decorated with different size and shape plasmonic NPs enabling them to serve as versatile SERS substrates, hence are investigated with considerable interest and can serve as templates for sensing applications. Plasmonic NPs and nanostructured materials have traditionally been popular choices as SERS substrates for sensing applications. PhC template-based detection platforms have sparked great interest because of their unique properties of photonic band gap (PBG), stop band, and frequency-dependent internal E- field distribution [1-4]. It provides not only good distribution of plasmonic NPs on its surface but also the internal E- field enhancement at the wedge region formed by two touching colloidal particles of a closed-packed structure of PhC (Fig. 4.3 (a), Chapter 4) contributes to significant enhancement of Raman intensity [1], [5], [6]. Various studies have been reported on the

detection of different molecules using different combinations of PhCs and plasmonic nanostructures. Tsvetkov et al. (2013) reported the detection of Rhodamine 6G on the surface of the Silica-opal gold nanorod (GNR) substrate. They have investigated the optimal opal PhC thickness and gold nanorod deposition density for the maximal SERS effect [8]. They have explored the colloidal crystalline array as a good template for the plasmonic NPs. Colloidal crystal arrays with deposited plasmonic nanofilms were investigated as effective SERS substrates in different studies[9], [10]. The plasmonic nano films form U-shaped and V-shaped dips inside the colloidal array and generate hotspots at these sharp edges, enhancing the Raman peak of the molecules in the vicinity. Yan et al. (2019) investigated the flexible SERS substrates based on cellulose PhC/ silver (AgNPs) using P-methyl thiophenol as the analyte, and they could detect to a concentration of 1 µM [45]. Mu et al. have proposed an opal and hydrogel inverse opal PhC beads as a 3D structure to improve Raman peaks from plasmonic staining and with the extra enhancement of local electromagnetic field at the band edge of the PhC employing a variety of biomolecules like mouse myoglobin (Mb) Cytochrome C (Cyt C), human hemoglobin (Hb) as analytes[4]. In another study, inverse opal PhC capillary tubes are employed to detect Creatinine to sub-molar detection limits [3].

While studies exist in the literature on templates based on colloidal particle arrays, detailed experimental investigations into on-resonance excitation for SERS studies, a property induced by the PhC structure, have been limited. Some studies have reported on monolayer colloidal particle arrays as templates, highlighting their ability to enhance the distribution and accessibility of hotspots created by plasmonic NPs or nanofilms [3], [10]. However, on-resonance excitation has been the primary focus in only a few of these studies [4], [11], where the emphasis was on combining plasmonic nanoparticles with bulk PhCs. In this chapter, the effect of the monolayer CPhC template on the Raman peak enhancement of certain dye molecules under on-resonance excitation was investigated. Along with the controlled

distribution of AuNPs, on-resonance excitation was explored to enhance the light-matter interaction through enhanced E-field intensity. In addition to achieving excellent control over the distribution of AuNPs, on-resonance excitation is investigated to enhance light-matter interaction through enhanced E-field intensity. FEM based electromagnetic simulations using COMSOL Multiphysics with the wave optics module were also performed on CPhC templates to analyze the internal E-field distribution and identify potential hotspots for enhanced SERS signals. These simulation findings qualitatively complement the experimental results reported in this study.

6.2 Experimental details

6.2.1 PSPhC monolayer SERS template

The monolayer of polystyrene colloidal photonic crystal (PSPhC) was fabricated using the technique described in chapter 2, section 2.3.3. To produce SERS-active templates, a 20 μl volume of the aqueous suspension of AuNPs is drop-casted on the surface of the PSPhC monolayer (Fig. 6.1). AuNPs of diameter of 20 nm with a polydispersity of 9% were synthesized using femtosecond laser ablation of pure gold in water with a Ti-Sapphire laser of wavelength 800 nm, pulse duration of ~50 fs, and a repetition rate of 1 kHz [12]. SERS active PSPhC monolayer -AuNPs template was fabricated by drop casting AuNPs on the PSPhC monolayer. Figure 6.2(b) SEM shows the hexagonal order of PS particles after drop-casting AuNPs. The comparison of Fig. 6.2(a) and (b) shows that the AuNPs are trapped inside the

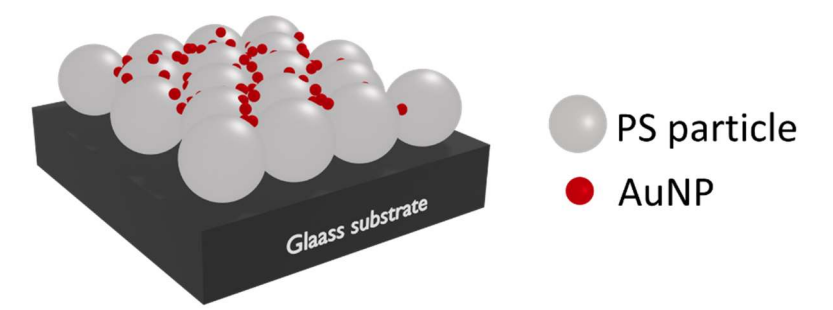


Fig. 6.1. The schematic representation of SERS active PSPhC monolayer -AuNPs template created by drop casting AuNPs on the PSPhC monolayer template and drying it.

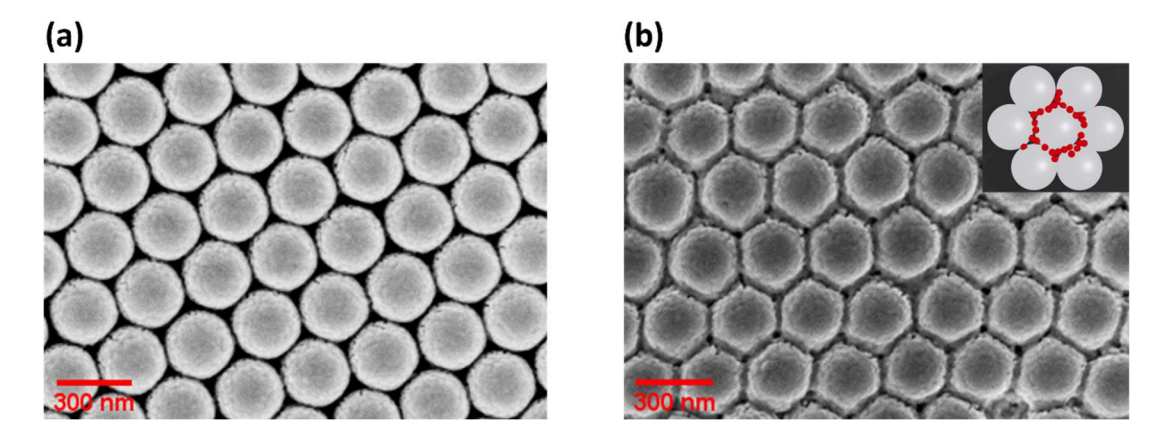


Fig. 6.2 (a) SEM image of PSPhC monolayer showing the highly close-packed hexagonal array. **(b)** SEM image of the drop casted AuNPs on the PSPhC monolayer showing the AuNPs trapped inside the voids of the PS spheres arranged in hexagonal array. The inset shows a schematic representation of AuNPs (red-colored tiny spheres) trapped inside the hexagonal array of PS colloidal particles (white spheres).

interstitial spaces (referred to as voids) of the hexagonal array of the PS colloidal particles. The inset of Fig. 6.2(b) is the schematic representation of AuNPs (red-colored spheres) trapped in the interstitial spaces of the PS colloidal particle array shown as white-colored spheres.

6.2.2 UV-Visible spectroscopic studies

UV-Visible spectroscopic studies using a JASCO V-670 Spectrophotometer have been carried out on PSPhC monolayer and AuNPs. The UV-Vis reflectance spectrum of the PSPhC monolayer shows the stop band with a peak centered around 629 nm (Fig. 6.3), which is also confirmed by observing red iridescence (inset in Fig. 6.3) due to Bragg diffraction of photonic crystalline order in the monolayer. Extinction spectra of the aqueous suspension of AuNPs are shown as the green line in Fig. 6.3, and notice that surface plasmon resonance (SPR) of AuNPs occurring at 528 nm. An excitation wavelength of 633 nm, which is clearly within the stop band of PSPhC monolayer (on-resonance excitation), is employed for the SERS studies. The on- resonance excitation wavelength position is shown in Fig. 6.3, as the red colour dashed line. We have shown using our simulations in Chapter 4, that under on-resonance condition, PSPhC monolayer enhances the E- field significantly at the void regions.

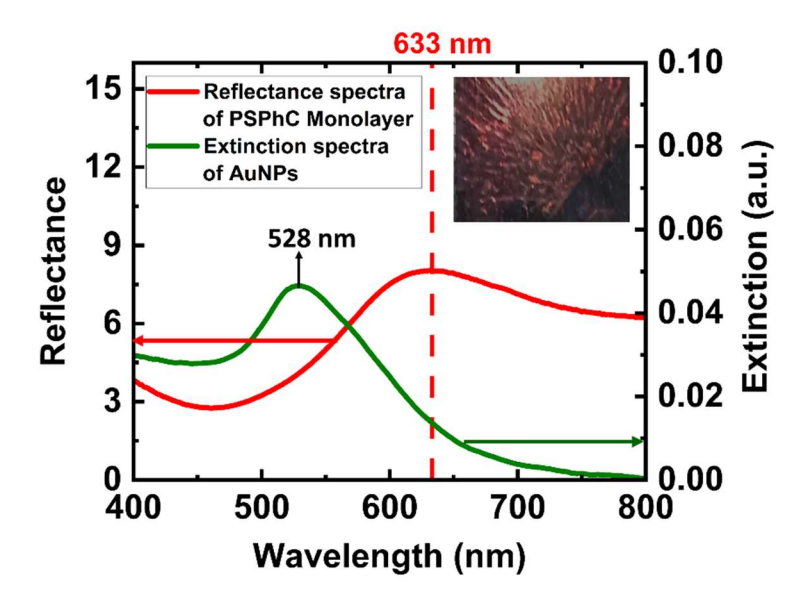


Fig. 6.3 The reflectance spectrum of the fabricated PSPhC monolayer (red line) and extinction spectra of AuNPs (green) having SPR wavelength at 528 nm (green line). The red colour dashed line indicates the excitation wavelength chosen for the Raman spectroscopy which lies inside the stopband of the PSPhC monolayer. Inset shows the photographic image of red iridescence from the PSPhC monolayer for visible light.

6.2.3 Surface enhanced Raman spectroscopic studies

The Raman spectroscopic measurements of the analyte molecules are recorded on Horiba LabRam Raman Spectrometer with the microscope objective of magnification of 50X and a numerical aperture of 0.5 with reflection geometry. The He-Ne laser source has been chosen with an excitation wavelength of 633 nm, which lies inside the stop band of the PSPhC monolayer and outside the extinction band of the AuNPs and has a beam diameter of 1.54 µm on the sample. The laser power is tunable from 0.002 mW to 20 mW. We have used 10% of the laser power (2 mW) with data acquisition time of 5s. All these parameters are kept constant during all the measurements. A plane glass substrate (glass slide) which is pre-cleaned using acetone, is chosen as the base substrate for the Raman spectroscopic studies. All the dye molecules used in this study are diluted in methanol. All the SERS spectra presented in the manuscript are the average of 12 spectra recorded at 12 different positions on the SERS substrate. The pre-processing of the Raman spectroscopic data is carried out using OriginPro

2018 software. Baseline correction was carried out using the Adjacent-Averaging smoothing method, and the spectra were smoothened using the Savitzky-Golay method.

6.2.4 Simulation details

To gain insights into how the SERS signal of analyte molecules is enhanced by a PSPhC monolayer template, further EM simulations were conducted closely mimicking the experimental conditions using COMSOL Multiphysics 5.6 software with the wave optics module. The schematic of the computation domain for PSPhC monolayer film is shown in Fig. 6.4(a). PSPhC monolayer film consists of PS particles (with refractive index n_{PS} =1.59 and diameter d=287 nm) surrounded by air -matrix (n_{air} =1) are assumed to have 2D-hexagonal

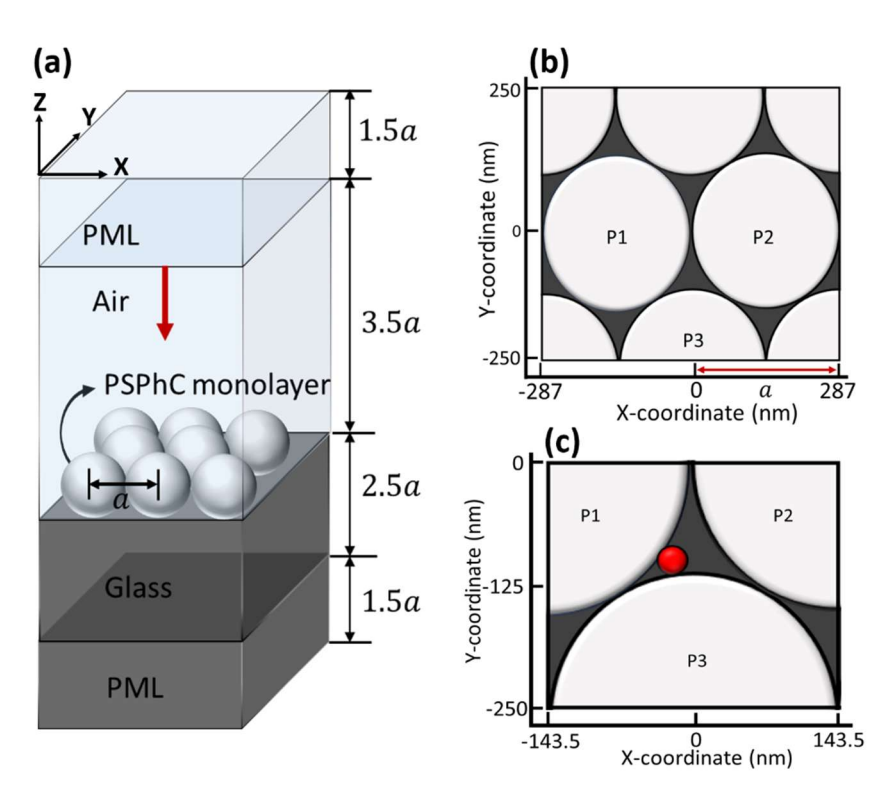


Fig. 6.4(a) Schematic representation of the computational domain of PSPhC monolayer on a glass substrate. Direction of incident light is shown as -ve Z- direction and perpendicular to the X-Y plane of the PSPhC monolayer indicated by red color arrow. **(b)** The top view of the PSPhC monolayer with close-packed hexagonal array of PS colloidal particles placed on a glass substrate at z=0. P1, P2 and P3 are the PS particles chosen to represent a void region under touching configuration. **(c)** Schematic of magnified wedge region formed by PS particles P1, P2 and P3 of the PSPhC monolayer with a AuNP which is shown in red colour.

order on a glass substrate (refractive index, $n_g = 1.56$) as shown in Fig. 6.4(a). A Y-polarized plane wave is incident on the PSPhC monolayer film at normal incidence along the -ve Zdirection. PBCs have been applied along X- and Y- directions to simulate 2D PSPhC array extended infinitely in the X-Y plane. PML conditions are implemented on the top and bottom of the computational domain to absorb the unwanted reflections from non-physical boundaries [13]. The refractive index of the top PML layer is chosen such a way that it matched with the refractive index of the adjacent domain, which is air, and the bottom PML is matched with the refractive index of the glass substrate. The source plane is placed below the top PML layer. The top view of the PSPhC monolayer is shown in Fig. 6.4(b), indicating the close-packed hexagonal array of PS colloidal spheres with the lattice constant, a = 287 nm. The particles P1, P2, and P3 in Fig. 6.4 (b) is chosen to represent the void region under touching configuration. To investigate further enhancement in the E- field due to surface plasmons of metal NPs, EM simulations were conducted. AuNPs with a diameter of 20 nm were placed in the wedge regions (see Fig. 6.4(c)) formed by the PS colloidal particles (between P1 and P3) in a hexagonally close-packed arrangement. The AuNP is shown as a red sphere in Fig. 6.4(c). Extremely fine mesh elements with a size of approximately 0.5 nm were employed on the AuNP to ensure an optimal grid resolution for capturing the accurate E- field distribution from the AuNP surface.

6.3. Results and discussion

6.3.1. Surface enhanced Raman spectroscopic studies

Methylene blue (MB) dye has been employed as the analyte molecule for the case study to understand the effect of the PSPhC template on the SERS signal enhancement. The Raman spectrum of MB with a concentration of 5 mM is recorded on a plane glass substrate (glass slide) and is shown in Fig. 6.5(a). The major characteristic Raman peaks of MB are 448 cm⁻¹(peak1) and 1626cm⁻¹ (peak 2) [Fig. 6.5(a)], which are assigned to C-N-C skeletal

bending and C-C stretching [14]. The Raman spectra of MB (5mM) are recorded individually with two different SERS-active templates, shown in Fig. 6.5(b). In Fig. 6.5(b), the average spectra recorderd at 12 different positions on the SERS substrate and its standard deviation is shown. The first SERS active template that we have chosen is the drop casted AuNPs on a plain glass substrate (Glass -AuNPs), and the second one is the drop casted AuNPs on a PSPhC monolayer (PSPhC monolayer -AuNPs) fabricated on a plane glass substrate. The drop casted AuNPs are heat treated on a temperature-controllable hotplate to evaporate the water.

As shown in Fig. 6.5(b), the intensity of Raman peaks (peak1:448 cm⁻¹ and Peak2: 1626 cm⁻¹) increased significantly when the PSPhC monolayer template was used. The percentage enhancement (%E) of peak1 for the PSPhC monolayer template is calculated as 408%± 14.8% using the formula % $E = \frac{I_{PSPC-AuNP}-I_{AuNP}}{I_{AuNP}} \times 100$, where $I_{PSPC-AuNP}$ is the Raman peak intensity when PSPhC monolayer -AuNPs is used, and I_{AuNP} is the Raman peak intensity when the Glass -AuNPs template is used. For peak 2 the %E is calculated as 213%± 7.9%. This implies that the PSPhC template enhances the SERS peak of the analyte molecules significantly.

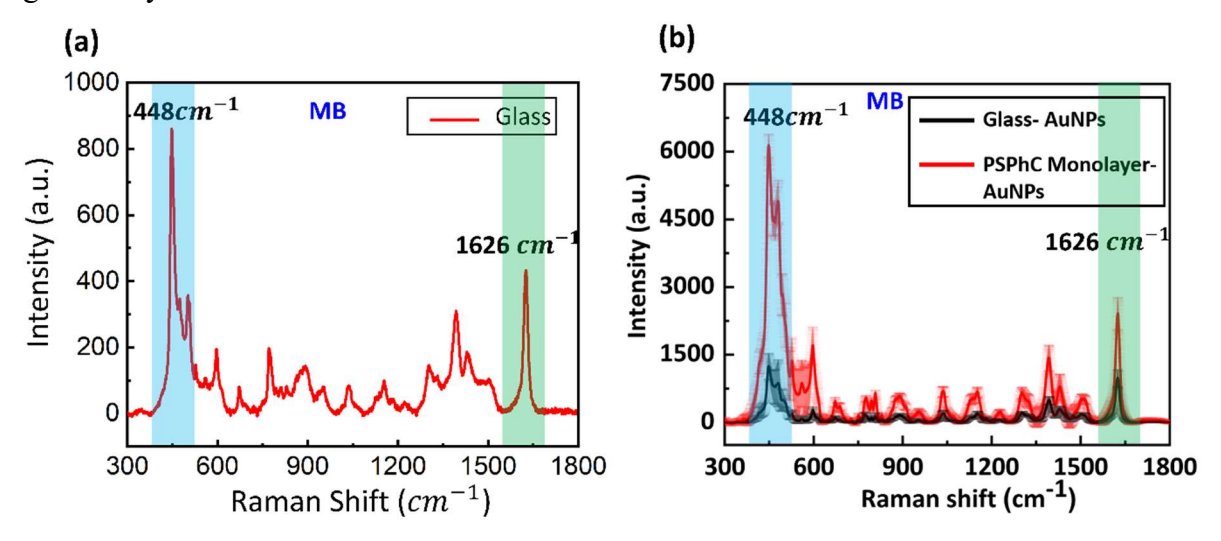


Fig. 6.5(a) Raman spectra of 5 mM concentration of methylene blue (MB) dye on a bare glass substrate and **(b)** Raman spectra of 5 mM concentration of MB molecules on different SERS substrates, viz. AuNPs drop casted on a bare glass plate and AuNPs drop casted on a PSPhC monolayer template.

A systematic study on the Raman spectra of MB dye molecules for different concentrations has been carried out on both Glass -AuNPs and PSPhC monolayer -AuNPs SERS active templates and is shown in Fig. 6.6. It is evident from Fig. 6.6(a) that the lowest concentration of the MB that can be detected using the Glass -AuNPs template is 50 μM while that of the fabricated PSPhC monolayer -AuNPs template is 500 nM (Fig. 6.6(a)). The concentration of the analyte molecules that could be detected with the PSPhC monolayer -AuNPs has improved by 100 times than the Glass -AuNPs for MB. These measurements demonstrate that PSPhC monolayer templates, as well as PSPhC decorated with AuNPs, significantly enhance Raman signals of analyte MB molecules, thus significantly improving the lowest concentration that can be detected for MB.To verify that the enhancement observed for MB molecules is also true for other molecules, we have investigated two more dye molecules viz., Rhodamine 6G (R6G) and Malachite Green (MG) with PSPhC monolayer as the template. The major characteristic peaks of R6G are 612 cm⁻¹, and 1504 cm⁻¹ which is

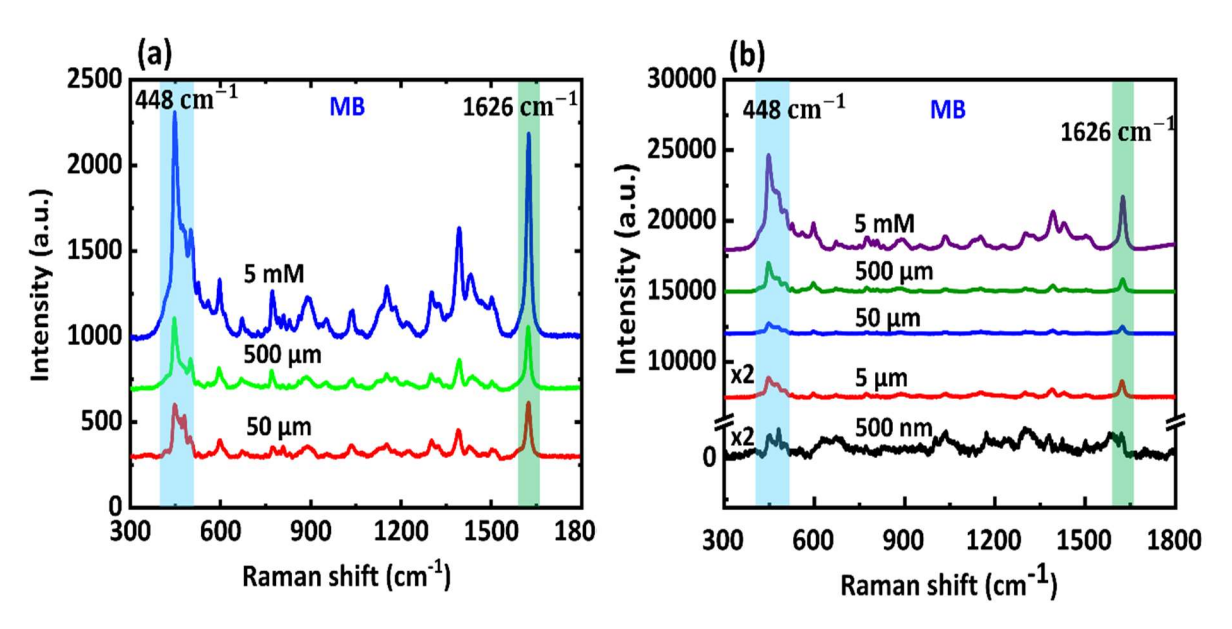


Fig. 6.6(a) Raman spectral measurements of different concentrations of MB on Glass -AuNPs SERS template. The lowest concentration of MB detected on this substrate is 50 μM. **(b)** Raman spectral measurements of different concentrations of MB on PSPhC monolayer -AuNPs template. The lowest concentration of MB detected on this substrate is 500 nM.

assigned to the C-C ring in-plane bending, and C-C stretching, respectively [15]. R6G is successfully detected on the PSPhC monolayer

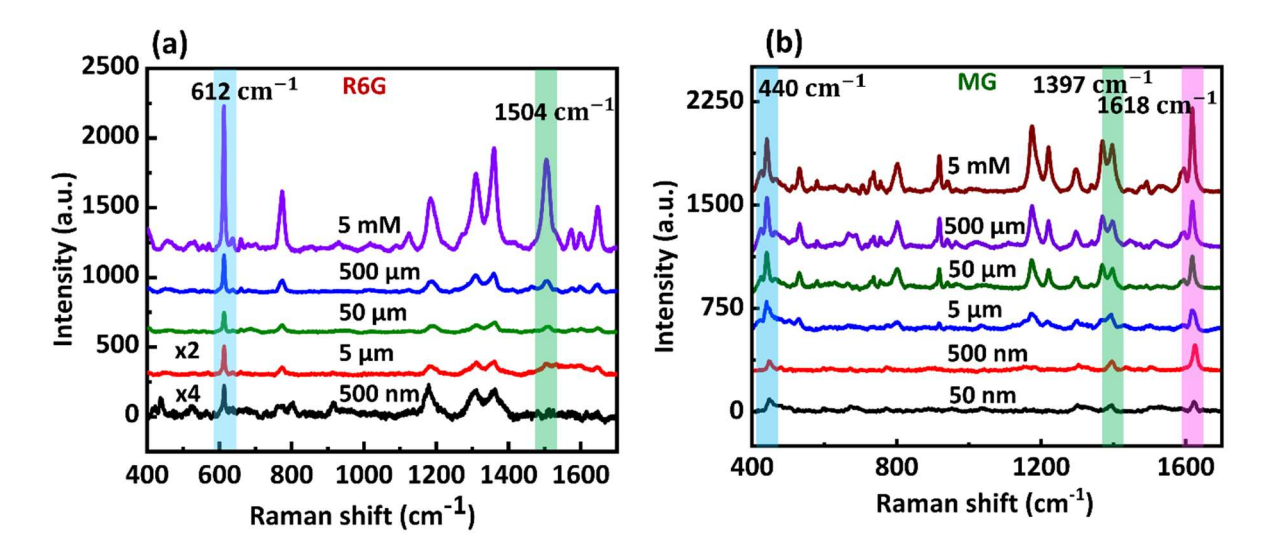


Fig. 6.7(a) Raman spectral measurements of different concentrations of R6G on PSPhC monolayer -AuNPs template. The lowest concentration of R6G detected on this substrate is 500 nM **(b)** Raman spectral measurements of different concentrations of MG on PSPhC monolayer -AuNPs template. The lowest concentration of MG detected on this substrate is 50 nM.

-AuNPs template with the lowest concentration of the molecules that could be detected is 500 nM, as shown in Fig. 6.7(a). The major characteristic Raman peaks of Malachite green (MG) are 440 cm⁻¹, 1174 cm⁻¹, and 1618 cm⁻¹ which are assigned to out-of-plane vibrations of phenyl- C-phenyl, in-plane vibrations of ring C-H and ring C-C stretching, respectively [16]. For MG, the lowest concentration of the molecules that could be detected is 50 nM, and the corresponding SERS spectra are shown in Fig. 6.7(b).

Figures 6.6 and 6.7 clearly show that the PSPhC monolayer template decorated with AuNPs significantly enhances the Raman signals of all the three analyte molecules, pushing the lowest concentration that could be detected to two orders in magnitude as compared to that detected by SERS with AuNPs alone. The corresponding linear dependencies of the SERS intensity (I) of the principal Raman mode at 448 cm⁻¹ (MB), 612 cm⁻¹ (R6G), and 1618 cm⁻¹

(MG) with respect to the analyte concentration (C) on PSPhC monolayer is illustrated in Fig. 6.8.

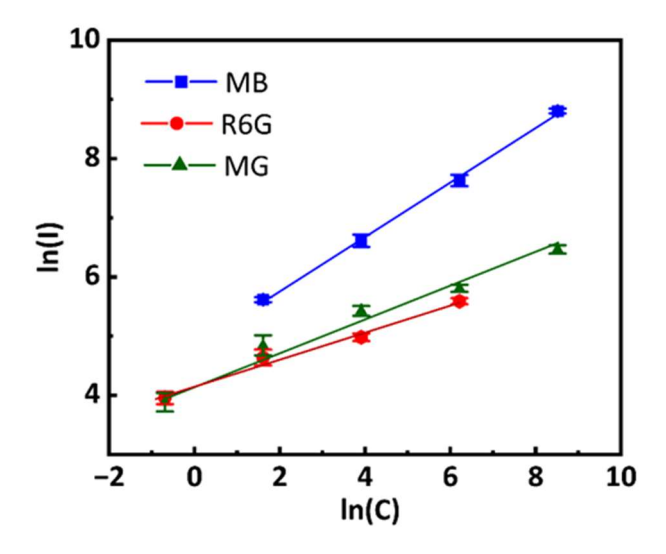


Fig. 6.8. Linear dependence of SERS intensity (I) vs. analyte concentration (C) for the principal modes of MB, R6G and MG molecule on PSPhC-AuNP template.

6.3.2. Electromagnetic simulations on PSPhC monolayer template

The normalized E- field distribution on the PSPhC monolayer templates (with and without AuNP) is simulated using the COMSOL Multiphysics software, and a quantitative comparison of the E- field enhancement on both PSPhC monolayer without AuNP and with AuNP is carried out at an incident wavelength of 633 nm, which was used as the wavelength of excitation in our SERS studies. The results are summarized in Fig. 6.9. Figure. 6.9 (a) gives the contour plot of the normalized E- field distribution on the PSPhC monolayer surface for an excitation wavelength of 633 nm, the on-resonance wavelength. The sampling plane is parallel to the X-Y plane (plane of periodicity) at z = a/2. Normalized E- field values have been calculated relative to the incident electric field ($|E/E_{inc}|$). Notice from Fig. 6.9(a) that the E-field gets redistributed due to the PSPhC monolayer. The EM simulations from chapter 4 showed that the redistribution of E- field in the thin CPhCs, results in enhanced E- field in the

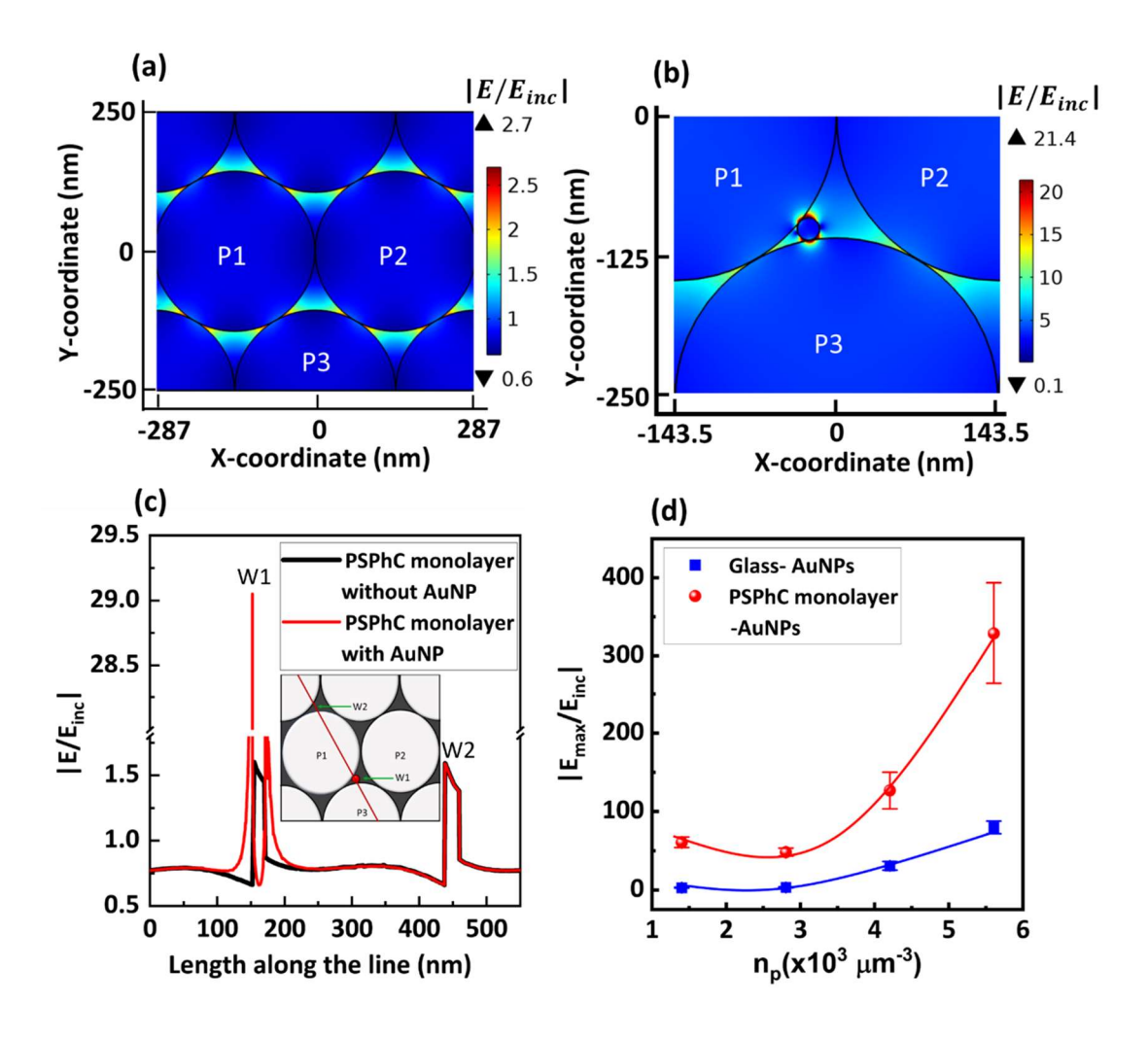


Fig. 6.9 Contour plot of normalized E- field distribution in (a) PSPhC monolayer upon excitation by 633 nm wavelength shows the redistribution of the electric field with E- field localized and enhanced at the wedge regions of the touching PS colloidal particles. (b) Normalized E- field distribution in the wedge region of PSPhC monolayer with AuNP, and E- field shows significant enhancement around AuNP. (c) The line plots of electric field along the line defined by y = -1.79x - 0.52a. The inset shows the line (red) passing through the wedge region, W1(with AuNP) and wedge region, W2 (without the AuNP). (d) The maximum E- field enhancement vs. number density, n_p of AuNPs on a glass substrate (blue) and void regions of PSPhC monolayer template (red). Simulations for different substrates were carried out under identical conditions of AuNP arrangement.

wedge regions (Fig. 6.9(a)) formed by the colloidal particles in touching configurations (the void region formed by the particles P1,P2, and P3). To understand the effect of a AuNP in the wedge region on the E- field enhancement, simulations by placing a AuNP of diameter 20 nm at W1 (see Fig. 6.4(c)) are performed. The E- field distribution is calculated and shown in Fig. 6.9(b). Indeed, we observed enhancement of E- field in the region of AuNP which is

determined to be about 21.4 times relative to the incident E- field (see Fig. 6.9(c)). The enhancement in E- field is determined by along the line defined by y = -1.79x - 0.52a (see inset of Fig. 6.9(c)) passing through two wedge regions denoted as W1 and W2 formed by PS spheres in touching configurations. In the case of the PSPhC monolayer without AuNP, two peaks in $|E/E_{inc}|$ with approximately equal strength are observed (black line Fig. 6.9(c)) corresponding to positions of W1 and W2 respectively. In the case of PSPhC monolayer with AuNP, the strength of E- field in the wedge region W1, where AuNP is placed, enhanced significantly, whereas the peak at W2 remained the same. The E- field maximum at wedge W1 with AuNP is determined to be about 21.4, whereas E- field maximum at W2 is 2.7. In a realistic scenario, there can be more than one AuNPs that sit in the void region. In order to understand the effect of more than one AuNP, we have performed EM simulations for varying number of AuNPs in the void regions of PSPhC monolayer template as well as that on glass substrate. We kept the volume occupied by AuNPs constant within the void region of PSPhC monolayer as well as on the glass substrate (in other words we varied the number density np AuNPs). In simulations we further assumed AuNPs to have non-touching random configurations. The enhancement in E- filed due to AuNPs in the void regions relative to that of AuNPs on the glass substrate is plotted as function of n_p and is shown as Fig. 6.9 (d). The number of AuNPs was varied from 1 to 4 to vary n_p . Standard deviation was calculated by averaging over ten different configurations of AuNPs. Notice that the enhancement in E- field occurs due a PSPhC template as compared to that of a glass substrate with the same n_p of AuNPs under similar arrangements.

To summarize, the EM simulation results on the PSPhC monolayer with and without AuNP particles have given insight on E- field distribution due to a PSPhC monolayer and that with AuNP placed in the wedge regions. Our simulations clearly indicate that when a monolayer of CPhC template at an on-resonance excitation wavelength of 633 nm, the

enhancement in the E- field occurs in wedge regions. These regions serve as hotspots. The Raman peak of analyte molecules recorded from these hotspots enhanced intensity significantly. Plasmonic NPs placed in these high E- field regions further enhance E- field leading to the observation of enhanced SERS signals from analyte molecules in a Raman scattering experiment. Enhancement of the SERS signals of the analyte molecules help in considerably lowering the detection limits of concentration of analytes, thus pushing the detection limits to ultra-low concentrations.

6.4. Summary

A systematic investigation of the effect of thin PSPhC templates with AuNPs for detecting dye molecules was conducted experimentally. Numerical simulations closely mimicking the experimental conditions were performed using COMSOL Multiphysics software with the wave optics module to understand the experimental findings. PSPhC monolayer templates with AuNPs are fabricated for the detection of analytes such as MB, R6G and MG by performing SERS measurements. MB is taken as the analyte molecule for the case study. Significant enhancement in the SERS peak of MB is observed by employing PSPhC monolayer with AuNPs as compared to the Glass -AuNPs substrate. As a result of enhancement, we could determine the lowest concentration MB to be as low as 500 nM, which is a hundred times lower than the lowest concentration detected when Glass -AuNPs are used as the substrate. PSPhC monolayer -AuNPs templates are also found to enhance the SERS signals from R6G and MG dyes. The lowest concentration detected are 500 nM and 50 nM for R6G and MG, respectively. The effect of PSPhC monolayer is well understood using the EM simulation of the normalized E- field distributions on the PSPhC monolayer template with and without AuNP. The E- field gets localized and enhanced at the wedge regions of the touching particles in the PSPhC monolayer array at an excitation wavelength of 633 nm, on-resonance wavelength. AuNPs sitting at the wedge regions experience enhanced E- fields resulting in

increased SERS signals, which in turn help in pushing the detection limits to significantly lower concentrations. Thus, the present results discussed in this chapter are expected to pave the way for novel PhC templates of different symmetries and lattice constants for developing improved molecular sensors. Enhanced SERS activity can be attained by modifying the PhC template in terms of its refractive index contrast and the excitation wavelength (on-resonance and off-resonance) down to picomolar detection limits which is the scope of future studies. In the previous chapter we showed that the PSPhC monolayer can serve as an alternative to the randomly distributed AuNPs based SERS substrate in enhancing the Raman signal of analyte molecules. In this Chapter we showed that, AuNPs together with PSPhC serve as a better template than just AuNPs in detecting the analyte molecules.

References

- [1] A. Y. Petrov and M. Eich, "Zero dispersion at small group velocities in photonic crystal waveguides," *Appl Phys Lett*, vol. 85, no. 21, 2004.
- [2] B. Liu *et al.*, "Ultrasensitive detection of protein with wide linear dynamic range based on core-shell SERS nanotags and photonic crystal beads," *ACS Sens*, vol. 2, no. 7, 2017.
- [3] X. Zhao, J. Xue, Z. Mu, Y. Huang, M. Lu, and Z. Gu, "Gold nanoparticle incorporated inverse opal photonic crystal capillaries for optofluidic surface enhanced Raman spectroscopy," *Biosens Bioelectron*, vol. 72, 2015.
- [4] Z. Mu, X. Zhao, Y. Huang, M. Lu, and Z. Gu, "Photonic Crystal Hydrogel Enhanced Plasmonic Staining for Multiplexed Protein Analysis," *Small*, vol. 11, no. 45, 2015.
- [5] P. Sahani, S. Narayanan, B. V. R. Tata, and S. V. Rao, "Numerical simulation of internal electric field distribution in colloidal photonic crystal thin films.
- [6] S. Narayanan, P. Sahani, J. Rathod, B. V. R. Tata, and S. V. Rao, "Thin Photonic Crystal Templates with Plasmonic Nanoparticles for Trace Molecule Detection using Surface Enhanced Raman Spectroscopy.", 30th DAE-BRNS National Laser Symposium (NLS-30), 519-524
- [7] D. Rout and R. Vijaya, "Role of Stopband and Localized Surface Plasmon Resonance in Raman Scattering from Metallo-Dielectric Photonic Crystals," *Plasmonics*, vol. 12, no. 5, pp. 1409–1416, Oct. 2017.

- [8] M. Y. Tsvetkov *et al.*, "SERS substrates formed by gold nanorods deposited on colloidal silica films," *Nanoscale Res Lett*, vol. 8, no. 1, 2013.
- [9] L. Baia, M. Baia, J. Popp, and S. Astilean, "Gold films deposited over regular arrays of polystyrene nanospheres as highly effective SERS substrates from visible to NIR," *Journal of Physical Chemistry B*, vol. 110, no. 47, 2006.
- [10] Z. Yi *et al.*, "Ordered array of Ag semi shells on different diameter monolayer polystyrene colloidal crystals: An ultrasensitive and reproducible SERS substrate," *Sci Rep*, vol. 6, 2016.
- [11] D. Qi, L. Lu, L. Wang, and J. Zhang, "Improved SERS sensitivity on plasmon-free TiO2 photonic microarray by enhancing light-matter coupling," *J Am Chem Soc*, vol. 136, no. 28, 2014.
- [12] R. Beeram, D. Banerjee, L. M. Narlagiri, and V. R. Soma, "Machine learning for rapid quantification of trace analyte molecules using SERS and flexible plasmonic paper substrates," *Analytical Methods*, 2022.
- [13] M. Li, X. Hu, Z. Ye, K.-M. Ho, J. Cao, and M. Miyawaki, "Perfectly matched layer absorption boundary condition in planewave based transfer-scattering matrix method for photonic crystal device simulation," *Opt Express*, vol. 16, no. 15, 2008.
- [14] G. N. Xiao and S. Q. Man, "Surface-enhanced Raman scattering of methylene blue adsorbed on cap-shaped silver nanoparticles," *Chem Phys Lett*, vol. 447, no. 4–6, 2007.
- [15] F. Zhong, Z. Wu, J. Guo, and D. Jia, "Porous silicon photonic crystals coated with Ag nanoparticles as efficient substrates for detecting trace explosives using SERS," *Nanomaterials*, vol. 8, no. 11, 2018.
- [16] X. Chen, T. H. D. Nguyen, L. Gu, and M. Lin, "Use of Standing Gold Nanorods for Detection of Malachite Green and Crystal Violet in Fish by SERS," *J Food Sci*, vol. 82, no. 7, 2017.

Summary and Future Work

This chapter covers the summary and conclusions from computational and experimental investigations, carried out on thin CPhCs. Important findings of the thesis as well as the scope for future studies are reported here.

7.1 Summary and Conclusions

In Chapter 1, an introduction to different types of photonic crystals (PhCs) and their theoretical and experimental background is presented. The focus is on colloidal photonic crystals (CPhCs), and their properties, including the photonic band structure. The stopband of a CPhC can be predicted using a modified form of Bragg's law, provided the particle size and effective refractive index are known. A comprehensive overview of the CPhC applications in variety of fields including display devices, biomedical applications, optical devices, sensors etc. are discussed. Among sensors, the PhC assisted SERS detection is the major focus. The existing literature on the SERS is presented in detail. The theoretical background of SERS technique and the enhancement mechanisms are also described chapter 1.

The experimental and simulation tools employed for carrying out the investigations on PhCs are discussed in detail in Chapter 2. The synthesis, and purification of colloidal particles and fabrication of different CPhC have been explained in chapter 2. The indigenous development of a laser light diffraction setup for the characterization of structural ordering and symmetry of the PhCs is presented in detail. The methodology to obtain structure factor from the measured diffraction/scattering patterns is described. The synthesized particles are characterized for particle size and size polydispersity using the dynamic light scattering (DLS)

technique. DLS measures the intensity- intensity autocorrelation function, $g^2(q,t)$ as function of delay time. The relation between $g^2(q,t)$ and electric field correlation function $g^1(q,t)$, which is related to intermediate scattering function f(q,t) is described in chapter 2. The methodology to find hydrodynamic diameter and size polydispersity from the measured $g^2(q,t)$ is also discussed. The stopband of the fabricated PhC is identified using the absorption/reflectance spectra recorded through UV-visible spectroscopy. The number density and volume fraction of the PhC fabricated in aqueous medium are also calculated from the Bragg peak obtained from the recorded UV-visible spectrum of CPhC samples. The ordering in thin CPhC films is characterized using laser diffraction set up and field emission scanning electron microscopy (FESEM). The fabricated PSPhCs have been investigated for the detection of Raman signal of analyte molecules using surface-enhanced Raman spectroscopy. The theory and the practice of Raman spectroscopy and SERS detection methods are discussed in chapter 2. The working principle of Raman spectrometer, used in the study is also explained in this section. Finally, the electromagnetic simulation details for the investigation to understand the E-field distributions in the PhC at different wavelengths have been presented. The finite element method (FEM) and the plane wave method (PWM) employed in our numerical simulations are also discussed in chapter 2.

Chapter 3 presents, the investigations of 2D PhCs made up of a square and hexagonal lattice of infinitely long dielectric rods using PWM and FEM methods. The band structure for both types of 2D PhCs is calculated through PWM using MIT Photonic band gap package. Details of the simulations have been presented. The reflection spectra of 2D PhCs with array size of 13x13 is presented. The bandgap is found to be saturated above this array size using simulations for varying the array size. The reflection spectra of 2D PhCs with and without defects are studied using FEM implementation of COMSOL Multiphysics software. The effect of doping in the defect is systematically studied for both type of 2D PhCs. Hole type defects

are created by removing the dielectric material from the defect i.e., refractive index of the defect is less than the refractive index of rest of the rods. Rod type of defects is created by adding dielectric material to the defect, where the refractive index of the material is higher than the refractive index of rest of the rods. In hole type defect, it is observed that the defect modes appear nearer to the dielectric band and moves towards the air band and disappear into the air band as the refractive index contrast of the defect increases for both square and hexagonal 2D PhCs. On the other hand, in rod type defects, it is observed that the defect mode appears nearer to the air band and moves towards the dielectric band as the refractive index contrast of the defect increases and disappears into the dielectric band. The E- field distribution is calculated for hole type defects and rod-type defect for both square, and hexagonal lattice of 2D PhCs. A monopole nature in the hole- type defect and a dipole nature in the rod- type defect for both square and hexagonal 2D PhCs is observed in the E-field distribution. The E- field strength is found to be higher in the defect created in a hexagonal lattice 2D PhC, where the rod-type defect has a higher maximum E- field value compared to a hole-type defect. These calculations are used to understand the PhC properties for different lattice symmetry and to optimize the bandgap by varying the structural parameters, and shed light on the nature of different types of defect modes and the corresponding E-filed enhancements.

In chapter 4, the numerical simulations of the E- field distributions in the thin CPhCs are investigated. The internal E- field distribution is investigated in monolayer, bilayer, and trilayer PSPhC thin films. Additionally, the effect of excitation wavelength that lies in different spectral regime, viz. on-resonance and off-resonance wavelengths on the E- field distribution in PSPhC thin films is studied. At the on-resonance wavelength, it is observed that the E- field remains localized and is enhanced in the air void regions between the closely packed spheres in the PSPhC thin films. The maximum E- field values remain almost the same and are unaffected by the addition of layers along the direction of light propagation. Conversely, at the

off-resonance wavelength, a significant variation in the internal E- field distribution is observed among the crystal planes of monolayer, bilayer, and trilayer CPhC thin films. Specifically, the E- field remains localized within the dielectric sphere regions in monolayer and bilayer PSPhC thin films, while it propagates within the crystal plane of the trilayer. An increase in the maximum E- field value is observed in the monolayer compared to the bilayer at the off-resonance wavelength, whereas E- field becomes significantly high (not at well-defined locations but random sites) in trilayer PSPhC. It has been noted that the mechanisms contributing to the field enhancement at the wavelengths considered primarily involve changes in the photonic band structure and random scattering from colloidal spheres. The selection of incident wavelength has been found to significantly influence enhanced E- field at specific CPhC sites, offering potential applications in various CPhC-based templates for sensing.

In chapter 5, a part of the numerical studies carried out in Chapter 4 are experimentally verified using Raman spectroscopic studies. The study on the effect of thin PSPhCs on the Raman signal enhancement is systematically carried out. The fabrication and characterization of the PSPhC monolayer is described. The Raman spectroscopic studies are carried out using an on-resonance excitation wavelength of 633 nm for Methylene blue (MB) dye molecules (test analyte molecule) are presented. The Raman signal intensity of MB is measured on a bare glass substrate and on a PSPhC template, and the signal intensities are compared and percentage enhancement (%E) is calculated. The %E for the peak 448 cm⁻¹ and 1626 cm⁻¹ are calculated as 186 % and 136% respectively for the PSPhC template compared to the bare glass substrate. The lowest concentration detected on the PSPhC monolayer template is 50 μM whereas on the bare glass substrate is 500 μM. The lowest concentration of MB detected on the PSPhC monolayer template is found to be same as that detected on the randomly distributed AuNPs on a glass substrate. The EM simulations close to the experimental conditions are performed for the bare glass substrate, PSPhC monolayer and AuNP placed on a glass

substrate, and are presented in this chapter. The relative electric field (|E/E_{inc}|) is plotted to understand the E- field distribution and enhancement in these templates. For the uniform glass substrate, a uniform E- field distribution is observed whereas the E- field is redistributed on the PSPhC monolayer in such a way that the maximum E-field is localized and enhanced in the wedge regions of the voids at on-resonance excitation. The mechanism in which the Raman signal enhancement occurs for a PSPhC monolayer template is explained in detail. When the analyte molecules experience the higher E- field at the wedge regions of the PSPhC monolayer, it exhibit an enhanced Raman signal intensity, favoring the detection of lower concentrations. The comparison of the E- field enhancement in the PSPhC monolayer and a AuNP is presente in this chapter. The AuNP showed plasmonic resonance at light excitation and hence forming hotspots on the surface of the AuNP on the opposite poles along the E- field polarization direction. The maximum E-field value on the AuNP hotspot is found to be almost same as that of the maximum E-field value on the PSPhC monolayer. Hence, these investigations suggested that PSPhC template can replace the randomly distributed AuNPs based SERS substrate.

In chapter 6, a systematic investigation of the combined effect of thin PSPhC monolayer and AuNPs for the detection of dye molecules using SERS technique is presented. The utilization of PSPhC monolayer decorated with AuNPs as the template for the detection of analytes such as MB, R6G and MG using SERS studies is described in detail. MB has been taken as the analyte molecule for the case study. Significant enhancement in the SERS peak of MB is observed by employing PSPhC monolayer- AuNPs template as compared to the Glass-AuNPs substrate. The lowest concentration of MB is detected as low as 500 nM, which is a hundred times lower than the lowest concentration detected when Glass -AuNPs are used as the substrate. PSPhC monolayer -AuNPs templates are also found to enhance the SERS signals from R6G and MG dyes. The lowest concentration detected are 500 nM and 50 nM for R6G and MG, respectively. The EM simulations to understand the effect of PSPhC monolayer-

AuNP template in enhancing the Ramn signal of the analyte molecules are also presented in this chapter. The simulation details of the calculation of normalized E- field distributions on the PSPhC monolayer template with and without AuNP are explained. Observations show that the E- field becomes localized and enhanced at the wedge regions between touching particles in the PSPhC monolayer array when excited at an on-resonance wavelength. AuNPs placed at these wedge regions experience enhanced E- fields, leading to amplified SERS signals that effectively lower detection limits.

Chapter 7 summarizes the findings and conclusions drawn from the research work carried out for this thesis. The future scope of work is also discussed.

7.2 Key Findings of the Thesis

- 1. A laser diffraction set-up has been built and using which the structure factor and symmetry of the CPhC have been investigated. The CPhC are shown to exhibit hexagonal symmetry with fcc structure, which is verified by FESEM studies.
- 2. By performing electromagnetic simulations on CPhC films (monolayer by layer and trilayer) it is shown that, at on-resonance wavelength (wavelength within the stop band) the E- field remains localized and gets enhanced in the air void regions between the close-packed spheres in the CPhC thin films where the maximum E- field values remain nearly the same and become independent of the addition of layers along the direction of propagation of light.
- 3. The internal E-field distribution is calculated at off-resonance wavelength (wavelength outside stop band), and is shown that, the E- field vary significantly in the crystal planes of monolayer, bilayer, and trilayer CPhC thin films. The E-field is found to remain localized within the dielectric sphere regions in monolayer and bilayer CPhC thin films whereas it was to propagate in the crystal plane of the trilayer at off-resonance conditions.

- 4. Raman scattering experiments are carried out to understand the effect of PSPhC monolayer templates in the enhancement of the Ramn signal of the analyte molecules (MB). The Raman signal of the MB molecules showed significant enhancement when the PSPhC monolayer template is employed, compared to the bare glass substrate. Whereas the lowest concentration of the analyte detected using PSPhC monolayer is found to be same as that detected on randomly distributed AuNPs on a glass substrate. This investigation suggests that, the PSPhC template can serve as an alternative AuNPs based SERS substrate.
- 5. The Raman scattering experiments of dye molecules has been carried out on a PSPhC monolayer template decorated with AuNPs. A Significant enhancement in the SERS signal of MB is observed for PSPhC monolayer AuNPs as compared to the Glass AuNPs substrate. As a result of enhancement, we could determine the lowest concentration MB to be as low as 500 nM, which is a hundred times lower than the lowest concentration detected when Glass -AuNPs are used as the substrate. PSPhC monolayer -AuNPs templates are also found to enhance the SERS signals from Rhodamine 6G (R6G) and Malachite green (MG) dyes. The lowest concentration detected are 500 nM and 50 nM for R6G and MG, respectively.
- 6. The E- field distribution is calculated numerically for PSPhC monolayer template with and without AuNPs at on- resonance condition. It has been observed that the E- field gets localized and enhanced at the wedge regions of the touching particles in the PSPhC monolayer array at an excitation wavelength of 633 nm (on-resonance wavelength). AuNPs trapped at the wedge regions experience enhanced E- fields resulting in increased SERS signals, which in turn help in pushing the detection limits to significantly lower concentrations.

7.3 Scope for Future studies

- 1. Thin photonic crystal templates with higher refractive index contrast, for larger E- field enhancement helps in the detection of explosives and biomolecules in trace concentrations. Simulations and experiments constitute the future study.
- 2. Fabricating 2D and 3D photonic crystals with engineered defects coupled with plasmonic nanostructures for higher E- field confinement and enhancement and testing for SERS detection constitute future scope of study.
- **3.** Studies on inverse opal photonic crystals as potential templates for SERS based detection by decorating with plasmonic particles, and the electromagnetic simulations to understand the enhanced E- field regions, constitute an important future study with practical application.
- **4.** Fabrication of 2D photonic crystals (air holes in a material vs. rods in air matrix) though e- beam lithography technique to experimentally verify the defect mode properties.
- **5.** Fabrication of gel immobilized (portable) colloidal photonic crystals for biosensing applications constitute an important study.

Publications Related to Thesis

- Pratyasha Sahani, Saranya Narayanan, B.V.R. Tata, Soma Venugopal Rao, "Numerical simulation of internal electric field distribution in colloidal photonic crystal thin films", Optics Communications, 528, 129026 (2023).
- Saranya Narayanan, Pratyasha Sahani, Jagnnath Rathod, B.V.R. Tata, Soma Venugopal Rao, and Ramachandrarao Yalla "Thin photonic crystal template for enhancing the SERS signal: Case study using low concentrations of dye molecules." *Phys. Scr.*, 99, 035512 (2024)
- 3. Saranya Narayanan and B. V. R. Tata, "Effect of doping on defect modes of 2D photonic band gap crystals", AIP Conference Proceedings 2269, 030015 (2020)

Workshops/Conferences attended

- 7. Saranya Narayanan, M.B. Bhavya, K. Lakshun Naidu, G. Krishna Podagatlapalli, Santhosh Kumar Balivada, and B.V.R Tata, "Detection of Dye Molecules Through Photonic Crystal Assisted Surface Enhanced Raman Scattering", 67th DAE Solid State Physics Symposium (DAE SSPS23), Vishakhapatnam, India, December 20-24, 2023
- 8. **Saranya Narayanan**, Nishant Shankhwar and B.V.R Tata, "Indigenous Development of Laser Diffraction Setup for Characterizing the Structure of Polystyrene colloidal crystals", **Frontiers in Physics (FIP-2023)**, **Hyderabad**, India, March 3-4, 2023.
- Saranya Narayanan, Nishant Shankhwar and B.V.R Tata, "Indigenous Development of Laser Diffraction Setup for Characterizing the Structure of Photonic crystals",
 International Conference on Frontier Areas of Science and Technology (ICFAST-2022), 12th India-Japan Science and Technology Conclave, Hyderabad, India, September 09-10, 2022. (Best Poster Award)
- 10. Saranya Narayanan, Pratyasha Sahani, B.V.R. Tata, and Soma Venugopal Rao, "Thin Photonic Crystal Templates with Plasmonic Nanoparticles for Trace Molecule

- Detection using Surface Enhanced Raman Spectroscopy", **DAE-BRNS National**Laser Symposium (NLS-30), Mumbai, India, January 19-22, 2022. (Oral Presentation) (Best Poster Award)
- 11. Saranya Narayanan *and* B. V. R. Tata, "Effect of doping on defect modes of 2D photonic band gap crystals", International Conference on Multifunctional Materials (ICMM-2019), Hyderabad, India, December 19-21, 2019
- 12. **Saranya Narayanan** *and* B. V. R. Tata, "Effect of Doping on the Reflection Spectra of 2D Photonic Band Gap Crystals", **Pressing for Progress-2019**, An IPA National conference towards gender equity in Physics, Hyderabad, India, September 19-21, 2019
- 13. Attended "Soft and Active matter" workshop conducted by School of Physics, University of Hyderabad on 11-17 February, 2018.

Plagiarism-free statement

Applications: Modelling, Fabrication, and Experiments" submitted by Ms. Saranya Narayanan (Reg. No. 17PHPH30) has been screened by the Turnitin software at the Indira Gandhi Memorial Library of the University of Hyderabad. The software shows a 31% similarity index out of which 22% came from the candidate's own three research articles related to this thesis, which are already published and available online. From the detailed similarity index report, it is obvious that the remaining 9% of the similarity index is due to the resemblance caused by the frequent use of the well-known standard terms such as, colloidal photonic crystal, normalized electric field distribution, surface enhanced Raman spectroscopy, localised surface plasmon resonance, electrostatic interaction, etc. The use of such terms is rampant in the literature and hence it is not surprising that the similarity index is artificially inflated. It should be noted that the use of such standard terms cannot be avoided.

Prof. Ramachandrarao Yalla 05/07/24

Co-supervisor

School of Physics

University of Hyderabad

Dr. RAMACHANDRARAO YALLA Assistant Professor School of Physics University of Hyderabad Hyderabad, INDIA - 500 046

Date: 05/07/2024

Photonic Crystal Templates for Sensing Applications: Modelling Fabrication and Experiments

by Saranya Narayanan

Librarian

Indira Gandhi Memorial Library UNIVERSITY OF HYDERABAD

Central University P.O. HYDERABAD-500 046

Submission date: 05-Jul-2024 03:02PM (UTC+0530)

Submission ID: 2412762751

File name: SARANYA_NARAYANAN.pdf (7.09M)

Word count: 35123 Character count: 185111

Photonic Crystal Templates for Sensing Applications: Modelling Fabrication and Experiments

ORIGINALITY REPORT

SIMILARITY INDEX

INTERNET SOURCES

PUBLICATIONS

STUDENT PAPERS

PRIMARY SOURCES

Saranya Narayanan, Pratyasha Sahani, Jagannath Rathod, Venugopal Rao Soma, Ramachandrarao Yalla, B.V.R Tata. "Thin photonic crystal templates for enhancing the SERS signal: A case study using very low concentrations of dye molecules.", Physica AMACHANDRARAO YALLA

Scripta, 2024

Publication

Assistant Professor School of Physics University of Hyderabad Hyderabad, INDIA - 500 046

Pratyasha Sahani, Saranya Narayanan, B.V.R. Tata, Soma Venugopal Rao. "Numerical simulation of internal electric field distribution in colloidal photonic crystal thin films", Communications, 2022

Publication

3

Dr. RAMACHANDRARAO YALLA

Assistant Professor School of Physics

Saranya Narayanan, Pratyasha Sahari Piversity of Hyderabad Saranya Narayanan, Pratyasha Sahari Piversity of Hyderabad Saranya Narayanan, Pratyasha Sahari Piversity of Hyderabad Jagannath Rathod, Venugopal Rao Soma, Ramachandrarao Yalla, B V R Tata. "Thin photonic crystal templates for enhancing the Wavaladow SERS signal: a case study using very low concentrations of dye molecules", Physica Scripta, 2024

Dr. RAMACHANDRARAO

Assistant Professor School of Physics University of Hyderabad Hyderabad, INDIA - 500 046

4	Saranya Narayanan, B. V. R. Tata. "Effect of doping on defect modes of 2D photonic band gap crystals", AIP Publishing, 2020	1% lavalander 05/07/24
5	Hyderabad Assi Sci	CHAND ARAO YALLA stant Professor nool of Physies sity of Hyderabad ad, INDIA - 500 046
6	lib.buet.ac.bd:8080 Internet Source	<1%
7	eprints.soton.ac.uk Internet Source	<1%
8	www.dartmouth.edu Internet Source	<1%
9	ab-initio.mit.edu Internet Source	<1%
10	www.db-thueringen.de Internet Source	<1%
11	Akhilesh K. Arora, B.V.R. Tata. "Interactions, structural ordering and phase transitions in colloidal dispersions", Advances in Colloid and Interface Science, 1998 Publication	<1%
12	D. Karthickeyan, R. G. Joshi, B. V. R. Tata. "FCC-HCP coexistence in dense thermo-	<1%

responsive microgel crystals", The Journal of Chemical Physics, 2017 Publication

13	Hanbin Zheng, Serge Ravaine. "Bottom-Up Assembly and Applications of Photonic Materials", Crystals, 2016 Publication	<1%
14	hdl.handle.net Internet Source	<1%
15	Submitted to University of Nottingham Student Paper	<1%
16	Uttara Biswas, Chittaranjan Nayak, Jayanta Kumar Rakshit. "Fabrication techniques and applications of two-dimensional photonic crystal: history and the present status", Optical Engineering, 2022	<1%
17	www.nature.com Internet Source	<1%
18	Van Nostrand's Scientific Encyclopedia, 1995.	<1%
19	mts.intechopen.com Internet Source	<1%
20	"Springer Handbook of Materials Measurement Methods", Springer Science and Business Media LLC, 2006 Publication	<1%

21	B.V.R. Tata, P.S. Mohanty, J. Yamanaka, T. Kawakami. "Dynamic Light Scattering Studies in Silica/Ethylene Glycol Charged Colloidal System", Molecular Simulation, 2006	<1%
22	export.arxiv.org Internet Source	<1%
23	old.duet.ac.bd Internet Source	<1%
24	Submitted to University of Leicester Student Paper	<1%
25	Tao Li, Guiju Liu, Hao Kong, Guozheng Yang, Gang Wei, Xin Zhou. "Recent advances in photonic crystal-based sensors", Coordination Chemistry Reviews, 2023	<1%
26	epdf.tips Internet Source	<1%
27	Alexander Tikhonov, Rob D. Coalson, Sanford A. Asher. "Light diffraction from colloidal crystals with low dielectric constant modulation: Simulations using single- scattering theory", Physical Review B, 2008 Publication	<1%
28	Basu, . "Z", Dictionary of Material Science and High Energy Physics, 2001.	<1%

29	Bing Liu, Hosein Monshat, Zhongze Gu, Meng Lu, Xiangwei Zhao. "Recent advances in merging photonic crystals and plasmonics for bioanalytical applications", The Analyst, 2018 Publication	<1%
30	Jianqing Wang, Qiong Wang. "Body Area Communications", Wiley, 2012	<1%
31	dspace.uohyd.ac.in Internet Source	<1%
32	www.science.gov Internet Source	<1%
33	"Reviews in Plasmonics 2017", Springer Science and Business Media LLC, 2019	<1%
34	Song-Yuan Ding, En-Ming You, Zhong-Qun Tian, Martin Moskovits. "Electromagnetic theories of surface-enhanced Raman spectroscopy", Chemical Society Reviews, 2017	<1%
35	Organic and Hybrid Photonic Crystals, 2015.	<1%
36	upcommons.upc.edu Internet Source	<1%

37	tuat.repo.nii.ac.jp Internet Source	<1%
38	Submitted to Higher Education Commission Pakistan Student Paper	<1%
39	Junlong Liao, Changqing Ye, Prajwal Agrawal, Zhongze Gu, Yu Shrike Zhang. "Colloidal Photonic Crystals for Biomedical Applications", Small Structures, 2021	<1%
40	"Electric and Magnetic Fields", Springer Nature, 1995	<1%
41	nemertes.library.upatras.gr	<1%
42	Alferenok, Artem(Lüdtke, Ulrich, Nacke, Bernard and Töpfer, Hannes). "Numerical simulation and optimization of the magnet system for the Lorentz Force Velocimetry of low-conducting materials", Digitale Bibliothek Thüringen, 2013.	<1%
43	Submitted to University of Nevada Reno Student Paper	<1%
	Submitted to University of Surrey	

45	www.peertechz.com Internet Source	<1%
46	I. V. Ketov, A. O. Spiridonov, A. I. Repina, E. M. Karchevskii. "Numerical Modeling of Lattice Modes of Photonic-Crystal Lasers by Galerkin Method with Exact Matrix Elements", Lobachevskii Journal of Mathematics, 2023	<1%
47	Richard Osgood, Xiang Meng. "Principles of Photonic Integrated Circuits", Springer Science and Business Media LLC, 2021 Publication	<1%
48	dyuthi.cusat.ac.in Internet Source	<1%
49	macsphere.mcmaster.ca Internet Source	<1%
50	Nathan Ida. "Engineering Electromagnetics", Springer Science and Business Media LLC, 2021	<1%
51	S. Kronholz. "Self-Assembly of Diblock- Copolymer Micelles for Template-Based Preparation of PbTiO3 Nanograins", Advanced Functional Materials, 12/04/2006	<1%
52	studentsrepo.um.edu.my Internet Source	<1%

53	D. Szymanski, S. Patela. "Modelling of photonic crystals", Proceedings of 2005 International Students and Young Scientists Workshop Photonics and Microsystems, 2005., 2005 Publication	<1%
54	Partially Ordered Systems, 2011. Publication	<1%
55	researchrepository.wvu.edu Internet Source	<1%
56	Submitted to Imperial College of Science, Technology and Medicine Student Paper	<1%
57	Johannes Elschner. Inverse Problems, 12/01/2001 Publication	<1%
58	M.A. Butt, S.N. Khonina, N.L. Kazanskiy. "Recent advances in photonic crystal optical devices: A review", Optics & Laser Technology, 2021 Publication	<1%
59	Submitted to Universiti Teknologi MARA Student Paper	<1%
60	Zhongyu Cai, Zhiwei Li, Serge Ravaine, Mingxin He, Yanlin Song, Yadong Yin, Hanbin Zheng, Jinghua Teng, Ao Zhang. "From	<1%

colloidal particles to photonic crystals: advances in self-assembly and their emerging applications", Chemical Society Reviews, 2021 Publication

61	"Printable Solar Cells", Wiley, 2017 Publication	<1%
62	Submitted to Savitribai Phule Pune University Student Paper	<1%
63	Soifer, . "Photonic crystals and light focusing", Diffractive Nanophotonics, 2014.	<1%
64	Xie, Ting, Guannan Liu, Baomei Wen, Jong Yoon Ha, Nhan V. Nguyen, Abhishek Motayed, and Ratan Debnath. "Tunable ultraviolet photoresponse in solution- processed p-n junction photodiodes based on transition metal oxides", ACS Applied Materials & Interfaces Publication	<1%
65	ar.scribd.com Internet Source	<1%
66	gyan.iitg.ac.in Internet Source	<1%
67	www.prolekare.cz Internet Source	<1%
68	www.vcbio.science.ru.nl Internet Source	

		<1%
69	Tiantian Yin, Zhun Wei, Xudong Chen. "Wavelet Transform Subspace-based Optimization Method for Inverse Scattering", IEEE Journal on Multiscale and Multiphysics Computational Techniques, 2018 Publication	<1%
70	Submitted to Universiti Teknologi Petronas Student Paper	<1%
71	Submitted to Visvesvaraya National Institute of Technology Student Paper	<1%
72	link.springer.com Internet Source	<1%
73	pubs.rsc.org Internet Source	<1%
74	spectrum.library.concordia.ca Internet Source	<1%
75	Nanostructure Science and Technology, 2014.	<1%
76	Rui Bastos, Sofia R. Fernandes, Ricardo Salvador, Cornelia Wenger, Mamede A. de Carvalho, Pedro C. Miranda. "The effect of inter-electrode distance on the electric field distribution during transcutaneous lumbar	<1%

spinal cord direct current stimulation", 2016 38th Annual International Conference of the IEEE Engineering in Medicine and Biology Society (EMBC), 2016
Publication

77	Thierry Letertre, Vikass Monebhurrun, Zeno Toffano. "Electromagnetic field measurements of WIMAX systems using isotropic broadband probes", 2011 IEEE MTT- S International Microwave Symposium, 2011 Publication	<1%
78	Submitted to University of Texas, Austin Student Paper	<1%
79	digitalscholarship.unlv.edu Internet Source	<1%
80	openaccess.city.ac.uk Internet Source	<1%
81	zqtian.xmu.edu.cn Internet Source	<1%
82	Jian-Feng Li, Yue-Jiao Zhang, Song-Yuan Ding, Rajapandiyan Panneerselvam, Zhong-Qun Tian. "Core-Shell Nanoparticle-Enhanced Raman Spectroscopy", Chemical Reviews, 2017	< <mark>1</mark> %
83	Lanying Yang, Chengang Hu, Ping Gao, Xiangang Luo. "Self-similar Chain of	<1%

Nanocrescents with Giant Electric Field Enhancement as a Novel Plasmonic Resonator", 2008 IEEE PhotonicsGlobal@Singapore, 2008 Publication

84	doi.org Internet Source	<1%
85	Ary O. Cavalcante. "Raman band shape analysis of a low temperature molten salt", The Journal of Chemical Physics, 2003 Publication	<1%
86	Barretta, Paolo, Federico Bordi, Cristina Rinaldi, and Gaio Paradossi. "A Dynamic Light Scattering Study of Hydrogels Based on Telechelic Poly(vinyl alcohol)", The Journal of Physical Chemistry B, 2000.	<1%
87	Busch, K "Periodic nanostructures for photonics", Physics Reports, 200706	<1%
88	Glauco R. Souza, J. Houston Miller. "Chapter 2 Elastic Light Scattering of Biopolymer/Gold Nanoparticles Fractal Aggregates", Springer Science and Business Media LLC, 2012 Publication	<1%
89	Jelena Mitrić. "Properties and characterization of rare-earth-activated phosphors", Elsevier	<1%

Publication

Submitted to Loughborough University 90 Student Paper

<1_%

Thomas Eversberg, Klaus Vollmann. 91 "Spectroscopic Instrumentation", Springer Science and Business Media LLC, 2015

Publication

Xuefeng Ding, Jingzhe Zhao, Yanhua Liu, 92 Hengbin Zhang, Zichen Wang. "Silica nanoparticles encapsulated by polystyrene via surface grafting and in situ emulsion polymerization", Materials Letters, 2004 Publication

<1%

Exclude quotes On Exclude bibliography On Exclude matches

< 14 words